SURFACE ENGINEERED CATALYSTS FOR EFFECTIVE PHOTO-CONVERSION AND UTILIZATION OF GREENHOUSE GASES

A Dissertation

by

XUHUI FENG

Submitted to the Graduate and Professional School of
Texas A&M University
in partial fulfillment of the requirements for the degree of

DOCTOR OF PHILOSOPHY

Chair of Committee,	Ying Li
Committee Members,	Matt Pharr
	Choongho Yu
	Hong-Cai Zhou
Head of Department,	Guillermo Aguilar

May 2022

Major Subject: Mechanical Engineering

ABSTRACT

Global warming and climate change are among the most critical issues in the 21st century. Emission control of CO_2 and CH_4, the top two greenhouse gases, is the key to dealing with those issues. As one of the most promising greenhouse gas control techniques, direct greenhouse gas conversion/utilization can be an economically-friendly option to mitigate greenhouse gas emissions.

In this dissertation, innovative catalyst designs in two greenhouse gas conversion/utilization processes, namely, CO_2 photoreduction on TiO_2-based catalysts and photo-thermal-chemical dry reforming of methane (PTC-DRM) on Pt/CeO_2-based catalysts, for performance enhancements are demonstrated and discussed.

In the CO_2 photoreduction process, the low catalyst surface-CO_2 affinity is one of the major factors that limit the CO_2 photoreduction performance on TiO_2 catalysts. In this dissertation, a highly porous TiO_2 material derived from MOF material MIL-125 was prepared, which showed a CO_2 photoreduction performance that is 4.2 times as high as commercialized P25 material under a 400 W Xe-lamp irradiation. To further enhance the CO_2 photoreduction performance, three types of alkali surface modifications with MgO, namely, (1) MgO ALD coating, (2) MgO ALD coating/Ag co-modifications, and (3) MgO doping, were applied on the porous TiO_2. All of the modifications were found to substantially enhance the CO_2 photoreduction performance up to ~60 times performance improvements compared with P25 materials.

In the PTC-DRM process, the occurrence of side reaction reverse water-gas shift reaction has long been an issue that affects the performance, especially the low H_2/CO production ratio, of DRM catalysts. This dissertation applied Pt/CeO_2 catalyst as an example and demonstrated a

simple approach to improve both H_2/CO production ratio and PTC-DRM reactivity by applying acidic metal oxide Al_2O_3 in catalyst preparation. Thanks to the favorable Al_2O_3-CeO_2 synergetic effects, under a reaction temperature of 700 ℃ with 30-sun equivalent solar irradiation, the Pt/Al_2O_3-CeO_2 catalyst exhibits a near-unity H_2/CO production ratio and 39.6% and 80.0% improvements in CO and H_2 generation efficiencies, respectively, compared with Pt/CeO_2 catalyst.

The demonstrated innovations should be directly transferable to advance catalytic greenhouse conversions/utilizations in mitigating greenhouse gas emissions and provide guidelines in catalyst design in other photo-driven and/or thermal-driven catalytic processes.

ACKNOWLEDGEMENTS

First and foremost, I would first express my gratitude to my Ph. D. research advisor, Dr. Ying Li, for giving me an opportunity to study in his group, for his continuous support of my Ph. D. study and research, for his patience, motivation, enthusiasm, and immense knowledge, and for his enormous advice to me in helping me improve research and teaching. I am fortunate to work with him.

My gratitude is extended to my committee members, Dr. Matt Pharr, Dr. Choongho Yu, and Dr. Hong-Cai Zhou, for their suggestions and advice on improving this dissertation. I also thank Dr. Hong-Cai Zhou for his kindness to share the BET surface area analyzer in his group for material surface area characterizations in Chapters 2 and 4.

I thank my colleagues at Texas A&M University, Dr. Fuping Pan, Dr. Wei Deng, Dr. Peng Zhang, Dr. Huilei Zhao, Dr. Xianmei Xiang, Dr. Chao Li, and Mr. Zichen Du, for the valuable help and useful discussions in research. Special thanks to Dr. Fuping Pan, who put great effort into material characterizations.

My thankfulness is also extended to my research group members in the Laboratory for Low Carbon Energy and Sustainable Environment at Texas A&M University, Dr. Fuping Pan, Dr. Wei Deng, Dr. Huilei Zhao, Dr. Xianmei Xiang, Dr. Chao Li, Mr. Xiaoyu Zheng, Mr. Zichen Du, Mr. Tianzhu Fan, Mr. Yang Gang, Mr. John E. Pellessier, and Mr. Manuel Suarez, for making an encouraging and motivating working environment to support my doctoral studies.

Lastly, I am thankful to my wife, son, my parents and parents-in-law, and my extended family members. The enormous support from family is critical in my graduate studies.

CONTRIBUTORS AND FUNDING SOURCES

Contributors

This Ph.D. dissertation was supervised by a dissertation committee consisting of Drs. Ying Li, Matt Pharr, Choongho Yu of J. Mike Walker ’66 Department of Mechanical Engineering and Dr. Hong-Cai Zhou of the Department of Chemistry and the Department of Material Science and Engineering.

In Chapter 2, the SEM and EDS characterizations were performed by Drs. Huilei Zhao and Wei Deng; material characterizations in TEM, UV-Vis-NIR, XPS, and photocurrent density were performed by Dr. Fuping Pan. BET surface area measurements were conducted by Dr. Peng Zhang.

In Chapter 3, Dr. Fuping Pan conducted material characterizations in TEM, UV-Vis-NIR, XPS, photocurrent density, and EIS Nyquist.

In Chapter 4, Dr. Fuping Pan performed material characterizations in TEM, UV-Vis-NIR, XPS, and photocurrent density; BET surface area measurements were conducted by Dr. Peng Zhang; Dr. Xiao Wang helped to conduct ICP-MS characterizations.

In Chapter 5, EDS analyses were performed by Dr. Wei Deng, Dr. Erik Sarnello conducted TEM characterizations, Mr. Cullen R. Petru assisted to obtain part of *in situ* DRIFTS results under methane atmosphere, and Mr. Zichen Du performed XPS measurements.

Instrument operations in TEM, SEM, UV-Vis-NIR, XPS by Drs. Huilei Zhao, Fuping Pan, Wei Deng, and Mr. Zichen Du were performed at the Material Characterization Facility at Texas A&M University. TEM characterizations by Dr. Erik Sarnello were performed at Argonne

National Laboratory. All other works, including material characterizations, data acquisitions, and data analyses, were completed by the student independently.

Funding Sources

The majority of the financial support on this dissertation was provided by the United States National Science Foundation under Grant Numbers CBET 1538404 and CBET 1924466. This dissertation was also partially supported by the 2020 Graduate Summer Research Grant and 2020 Preparing for Future Faculty in Mechanical Engineering (PF2ME) Fellowship, both were sponsored by J. Mike Walker ’66 Department of Mechanical Engineering at Texas A&M University.

NOMENCLATURE

O_A	Adsorbed oxygen
ALD	Atomic layer deposition
BET	Brunauer–Emmett–Teller
CTAB	Cetyl trimethyl ammonium bromide
DRIFTS	Diffuse reflectance infrared Fourier-transform spectroscopy
DRM	Dry reforming of methane
DMF	Dimethyl formamide
e^-	Photoexcited electron
E_a	Activation energy
FESEM	Field emission scanning electron microscope
EIS	Electrochemical impedance spectroscopy
FID	Flame ionization detector
GC	Gas chromatography
h^+	Photoexcited hole
H_2BDC	Terephthalic acid
ICP-MS	Inductively coupled plasma mass spectrometry
ITO	Indium doped tin oxide
MA	Magnesium adsorption
MOF	Metal-organic frameworks
NP	Nanoparticles
O_L	Lattice oxygen

PL	Photoluminescence
PTC-DRM	Photo-thermal-chemical dry reforming of methane
RWGS	Reverse water-gas shift
sccm	Standard cubic centimeter per minute
SEM	Scanning electron microscope
SMR	Steam methane reforming
TCD	Thermal conductivity detector
TEM	Transmission electron microscope
TTIP	Titanium tetra isopropoxide
USP	Ultrasonic spray pyrolysis
UV-Vis-NIR	Ultraviolet-visible-near-infrared
V_O	Oxygen vacancy
WI	Wet impregnation
XPS	X-ray photoelectron spectroscopy
XRD	X-ray diffraction

TABLE OF CONTENTS

Page

LIST OF FIGURES

Page

LIST OF TABLES

Page

1. INTRODUCTION

Over the past 150 years, mankind has witnessed the largest scale of greenhouse gases emission in history. Carbon dioxide (CO_2) and methane (CH_4) are the top two greenhouse gases [1, 2]. According to the United States Environmental Protection Agency, in 2019 in the United States alone, more than 6 million metric tons of greenhouse gases were emitted [3]. The environmental consequences, including climate change and global warming, as the result of greenhouse gas over-emission, has become one of the most serious concerns in the 21st century. Among all of the greenhouse emission, CO_2 is responsible for 80% of total emission, while CH_4 ranks the second, accounting for 10% [4], largely due to human activities [3]. Despite the lower proportion of CH_4 than that of CO_2, CH_4 is more than 25 times as potent as CO_2 in trapping heat [5], making it an even more powerful greenhouse gas than CO_2. To mitigate greenhouse gases related environmental complications, effective control of CO_2 and CH_4 is a crucial step.

In this dissertation, innovative catalyst designs in two photo-driven/photo-assisted greenhouse gas conversion/utilization processes, namely, (1) photocatalytic CO_2 reduction and (2) photo-thermal-chemical dry reforming of methane (PTC-DRM), are demonstrated and discussed.

1.1. Photocatalytic CO_2 reduction

Currently, the most dominant approach to deal with CO_2 emission is carbon capture and storage (CCS) [6], where CO_2 is separated from other gases produced in industrial processes, such as coal-powered electricity generation, and then stored underground in permanent containers [7]. While the CCS process offers a rapid solution for CO_2 emission reduction, the cost required to process and store the capture CO_2 could make this process economically disadvantageous [8].

Compared with CO_2 capture and storage process, CO_2 reduction and conversion process, where CO_2 is converted into clean fuels and value-added chemicals (CO, methanol, formic acid, etc.), can be a promising way for CO_2 emission control while producing valuable chemicals as products [9, 10]. As of now, techniques including electrochemical CO_2 reduction [11, 12], photocatalytic CO_2 reduction [13-15], CO_2 hydrogenation [16, 17], etc., have been developed. Among all of the available approaches, photocatalytic CO_2 reduction process, which utilizes free and abundant solar energy to activate chemical reactions under mild reaction conditions, is a promising method for cost-effective CO_2 conversion into value-added chemicals and fuels [18-20].

Figure 1-1 illustrates a typical process for photocatalytic CO_2 reduction. In the photocatalytic CO_2 reduction process, CO_2 molecules are firstly adsorbed on the surface of a photocatalyst. Upon the excitation of incident photons with appropriate energy, the photocatalyst generates pairs of electrons and holes, which are transferred to the conduction band and the valance band of the photocatalyst, respectively [21]. The photoexcited electrons are capable to participate in CO_2 reduction reactions and produce valuable chemicals and fuels including CO, CH_4, HCOOH, CH_3OH, etc. [22] In the CO_2 photoreduction process, a reducing agent is also applied to scavenge the photogenerated holes and balance the surface charge [23]. Due to the abundancy and low-cost properties, water vapor (H_2O) is the most widely used [9]. The hole scavenging process with water vapor leads to the production of oxygen molecules [24].

Up to now, a variety of photocatalyst materials such as TiO_2 [25-28], BiOCl [29], ZrO_2 [30], and metal-organic frameworks [31, 32] have been reported for applications in CO_2 photoreduction processes. Among the wide range of available photocatalysts, TiO_2 is the most studied for CO_2 photoreduction because of its merits including chemical stability, nontoxicity, high

oxidizing power, low-cost as well as abundant supply [33-35]. However, many drawbacks of TiO_2, including (1) limited CO_2 adsorption capacity, (2) fast recombination of photo-induced holes and electrons, and (3) wide band gap (3.0 eV for rutile and 3.2 eV for anatase), restrict photoactivity of TiO_2 and narrow the applications of TiO_2 in photocatalytic CO_2 reduction [9, 18, 33].

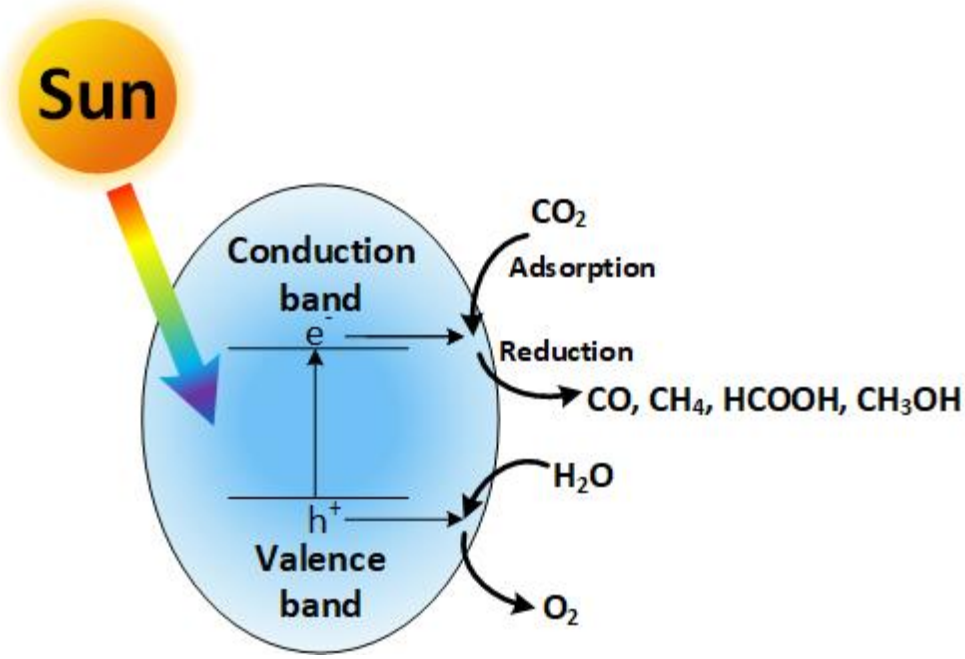

Figure 1-1 Schematic illustration of photocatalytic CO_2 reduction process with water vapor.

To overcome the drawbacks of TiO_2 materials and enhance the CO_2 photoreduction performance, several TiO_2 surface engineering/modification approaches have been applied [33, 36-38]. Among them, alkali modification on TiO_2, noble metal deposition on TiO_2, and heteroatom doping in TiO_2 have been widely investigated [9, 22, 39].

1.1.1. Alkali modification on TiO_2

As a gas-solid heterogeneous catalytic process, the photocatalytic CO_2 reduction can

expect a significant enhancement by improving the adsorption of CO_2 on the TiO_2 surface [40]. Since CO_2 is a type of Lewis acid, alkali modification on the TiO_2 surface can be considered as one of the most influential approaches to improve the adsorption of CO_2 on the TiO_2 surface [24]. The alkali modification does not merely enhance the CO_2 uptake amount, but also strengthen the bonding between the CO_2 with the catalyst surface through the chemisorption process, which can lead to an improved CO_2 photoreduction performance [24].

As for the approach of alkali modifications, recently, TiO_2 amine functionalization has been demonstrated as an effective way to enhance the CO_2 chemisorption capability of TiO_2 photocatalyst [41, 42]. For example, Liao *et al.* [43] developed a type of amine-rich TiO_2 catalyst by attach monoethanolamine on TiO_2 material (MEA-TiO_2). CO_2 adsorption test shows that the CO_2 uptake capability of the MEA-TiO_2 is nearly 8 times compared with that of pristine TiO_2 catalyst. The adsorption promotion effect of the amine functionalization was confirmed by FTIR through the detection of carbamate functional group ($-OCH_2CH_2NHCOO^-$) formation after the MEA-TiO_2 has been exposed in the CO_2 atmosphere. Due to the enhanced CO_2 adsorption capacity, MEA-TiO_2 exhibits considerable higher production rates in both CH_4 (8.61 ppm/h) and CO (66.75 ppm/h) compared with the pristine TiO_2 catalyst (CH_4: 0.91 ppm/h, CO: 10.5 ppm/h). In addition to the amine functionalization approach, the possibilities of employing magnesium oxide (MgO) have also recently drawn many attentions in the CO_2 photoreduction research field [44-46]. MgO is a type of low-cost and non-toxic metal oxide with weak alkalinity when exposed to water and converts into magnesium hydroxide [$Mg(OH)_2$], the favorable properties of MgO make it a promising candidate as an alkali modification on TiO_2 for CO_2 photoreduction. For example, Liu *et al.* [47] employed an ultrasonic spray pyrolysis approach and prepared a type of MgO modified TiO_2 catalyst (MgO-TiO_2). At 150 ℃, the MgO-TiO_2 catalyst showed a

photocatalytic CO_2 reduction performance that is nearly 4 times as high as that of the bare TiO_2 catalyst. To investigate the effect of MgO surface modification on CO_2 adsorption, *in situ* diffuse reflectance infrared Fourier transform spectroscopy (*in situ* DRIFTS) was applied to determine the intermediate generated from CO_2 exposure. The *in situ* DRIFTS analyses revealed that the bidentate carbonate (b-CO_3^{2-}) is the main surface intermediates generated after CO_2 adsorption on the bare TiO_2 surface. The MgO-TiO_2 catalysts were found to favor the generation of surface bicarbonate (HCO_3^-), which is a more active surface intermediate over bidentate carbonate, as the major product upon CO_2 exposure, leading to an enhanced photocatalytic CO_2 reduction reaction rate over bare TiO_2 catalyst.

1.1.2. Noble metal deposition on TiO_2

Nobel metal deposition (Pt, Pd, Ag, Au, etc.) on TiO_2 is also a powerful method to promote photoactivity of TiO_2 materials [48]. Noble metal normally does not show significant photoactivity in bulk [49]. In contrast, when deposited on the surface of semiconductor materials such as TiO_2 as fine nanoparticles, the noble metal depositions exhibit distinct optical and catalytic properties that can be beneficial in the photocatalytic CO_2 reduction process [50]. A photoexcited negative charge can be transferred from TiO_2 material through fast interfacial electron transfer onto the noble metal nanoparticles, which act as an electron trap and promote the photoexcited electron/hole separation [33, 49]. The trapped electron can participate in the CO_2 reduction process and convert CO_2 molecules into products [44].

Platinum (Pt), for example, is one of the most used elements in heterogeneous catalysis. In the research of CO_2 photoreduction, the application of Pt/TiO_2 nanocomposite has been explored and studied [51-53]. For example, Tasbihi *et al.* [51] prepared a type of Pt decorated TiO_2 catalysts,

which was supported on COK-12 porous silica substrates. The deposited Pt nanoparticles on the TiO_2 catalysts were found to significantly enhance the overall photocatalytic CO_2 reduction performance and promote the product of CH_4, which is a more favorable production in the CO_2 photoreduction process. The electron trapping effect of Pt nanoparticles was determined to be the main contributing factor to the CO_2 photoreduction performance enhancements. However, it was also found that a Pt deposition amount that is too high does damage the CO_2 photoreduction performance as over concentrated noble metal nanoparticles can act as recombination centers. Similarly, in a separate study, Wang *et al.* [26] investigated the effect of Pt nanoparticle size on the CO_2 photoreduction performance by applying a sputter coating to deposit Pt nanoparticles with varied sizes (0.5 – 2.0 nm) on a TiO_2 catalyst. The size of the Pt nanoparticle was found to be a crucial factor in the performance: a Pt nanoparticle that is extremely small may experience restricted electron transfer due to a higher energy band separation resulting from quantum confinement; on the other hand, the large size of Pt nanoparticle makes it possible to capture both photoexcited electrons and holes, acting as recombination center and lead to a decline in photocatalytic CO_2 reduction performance. In their study, a Pt particle size of ~1.0 nm was determined to be optimal, delivering CH_4 and CO production rates of ~1400 $\mu mol \cdot g^{-1} \cdot h^{-1}$ and ~180 $\mu mol \cdot g^{-1} \cdot h^{-1}$, respectively (compared with pristine TiO_2 material, CH_4: 0 $\mu mol \cdot g^{-1} \cdot h^{-1}$ and CO: ~250 $\mu mol \cdot g^{-1} \cdot h^{-1}$).

In addition to the favorable electron trap effect of noble metal deposition, the localized surface plasmon resonance (LSPR) effect is also a beneficial feature to enhance the photocatalytic CO_2 reduction performance on noble metal deposited TiO_2 catalysts [14, 50]. The LSPR effect is originated from the interaction of noble metal nanoparticles conduction electrons with incident photons, which leads to the generation of hot electrons to reduce CO_2 molecules and accelerated

the reaction rate [54]. For example, Zhao *et al.* [50] investigated the separated contributions of charge separation of SPR effect of Au nanoparticles on a Al_2O_3 coated TiO_2 catalyst in the photocatalytic CO_2 reduction process. Interestingly, it was found that the contribution of the two effects correlates closely with the size of Au nanoparticles on the TiO_2 surface: the charge separation effect dominates when the Au particle sizes are small while the plasmonic near-field enhancements become stronger as the Au particle size enlarges.

1.1.3. Heteroatom doping in TiO_2

The wide bandgap of TiO_2 (3.2eV) requires UV photons to activate the photocatalytic effects of TiO_2 [48]. However, UV light only consists of 5% of total energy in solar irradiation, leading to a low sunlight utilization efficiency on pristine TiO_2 materials [55]. Narrowing down the bandgap of TiO_2 materials can be an effective solution to enhance the photoactivity of TiO_2 materials in the photocatalytic CO_2 reduction process [56]. Heteroatom doping in TiO_2 materials can be an effective solution to lower the bandgap of TiO_2 and enhance the performance of the CO_2 photoreduction process on TiO_2 catalysts [21]. The heteroatoms can substitute the Ti atoms in the TiO_2 crystal lattice and create empty energy levels below the conduction band of TiO_2 [57], which results in a narrower bandgap and thus improved photoactivity that is beneficial to the overall CO_2 photoreduction performance.

For example, Bhattacharyya *et al.* [58] applied a sol-gel method and prepared Cu-doped TiO_2 photocatalysts for applications in CO_2 photoreduction. The bandgap energy of the Cu-TiO_2 catalyst was determined to decrease with increased Cu doping concentration. Under the irradiation of a simulated white light in the range of 350 – 700 nm, no CO_2 photoreduction production was detected on bare TiO_2 photocatalyst, while the best performing sample, on the other hand,

delivered a CH_4 generation performance of 1081 $\mu L \cdot h^{-1} \cdot g^{-1}$. In addition to the bandgap narrowing effect, the Cu dopant on the Cu-TiO_2 catalysts was found to facilitate the generation of Cu^+ and oxygen vacancies, both of which serve as the active sites and improve the performance of the photocatalytic CO_2 reduction process.

The heteroatom doping in TiO_2 has also been demonstrated to promote the photoexcited charge separation [59, 60]. By substituting into TiO_2 crystal lattice, an increased amount of surface defects can be observed on TiO_2 [61, 62], which contributes to the hindrance of photoexcited electron/hole separation. For example, Wu *et al.* [63] recently reported enhanced photocatalytic CO_2 reduction performance on boron-nitrogen co-doped TiO_2 photocatalysts, which shows 5 times higher CO production compared with pristine TiO_2. Photocurrent density analyses determined that the B-N co-doped TiO_2 showed a photocurrent density that is about 2.5 times as high as that of bare TiO_2 catalysts. XPS analysis determined that the B-N doped TiO_2 exhibits a high concentration of both Ti^{3+} and oxygen vacancies, which contributes to the improvements in the enhancement in photocurrent density and CO_2 photoreduction performance.

1.2. Photo-thermal-chemical dry reforming of methane

CH_4, on the other hand, is the major component of natural gas and has long been applied as an energy resource and burnt as a fossil fuel. In addition, CH_4 is also an important raw material for syngas production through the methane reforming process [64]. A few techniques, such as steam reforming of methane (SRM, $CH_4 + H_2O \rightarrow 3\ H_2 + CO$, ΔH^o = 206 kJ/mol) [65] and dry reforming of methane (DRM, $CH_4 + CO_2 \rightarrow 2\ H_2 + 2\ CO$, ΔH^o = 247.3 kJ/mol) [66], are currently available in methane reforming process, As of now, SMR, where water vapor interacts with methane under high temperature and pressure conditions (700-1000 ℃ and 3-25 atm) [66] and

produces H_2 and CO, is the most widely applied approach for industrial-scale methane reforming [65]. One of the drawbacks of the SMR process is the excessive amount of energy input required for water steam generation and reaction gas compression [65, 66]. In addition, as a common impurity, CO_2 can have a volume fraction of as high as ~50% in raw natural gas [67]; similarly, in biogas, another common source of CH_4, CO_2 also takes a significant proportion (~60% CH_4 + ~40% CO_2 [68], which make purification a requirement for SRM process. Currently, the conventional approach to separate CO_2 and purify raw natural is cryogenic distillation [69, 70], which is an energy intensive process and economically disadvantageous. In this sense, the DRM process, which takes place at relatively milder conditions (650-850 ℃, atmospheric pressure) to convert CO_2 and CH_4, the two major greenhouse gases react simultaneously and produce syngas, can be an ideal approach for methane reforming [71]. However, despite the advantages of DRM and the reduced energy consumption compared with SMR, a relatively high temperature, still entails a high energy consumption [72, 73].

As a clean and sustainable energy source, solar energy can potentially fulfill the global energy demands without the emission of greenhouse gases. Concentrated solar technique, in particular, has been demonstrated as a promising way to partially provide thermal energy to facilitate less energy extensive thermal-driven chemical conversion processes including petroleum coke gasification [74], thermochemical water splitting [75], etc. The incorporation of concentrated solar technique into the thermal-driven DRM process is promising as it significantly reduces the energy input. In addition to the thermal contribution to the concentrated solar technique, the possibility to incorporate photo-induced effects such as photocatalysis also provides the potential to further promote the efficiency of the thermal-driven DRM process [76, 77].

The development of photoactive catalysts is critical for utilizing solar energy and further

enhancing the performance of the PTC-DRM process. In conventional DRM process, a catalyst is mostly composed of a metal oxide substrate (e. g., TiO_2, CeO_2, SiO_2, ZrO_2, etc.) with a type of active metal nanoparticle deposition (e. g., Ni, Co, Pt, Rh, Ru, Pd, etc.) [78, 79]. Generally, it is believed that the metal oxide substrate interacts with CO_2, while the active metal nanoparticles participate in CH_4 activation and dissociation [80]. To be able to convert the solar energy and facilitate the DRM reaction process, at least one component in the PTC-DRM catalyst should be photoactive. Generally, catalysts in the PTC-DRM process harvest solar energy through two distinct pathways: (1) photocatalysis process on semiconductor materials, and (2) localized surface plasmon resonance (LSPR) effects [77].

1.2.1. Photocatalysis-promoted DRM process

Similar to the photocatalytic CO_2 reduction process, the photocatalysis-promoted PTC-DRM process exploits the photoexcited carriers in semiconductor catalysts. Upon the activation of photons with adequate energy, the photoexcited electrons and holes can participate in the DRM reaction to facilitate syngas production. The related research started from pure photocatalysis-driven DRM reactions, which take place at a relatively low temperature (100 – 200 ℃) [81]. In 1997, Yoshida *et al.* [82] for the first time reported the application of pure photocatalysis concepts to convert a CO_2/CH_4 mixture into syngas, where UV irradiation (500 W ultrahigh-pressure Hg lamp) was applied on ZrO_2 material to produce CO (0.141 μmol/h) and H_2 (0.006 μmol/h). Later, with the same light source, the same research group reported syngas production on MgO material [83], which led to a slightly better photocatalytic DRM performance (CO: 0.720 μmol/h, H_2: 0.009 μmol/h) compared with the previous work. The two pioneering works inspired a number of later works on low-temperature photocatalysis-driven DRM on a variety of photocatalysts including β-

Ga_2O_3 [84], La-TiO_2 [85], TiO_2-C_3N_4 [86], etc., which demonstrated the effectiveness of photocatalysis in promoting the DRM reaction efficiency.

As for the conventional DRM process, which takes place under a relatively high temperature (>500 ℃), the advancements in the pure photocatalysis-driven DRM process brought new opportunities in the incorporation of photocatalysis into thermal-driven DRM process, in other words, the PTC-DRM process [81]. For example, in 2016, Han *et al*. [87] prepared a type of Pt decorated oxygen-deficient black TiO_2 catalyst for the PTC-DRM process under AM 1.5G simulated sunlight (100 mW/cm^2). At a reaction temperature of 650 ℃ under light irradiation, the catalyst exhibit CO and H_2 production rates of 370 mmol·h^{-1}·g^{-1} and 129 mmol·h^{-1}·g^{-1}, respectively, which is significantly higher than those obtained without simulated solar irradiation (CO generation rate: 99 mmol·h^{-1}·g^{-1}, H_2 generation rate: 9 mmol·h^{-1}·g^{-1}). The visible light responsive black TiO_2 substrate was determined to be the major contributor to the high DRM efficiency under simulated sunlight irradiation. Despite the high DRM catalyzing performance, the DRM catalytic efficiency on Pt/black TiO_2 catalyst was found to decline shortly after the reaction begins, which was attributed to the phase transformation of TiO_2 material under high temperature.

To design a stable catalyst for the PTC-DRM process, more recently, Mao *et al.* [88] applied CeO_2 material as the substrate to support active Pt nanoparticles for the PTC-DRM process. As a type of reducible photocatalyst that exhibits a bandgap of ~2.8 eV [89], CeO_2 shows exceptional surface oxygen mobility [90], which is beneficial for potential coke formation avoidance to maintain a stable DRM performance [91]. A simulated concentrated sunlight that equivalents to a ~240-sun irradiation was applied, which can elevate the temperature of the catalyst to ~700 ℃ without axillary heating. Under such reaction conditions, the Pt-CeO_2 catalyst showed the PTC-DRM promoting capability for at least 100 h, with CO and H_2 generation rate of 6.0

mmol·min^{-1}·g^{-1} and 5.7 mmol·min^{-1}·g^{-1}, respectively. In addition to the photocatalyst nature of CeO_2 substrate, the high oxygen mobility on the surface of CeO_2 also facilitates the dissociation of CH_4, which further accelerates the PTC-DRM reaction rate.

Pan *et al*. [91] later further improved the PTC-DRM performance on Pt-CeO_2-based catalysts by incorporating SiO_2 into the CeO_2 substrate. Under 600 ℃ and a 30-sun equivalent solar irradiation, the Pt-Si-CeO_2 shows stable PTC-DRM performance for at least 30 h and CO and H_2 production rate of 15 4 mmol·h^{-1}·g^{-1} and 90 mmol·h^{-1}·g^{-1}, respectively, which is considerable improved compared with Pt-CeO_2 catalyst under the same reaction conditions (CO: 108 mmol·h^{-1}·g^{-1}, H_2: 50 mmol·h^{-1}·g^{-1}). Photocatalysis effects were also found to be highly effective in promoting the PTC-DRM performance on Pt-Si-CeO_2 materials, under dark conditions at 600 ℃, only CO and H_2 generation rate of 90 mmol·h^{-1}·g^{-1} and 14 mmol·h^{-1}·g^{-1} was observed. XPS analyses revealed that both SiO_2 incorporation and the concentrated solar irradiation facilitate the surface oxygen vacancies generation on catalyst surface, which led to improved DRM performances.

1.2.2. LSPR-promoted DRM process

Recently, the applications of localized surface plasmon resonance (LSPR) active catalysts to harvest photon energy for enhancement of PTC-DRM performance have also attracted enormous attentions [92-94]. The localized surface plasmon resonance effect in DRM process refers to applying a plasmonic metal nanoparticles as the active metal in PTC-DRM catalyst design [95]. Similar to the favorable performance promotion effect of LSPR in photocatalytic CO_2 reduction process, the LSPR effects can be also beneficial in the PTC-DRM process [81]. The photo-induced plasmon can directly participate in the DRM process and promote the performance

of syngas production [77]. In addition, the LSPR effect may also lead to photo-induced heating on the plasmonic metal surface, which further stimulate the PTC-DRM reaction rate [96]. Up to now, non-noble metals such as nickel (Ni) [97], cobalt (Co) [76], and copper (Cu) [92]; noble metal such as ruthenium (Ru) [98], and rhodium (Rh) [99], etc., have been demonstrated to be effective in PTC-DRM process.

Due to the abundancy and being low-cost, the application of plasmonic active economic metals in the PTC-DRM process have been intensively studied recently [95, 100]. Among the available metal species, nickel was studied the most due to its high activity in conventional DRM process [101]. For example, Liu *et al.* [102] prepared core-shell Ni@SiO_2 nanostructures for syngas production applications in the PTC-DRM process. At a reaction temperature of 550 °C and without light irradiation, the Ni@SiO_2 core-shell nanostructure showed initial CO and H_2 production rate of 476 $\mu mol \cdot g^{-1} \cdot min^{-1}$ and 378 $\mu mol \cdot g^{-1} \cdot min^{-1}$. The DRM performance saw a considerable enhancement when light irradiation (1.07 W/cm^2, wavelength range: 300 nm – 800 nm) is applied, the initial CO and H_2 production rates were improved to 822 $\mu mol \cdot g^{-1} \cdot min^{-1}$ and 672 $\mu mol \cdot g^{-1} \cdot min^{-1}$. To determine the origin of catalytic performance enhancement under light irradiation, a finite-difference time-domain method was applied, which demonstrated that the light irradiation boosted the performance of Ni@SiO_2 catalyst through both plasmonic effects and electronic interband transition effects on the Ni nanoparticles. Despite the high performance, however, severe coke formation was observed as a side reaction of the methane dissociation, which led to quick catalyst deactivation.

Despite being low-cost and highly active in the PTC-DRM process, a strong tendency of coke formation and accumulation is the most detrimental flaw of almost all non-noble metal DRM catalysts [97, 103]. Accumulation of coke adds resistance on reactant/product diffusion and leads

to deteriorated stability in the PTC-DRM process [66]. To enhance the stability of Ni-based PTC-DRM catalyst, Huang *et al*. [104] recently applied a co-precipitation method and prepared a type of silica-cluster-modified Ni (SCM-Ni/SiO_2) catalyst the PTC-DRM process. The LSPR capacity of the Ni nanoparticles was able to allow plasmonic heating under >200-sun equivalent concentrated sunlight to teach a high temperature of 700°C. It was demonstrated that the high light irradiance can assist the Ni-SiO_2 catalyst maintain a stable PTC-DRM reaction for ~600 h with almost no carbon deposition. As determined, the silica clusters helped to expose the Ni [111] facet, which, as demonstrated by the density functional theory calculations, decreased the activation of methane dissociation and the oxidation of potential coke, leading to an exceptional stability.

More recently, Zhou *et al*. [92] reported the LSPR-promoted PTC-DRM application with a type of Cu-Ru bimetallic alloy catalyst. The LSPR active Cu component strongly absorbs light irradiation and generates hot carriers and the Ru component serves as the reaction sites. A Ru molar proportion of 1% in the Cu-Ru alloy was found to show the best reaction stability and highest reaction rate per each single atomic Ru reaction site. Density functional theory calculation results showed that a Ru atomic ratio of 1% reduces the reaction barrier of methane dehydrogenation without promoting side reactions such as coke formation and RWGS, resulting in a promoted PTC-DRM catalytic performance.

1.3. Dissertation overview

This dissertation concerns innovations in catalyst surface engineering for applications in two greenhouse gas conversion processes: (I) Photocatalytic CO_2 reduction with water into solar fuels (Chapters 2, 3, and 4); and (II) Photo-chemical-thermal dry reforming of methane for syngas production (Chapter 5).

In Chapter 2, a porous TiO_2 photocatalyst was developed with MOF material MIL-125 as the template. To further enhance the photocatalytic CO_2 reduction efficiency, atomic layer deposition (ALD) technique was employed to coat an ultrathin MgO overlayer on the porous TiO_2 catalyst. As a comparison, the performance of ALD modified samples was compared with those of TiO_2 samples prepared by wet impregnation (WI) method. Comparisons between the two surface modification approaches in surface chemistry, structure, morphology, and more importantly, photocatalytic CO_2 reduction performance, were discussed in detail.

In Chapter 3, photocatalytic CO_2 reduction process was assessed with pristine porous TiO_2 material derived from MIL-125 decorated by both atomic layer deposited MgO and photodeposited Ag nanoparticles at different orders: MgO deposition followed by Ag (i.e. Ag/MgO/TiO_2), or Ag deposition followed by MgO (i.e. MgO/Ag/TiO_2). The addition of Ag promoted transfer of photoinduced electrons, while the coating of an ultrathin MgO layer inhibited surface charge recombination and enhanced CO_2 adsorption. It was found that the sequence of MgO/Ag decoration influenced the catalytic activity. The effect of the modification sequence on the porous TiO_2 in the CO_2 photoreduction performance was studied and investigated.

In Chapter 4, an easy and facile method to prepare MgO doped porous TiO_2 photocatalysts by applying a Mg^{2+} adsorption (MA) process on MIL-125 was described. The performance of the MgO doped porous TiO_2 catalyst was tested and studied. Investigations were performed on the role of Mg^{2+} doping in promoting the performance of CO_2 reduction on TiO_2 catalyst in photocatalytic CO_2 reduction.

Innovations in advanced catalyst design in the PTC-DRM process is described in Chapter 5, where a Pt decorated equimolar Al_2O_3-CeO_2 binary oxide catalyst (Pt-Al-Ce) was applied. A Pt deposited CeO_2 catalyst and a Pt decorated Al_2O_3 material were applied for control experiments

to unravel the favorable synergetic effects between Al_2O_3 and CeO_2 in the Pt-Al-Ce catalyst. *In situ* diffuse reflectance infrared Fourier transform spectroscopy (*in situ* DRIFTS) analyses were applied to identify surface active intermediates in the PTC-DRM process. The mechanism of the performance promotion effects of the light irradiation was also studied in detail.

2. ATOMIC LAYER DEPOSITION ENABLED MEGNISIUM OXIDE SURFACE COATING ON POROUS TITANIUM DIOXIDE FOR IMPROVED CARBON DIOXIDE PHOTOREDUCTION[*]

2.1. Introduction

Preparation of high surface area TiO_2 materials is an effective approach to improve the CO_2 photoreduction performance of TiO_2 by enhancing CO_2 adsorption and generate more active sites for the desired reactions [26, 105]. Metal-organic framework (MOF) materials, which exhibit very high surface area and tunable framework structure [106], have recently demonstrated their applicability as an appropriate precursor to prepare porous metal oxide with high surface area and hierarchical porous structure [107, 108]. Recently, porous TiO_2 derived from metal-organic framework MIL-125 has drawn much attention due to the favorable hierarchical porous structure and high surface area. According to previous reports, MIL-125 derived porous TiO_2 exhibits a high surface area ranging from 125 m^2/g to 220 m^2/g [109, 110]. Due to those favorable properties, MIL-125 derived porous TiO_2 has been reported in applications of photocatalytic hydrogen production [110], solar cell [111]. and lithium-ion batteries [109, 112-114].

Besides the preparation of porous TiO_2, the incorporation of noble metals (e.g., Pt, Pd, Ru, and Ag) [44, 110, 115] or low-cost metal oxides (e.g. Fe_2O_3 [116], NiO [117], and CuO [118]) have been demonstrated for their potential in effectively promoting photocatalytic activity by hindering the charge recombination, enhancing visible light absorption, and altering surface states

[*] Part of this chapter is reprinted with permission from "Atomic layer deposition enabled MgO surface coating on porous TiO_2 for improved CO_2 photoreduction" by Xuhui Feng, Fuping Pan, Huilei Zhao, Wei Deng, Peng Zhang, Hong-Cai Zhou, and Ying Li, *Applied Catalysis B: Environmental*, 2018, 238, 274-283. Copyright [2018] by Elsevier B.V.

or defects [55, 119, 120]. Previous studies [23, 24, 36, 45, 47] demonstrated the role of MgO in boosting CO_2 photoreaction performance by decreasing electron-hole recombination and promoting adsorption of CO_2 because of the basic nature of MgO. Conventional approaches of TiO_2 surface modification includes wet impregnation (WI) [24, 47] and ultrasonic spray pyrolysis (USP) [47], which are easy and economical ways for surface modification of TiO_2. However, those methods produce segregated, irregular-shape islands or patches of MgO deposited on TiO_2 without full coverage of the TiO_2 surface. In order to take advantage of porous, high surface area TiO_2, it is desirable to incorporate more uniformly distributed MgO on TiO_2 with maximized contact between the two species. The recently emerged atomic layer deposition (ALD) technique, compared with conventional methods, allows easy yet precise control on the growth and thickness of multilayer deposition structure, and thus is a desirable way to coat uniform thin films [34]. To the best of our knowledge, no work has been investigated on TiO_2 modified by ALD coated MgO overlayer for CO_2 photoreduction. Furthermore, despite that MgO is cheap, nontoxic and naturally abundant, only a limited number of studies are reported on MgO modified TiO_2 for CO_2 photoreduction [24, 38, 47], and the effect of MgO nanostructure on CO_2 photoreduction is not fully understood.

The objective of this chapter was to prepare porous and high surface area TiO_2 derived from metal-organic framework MIL-125 and modify the surface with uniformly dispersed MgO to improve the efficiency of photocatalytic CO_2 reduction. Based on the aforementioned literature review, we hypothesize that porous TiO_2 is superior to traditional nanopowder photocatalysts such as P25 and that MgO coated on TiO_2 surface through the ALD method is advantageous over non-modified TiO_2 or MgO modified TiO_2 by traditional methods such as wet impregnation. In this chapter, porous TiO_2, ALD and WI modified porous TiO_2 photocatalysts were prepared and

compared in terms of surface morphology, optical properties, surface chemical states as well as CO_2 photoreduction activity. The advantages of ALD as an enabling technique for fabricating efficient CO_2 photoreduction catalysts were elucidated.

2.2. Experimental

2.2.1. Preparation of MIL-125 template

MIL-125 was prepared based on a previously reported method [109, 110]. In a typical experiment, 6.0 g of terephthalic acid ($C_8H_6O_4$, >99.0%, Tokyo Chemical Industry) was dissolved in a solvent mixture prepared with 108 ml of N,N-dimethylformamide (DMF, C_3H_7NO, ≥99.8%, BDH Chemicals), and 12 ml of methanol (C_2H_6O, ≥99.8%, EMD Millipore). 3.12 ml of titanium tetraisopropoxide (TTIP, $TiC_{12}H_{28}O_4$, 97+%, Alfa Aesar) was added into the solution under stirring. The mixture was then transferred into a Teflon-lined autoclave. The autoclave was placed in a conventional oven and maintained at 150 °C for 24 h. After hydrothermal treatment, white powder was collected by centrifugation. The powder was rinsed with methanol three times before drying in a vacuum oven at 80 °C overnight, yielding MIL-125.

2.2.2. Preparation of porous TiO_2 photocatalyst

Porous-TiO_2 catalyst was prepared using MIL-125 as a template. The MIL-125 powder was firstly pyrolyzed in a tube furnace at 500 °C for 2 h under an argon atmosphere, and the resultant black powder was then calcined in air at 450 °C for 2 h to obtain white TiO_2 powder.

2.2.3. Wet impregnation (WI) of MgO on porous-TiO_2

In a typical preparation, 100 mg porous-TiO_2 was mixed with 40 ml $Mg(NO_3)_2$ (99%,

Sigma-Aldrich) aqueous solution at a certain concentration. The mixture was stirred at room temperature for 24 h and then dried in a vacuum at 80 °C overnight. The white powder was then collected and calcined at 450 °C in the air for 2 h. The obtained samples are denoted as *x*%WI, where *x*% indicates a weight ratio of Mg^{2+} : TiO_2 = *x*% : 1 in the recipe.

2.2.4. Atomic layer deposition (ALD) of MgO overlayer on porous-TiO_2

An Ultratech Savannah S200 ALD system was used to coat a MgO overlayer on porous-TiO_2. A homemade powder holder loaded with 30 mg of porous-TiO_2 powder was placed in the center of the ALD chamber, which was maintained at 200 °C during the ALD process. Bis(ethylcyclopentadienyl) magnesium [$Mg(C_5H_4C_2H_5)_2$, min. 98%, Strem Chemicals Inc.] was used as the Mg precursor. In each ALD cycle, "expo mode" was used for coating porous materials, and the pulse time of water and Mg precursor was set to 2 s each to introduce an adequate amount of reactants to the reaction chamber and ensure even ALD coating on porous-TiO_2. After the ALD process, a grey powder was obtained and calcined at 450 °C for 30 min to remove any potential organic residues from the ALD process. A white powder was eventually obtained. The ALD samples are denoted as *x*ALD, where *x* is the number of ALD cycles applied on porous-TiO_2.

2.2.5. Photocatalyst characterizations

X-ray diffraction (XRD) analysis was performed on a Bruker-AXS D8 Advance diffractometer using Cu Kα1 irradiation (λ=1.54059 Å) at 40 kV and 40 mA at room temperature. The step increment was set at 2θ=0.05° and the counting time per step was 1s. The morphology and structure were analyzed with a JEOL JSM7500F field-emission scanning electron microscope (FE-SEM) and a FEI Tecnai G2 F20 ST transmission electron microscope (TEM). UV–vis diffuse

reflectance spectra were measured on a Hitachi U4100 UV–vis-NIR Spectrophotometer with Praying Mantis accessory. Brunauer-Emmett-Teller (BET) surface area analysis was performed on a Micromeritics ASAP 2420 physisorption analyzer. Prior to surface area measurements, the photocatalyst samples were degassed in a vacuum at 100 °C for 12 h. X-ray photoelectron spectroscopy (XPS) analysis was performed on an Omicron XPS system. Photoluminescence spectra (PTI QuantaMaster series Spectrofluorometer) were obtained to investigate the charge recombination emission using 300 nm incident light, scanning from 400 to 600 nm with a scan rate 0.1 nm/s. Photocurrents of prepared samples were measured with a Gamry Reference 3000 potentiostat. 1.2 mg sample was loaded on the conductive surface of a piece of ITO glass and a 0.05 M Na_2SO_4 solution was used as the electrolyte. A 450 W Xe lamp was used as the light source, a 3M Ag/AgCl electrode was used as the reference, and a Pt slice was used as the counter electrode.

2.2.6. CO_2 photoreduction performance test

The experimental setup for CO_2 photoreduction was similar to that in our previous report [34]. A piece of glass fiber filter paper (Pall Corporation) was used as the support for powder photocatalyst. Prior to catalyst loading, the glass fiber paper was calcined in air at 450 °C to remove organics on the surface, if any. Then, 10 mg of the photocatalyst was dispersed in 2 ml deionized water and sonicated for 10 min. The obtained suspension was dropped onto the glass fiber paper, which was later dried in a vacuum oven at 80 °C for 30 min. The catalyst-loaded glass fiber paper was then placed into a tubular quartz reactor with the photocatalyst side facing the light source. Ultra-high purity CO_2 (99.999%, Airgas) was bubbled into a water reservoir to generate a CO_2/H_2O gas mixture (water vapor concentration ≈ 2.3% by volume) before being purged into the

tube reactor. Before turning the light on, the system was flushed at a CO_2 flow rate of 298.0 standard cubic centimeter per minute (sccm) for 1 h and then maintained at 3.0 sccm. The light source used in this study was a 450 W Xe lamp (Newport, Inc.) equipped with a water filter to diminish infrared irradiation, the distance between the Xe lamp and the photocatalyst was 30 cm. The light spectrum of the lamp measured 30 cm away from the lamp is shown in Figure A-1 in Appendix A. The intensity of UV, visible, IR light of the Xe lamp measured before/after passing the quartz tube is listed in Table A-1. The outlet of the reactor was connected with a Shimadzu GC-2014ATF gas chromatograph, which was equipped with an autosampler, a thermal conductivity detector (TCD), and a flame ionization detector (FID) coupled with a methanizer (to detect CO and CH_4 when applicable).

2.3. Result and discussion

2.3.1. Crystal structure

The XRD patterns of all prepared photocatalysts are shown in Figure 2-1. It was found that all samples are consist of both anatase and rutile phases. The existence of the rutile phase is possibly a result of anatase to rutile phase change induced by elevated pyrolysis temperature in porous-TiO_2 preparation. The weight ratio of anatase/rutile was calculated by Rietveld refinement method [121]. Phase composition and crystallite size of anatase and rutile in the three representative samples are listed in Table 2-1. The prepared samples show a comparable phase composition made of anatase and rutile. WI and ALD samples had a slightly higher rutile phase and a slightly larger rutile crystallite size than porous-TiO_2, probably due to the extended thermal treatment processes undergone on those samples.

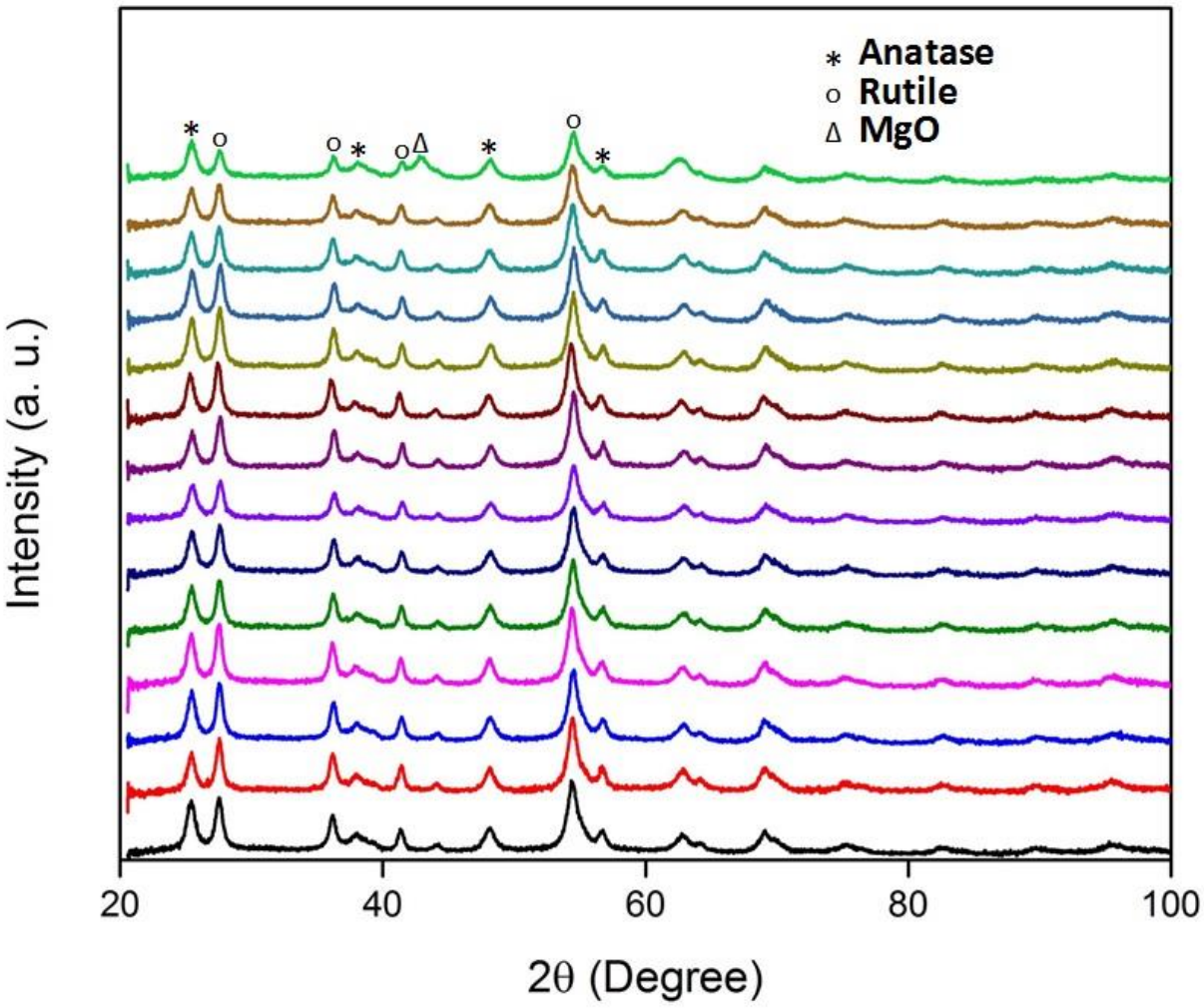

Figure 2-1 XRD patterns of (a) porous-TiO_2, (b) 0.1%WI, (c) 0.5%WI, (d) 1%WI, (e) 2%WI, (f) 5%WI, (g) 10%WI, (h) 1ALD, (i) 2ALD, (j) 5ALD, (k) 10ALD, (l) 20ALD, (m) 50ALD, (n) 100ALD.

For most samples, diffraction peaks for MgO were not found, which is likely due to the small weight percentage of MgO and its good dispersion on porous-TiO_2. The exception is 100ALD, where the existence of MgO was confirmed by the characteristic peak of MgO at 2θ = 42.9°. With 100 layers of MgO addition, the MgO loading amount was considerably higher than other samples and detectable by XRD.

Table 2-1 Phase composition and crystallite size of prepared samples.

Sample ID	Anatase %	Rutile %	Anatase Crystallite Size (nm)	Rutile Crystallite Size (nm)
porous-TiO_2	43.9	56.1	11.3	13.9
0.1%WI	39.2	60.8	14.0	16.1
0.5%WI	39.5	60.5	12.2	15.5
1%WI	39.2	60.8	12.1	15.1
2%WI	40.2	59.8	12.6	15.0
5%WI	39.8	61.2	11.0	14.9
10%WI	33.7	66.3	12.7	15.5
1ALD	39.4	60.6	13.4	14.8
2ALD	39.4	61.6	12.7	15.2
5ALD	39.0	61.0	12.1	14.8
10ALD	38.8	61.2	11.9	14.2
20ALD	39.1	60.9	12.8	14.7
50ALD	39.2	60.8	12.2	15.4
100ALD	49.8	50.2	11.6	15.5

2.3.2. Morphology and structure

The morphologies of porous-TiO_2, 2%WI, and 5ALD are shown in SEM images in Figure 2-2. porous-TiO_2 particles exhibit a cubic shape with an average particle size of ~270 nm. Compared with porous-TiO_2, 2%WI (Figure 2-2b) and 5ALD (Figure 2-2c) have a similar particle size, but the surface of the 2%WI sample has a considerable level of roughness and irregular agglomeration of ultrafine particles. In the preparation procedure of WI samples, $Mg(NO_3)_2$ was firstly crystallized on the surface of porous-TiO_2 nanoparticles after the evaporation of $Mg(NO_3)_2$ solution. The surface $Mg(NO_3)_2$ deposition was then converted to MgO nanoparticles during the subsequent calcination process, which likely resulted in the elevated surface roughness and irregularity [38, 122]. In contrast, 5ALD (Figure 2-2c) has a smooth surface similar to porous-TiO_2, in coincident with the morphology of coating. In addition, shown in Figure 2-2c, the SEM image is blurry, which is likely due to the reduced surface conductivity of the photocatalyst caused

by the MgO overlayer. Since MgO is an insulator, the reduction in conductivity indicates the successful coating of MgO overlayer on the porous-TiO_2.

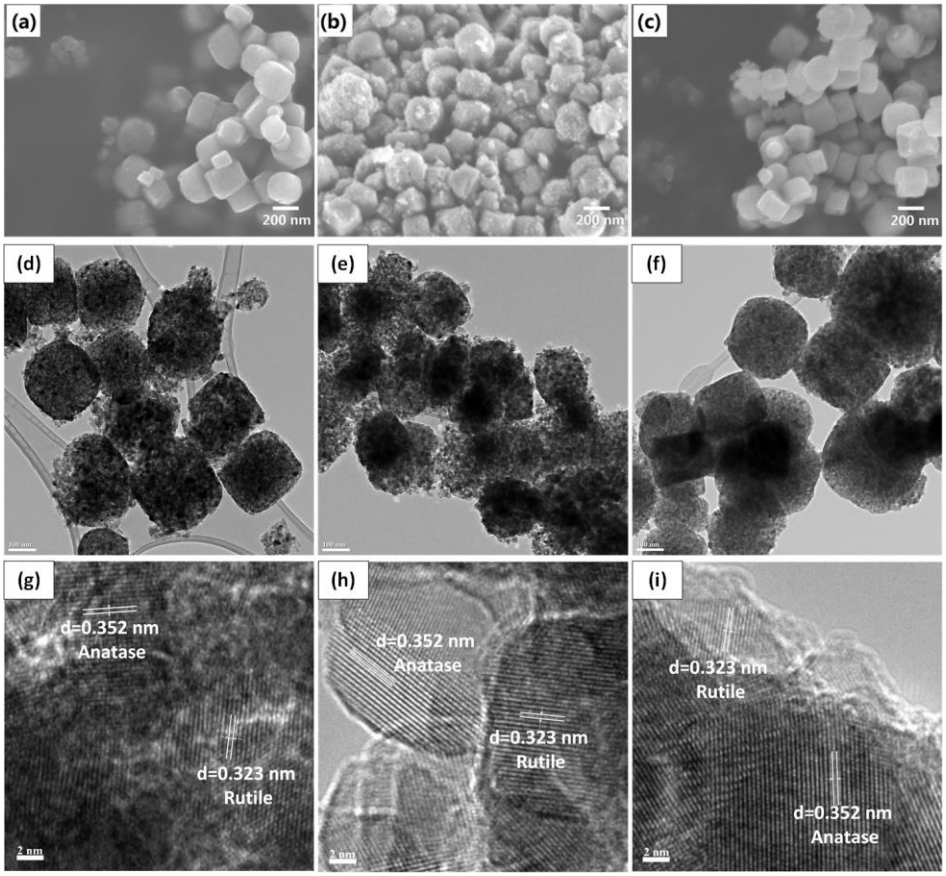

Figure 2-2 SEM images of (a) porous-TiO_2, (b) 2%WI, and (c) 5ALD, and TEM images of (d) (g) porous-TiO_2, (e) (h) 2%WI, (f) (i) 5ALD.

TEM analysis was also performed on porous-TiO_2, 2%WI, and 5ALD to further investigate the crystal structure of the photocatalysts (Figure 2-2d-i). As shown in Figure 2-2d, porous-TiO_2 crystals showed a crystal size of ~270 nm, which is similar to the reading from SEM analysis. From the TEM image, it can be found that porous-TiO_2 crystals were consisted of firmly interconnected ultrafine nanoparticles, which were also found on the structure of 5ALD and 2%WI crystals. 2%WI crystals exhibited a relatively loosened nanoparticle packing, which coincides with the relatively higher surface roughness observed on 2%WI crystals compared to the other two

samples. The packing of ultrafine nanoparticles in the prepared photocatalyst suggests apparent porous structures on the samples. As displayed in Figure 2-2g-i, both anatase phase (d = 0.352 nm) and rutile phase (d = 0.323 nm) were found on porous-TiO_2, 2%WI, and 5ALD samples, confirming the coexistence of anatase and rutile phases on those samples. This result is also supported by the XRD results. However, due to the very low amount of MgO addition, the characteristic lattice of MgO was not observed.

TEM analysis on 100ALD was also performed to probe the morphology and crystal structure of MgO at a higher loading level (Figure 2-3). All of anatase (d = 0.352 nm), rutile (d = 0.323 nm) and MgO (d = 0.21 nm) were found on 100ALD. Instead of being a uniform overcoating layer, the ALD added MgO was found to be in the form of nanoparticle deposition on 100ALD. As mentioned earlier, all ALD prepared samples were calcined in air at 450 °C after ALD treatment to eliminate organic residue from the ALD process. For an ALD deposited MgO layer as thick as 100 layers, the MgO layers were probably sintered during the calcination process and turned into fine nanoparticle depositions on the surface of the photocatalyst. Nonetheless, for the 5ALD sample, as the ALD coated layer was ultrathin, the sintering effect of MgO was not observed (Figure 2-2c, f, i).

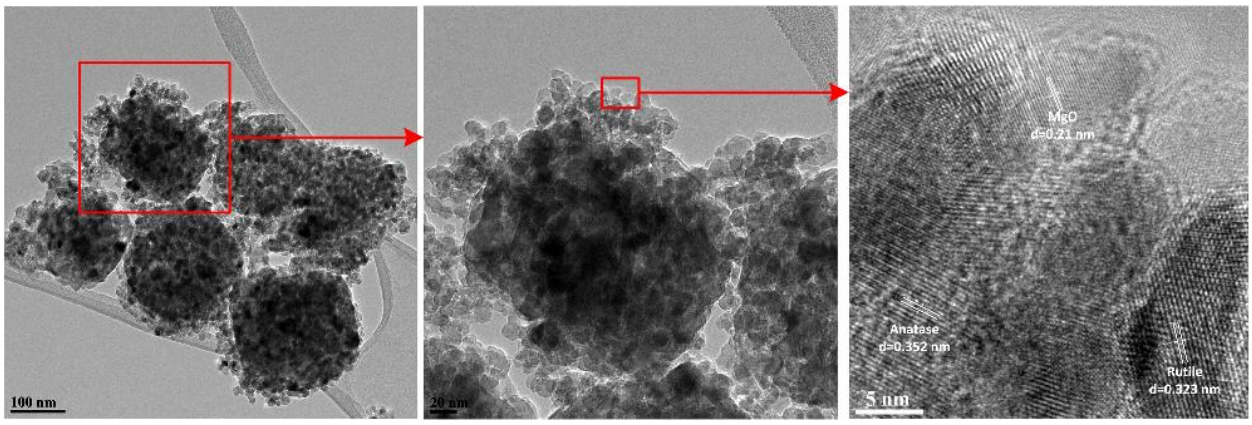

Figure 2-3 TEM image of 100ALD.

2.3.3. Porous structure

In order to evaluate the porosity of as-prepared photocatalysts in this study, Brunauer-Emmett-Teller (BET) analysis was performed. The of N_2 adsorption-desorption isotherms of porous-TiO_2, 2%WI, and 5ALD are printed in Figure 2-4. All of the three samples exhibit type III isotherms, indicating weak gas-solid interaction on the surface of photocatalysts [123]. Porous-TiO_2 displays a type H2 hysteresis loop, demonstrating disordered pore size and shape. On the other hand, 2%WI and 5ALD samples show type H3 hysteresis loops, meaning slit-shaped pore shape [123]. It is likely that the added ALD-MgO layer stuffed on pore channels of porous-TiO_2 and narrowed the pore size. In Table 2-2, BET surface area and pore size of selected photocatalysts are listed, the related N_2 adsorption-desorption isotherms were included in Figure A-2.

BET surface area of porous-TiO_2 was measured to be 47.6 m^2/g, which is less than the value reported in the literature [109, 110]. This likely is because a higher calcination temperature was used in this chapter to ensure removal of potential carbon residues from the synthesis process, which on the other hand sintered the porous-TiO_2 porous structure. Nevertheless, porous-TiO_2 still exhibited comparable surface area to commercial P25 nanopowder (~50 m^2/g). With the addition of MgO, samples prepared by both WI and ALD methods showed an increase in surface area at a very low MgO concentration (0.1%) or 1 ALD cycle MgO coating. It is possible that the addition of a trace amount of MgO or an ALD overlayer caused increased surface roughness at a length scale smaller than the crystal size of porous-TiO_2, thus increasing the surface area. While with a higher amount of MgO incorporation, pore channels in TiO_2 became stuffed with larger size MgO, leading to a decrease in surface area. The 10%WI sample had a similar surface area to those of the 2%WI sample and porous-TiO_2, indicating the morphology and nanostructure of MgO are similar to that of TiO_2. For the ALD samples, the surface area decreased more dramatically with the

number of ALD cycles, and the 100ALD sample had a lower surface area than porous-TiO_2, possibly because of the porous structure of porous-TiO_2 was smoothened by the denser ALD overlayer.

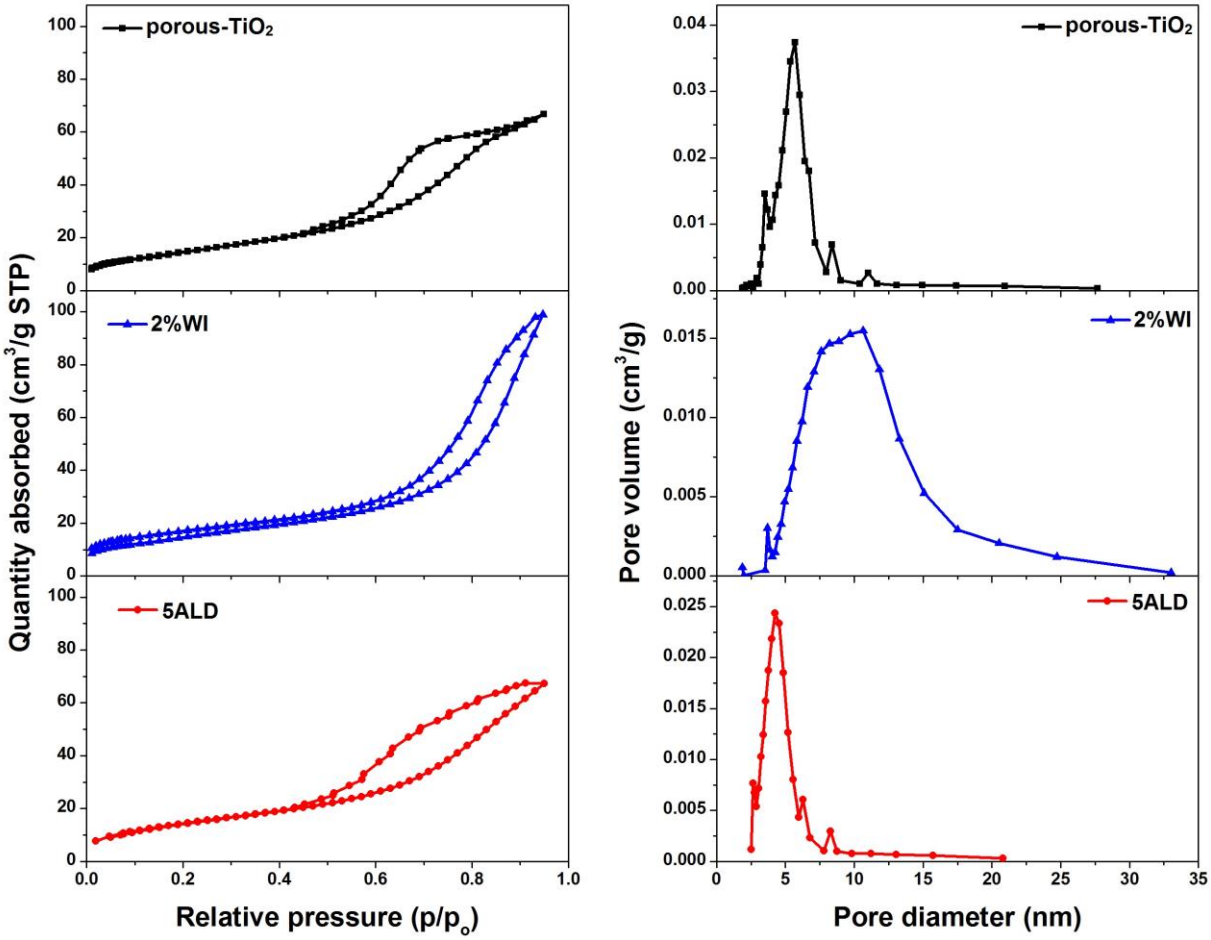

Figure 2-4 N_2 adsorption-desorption isotherm (left) and pore size distribution (right) of porous-TiO_2, 2%WI and 5ALD.

Pore size distribution of porous-TiO_2, 2%WI, and 5ALD were also plotted with BJH desorption data in Figure 2-4. Average pore sizes are listed in Table 2-2. A sharp peak centered at 5.7 nm was observed for porous-TiO_2, indicating narrow pore size distribution. Compared with porous-TiO_2, pores on 2%WI expanded significantly, centered at ~10 nm, ranging from ~3.5 nm to ~30 nm. All WI prepared samples showed expanded pore size, it seems that pore size expansion

takes place during final calcination, where surface deposited $Mg(NO_3)_2$ was converted into MgO deposition on the surface. Similar to porous-TiO_2, 5ALD shows a sharp pore size distribution. The peak slightly shifted towards a lower pore size, centering at ~4.2 nm. For the three ALD prepared samples listed in Table 2-2, shrink in pore size was observed, which is reasonable because the ALD layer decreases the space in between the TiO_2 crystals.

Table 2-2 Surface area, average pore size, and bandgap of representative photocatalysts.

Sample ID	BET surface area (m^2/g)	Average pore size (nm)	Bandgap (eV)
porous-TiO_2	48.0	5.4	3.0
0.1%WI	62.0	6.0	3.0
2%WI	49.0	8.7	3.0
10%WI	49.0	7.7	3.1
1ALD	61.0	3.7	3.0
5ALD	52.0	4.4	3.0
100ALD	31.0	5.2	3.2

2.3.4. Elemental analysis

To determine the chemical composition of prepared samples, EDS elemental mapping analysis was performed. Mg element was not detected on 2%WI and 5ALD on EDS mapping analysis, which is likely due to the very low amount of MgO deposition on those samples. Instead, porous-TiO_2, 10%WI and 100ALD were used as representative samples in EDS analysis. EDS mapping results of porous-TiO_2, 10%WI, and 100ALD are displayed in Figure 2-5. As revealed by the EDS mapping, Ti was found to be evenly distributed on all of the three samples. As expected, Mg was not detected on porous-TiO_2 (Figure 2-5a). On 10%WI, and 100ALD, the existence of Mg elements was found on the surface (Figure 2-5b and c), suggesting successful deposition of MgO on the surface of 10%WI and 100ALD.

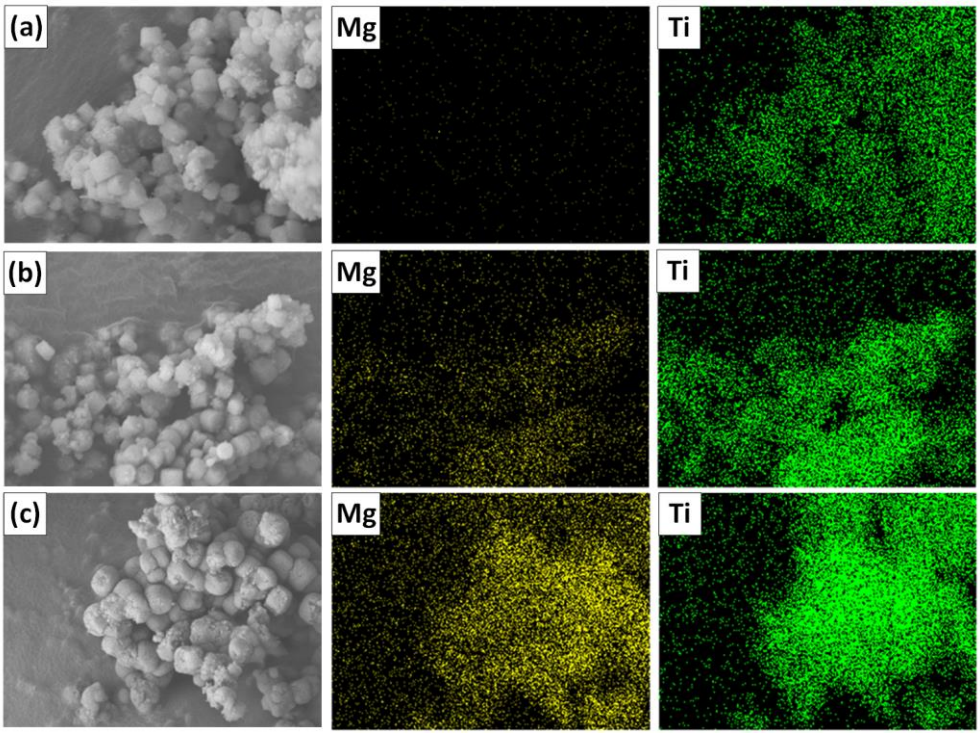

Figure 2-5 SEM image of (a) porous-TiO_2, (b) 10%WI, (c) 100ALD and respective elemental mapping of Mg and Ti.

2.3.5. Photocatalyst surface analysis

Surface chemical states of representative samples were analyzed with X-ray photoelectron spectroscopy (XPS). XPS survey of porous-TiO_2, 2%WI, and 5ALD samples can be found in Figure A-3. To confirm the presence of surface Mg, an analysis of the Mg *2p* peak was conducted. However, due to the low concentration of Mg and detection limit of the XPS instrument, the Mg *2p* peak was only found on samples with higher amounts of Mg addition. Mg *2p* XPS spectra of 100ALD and 10%WI are printed in Figure A-4. Mg *2p* peaks found at ~50 eV confirms the existence of Mg element on both of the photocatalysts.

It has been reported that the addition of MgO enables alternation of surface states on TiO_2 and promotes the generation of defects such as Ti^{3+} and oxygen vacancy [38]. Ti^{3+} has been reported to improve the light absorption of TiO_2, hinder electron-hole recombination and improve photoactivity [25, 39]. In addition, oxygen vacancies may serve as active sites in CO_2

photocatalytic reduction process [25, 34]. However, oxygen vacancies are unstable and have a tendency to react with surface absorbed water and form surface hydroxyl groups (-OH), which also is another reactive species in CO_2 photoreduction by enhancing CO_2 adsorption and conversion [124]. Therefore, XPS was applied to study the chemical states of Ti (Ti^{3+} and Ti^{4+}) and O (surface hydroxyl bonded with Mg (Mg-OH) or Ti (Ti-OH) and lattice oxygen bonded with Mg (Mg-O) or Ti (Ti-O)), by analyzing Ti *2p* and O *1s* peaks. The Ti *2p* peaks in the photocatalyst are located at binding energies 458.7 eV (Ti^{4+} $2p_{3/2}$), 464.6 eV (Ti^{4+} $2p_{1/2}$), 457.7 eV (Ti^{3+} $2p_{3/2}$), and 463.4 eV (Ti^{3+} $2p_{1/2}$); while O *1s* peaks are located at binding energies 532.6 eV (Mg-OH), 530.5 eV (Mg-O), 531.9 eV (Ti-OH) and 529.9 eV (Ti-O) [38, 125, 126].

Deconvolution analyses of Ti *2p* spectra for porous-TiO_2, 2%WI, and 5ALD are shown in Figure 2-6. Surface Ti^{4+} and Ti^{3+} contents of selected samples are listed in Table 2-3. The surface of porous-TiO_2 is of 100% Ti^{4+} due to the process of calcination in air at a high temperature. On the surface of WI samples, a small fraction of Ti^{3+} was detected, and it increased with MgO concentration and became saturated at about 6.7% Ti^{3+} for 10%WI. As previously reported [38]. The introduction of MgO on the surface of TiO_2 results in the generation of surface Ti^{3+}, due to the interaction of Mg with surface TiO_2. For ALD coated samples, 5.4% of Ti^{3+} was detected with the addition of 1 layer of ALD coating, while it drastically increased to 12.0% and 30.3% for samples with 2 and 5 ALD layers, respectively. This result clearly demonstrates a more significant impact of ALD coating than wet impregnation on the alternation of surface chemical states. For samples with 20 and 100 ALD layers, Ti peaks were hardly distinguishable from noises (Figure A-5) and thus were considered non-detectable. This is reasonable given the thicker coating of MgO masked X-ray exposure to the TiO_2 and XPS is sensitive only to a depth of a couple of nanometers on the surface. By comparing the Ti^{3+} percentage on the WI and ALD samples, it is clear that the

extent of Mg species in generating/altering Ti surface states depends more on MgO coverage (by ALD) than on MgO loading amount (by WI).

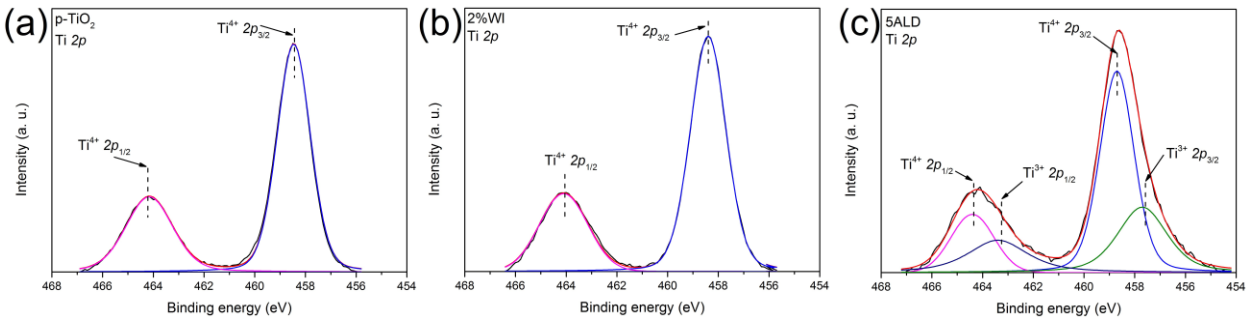

Figure 2-6 Ti *2p* XPS spectra of (a) porous-TiO_2, (b) 2%WI, (c) 5ALD.

Table 2-3 Surface chemical states and their contents on the surface of photocatalyst samples.

Sample ID	Ti *2p* (%)		O *1s* (%)			
	Ti^{3+}	Ti^{4+}	Mg-OH	Mg-O	Ti-OH	Ti-O
porous-TiO_2	0.0	100.0	-	-	5.9	94.1
0.1%WI	0.7	99.3	0.6	20.0	5.0	74.4
1%WI	1.0	99.0	1.0	37.2	9.5	52.3
2%WI	2.6	97.4	3.2	40.3	7.0	49.5
5%WI	6.3	93.7	3.0	42.4	1.6	53.0
10%WI	6.7	93.3	3.0	44.1	2.9	50.0
1ALD	5.4	94.6	0.9	8.7	2.6	88.3
2ALD	12.0	88.0	1.0	10.2	2.3	86.5
5ALD	30.3	69.7	2.2	41.8	3.7	52.3
20ALD	N/A	N/A	8.3	84.5	0.0	7.2
100ALD	N/A	N/A	8.6	91.4	0.0	0.0

Deconvolution analyses of O *1s* spectra for porous-TiO_2 and 2%WI, and 5ALD are displayed in Figure 2-7. The percentages of Ti-OH, Ti-O, Mg-OH, and Mg-O based on the O *1s* analyses are calculated and listed in Table 2-3. On the surface of the porous-TiO_2 sample, Ti-OH accounts for 5.9% of the surface species while the rest are Ti-O. The generation of a small amount

of surface OH groups is likely due to the adsorption of moisture from air. For WI samples, the percentages of surface Mg-OH and Mg-O have a positive correlation with MgO content in the range from 0.1% to 2% of MgO, while the percentages of total Ti coverage decreases, indicating an increased MgO surface coverage. From WI samples with larger than 2% MgO content, it is observed that the percentages of Mg-OH and Mg-O, as well as those of Ti-OH and Ti-O, remain relatively constant. This implies that the MgO coverage on the WI catalyst surface reached a maximum value at around 2% MgO and further increasing the MgO content only caused aggregation of MgO particles rather than extending the coverage on the catalyst. For the ALD samples, the percentages of Mg-OH and Mg-O increased with the number of ALD layers in the range from 1 to 100 layers, while the Ti coverage decreased accordingly. When the number of ALD layers was more than 20, the catalyst surface was covered by almost all Mg species with minimal exposure of Ti species. These results again reveal the more significant impact on the surface coverage by the ALD method than by the WI method.

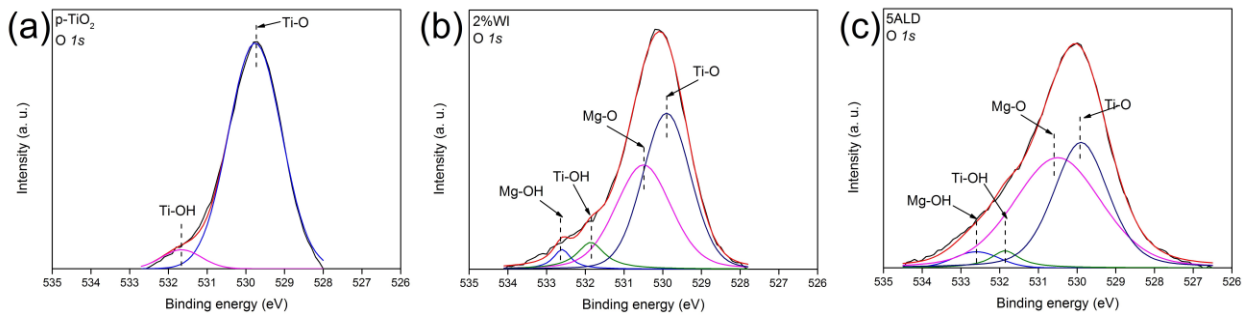

Figure 2-7 O *1s* XPS spectra of (a) porous-TiO_2, (b) 2%WI, (c) 5ALD.

2.3.6. Photocurrent measurements

As shown in Figure 2-8, under Xe lamp irradiation, the photocurrent density of porous-TiO_2 was measured to be 2.0 $\mu A/cm^2$. With the surface modification of MgO, the transient photocurrent density of 2%WI improved to 6.9 $\mu A/cm^2$, about 3.3 times as high as that of porous-

TiO_2. This result suggests the MgO modification improved photo-induced charge separation and transfer to the surface. The lower photocurrent generated on 5ALD than on 2%WI might be attributed to the more uniformly distributed MgO on the TiO_2 surface that adds more resistance to charge transfer.

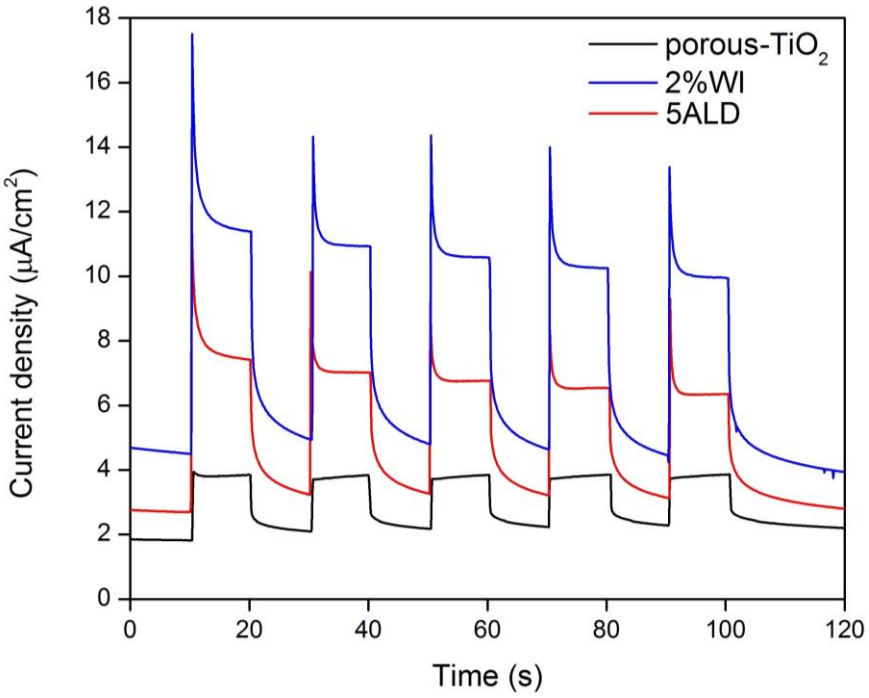

Figure 2-8 Transient photocurrent curves for porous-TiO_2, 2%WI, and 5ALD.

2.3.7. Optical properties

The UV-vis diffuse reflectance spectra and bandgap analyses are presented in Figure 2-9. The bandgap of porous-TiO_2 is measured at 3.0 eV, smaller than that of P25 (3.2 eV). The higher rutile phase percentage in porous-TiO_2 (56.1% rutile in porous-TiO_2 vs. ~15% rutile in P25 [127]) is possibly responsible for the reduced bandgap width. With the addition of MgO species, no significant change in bandgap and light absorption capacity was observed for both WI and ALD prepared samples, compared with that of porous-TiO_2. The bandgap variated from 3.0-3.1 eV for WI samples. The bandgap of all ALD samples except 100ALD was measured to be 3.0 eV; while

100ALD showed a slightly enlarged bandgap value of 3.2 eV. It is possible that a thicker layer of MgO such as 100ALD may have changed the surface optical property. Overall, neither WI nor ALD modification caused significant changes in the optical properties of porous-TiO_2.

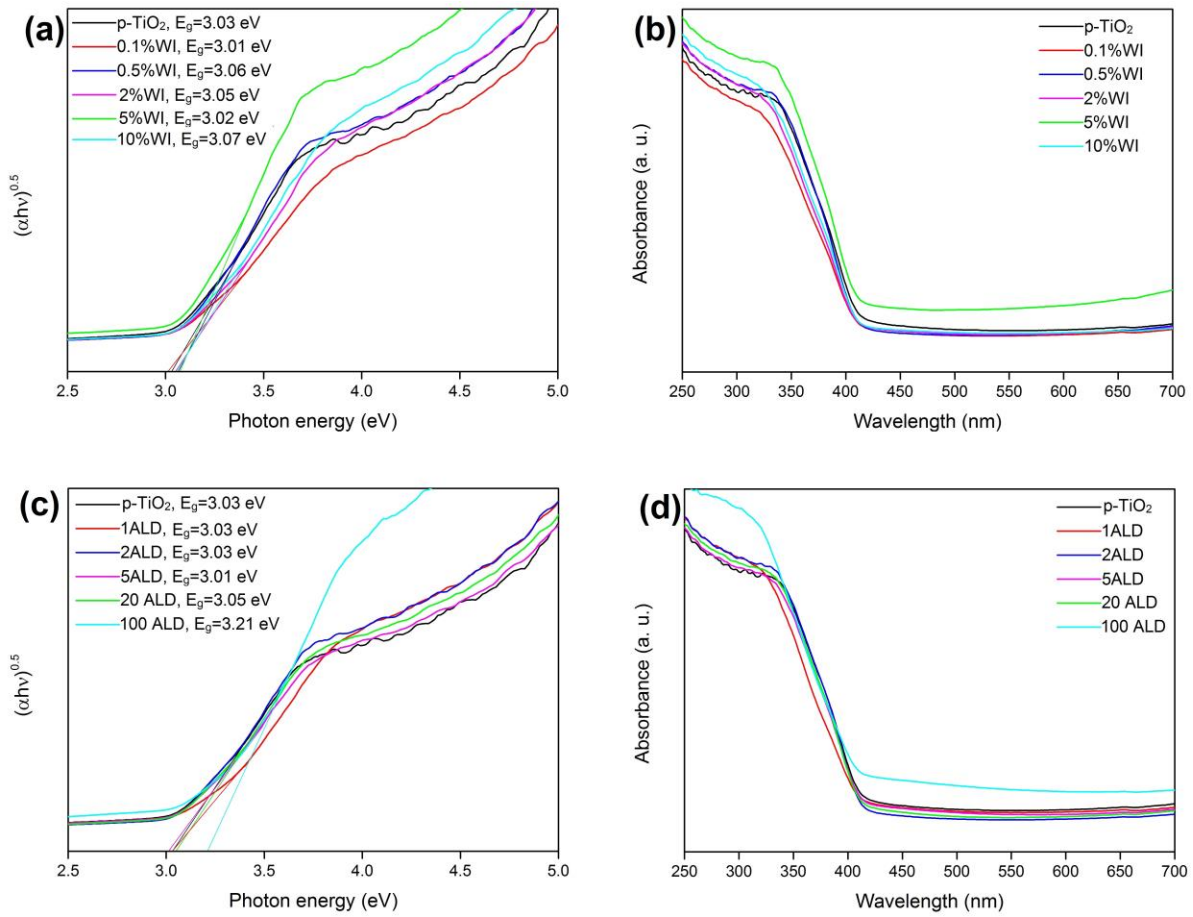

Figure 2-9 Band gap (a) and light absorption (b) analysis of porous-TiO_2 and WI samples; and band gap (c) and light absorption (d) analysis of porous-TiO_2 and ALD samples.

To understand the surface electron-hole recombination characteristic of the prepared samples, photoluminescence spectra were measured. Since photoluminescence spectra record light emission generated by electron-hole recombination, quenched photoluminescence intensity indicates improved charge separation. As shown in Figure 2-10, among the tested samples, porous-TiO_2 displayed the highest light emission, suggesting the largest surface recombination effect.

Among WI samples, it was observed that with only 0.1% of MgO addition, surface charge-hole recombination was suppressed, 2%WI showed an even weaker surface recombination effect. Reduction in photoluminescence suggests surface MgO played a key role in surface charge-hole separation. However, with a MgO concentration that is too high, the 10%WI showed higher photoluminescence than 0.1%WI, which suggests that excess MgO content on the porous-TiO_2 surface formed recombination centers. For ALD prepared samples, it was noticed that with only 1 layer of MgO overcoating, the photoluminescence was significantly reduced compared with porous-TiO_2, the reduction in photoluminescence did not change much with more added ALD layers. Overall, the ALD samples showed lower photoluminescence intensity than the WI samples. This is likely due to the surface state passivation effect of ALD overcoating that helps to reduce surface recombination. This mechanism was reported in our previously published work on CO_2 photoreduction by TiO_2 nanorods coated with an Al_2O_3 overlayer by ALD method [34].

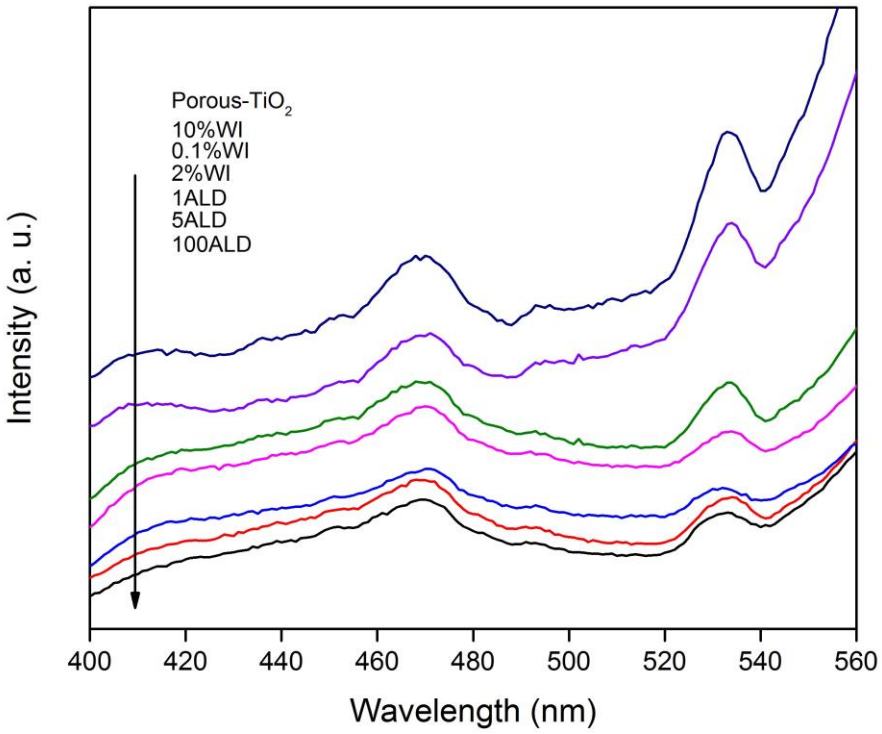

Figure 2-10 Photoluminescence spectra of porous-TiO_2, WI and ALD samples.

2.3.8. CO_2 photoreduction performance under UV-vis irradiation

The CO_2 photoreduction tests were conducted with a continuous flow of CO_2 and water vapor under UV-vis irradiation. The performances of WI and ALD samples in terms of CO production in comparison with P25 and porous-TiO_2 are shown in Figure 2-11. It is necessary to mention that several control experiments were conducted: (a) CO_2 + H_2O without photocatalysts under UV-vis irradiation; (b) CO_2 + H_2O with photocatalysts in the dark; (c) Ar + H_2O with photocatalysts under UV-vis irradiation. For none of those control experiments were carbon-containing products observed, indicating that the CO produced was indeed derived from CO_2. In this chapter, CO was found to be the major product, while trace CH_4 production was found only on 2ALD, 5ALD, and 10 ALD samples. Thus, only CO production was given and compared among the various catalysts. Commercially available P25 was used as a reference to demonstrate the improved performance of pristine and MgO modified porous-TiO_2. The CO produced by porous-TiO_2 (12.7 μmol/g) was 4.4-fold higher than that of P25 (2.5 μmol/g). Since porous-TiO_2 and P25 exhibited similar surface area (47.6 m^2/g for porous-TiO_2 vs. ~50 m^2/g for P25), the enhanced CO_2 photoreduction performance was attributed to the following two factors: (a) the porous hierarchical structure of porous-TiO_2; (b) the higher rutile to anatase ratio. The porous structure of porous-TiO_2 allows favorable inter- and intra- particle gas diffusion and reactant-product exchange with the bulk, leading to relatively high reactant and low product concentrations around the surface of the photocatalyst. In addition, according to previous reports [128-130]. A phase weight ratio of 50-60% rutile in anatase/rutile mixed TiO_2 presents highly improved photocatalytic performance compared with TiO_2 with a higher anatase content. It is possible that the proper rutile percentage in porous-TiO_2 (~56%) contributes to the improved performance in CO_2 photocatalytic reduction performance of porous-TiO_2 compared to P25.

With the modification of MgO, all WI samples and ALD samples displayed enhancement in photocatalytic CO_2 reduction performance. Due to the alkaline earth oxide nature of MgO, it is prone to generate surface hydroxyl even with the presence of a trace amount of water vapor. The surface hydroxyl groups on MgO have higher basicity than those on TiO_2 that are slightly acidic [131]. For WI samples, the CO_2 photoreduction performance improved with MgO addition amount from 0.1% to 2%. Among all WI samples, the 2%WI sample presented the best photoreduction performance, 40.5 μmol/g, which is 3.1 times higher than porous-TiO_2 and 16.2 times higher than P25. The improvement of 2%WI compared with porous-TiO_2 is attributed to favorable properties originating from the MgO modification such as surface Ti^{3+} species and Mg-OH groups as seen in Table 2-3. However, too much amount of MgO addition on the photocatalyst surface can reduce the contact of CO_2 molecules with TiO_2. In addition, the CO production is normalized by the total mass of TiO_2 and MgO, while TiO_2 is the only photo-active material. Increasing the MgO content above 5 wt. % did not increase the Ti^{3+} and Mg-OH significantly (Table 2-3) but reduced the amount of active TiO_2 content. As can be seen in Figure 2-11a, with MgO percentage higher than 2%, CO_2 photoreduction performance started to drop.

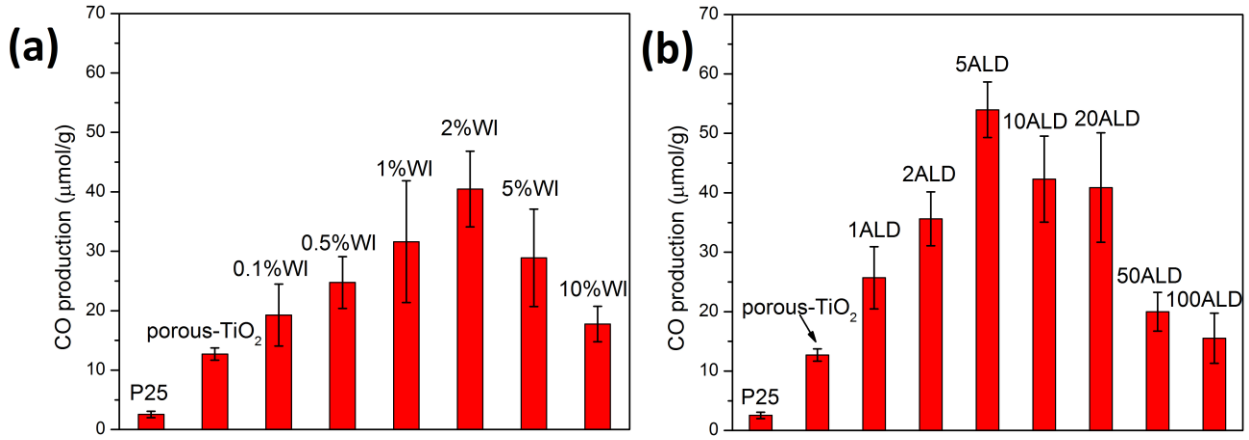

Figure 2-11 CO production by (a) WI and (b) ALD samples during 4-h CO_2 photoreduction with water vapor.

The performance of CO_2 photoreduction by ALD samples is shown in Figure 2-11b. The addition of a single atomic layer of MgO doubled the amount of CO production compared with pristine porous-TiO_2. The CO_2 photoreduction performance increased with the number of ALD layers from 1 to 5 layers and then decreased with more than 5 layers. The 5ALD sample was the optimum one among all ALD samples, producing 54.0 μmol/g CO, which was 4.3 times higher than porous-TiO_2 and 21.3 times higher than P25. With 30.3% surface Ti^{3+} concentration, 2.2% Mg-OH, and 41.8% MgO concentration, it is reasonable that the 5ALD sample performed significantly better than porous-TiO_2, which had none of the above active species However, similar to WI samples, ALD samples with too "thick" a MgO overlayer (>5 layers) experienced a decrease in CO_2 photoreduction performance. The decline in CO production can be attributed to the following reasons: (1) a decrease in surface area is observed with too many ALD layers, as seen in Table 2-2, which hinders the transport and adsorption of CO_2 in the porous TiO_2; and (2) an increase in the thickness of ALD overlayer increases the resistance for photoexcited electrons and holes to transfer to the surface of photocatalyst to initiate CO_2 reduction process. However, for catalysts with relatively "thick" layers such as 50ALD and 100ALD, the catalytic performance was not inferior to that of porous-TiO_2 thanks to the surface passivation effect of ALD layers that prevent surface charge recombination [34].

By comparing the photocurrent density data and CO_2 photoreduction performance of 2%WI and 5ALD, it was noticed that 2%WI showed higher photocurrent density but showed worse photocatalytic CO_2 performance compared to 5ALD. According to previously discussed, the major difference between 2%WI and 5ALD is the MgO morphology. Due to the nature of the WI method, MgO is deposited on 2%WI as ultrafine nanoparticles, while the MgO layer is more uniformly distributed on 5ALD. The difference in MgO morphology results in variations in surface

interaction with CO_2 molecules and thus affects CO_2 adsorption. The inconsistency in photocurrent density and overall CO_2 photoreduction performance and the difference in MgO morphology suggests a better affinity of CO_2 with 5ALD over 2%WI. Because of high coverage on photocatalysts, 5ALD has more surface area to serve as an absorbent to CO_2 molecules, as a result, photoexcited electrons can be more easily transferred to CO_2 molecules and thus the overall performance is improved.

In order to further demonstrate that porous-TiO_2 as a better candidate for photocatalytic CO_2 reduction applications over commercial P25, MgO modified P25 was prepared with 5 layers of MgO coating (denoted as 5ALD-P25) and 2% MgO of wet impregnation (denoted as 2%WI-P25). It was found that 2%WI-P25 produced 11.8 μmol/g of CO (equivalent to 29.1% of that produced by 2%WI-porous-TiO_2), 5ALD-P25 sample produced 15.5 μmol/g of CO (equivalent to 28.7% of that produced by 5ALD-porous-TiO_2). Combining the result that P25 produced only 2.5 μmol/g of CO (equivalent to 19.2% of that produced by porous-TiO_2), it is apparent that porous-TiO_2 is advantageous over P25 no matter with or without MgO modification.

To investigate the effect of coating materials on the catalytic activity, we have conducted another experiment using ALD to coat 5 layers of Al_2O_3 on porous-TiO_2. The sample is denoted as 5ALD(Al_2O_3), and its catalytic activity is compared with that by 5ALD(MgO). The 5ALD(Al_2O_3) sample produced 19.2 μmol/g of CO, which is higher than the pristine porous-TiO_2 (12.7 μmol/g) but much lower than 5ALD(MgO) (54.0 μmol/g) as shown in Figure 2-11. According to our previous report [34], an Al_2O_3_ALD overlayer on TiO_2 exhibits a surface state preservation effect and thus promotes CO_2 photoreduction performance. This conclusion is once again confirmed in this chapter by comparing 5ALD(Al_2O_3) with porous-TiO_2. The difference in catalytic activity between 5ALD(Al_2O_3) and 5ALD(MgO) suggests that, in addition to the surface

state preservation effect, the MgO layer may promote adsorption of CO_2 due to higher surface basicity. Because of the extremely trace amount of ALD coated MgO present on the surface, it was not possible to differentiate the equilibrium CO_2 adsorption capacity on the MgO-coated and Al_2O_3-coated or non-coated samples. Given that the 2%WI sample had 40.5 μmol/g CO production that is still much higher than the 5ALD(Al_2O_3) sample, it is likely the surface CO_2 adsorption enhancement due to MgO is one of the main reasons for the promoted CO_2 photoreduction activity, as also evidenced in previous studies [108, 109].

By comparing the best-performing ALD sample (5ALD) with the best-performing WI sample (2%WI), one can see that the performance of 5ALD in CO production was 28% better than that of 2%WI. The phase composition, surface area, crystal size, and bandgap of 5ALD and 2%WI were similar (Table 2-2). The surface Mg atomic concentrations of the two samples were also very close (Table 2-3). The most extinct difference between the two materials is the surface Ti^{3+} concentration (30.3% on 5ALD and 2.6% on 2%WI), which may account for the better performance of 5ALD than 2%WI. This is because Ti^{3+} is usually paired with oxygen vacancies and those defect sites play a crucial role in facilitating charge transfer and separation as well as CO_2/H_2O adsorption and dissociation on the catalyst surface [9, 25, 39, 132].

2.3.9. CO_2 photoreduction mechanism

With regard to the CO_2 photoreduction mechanism, it has been widely reported in the literature [133-135] that the formation of CO and CH_4 follows the two- and eight-electron reduction processes, respectively. It is reasonable that CO is found to be the major product in this chapter because much fewer electrons are needed to form CO than to form CH_4.

$CO_2 + 2H^+ + 2e^- \rightarrow CO + H_2O$ (1)

$CO_2 + 8H^+ + 8e^- \rightarrow CH_4 + 2H_2O$ (2)

Moreover, the surface oxygen vacancy/Ti^{3+} species is believed to improve CO_2 adsorption and activation on the surface, according to the following reactions, where CO_2^-, HCO_3^-, and CO_3^{2-} species could be intermediate species for CO_2 reduction (Spontaneous dissociation of CO_2 to CO on the defective surface of Cu (I)/TiO_{2-x} nanoparticles at room temperature [136].

$Ti^{3+} + CO_2 \rightarrow Ti^{4+}\text{-}CO_2^-$ (3)

$OH^- + CO_2 \rightarrow HCO_3^-$ (4)

$Ti^{4+}\text{-}O^{2-} + CO_2 \rightarrow Ti^{4+}\text{-}CO_3^{2-}$ (5)

In this chapter, MgO modified on the TiO_2 surface, especially ALD-coated MgO significantly increased the surface Ti^{3+} and OH species, and thus contributed to the production of CO_2 reduction intermediates as shown in Reactions (3) - (5).

2.4. Conclusions

The work in this chapter for the first time applied ALD to effectively coat a thin, uniform layer of MgO on a MOF-derived porous TiO_2 photocatalyst and demonstrated significantly promoted CO_2 photoreduction performance, which was more than 4 times and 18 times higher than those of porous TiO_2 and commercial P25, respectively. A conventional wet-impregnation (WI) method was also applied to incorporate MgO on porous TiO_2 to compare against the ALD method. MgO modified catalysts prepared by both methods showed enhancement in CO

production because of the added surface basicity to enhance CO_2 adsorption and the introduction of defect sites such as Ti^{3+} to promote electron-hole transfer. The ALD samples were advantageous over WI samples due to the generation of higher concentrations of surface Ti^{3+} and the surface passivation effect of ALD coating that inhibits surface recombination. Material property analysis and photocatalytic activity results showed that the ALD method is likely a better way to compare with the conventional WI method with higher surface Ti^{3+} concentration, ALD coating surface state preservation effects as well as lower charge/hole recombination effects. The application of ALD as an enabling technique of surface modification to enhance catalytic performance successfully demonstrated in this chapter may be extended to catalysts beyond TiO_2 and to catalytic reactions beyond CO_2 reduction.

3. PHOTOCATALYTIC CARBON DIOXIDE REDUCTION ON POROUS TITANIUM DIOXIDE SYNERGISTICALLY PROMOTED BY ATOMIC LAYER DEPOSITED MAGNESIUM OXIDE OVERCOATING AND PHOTODEPOSITED SILVER NANOPARTICLES[†]

3.1. Introduction

As demonstrated in Chapter 2, the combination of highly porous TiO_2 with atomic layer deposition enabled alkaline MgO coating significantly promote the CO_2 photoreduction performance. However, as an insulator, MgO does not promotes photocatalytic CO_2 reduction; although it may induce surface Ti^{3+} and oxygen vacancy generation, which further promotes CO_2 adsorption and photoreduction [38].

To reduce charge recombination, the deposition of nanoparticles (NPs) of precious metals (e.g. Au, Pt, Rh, Ag) on TiO_2 has been used, and the deposited metal NPs serve as electron traps and promote charge migration to the photocatalyst surface [18, 21, 48, 50, 110]. Among all the precious metals, Ag has a relatively lower cost but demonstrated high efficiency in promoting photocatalytic reactions [137-139]. In addition, metal modifications can alter the selectivity of CO_2 reduction products (e.g. CO, CH_4, etc.). A higher CH_4 selectivity has been reported in the presence of Ag NPs, because of the increased density of electrons on the catalyst surface due to the electron trapping effect of Ag modification [140, 141].

Since both MgO and Ag modifications on TiO_2 have shown promotional effects on CO_2 photoreduction, a co-modification strategy has been applied recently by Li *et al.* [44], in which

[†] Part of this chapter is reprinted with permission from "Photocatalytic CO_2 reduction on porous TiO_2 synergistically promoted by atomic layer deposited MgO overcoating and photodeposited silver nanoparticles" by Xuhui Feng, Fuping Pan, Brandon Z. Tran, and Ying Li, *Catalysis Today*, 2020, 339, 328-336. Copyright [2020] by Elsevier.

MgO and Ag nanoparticles were deposited on TiO_2 by wet impregnation and photodeposition methods, respectively. This work showed that the co-modification of MgO and Ag on TiO_2 further improved the CO_2 photoreduction performance compared with individual modification of MgO and Ag separately. However, more research is required to investigate the compositional and morphological impacts of MgO/Ag co-modification and to better understand the correlation between the MgO/Ag materials structure and photocatalytic activity.

In light of the advantages of MgO coating by ALD and the photodeposition of Ag NPs on TiO_2, the objective of this chapter was to apply co-modification of the two promoter species on porous TiO_2 and investigate the correlations between the nanostructure of MgO/Ag co-modification and the photocatalytic activity on CO_2 reduction. Even though the chemical compositions of the MgO/Ag co-modification are the same or similar, there may be two different nanostructures of co-modification by altering the sequence of MgO coating and Ag deposition. We hypothesize that the different nanostructure (i.e. whether Ag NPs are on the outermost surface of MgO coated TiO_2 or Ag NPs are sandwiched between MgO and TiO_2) will result in differences in photocatalytic CO_2 reduction performance due to the change in surface chemistry. The new materials design and structure-property correlation investigation present the novelty of this work that has not been reported in the literature.

3.2. Materials and methods

3.2.1. Ag modification on pristine TiO_2

Pristine porous TiO_2 preparation procedure was the same as mentioned in Chapter 2. In a typical preparation of Ag modified porous TiO_2, 50 mg of pristine TiO_2 was dispersed in 40 ml aqueous solution where a predetermined amount of $AgNO_3$ was dissolved. The suspension was

treated under a 100 W UV lamp (365 nm, UV irradiation intensity 8 mW/cm^2) for 1 h. The photocatalyst was collected by centrifugation and rinsed with water three times and then dried in a vacuum oven overnight at 80 °C. The samples were then calcined in air at 450 °C for 30 min. The obtained Ag/TiO_2 samples were denoted as "*x*Ag", where *x* represents the weight percentage of Ag relative to TiO_2 in the precursor solution. In this chapter, the value of *x* was designed to be 1, 2, 5, or 10 wt.%, corresponding to 0.74, 1.48, 3.70, or 7.40 at.%, respectively.

3.2.2. MgO atomic layer deposition on pristine TiO_2

An Ultratech Savannah S200 ALD system was used to coat an ultrathin MgO layer on pristine TiO_2. A homemade powder holder loaded with 100 mg of pristine TiO_2 powder was placed in the center of the ALD chamber, which was maintained at 200 °C during the ALD process. Bis(ethylcyclopentadienyl) magnesium [$Mg(C_5H_4C_2H_5)_2$, min. 98%, Strem Chemicals Inc.] was used as the Mg precursor. In each ALD cycle, "expo" mode was used for coating porous materials, and the pulse time of water and Mg precursor was set to 2 s each to introduce an adequate amount of reactants to the reaction chamber and ensure an even ALD coating on pristine TiO_2. A predetermined number of cycles was applied on pristine TiO_2 powder. After the ALD process, a grey powder was obtained and calcined at 450 °C for 30 min to remove any potential organic residues from the ALD process. The obtained MgO/TiO_2 sample was denoted as "*y*Mg", where *y* was the number of ALD cycles and was chosen to be 1, 3, 5, 7, or 10. As observed in Chapter 2, the optimum ALD coating to promote photocatalytic performance was found to be less than 10 cycles or in the sub-nanometer range, as too "thick" a coating can inhibit charge migration to the catalyst surface [15, 34, 50, 142].

3.2.3. Preparation of Ag and MgO co-modified TiO_2

The pristine TiO_2 was co-modified by both ALD-coated MgO and photodeposited Ag at different orders: (1) MgO deposition followed by Ag (i.e. Ag/MgO/TiO_2), or (2) Ag deposition followed by MgO (i.e. MgO/Ag/TiO_2). For the co-modified TiO_2 samples, Ag content was kept constant at 5 wt.% (as identified to be the optimum from preliminary tests presented later in the paper), while the thickness of MgO (number of ALD cycles) varied. A schematic of the preparation procedure and proposed materials morphology is illustrated in Figure 3-1.

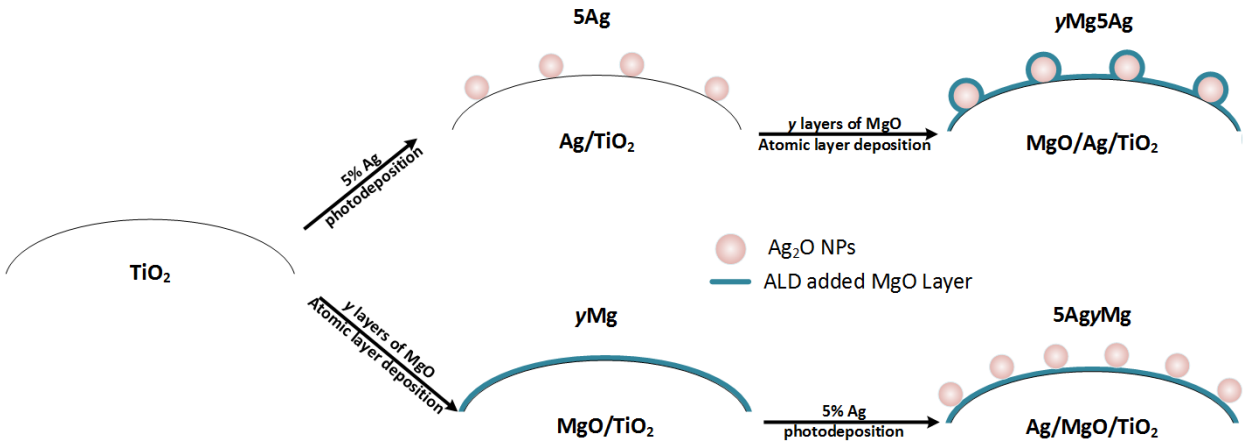

Figure 3-1 Schematic of Ag and MgO co-modified TiO_2 samples prepared in two different ways by varying the modification sequence.

In a typical procedure of preparing Ag/MgO/TiO_2 samples, 50 mg of *y*Mg (MgO/TiO_2) powder was dispersed in 40 ml of water where 3.92 mg of $AgNO_3$ was dissolved, and the weight of Ag in the solution was 5% relative to the *y*Mg powder. The suspension was treated under a 100 W UV lamp for 1 h. After UV treatment, the photocatalyst was centrifuged and rinsed with water three times and then dried overnight in a vacuum oven at 80 °C. The collected sample powder was

then calcined in air at 450 °C for 30 min. The obtained Ag/MgO/TiO_2 samples were denoted as 5Ag*y*Mg.

In a typical procedure of preparing MgO/Ag/TiO_2 samples, 100 mg of 5Ag (Ag/TiO_2) powder was treated by the ALD process described previously. After the ALD process, the obtained powder was calcined at 450 °C for 30 min to remove any potential organic residues from the ALD process, and then a grey powder was obtained. The obtained MgO/Ag/TiO_2 samples were denoted as *y*Mg5Ag.

3.2.4. Materials characterization and CO_2 photoreduction performance test

Material characterization procedure applied in this chapter is similar to what was described in Section 2.2.5. The experimental setup for CO_2 photoreduction was similar to that in Section 2.2.6.

3.2.5. Transient photocurrent and electrochemical impedance spectroscopy testing

Transient photocurrent density and electrochemical impedance spectroscopy (EIS) of prepared samples were measured with a Gamry Reference 3000 potentiostat. In a typical transient photocurrent density measurement, 1.2 mg of photocatalyst was loaded on the conductive surface of a piece of ITO (indium tin oxide) glass, and a 0.05 M Na_2SO_4 solution was used as the electrolyte. A 450 W Xe-lamp was used as the light source, a 3M Ag/AgCl electrode was used as a reference, and a Pt slice was used as the counter electrode. EIS measurements were conducted with the same experimental setup. The EIS measurements were measured under Xe-lamp irradiation, over a frequency range of 0.2 Hz to 100 kHz, and under a perturbation of 10 mV.

3.3. Results and discussion

3.3.1. Crystal structure

The XRD patterns of as-prepared photocatalysts are shown in Figure 3-2. It was found that all samples consisted of both anatase and rutile TiO_2. However, the fingerprint peaks for MgO or Ag were not detected, likely because the amount of surface MgO and Ag was low or they were in amorphous form. The TiO_2 phase composition and crystallite size of anatase and rutile in the samples are listed in Table 3-1. The anatase/rutile ratio was calculated by the Rietveld refinement method [121].

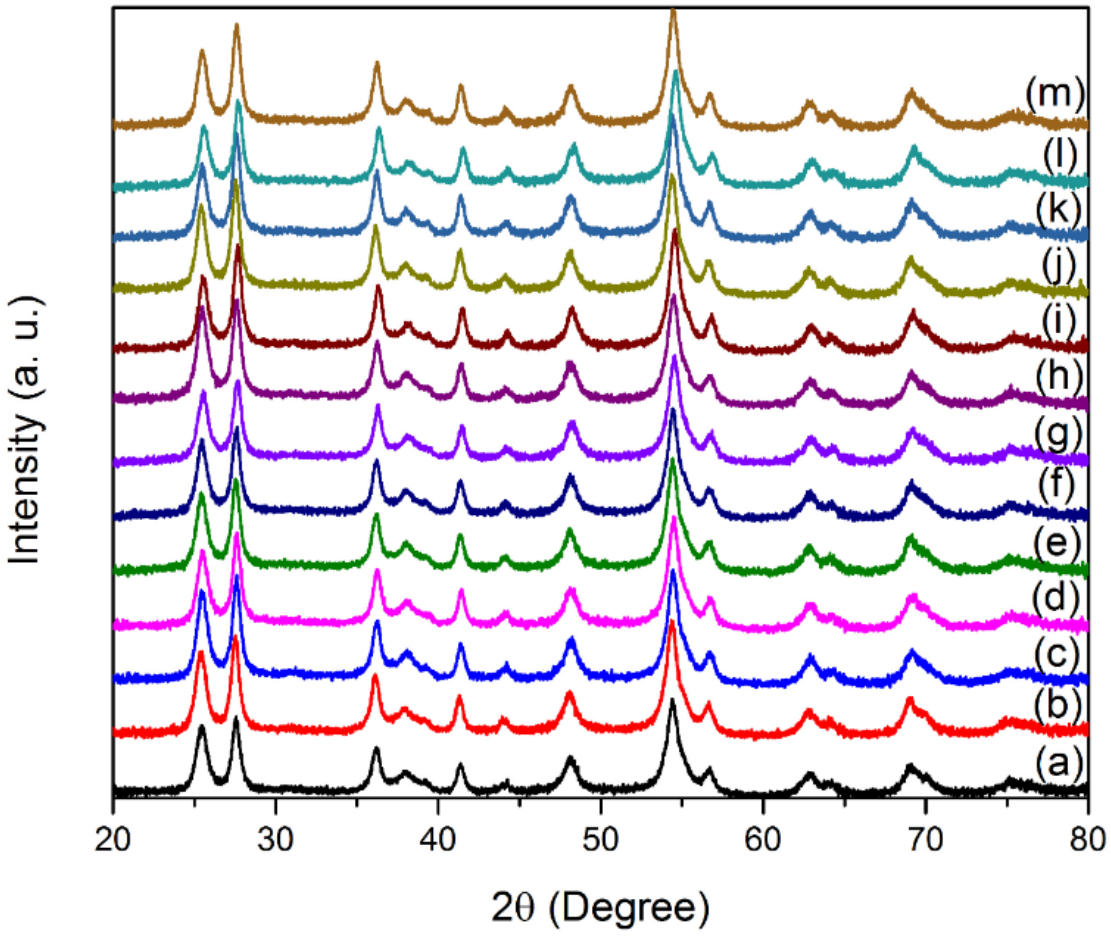

Figure 3-2 XRD pattern of prepared samples, (a) pristine TiO_2, (b) 7Mg, (c) 5Ag, (d) 1Mg5Ag, (e) 3Mg5Ag, (f) 5Mg5Ag, (g) 7Mg5Ag, (h) 10Mg5Ag, (i) 5Ag1Mg, (j) 5Ag3Mg, (k) 5Ag5Mg, (l) 5Ag7Mg, (m) 5Ag10Mg.

It can be seen from Table 3-1 that the percentage of rutile slightly increases with the complexity of materials preparation (e.g. rutile content in pristine TiO_2 < Ag or MgO individually modified TiO_2 < Ag and MgO co-modified TiO_2). It is likely the extended calcination treatment of co-modified samples promoted the transformation of anatase into rutile. Nevertheless, there were no significant variations in terms of phase composition and crystallite size for all the samples.

Table 3-1 Phase composition and crystallite size of prepared samples.

Sample ID	Anatase %	Rutile %	Anatase crystallite size (nm)	Rutile crystallite size (nm)
Pristine TiO_2	47.8	52.2	11.3	13.9
7Mg	45.5	54.5	11.5	14.6
5Ag	46.4	53.6	11.5	16.3
1Mg5Ag	42.7	57.3	11.5	15.7
3Mg5Ag	44.6	55.4	11.5	14.6
5Mg5Ag	45.0	55.0	11.5	16.3
7Mg5Ag	44.8	55.2	12.1	15.4
10Mg5Ag	45.1	54.9	11.0	14.9
5Ag1Mg	44.0	56.0	12.9	16.0
5Ag3Mg	43.6	56.4	11.4	15.2
5Ag5Mg	43.1	57.0	11.6	15.3
5Ag7Mg	42.6	57.4	12.2	15.3
5Ag10Mg	42.0	58.0	12.0	15.1

3.3.2. Morphology

SEM images of pristine TiO_2, 7Mg5Ag, and 5Ag7Mg samples are shown in Figure 3-3. All samples exhibited similar morphology and cubic shape of particles at an average size of ~270 nm. High-resolution TEM analysis was performed on 7Mg5Ag and 5Ag7Mg to investigate the differences in nanostructure resulting from different preparation procedures, the results are shown in Figure 3-4.

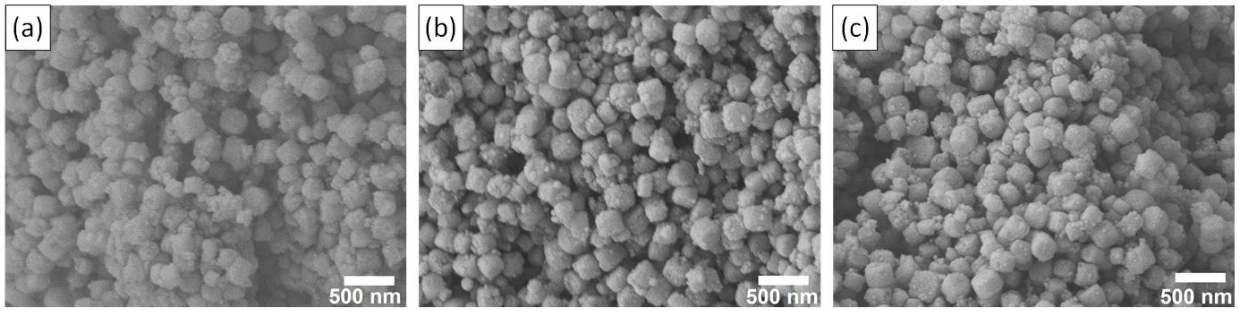

Figure 3-3 SEM image of (a) pristine TiO_2, (b) 7Mg5Ag, (c) 5Ag7Mg.

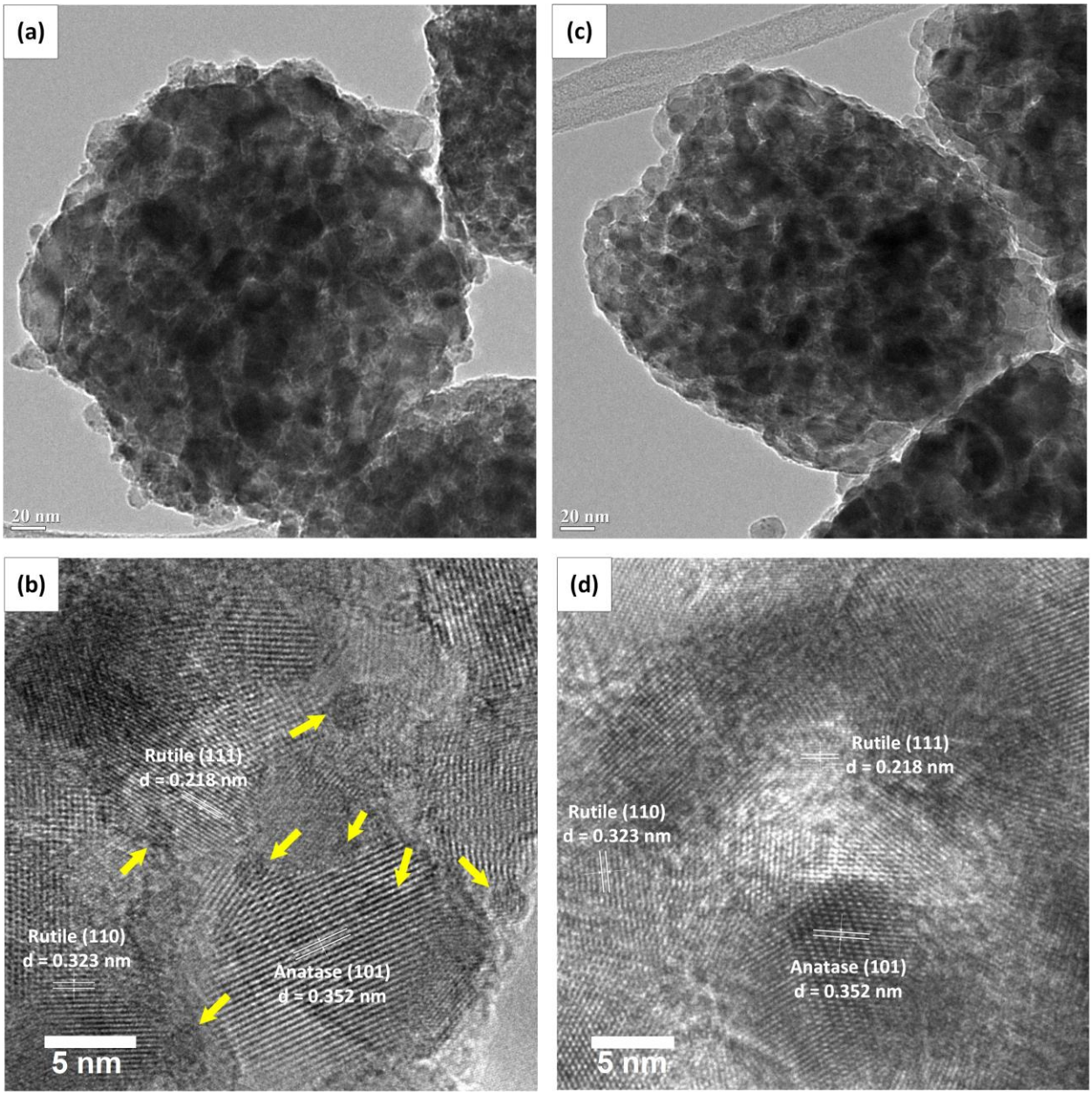

Figure 3-4 TEM and HRTEM images of 7Mg5Ag (a, b) and 5Ag7Mg (c, d).

As shown in Figure 3-4a and c, 7Mg5Ag and 5Ag7Mg demonstrate the assembly of primary ultrafine particles (< 20 nm) into a larger cubic shape, porous particle at a size of ~270 nm, which is consistent with the particle size observed from the SEM images and to the morphology of porous TiO_2 reported from the literature [15]. As displayed in Figure 3-4b and d, anatase [101] (d = 0.352 nm), rutile [110] (d = 0.323 nm) and rutile [111] (d = 0.218 nm) were found on the two samples. The existence of the MgO phase was not observed in TEM images, this is likely due to the small amount of addition. In Figure 3-4b, as indicated by the yellow arrows, there seem to be some Ag nanoparticles on 7Mg5Ag. But due to heavy overlapping with TiO_2 crystallites, the characteristic lattice of neither Ag nor Ag_2O could be clearly identified in the TEM image. For 5Ag7Mg as displayed in Figure 3-4d, Ag nanoparticles with well-defined shape were not observed. It is possible that the size of the Ag nanoparticles or clusters on this sample was too small to be detected.

3.3.3. Surface analysis

In order to investigate the surface chemical states and compositions of the prepared samples, XPS analyses were performed. The XPS survey spectra of all prepared samples are shown in Figure B-1. The presence of Ti and O elements was confirmed on the pristine TiO_2, and no Ag elements were found on the 7Mg sample. It has to be made clear that the C *1s* peak observed in the survey spectrum is the result of double-sided tape used in the XPS analyses. The existence of MgO on 7Mg, 7Mg5Ag, and 5Ag7Mg was also confirmed by XPS spectra on Mg *2s* orbitals in Figure B-2. XPS spectra on Ti *2p* peaks of pristine TiO_2, 7Mg, 5Ag, 7Mg5Ag, and 7Mg5Ag are shown in Figure 3-5a. It was found that the Ti $2p_{3/2}$ peak of 5Ag, 7Mg5Ag, and 5Ag7Mg shifted from 458.5 eV (pristine TiO_2 and 7Mg) to 458.2 eV (after Ag addition), suggesting the formation

of surface Ti^{3+} species [143]. In the XPS spectra of O *1s* (Figure 3-5b). A slight negative shift of binding energy was observed on 5Ag, 5Ag7Mg and 7Mg5Ag compared with pristine TiO_2 and 7Mg, which might be ascribed to the formation of surface oxygen vacancies.

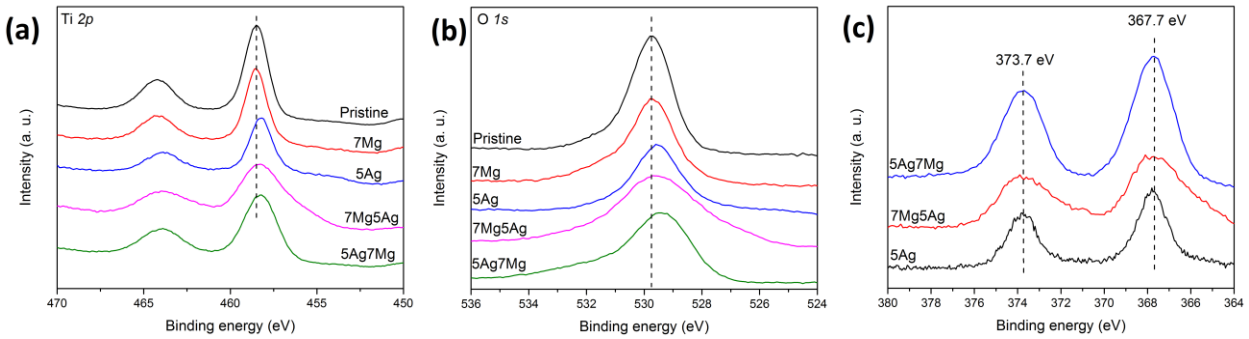

Figure 3-5 XPS spectra of (a) Ti *2p* spectra, (c) O *1s* spectra, (c) Ag *3d* spectra of as-prepared samples.

The generation of oxygen vacancies and Ti^{3+} under aerobic calcination condition on MgO and/or Ag surface modifications was also reported previously [15, 38]. According to Manzanares *et al.* [38], the generation of oxygen vacancy on MgO modified TiO_2 may result from Ti^{4+} substituted by Mg^{2+}, as expressed as follows,

$$MgO \xrightarrow{TiO_2} Mg_{Ti} + V_O + O_L, \quad (1)$$

where Mg_{Ti} indicates Mg^{2+} in a Ti^{4+} site, V_O and O_L indicate oxygen vacancy and lattice oxygen, respectively. The generated oxygen vacancies are not stable, and they might be neutralized either by chemically adsorbed water to form surface hydroxyl [144] or by crystalline structure reorganization to create Ti^{3+} [145].

Similar results were observed on Ag modified TiO_2 by Gannoruwa *et al.* [146], where Ti^{3+} may also be generated on Ag/TiO_2 through the following reactions,

$Ag_2O + h\nu \rightarrow Ag_2O(h^+\text{-}e^-)$ (2)

$TiO_2/Ag_2O(h^+\text{-}e^-) \rightarrow TiO_2(e^-)/Ag_2O(h^+)$ (3)

The photoexcited electrons and holes are generated by Ag_2O by absorbing diffuse light from the surroundings and consequently transferring from Ag_2O to TiO_2 to generate Ti^{3+}.

To better understand the chemical state of oxygen on the MgO/Ag co-modified samples, deconvolution of O *1s* was conducted according to a previous report [147], where O *1s* was deconvoluted into lattice oxygen (O^{2-}, ~529.0 eV), hydroxyl (-OH, ~531.6 eV), and adsorbed water (~533.2 eV). As shown in Figure 3-6, O^{2-} and -OH were present on both 7Mg5Ag and 5Ag7Mg samples and absorbed water was not found, likely due to the evaporation of water under ultra-high vacuum conditions in the XPS chamber. By comparing the oxygen chemical state on both 7Mg5Ag and 5Ag7Mg samples, it was found that 5Ag7Mg shows more concentrated surface -OH (5Ag7Mg 23.8% -OH vs. 7Mg5Ag 9.9% -OH, which can be generated by partial neutralization of oxygen vacancies in the presence of water [15].

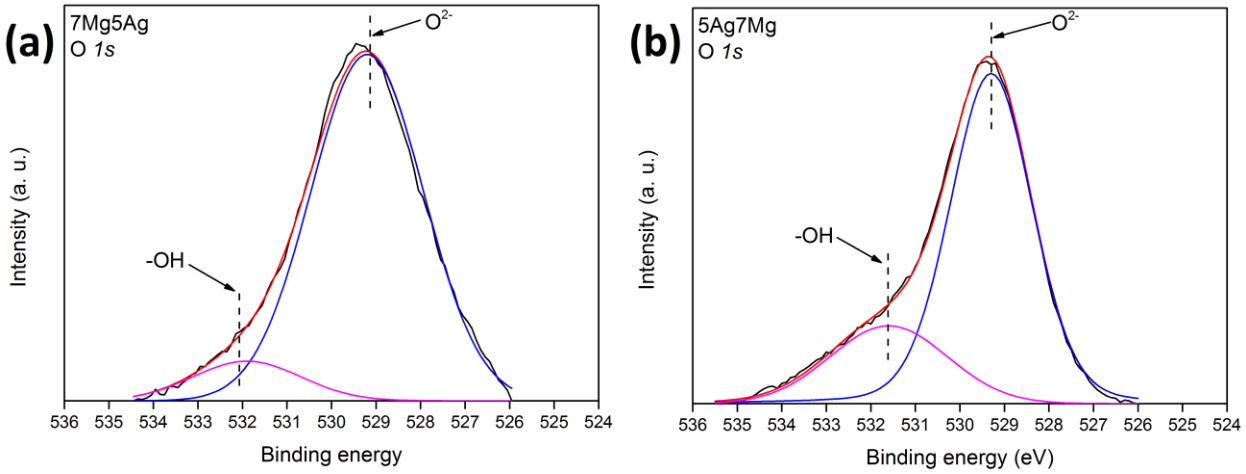

Figure 3-6 XPS deconvolution of O *1s* on (a) 7Mg5Ag and (b) 5Ag7Mg samples.

On the XPS spectra of 5Ag, 7Mg5Ag, and 5Ag7Mg, strong Ag *3d* doublet peaks were found (Figure 3-5c), confirming the successful Ag surface modification. The Ag *3d* peaks on both 7Mg5Ag and 5Ag7Mg were found to be located at 367.7 eV and 373.3 eV, which correspond to the binding energy of Ag_2O [148]. Since all of the prepared samples were calcined at 450 °C after Ag photodeposition, it is reasonable that silver oxide was formed. The XPS results reveal that the Ag concentration on the surface of 7Mg5Ag and 5Ag7Mg were 2.25 and 4.92 at.%, respectively, while the nominal Ag atomic concentration was 3.70 at.% (or 5 wt.%) for both samples assuming that Ag in the precursor solution was completely deposited on TiO_2. Because XPS is a surface analysis technique, it is reasonable that the surface Ag concentration measured by XPS is greater than the nominal concentration in the bulk. To obtain accurate silver deposition concentration on both of the two samples, inductively coupled plasma (ICP) analysis has been conducted on 7Mg5Ag and 5Ag7Mg. The ICP results show that the silver concentrations on both 7Mg5Ag and 5Ag7Mg are 1.92 wt.% and 2.66 wt.%. Both XPS and ICP results indicate that more Ag was deposited on the surface of the 5Ag7Mg sample than on 7Mg5Ag.

3.3.4. Optical properties

The UV-vis diffuse reflectance spectra and calculated bandgap energy of the samples are presented in Figure 3-7. All of the Ag modified samples showed an increased capability in visible light absorption (>400 nm) compared with pristine TiO_2. However, neither Ag nor MgO modification significantly altered the bandgap energies. All the samples had a bandgap in a small range of 2.98 ~ 3.08 eV with no particular correlation to the structure of the materials. This bandgap energy well matches that of TiO_2 with a significant phase content of rutile.

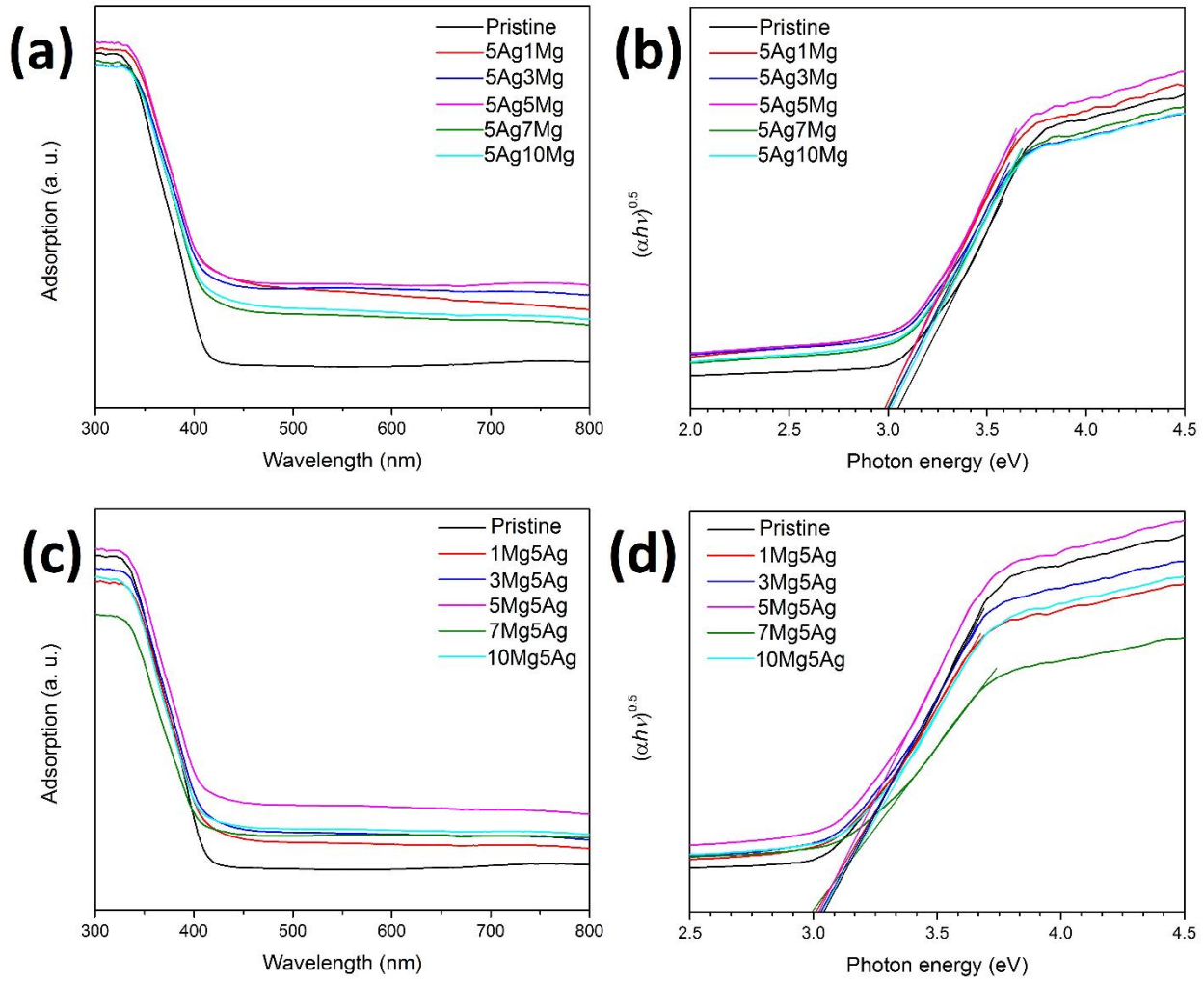

Figure 3-7 UV-vis diffuse reflectance spectra and Tauc plots of 5AgyMg (a, b) and yMg5Ag (c, d).

The surface electron-hole recombination characteristics of the pristine TiO_2, 7Mg, 5Ag, 7Mg5Ag, and 5Ag7Mg were investigated with photoluminescence (PL) analyses. The PL spectra record the light emission generated by the recombination of electron-hole pairs, and thus lower PL intensity suggests hindered recombination. As shown in Figure 3-8, pristine TiO_2 displayed the highest light emission among the tested samples. With 7 layers of ALD added MgO coating (7Mg sample), the PL intensity decreased significantly, and his observation is consistent with our previous work where an ALD overlayer passivates surface states and hinders surface charge recombination [15, 34]. The 5Ag sample shows an even lower PL intensity, demonstrating the

promoted electron-hole separation after adding Ag NPs. The 7Mg5Ag and 5Ag7Mg samples, which are co-modified with MgO and Ag, show the comparable and lowest levels of PL intensity. This clearly reveals the synergy of MgO and Ag co-modification that facilitates the charge separation on the TiO_2 surface.

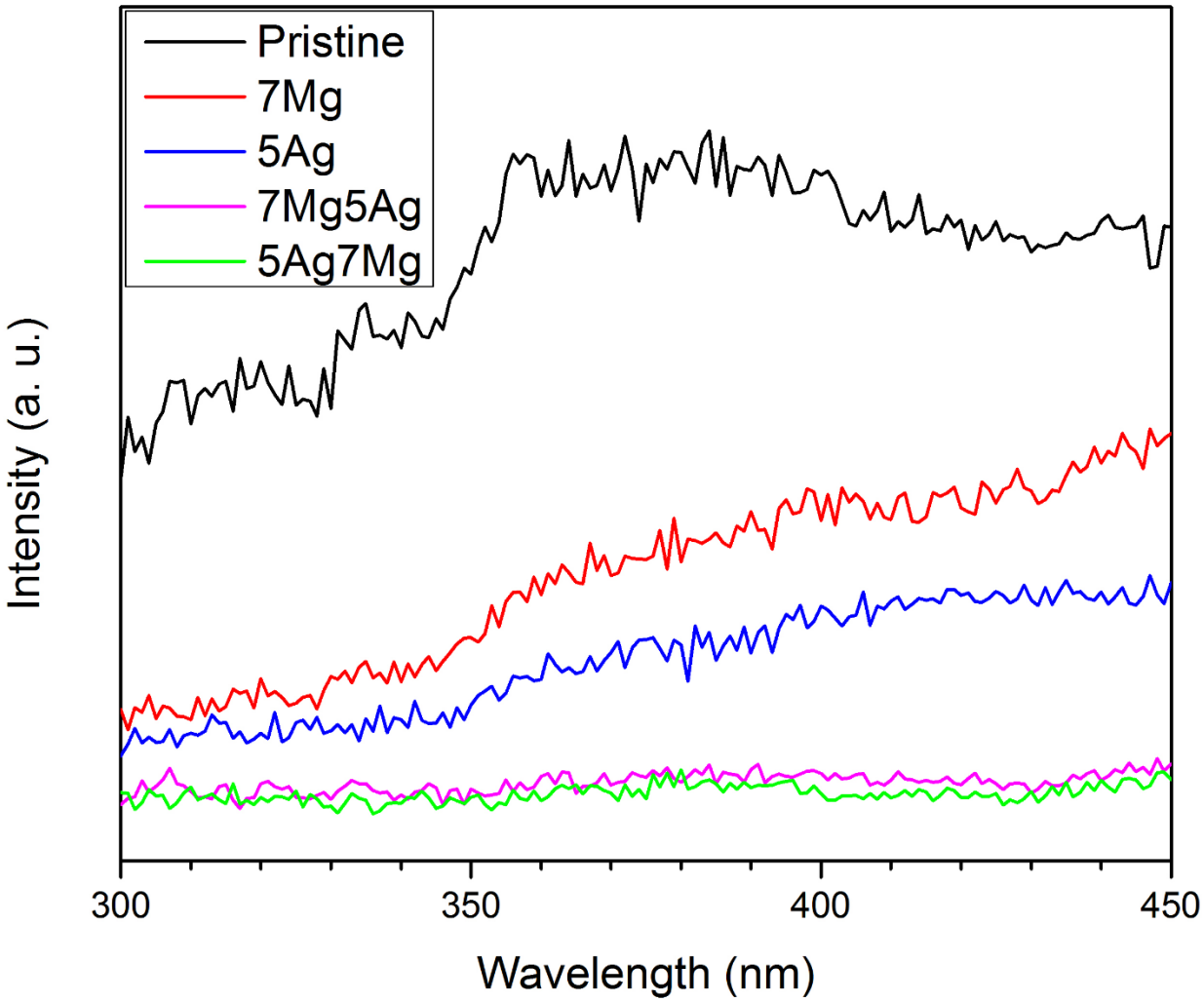

Figure 3-8 Photoluminescence spectra of as-prepared samples.

3.3.5. CO_2 photoreduction performance under UV-vis irradiation

The CO_2 photoreduction tests were conducted with a continuous flow of CO_2 and water vapor under a UV-vis irradiation. Several control experiments have been conducted: (a) CO_2 +

H_2O without photocatalysts under the UV-vis irradiation; (b) CO_2 + H_2O with the photocatalysts under the dark; (c) Ar + H_2O with the photocatalysts under the UV-vis irradiation. No carbon-containing products were observed in those control experiments, indicating that CO and/or CH_4 produced in the CO_2 photoreduction process were indeed derived from the CO_2 in the feed gas.

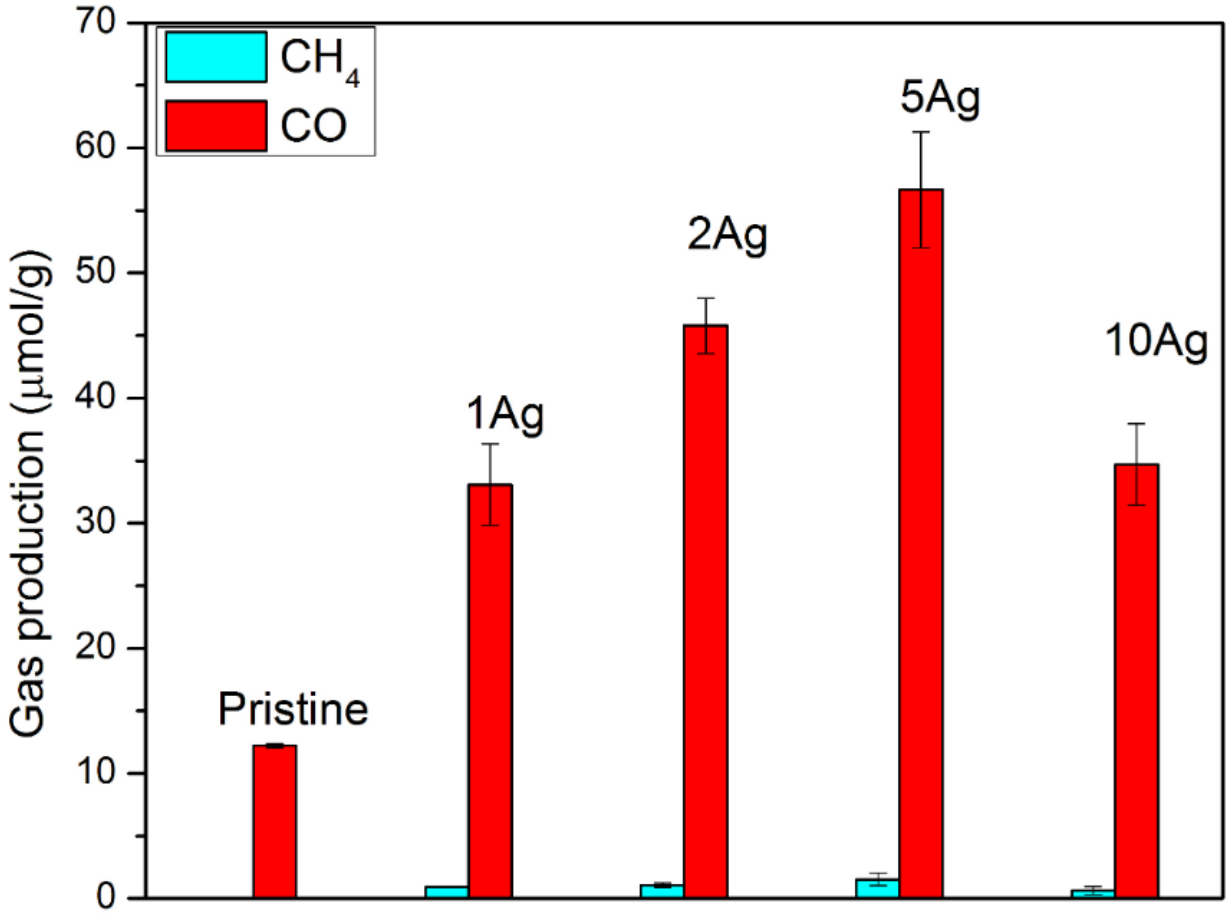

Figure 3-9 Activity of CO_2 photoreduction with water vapor by pristine TiO_2 and xAg samples under UV-vis irradiation for 4 h.

The comparison of photoactivity of *x*Ag and pristine TiO_2 is demonstrated in Figure 3-9. Under UV-vis irradiation, CO was found to be the only product of pristine TiO_2, at a production amount of 12.2 μmol/g in 4 h. For all the *x*Ag photocatalysts, the CO production was higher than pristine TiO_2 and a small amount of CH_4 was also produced. This change in photoactivity and

selectivity agreed with our previous work when precious metals such as Au or Ag were added to TiO_2 [50, 140, 141]. The CO_2 photoreduction activity increased with the Ag amount and reached the highest for the 5Ag sample, which was 4.6 times higher CO production than that of pristine TiO_2, respectively. Further increasing the Ag content to 10%, however, decreased the CO production but the activity of 10Ag was still higher than that of pristine TiO_2. It is likely that too many Ag NPs on the surface acted as recombination centers and thus lowered the photoactivity. Since 5Ag outperformed other *x*Ag samples, for the follow-up studies on Ag/MgO co-modified samples, the Ag content was fixed at 5 wt.%, while the number of MgO coating layers and the modification sequence were varied.

Figure 3-10 compares the CO_2 photoreduction performance of pristine TiO_2, single-modified TiO_2 (7Mg and 5Ag), and co-modified TiO_2 (*y*Mg5Ag and 5Ag*y*Mg) samples. Compared to pristine TiO_2, the single-modified TiO_2, i.e. either 7Mg or 5Ag samples showed much higher CO_2 conversion performance. The 7Mg sample did not produce CH_4 despite the higher production in CO than pristine TiO_2, while the 5Ag sample had a higher CO production than 7Mg and a small production of CH_4. All co-modified samples (*y*Mg5Ag and 5Ag*y*Mg, where y = 1~10) showed higher CO and CH_4 production than single-modified samples. In the range of y = 1~7, the CO and CH_4 production increased with the thickness of MgO coating, and 7 layers of ALD coating was the optimum thickness for both *y*Mg5Ag and 5Ag*y*Mg samples. When the thickness of MgO increased to 10 layers (10Mg5Ag and 5Ag10Mg), both CO and CH_4 production decreased compared to those with 7 layers. This trend agrees with our previous findings that an ultrathin layer of ALD coating increases photoactivity by passivating surface states while a “thick” layer prohibits charge transfer, and an optimum layer thickness exists determined by the trade-off between the positive and negative effects of the ALD layer [15, 34, 50].

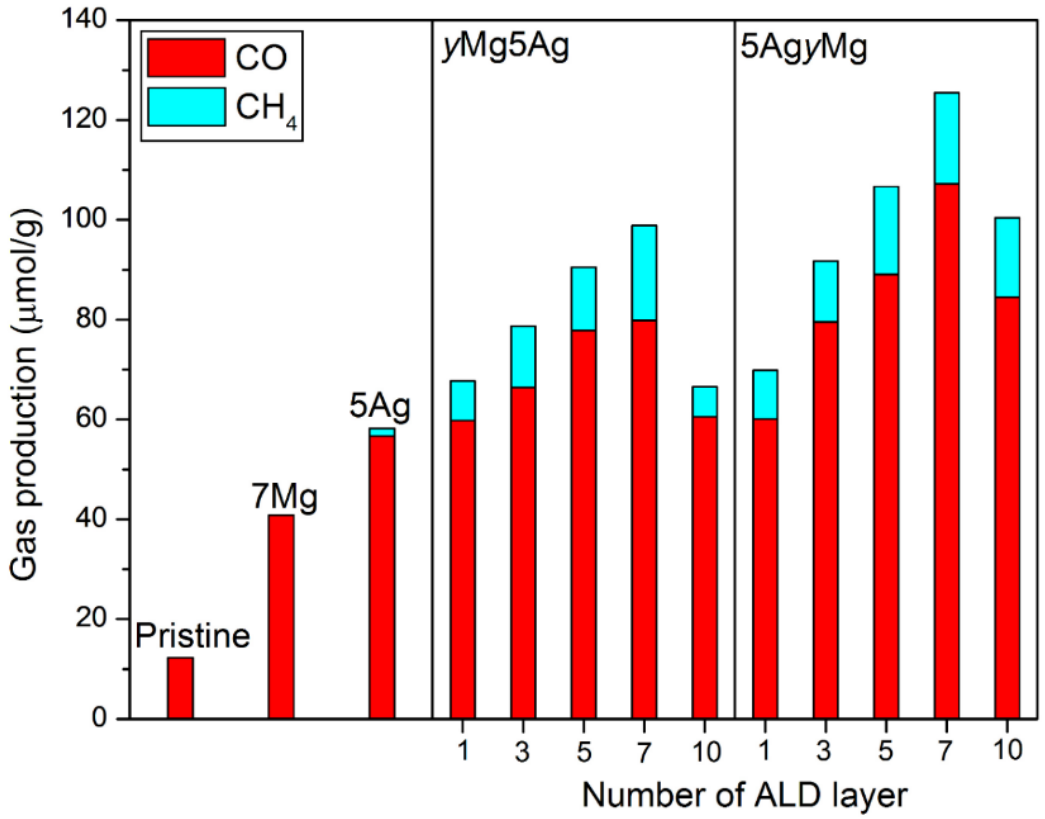

Figure 3-10 CO_2 photoreduction performance of as-prepared samples under UV-vis irradiation for 4 hours with presence of water vapor.

In order to better compare the overall photoactivity and investigate the synergy of co-modification, the total number of photoinduced electrons was calculated for each sample and listed in Table 3-2. Note that it takes 2 electrons to produce one molecule of CO and 8 electrons to produce one molecule of CH_4. Thus, the total number of electrons generated in the reaction is a better indicator of the overall activity of the sample. The promotion factor in Table 3-2 is defined as the ratio of the total number of electrons generated on a sample to that generated on the pristine TiO_2. By comparing the total number of electrons or the promotion factor, one can tell that the co-modified samples significantly outperformed the pristine TiO_2 and single-modified TiO_2. The best sample among *y*Mg5Ag is 7Mg5Ag, which has a promotion factor of 13; while the best sample among 5Ag*y*Mg is 5Ag7Mg, which has a promotion factor of 15.

Table 3-2 Summary of CO_2 photoreduction performance, including the production and ratio of CO and CH_4, number of photoinduced electrons, and promotion factor.

Sample ID	CO Production (μmol/g)	CH_4 Production (μmol/g)	CH_4/CO Molar Ratio	Photoinduced Electron (μmol/g)	Promotion Factor
Pristine TiO_2	12.2	0	0	24	1.0
7Mg	40.8	0	0	81	3.4
5Ag	56.7	1.5	0.03	126	5.3
1Mg5Ag	59.8	7.9	0.13	183	7.6
3Mg5Ag	66.4	12.3	0.19	231	9.6
5Mg5Ag	77.8	12.7	0.16	257	10.7
7Mg5Ag	79.8	19.1	0.24	312	13.0
10Mg5Ag	60.5	6.0	0.10	169	7.0
5Ag1Mg	60.1	9.8	0.16	198	8.3
5Ag3Mg	79.5	12.1	0.15	256	10.7
5Ag5Mg	89.0	17.6	0.20	319	13.3
5Ag7Mg	107.2	18.3	0.17	360	15.0
5Ag10Mg	84.5	15.9	0.19	296	12.3

It is also noticed that 5Ag*y*Mg samples always outperformed *y*Mg5Ag samples at the same *y* value, demonstrating the structural advantage of Ag NPs deposited on the outermost layer of MgO/TiO_2 over Ag NPs sandwiched between MgO and TiO_2. One possible reason is the difference of Ag concentration and distribution on the catalyst surface. According to the XPS analysis result, the Ag concentration on the surface of 5Ag7Mg was 4.92 at.%, twice as much as that on the surface of 7Mg5Ag (2.25 at.%). However, from the HRTEM analysis (Figure 3-4), there are no discernable Ag NPs on 5Ag7Mg, whereas noticeable Ag NPs are observed on 7Mg5Ag despite a lower Ag surface concentration. This suggests that Ag was more uniformly distributed on the 5Ag7Mg sample and their sizes were probably too small to be detected by TEM. Note that in the materials preparation Ag is photodeposited on the catalyst surface through photoreduction of Ag ions to elemental Ag on photoactive sites. As MgO coated TiO_2 (e.g. 7Mg) is demonstrated to be more active than pristine TiO_2 (Figure 3-10), the 7Mg sample had more active sites than pristine TiO_2

and thus a more uniform and larger number of Ag deposition on the catalyst surface (to form 5Ag7Mg) than on the less active pristine TiO_2 (to from 5Ag). For the 7Mg5Ag sample, the final ALD coating process would not change the Ag concentration. Hence, it is reasonable that 5Ag7Mg had a higher concentration but smaller size of Ag than 7Mg5Ag, contributing to its higher photocatalytic activity as observed in Figure 3-10.

The synergy effect of MgO and Ag co-modification can be demonstrated by the promotion factor and the CH_4/CO ratio, as listed in Table 3-2. The promotion factors for 7Mg and 5Ag are 3.4 and 5.3, respectively, while the promotion factors of 7Mg5Ag and 5Ag7Mg were 13.0 and 15.0, respectively. Clearly, the promotion factor of a co-modified sample (13 or 15) is larger than the sum of those of 7Mg and 5Ag (3.4 + 5.3 = 8.7), confirming the synergy of co-modification. The synergy of co-modification can also be observed from the product selectivity or the CH_4/CO molar ratio. The CH_4/CO ratio on pristine TiO_2 and 7Mg is zero as no CH_4 production was produced. With Ag modification, a small amount of CH_4 was produced on 5Ag and resulted in a CH_4/CO ratio of 0.05. With MgO and Ag co-modification, the selectivity of CH_4 was significantly increased to the range of 0.13 ~ 0.24, a few times higher than that by 5Ag.

As mentioned earlier, surface Ag concentrations on 7Mg5Ag and 5Ag7Mg determined by XPS were 2.25 at. % and 4.92 at. %, respectively. To rule out the possibility that the better catalytic performance of 5Ag7Mg than 7Mg5Ag is not merely due to the higher Ag concentration, we have tried to synthesize a 7MgyAg sample that would have a similar Ag content as that in 5Ag7Mg. To achieve that, we have increased the amount of Ag in the precursor solution and synthesized 7Mg7Ag and 7Mg10Ag samples. The 7Mg10Ag is anticipated to have twice as much silver as on 7Mg5Ag, but the XPS analysis reveals 3.60 at. % Ag, just 50% more than that on 7Mg5Ag. Nevertheless, their CO_2 photoreduction performances were tested and compared with 7Mg5Ag,

and the result is shown in Figure 3-11. There is a clear trend that the CO_2 photoreduction performance deteriorated with increased surface silver concentration. This result agrees with the literature that too much silver modification may act as the recombination center that hinders the performance of photocatalysts [141]. It is expected that with an even higher surface silver concentration, the photocatalytic reduction performant might be even worse; thus no attempt was made to synthesize a 7MgyAg sample that has close to 4.92 at.% silver to match that of 5Ag7Mg. It can be concluded that the higher CO_2 photoreduction performance of 5Ag7Mg than 7Mg5Ag and was not directly related to the surface silver concentration, but rather, to the finer and better distributed silver nanoparticles and more concentrated surface hydroxyls on the surface.

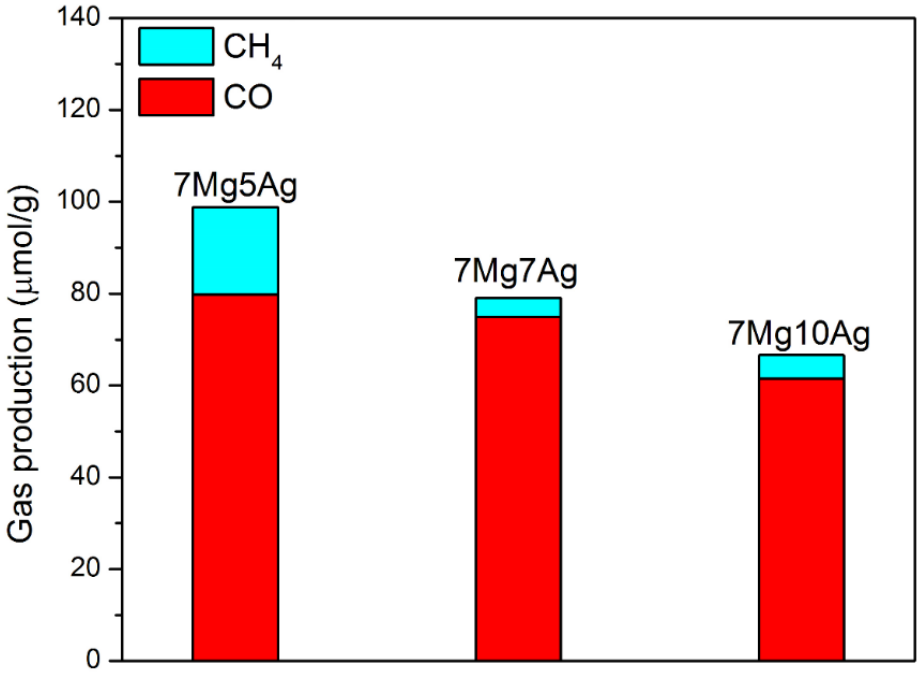

Figure 3-11 CO_2 photoreduction performance on 7MgyAg with varied y value.

3.3.6. Photocurrent density and electrochemical impedance spectroscopy measurement

To further understand the charge transfer characteristic of the photocatalysts, transient photocurrent tests were conducted on pristine TiO_2, 7Mg5Ag, and 5Ag7Mg samples and the results

are presented in Figure 3-12. The measurement was taken with the same Xe-lamp used in the CO_2 photoreduction experiments. The average photocurrent density (ΔJ as illustrated in Figure 3-12) was calculated based on five measurements of ΔJ as shown in Figure 3-12. Under Xe-lamp irradiation, the average photocurrent density of pristine TiO_2 was 2.0 $\mu A/cm^2$. The photocurrent densities of 7Mg5Ag and 5Ag7Mg were 9.8 $\mu A/cm^2$ and 12.4 $\mu A/cm^2$, respectively, which are 4.9 times and 6.2 times as much as that of pristine TiO_2. The promotion by Ag and MgO co-modification on boosting TiO_2 photocurrent density is very clear. The photocurrent density of 5Ag7Mg was 27% higher than that of 7Mg5Ag, matching the results from CO_2 photoreduction experiments. The higher charge transfer capability of 5Ag7Mg may be attributed to a higher Ag content and smaller Ag NP size on the catalyst surface that leads to the increased contact area and shorter travel path for electron transfer to initialize the CO_2 photoreduction process [50, 149].

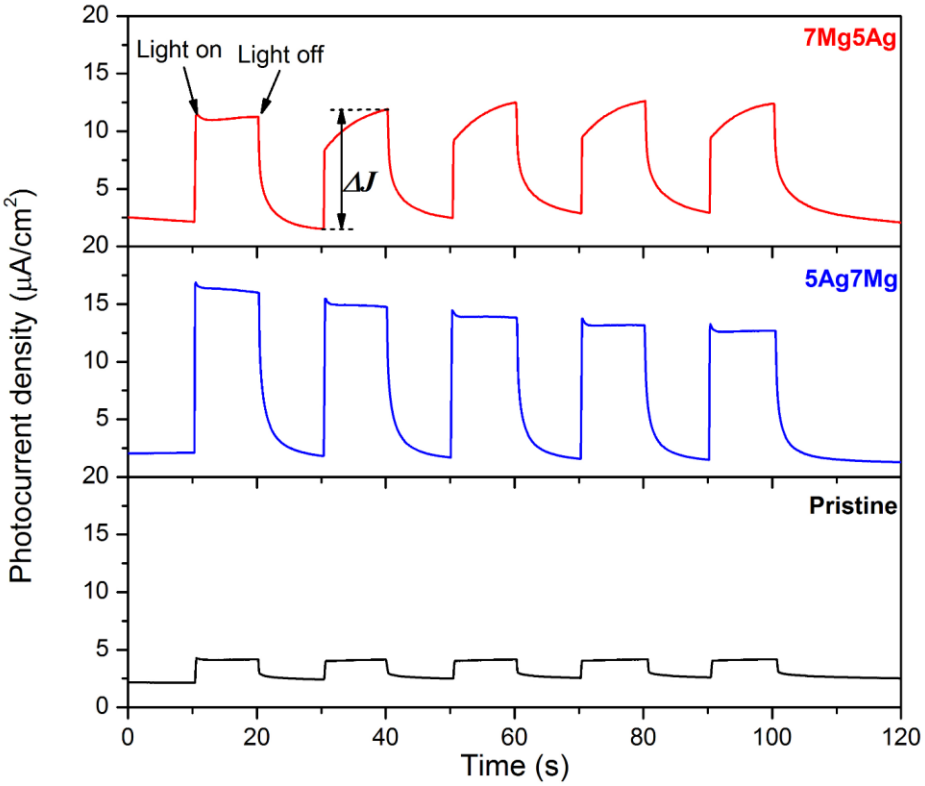

Figure 3-12 Transient photocurrent curves for pristine TiO_2, 7Mg5Ag, and 5Ag7Mg.

To understand the charge transfer properties of the prepared samples, electrochemical impedance spectroscopy tests were conducted. The EIS Nyquist plots of pristine TiO_2, 7Mg5Ag, and 5Ag7Mg under UV-vis irradiation are shown in Figure 3-13. The radius of the arc of EIS reflects the charge transfer resistance [12, 150-152]. Generally, a greater diameter indicates a larger charge transfer resistance and thus a lower reaction rate. The charge transfer resistance is in the order of 5Ag7Mg (43 Ω) < 7Mg5Ag (58 Ω) < pristine porous TiO_2 (92 Ω). This result correlates well with the catalytic activity and the photocurrent data of the three samples, further validating the benefit of co-modification of Ag and MgO and the importance of Ag content and distribution on the surface.

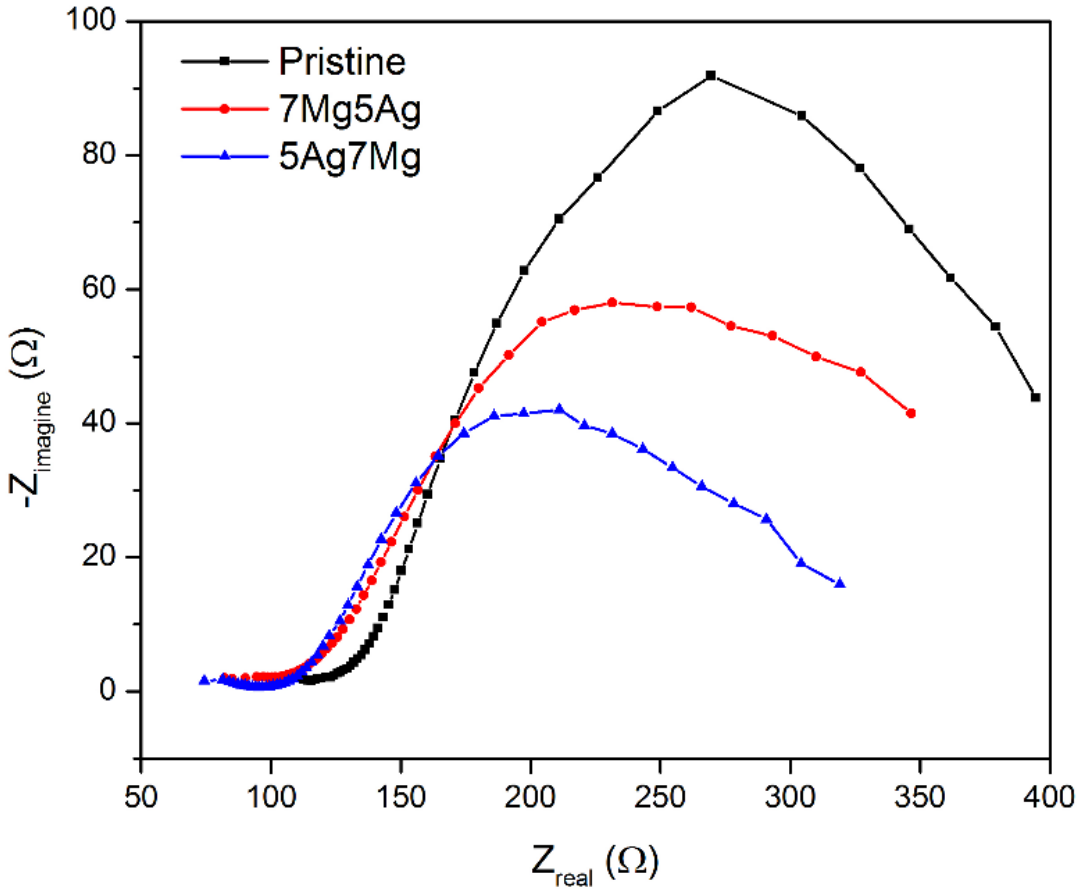

Figure 3-13 EIS Nyquist plot of pristine TiO_2, 7Mg5Ag and 5Ag7Mg.

3.4. Conclusions

Novel structured nanocomposite photocatalysts were prepared by modifying porous TiO_2 with ALD overcoating of MgO and surface deposition of Ag NPs to promote CO_2 photoreduction activity. The MgO and Ag co-modified TiO_2 showed significantly higher photocatalytic activity than pristine TiO_2 and single-modified TiO_2. With 7 ALD layers of MgO coating and 5 wt.% Ag loading on TiO_2, the overall activity of CO_2 reduction to CO and CH_4 was enhanced by 14 times compared with pristine TiO_2. The synergy of co-modification was also manifested by the higher CH_4 selectivity in the products. The optimum number of overcoating, i.e., 7 ALD layers, was determined by the trade-off between the positive surface passivation effect to mitigate charge recombination and the negative insulation effect to hinder charge transfer to the surface. The sequence of MgO/Ag modification and thus the different surface materials structures were found to have a clear impact on the materials property and photocatalytic performance. Catalysts with Ag NPs being at the outermost layer of MgO coated TiO_2 were always more active than those with Ag NPs sandwiched between MgO and TiO_2 at the same thickness of MgO coating. The higher activity may result from a more uniform distribution of Ag and a larger number of Ag NPs or clusters on the surface. Findings from this work have provided insights on advancing materials design to achieve efficient photocatalysis.

4. METAL-ORGANIC FRAMEWORK MIL-125 DERIVED MAGNESIUM DOPED MESOPOROUS TITANIUS DIOXIDE FOR PHOTOCATALYTIC CARBON DIOXIDE REDUCTION[‡]

4.1. Introduction

Besides the surface decoration modifications described in Chapters 2 and 3, metal ion doping modifications in TiO_2 is also an interesting research topic in the photocatalysis research field [153, 154]. Unlike surface decorations on TiO_2 substrates, which only alters the chemistry on the TiO_2 surface, TiO_2 heteroatom doping functions in the bulk of the crystal and creates more defects in the lattice and thus considerably enhances the photoactivity [55, 155]. Although metal ion doping in TiO_2 for photocatalysis application has been studied extensively [55, 155]. there are only very few works in the photocatalytic applications of Mg-doped TiO_2 [156-158]. Among the few studies, Pozan *et al*. applied the co-precipitation method to prepare Mg^{2+} doped TiO_2 for 4-chlorophenol degradation in wastewater [158]. It was found that the Mg-doped TiO_2 exhibited a degradation efficiency that is more than 14 times higher compared with commercially available P25. Apparently, Mg^{2+} doping is favorable for the enhancement of TiO_2 photoactivity, but due to the limited amount of research work in this area, the mechanisms behind the enhancement are not fully understood [156-158]. Therefore, different from previous works from our group [15, 24, 47], which investigated the effects of surface engineered MgO on TiO_2 for photocatalytic CO_2 reduction, this work investigates the role of Mg^{2+} doping in TiO_2 in photocatalytic CO_2 reduction

[‡] Part of this chapter is reprinted with permission from "Metal-organic framework MIL-125 derived Mg^{2+}-doped mesoporous TiO_2 for photocatalytic CO_2 reduction" by Xuhui Feng, Fuping Pan, Peng Zhang, Xiao Wang, Hong-Cai Zhou, Yongheng Huang, and Ying Li, *ChemPhotoChem*, 2021, 5, 79-89. Copyright [2021] by John Wiley & Sons, Inc.

and fills this knowledge gap.

Another objective of this study is to promote an easy and facile method to prepare Mg-doped mesoporous TiO_2 materials, allowing favorable intra- and inter-particle gas diffusion, which are especially beneficial to solid/gas phase reaction processes [159, 160]. In our literature search, we noticed the possibility to achieve Mg^{2+} doping modification on TiO_2 with mesoporous structure through Mg^{2+} adsorption process on MIL-125 materials, thanks to the high surface area of metal-organic framework materials. In the cation adsorption process on MOF materials, the free cations in the solution are adsorbed onto the frameworks of MOF nanoparticles, resulting in well-dispersed hetero-cation distribution while maintaining the 3-D crystal structure of the MOF materials [161]. This cation adsorption process produces additional favorable properties and broadens the functionalities and applications of MOF-derived metal oxide materials. For example, Valero-Romero *et al.* [162] reported Fe-doped porous TiO_2 photocatalysts prepared by applying Fe^{3+} adsorption process on MIL-125 followed by thermal treatments. The Fe-doped porous TiO_2 significantly enhanced photocatalytic water splitting performance and lowered the electron-hole recombination rate compared with pristine TiO_2.

In this chapter, we present an easy and facile method to prepare Mg^{2+} doped mesoporous TiO_2 derived from thermal treatments on Mg^{2+} treated metal-organic framework material MIL-125 and investigate the effect of Mg^{2+} doping in TiO_2 on CO_2 photoreduction. To the best of our knowledge, no works have reported applications of Mg-doping on TiO_2 for the CO_2 photoreduction process. Based on the aforementioned literature review, it was hypothesized that the Mg^{2+} adsorption process on MIL-125 and followed by thermal treatments can lead to Mg^{2+} doped TiO_2 materials with mesoporous structures. The doped Mg^{2+} into TiO_2 lattice does not merely function as doped Fe^{3+} [162], which mainly facilitates charge separations; more

importantly, the Mg^{2+} doping on TiO_2 is further beneficial for enhancing CO_2 affinity due to the alkaline nature of Mg. The merits of Mg^{2+} doping should considerably enhance photocatalytic performance for the CO_2 reduction process.

4.2. Experimental section

The preparation procedure of MIL-125 and pristine mesoporous TiO_2 was the same as that described in Chapter 2. To prepare Mg^{2+} doped mesoporous TiO_2, 200 mg MIL-125 was dispersed into 60 ml $Mg(NO_3)_2 \cdot 6H_2O$ (Sigma-Aldrich, 99%) methanol solution. The final weight composition in the suspension was adjusted as MgO : TiO_2 = *x* : 100, where *x* = 0.1, 0.2, 0.5, 1.0, 2.0, 5.0 and 10.0. The suspension was stirred for 24 h. The mixture was then centrifuged to obtain Mg^{2+} treated MIL-125. Methanol rinsing was applied once on the collected solid. The collected powder was then placed in a vacuum oven and maintained at 80 ℃ overnight. The obtained powder was pyrolyzed under Ar atmosphere at 500 °C for 2 h and then calcined for 2 h at 450 °C in air. The obtained powder was denoted as "*x*MA" (Mg^{2+} adsorption), where *x* indicates that in the Mg^{2+} adsorption gel, the weight composition of MgO : TiO_2 = *x* : 100.

Material characterization procedure applied in this chapter is similar to what was described in Section 2.2.5. The experimental setup for CO_2 photoreduction was similar to that in Section 2.2.6.

4.3. Results and discussion

4.3.1. Crystal structure

Figure 4-1 shows the XRD patterns of the prepared photocatalysts and standard XRD patterns of rutile and anatase. Both anatase and rutile are presented in all samples. MgO was not

detected by the XRD analyses in any photocatalysts, likely because the amount of doped Mg^{2+} was very low or MgO was in the amorphous form. Despite this, the existence of Mg^{2+} in 0.1MA, 1MA, and 10MA was confirmed and measured by inductively coupled plasma mass spectrometry (ICP-MS). The results are listed in Table 4-1. The Mg^{2+} weight concentration in photocatalyst samples measured by ICP-MS shows a positive correlation with the Mg^{2+} concentration applied in the Mg^{2+} adsorption process. The fact that no MgO peak was found in any XRD pattern is consistent with the low concentration of Mg^{2+} measured by ICP. The Rietveld refinement method [121] was used to calculate the weight percentage of both anatase and rutile. The anatase crystallite size in the as-prepared photocatalysts was also calculated. Both of the results are listed in Table 4-2. The pristine mesoporous TiO_2 shows a slightly higher concentration of rutile. The existence of rutile in the samples is reasonable as extended thermal treatments were involved in the sample preparation procedures. However, it can be seen that with Mg^{2+} doping, there is a trend where the rutile ratio decreased with increased Mg^{2+} doping concentration. The pristine TiO_2 showed a rutile weight percentage of 52.2%, while 0.1MA shows a rutile weight percentage of 49.6%, this trend continues to a rutile weight percentage of 23.4% on 10MA. Anatase crystallite size also showed a similar trend as the Mg^{2+} concentration increased, which suggested successful Mg^{2+} doping, as heteroatom doping can penetrate into crystallite lattice and causes disorder/discontinuity within crystallites and subsequently decreases the crystallite size [163, 164]. The increase in anatase crystalline size observed on 5MA and 10MA is likely related to the increased weight ratio of anatase in the two samples. It seems that the Mg^{2+} dopant hindered the transformation of anatase to rutile at elevated temperatures. As previously demonstrated by Li *et al.* [165], anatase to rutile transformation starts from small domains of rutile clusters. Similarly, Zhang *et al.* [166], indicated that the small domains of rutile are firstly formed at anatase crystalline interfaces, and suggested that the

presence of dopants hinder direct contact between anatase crystallines, leading to retarded TiO_2 phase transformation despite the high-temperature calcination [166]. Similar effects of doped species in TiO_2 that elevate the anatase to rutile transformation temperature were also observed on N-doped [167], SiO_2-doped [168], S-doped [169], and Ru-doped [170] TiO_2 materials.

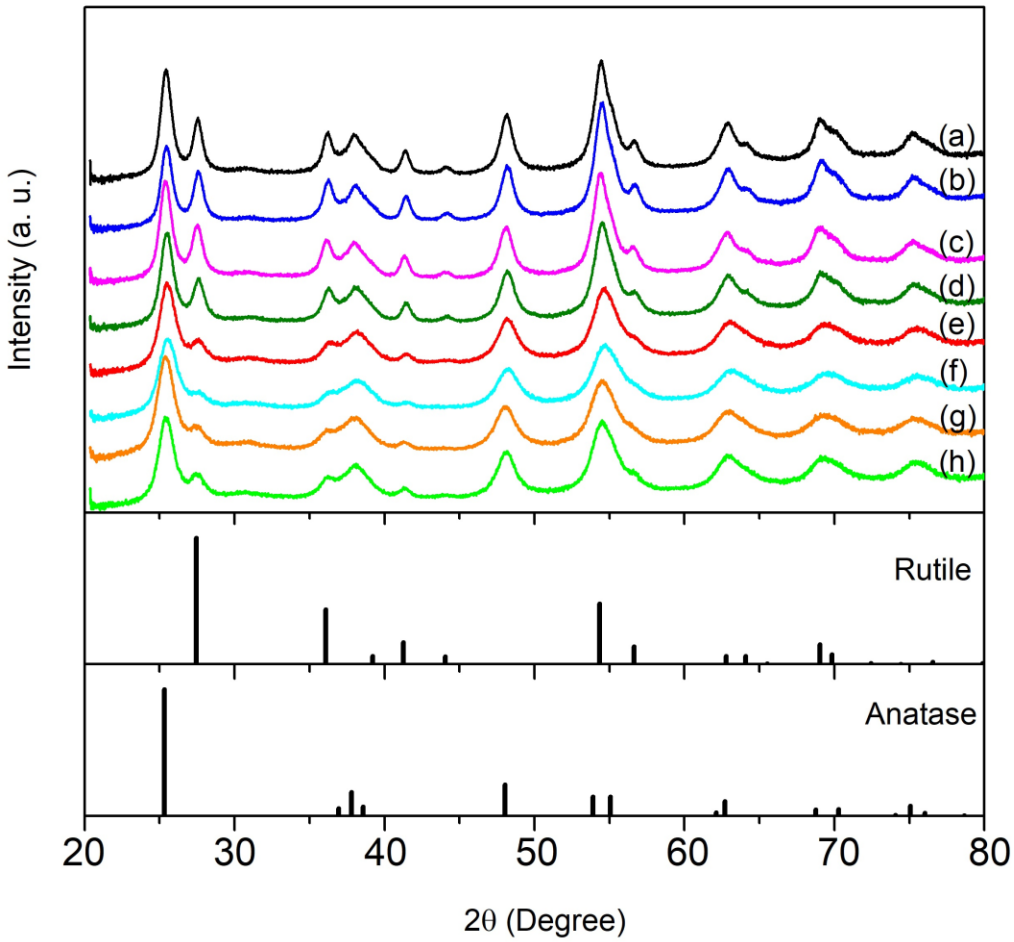

Figure 4-1 XRD patterns of (a) pristine mesoporous TiO_2, (b) 0.1MA, (c) 0.2MA, (d) 0.5MA, (e) 1MA, (f) 2MA, (g) 5MA, (h) 10MA, compared with standard rutile and anatase patterns.

Table 4-1 Photocatalyst Mg^{2+} weight concentration determined by ICP-MS method.

Sample ID	Mg^{2+} weight concentration (mg/g)
0.1MA	0.35
1MA	2.20
10MA	4.42

Table 4-2 Anatase/rutile weight percentage and anatase crystalline size of as-prepared photocatalysts.

Sample ID	Anatase %	Rutile %	Anatase crystallite size (nm)
Pristine	47.8	52.2	10.98
0.1MA	50.4	49.6	10.99
0.2MA	57.6	42.4	10.18
0.5MA	55.9	44.1	9.99
1MA	62.1	37.9	8.47
2MA	64.9	35.1	7.38
5MA	72.5	27.5	7.87
10MA	76.6	23.4	8.44

4.3.2. Morphological analyses

Figure 4-2 shows the SEM and TEM images of pristine mesoporous TiO_2 and 1MA. Both pristine mesoporous TiO_2 and 1MA exhibit similar cubic shape (Figure 4-2a and d). The low magnitude TEM images of pristine mesoporous TiO_2 (Figure 4-2b) 1MA (Figure 4-2e) shows that both of the samples are structured by firmly interconnected ultrafine nanoparticles. 1MA exhibits a slightly smaller particle size than pristine mesoporous TiO_2 (pristine mesoporous TiO_2 : ~270 nm, 1MA: ~220 nm). It is likely that the cation adsorption process damaged the framework of the MOF material to some extent [171], which caused shrinking in the size of the Mg^{2+} doped mesoporous TiO_2. Anatase [101] (d = 0.352 nm), anatase [103] (d = 0.243 nm) and rutile [110] (d = 0.323 nm) were found in high resolution TEM images of pristine mesoporous TiO_2 (Figure 4-2c) and 1MA (Figure 4-2f), which verifies the existence of anatase and rutile phases indicated by the XRD analyses. However, MgO was not detected in high-resolution TEM images, which can possibly be attributed to the low concentration of Mg^{2+} doping.

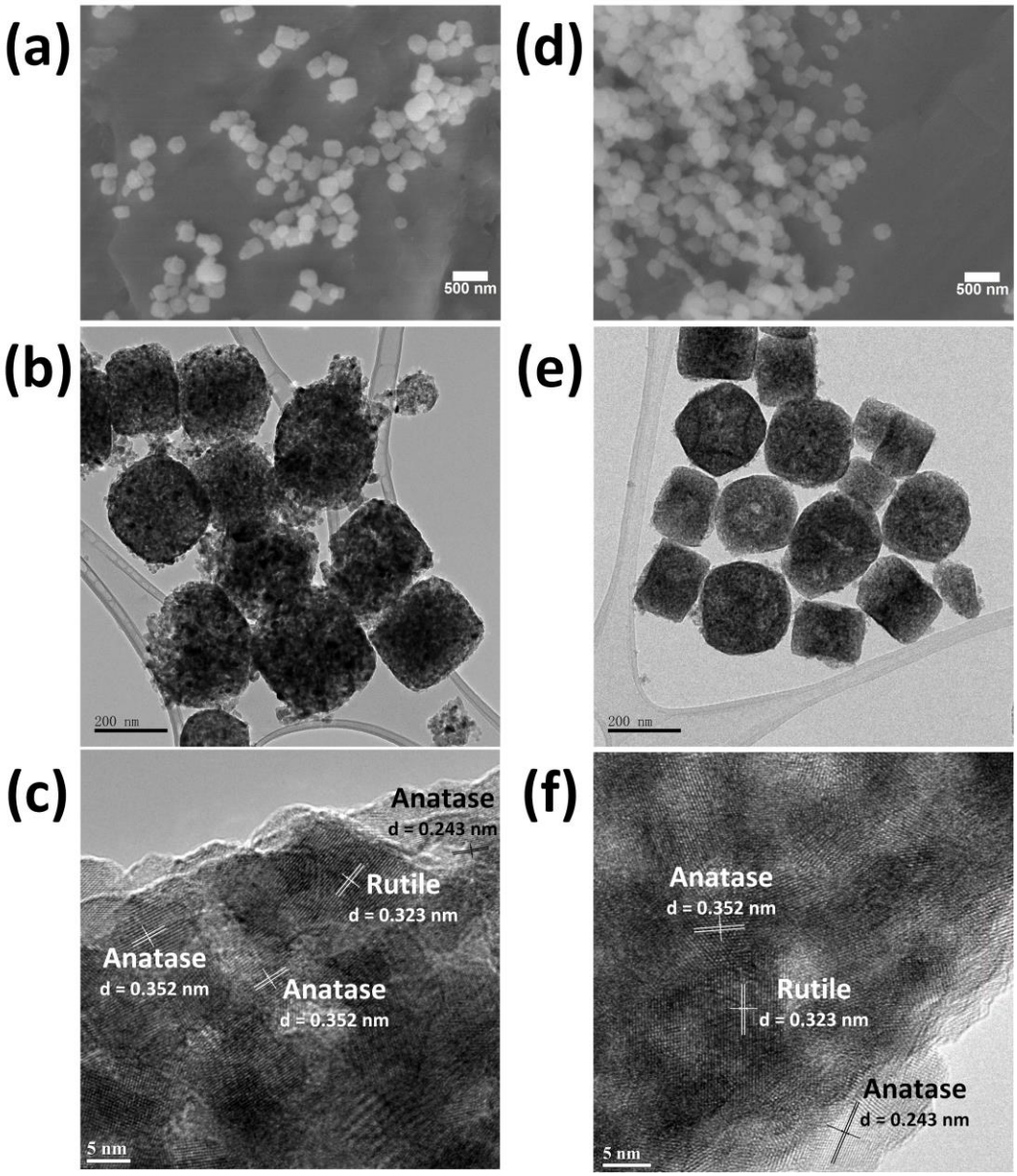

Figure 4-2 SEM images of (a) pristine mesoporous TiO_2, (d) 1MA; TEM images of (b), (c) pristine mesoporous TiO_2 and (e), (f) 1MA.

4.3.3. Pore structure

Brunauer-Emmett-Teller (BET) analyses were performed to evaluate the pore structure of pristine mesoporous TiO_2, 0.1MA, 1MA, and 10MA. Figure 4-3 shows the N_2 adsorption-desorption isotherms and pore size distribution of the four photocatalysts. All of the photocatalysts show type IV isotherms and type H2 hysteresis loops, which indicates mesoporous structures and

narrow-mouth shaped pores, respectively [123]. The results are consistent with the sample structure consisting of interconnected ultrafine nanoparticles observed in SEM/TEM images.

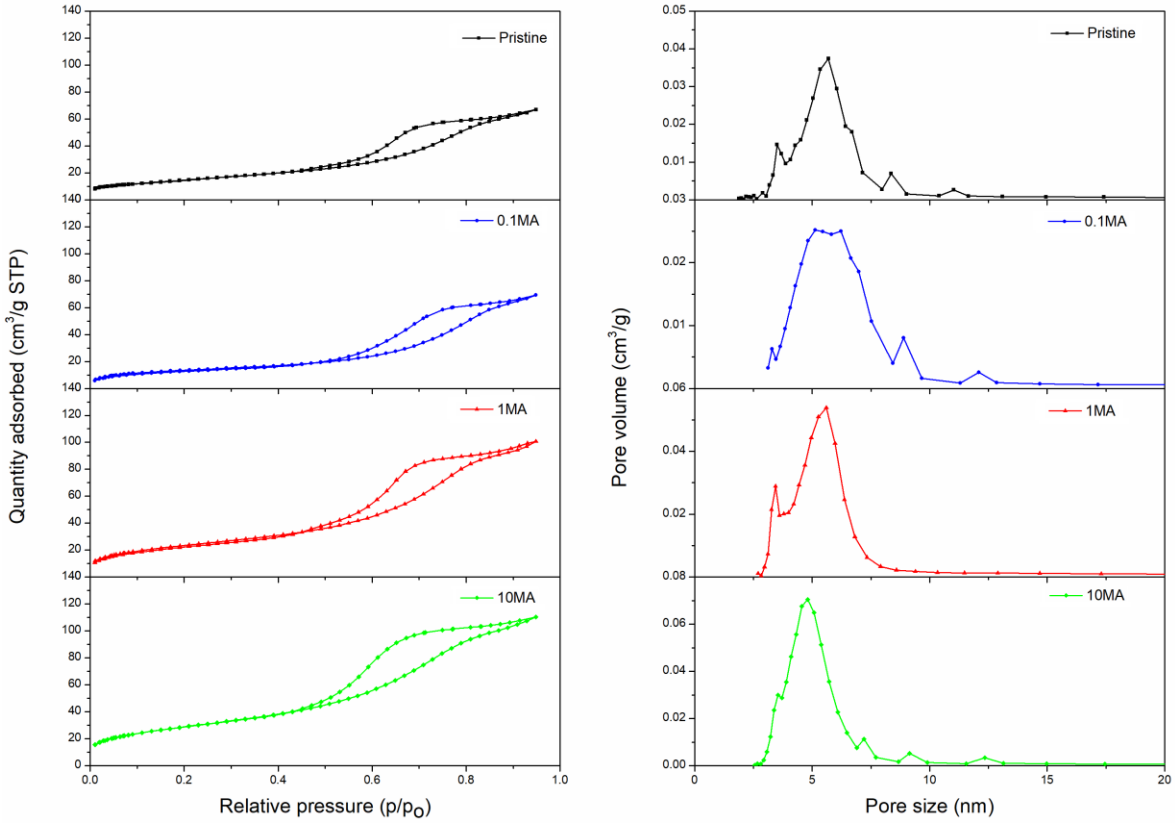

Figure 4-3 N_2 adsorption-desorption isotherm (left) and pore size distribution (right) of pristine mesoporous TiO_2, 0.1MA, 1MA and 10MA.

Table 4-3 lists pore structures of pristine mesoporous TiO_2, 0.1MA, 1MA, and 10MA. The four samples exhibit relatively low surface areas compared with those reported previously [109, 113]. In this work, the relatively high temperature was applied for MIL-125 to mesoporous TiO_2 conversion (500 and 450 ℃ in this work vs. 350-380 ℃ in previous reports [109, 113]). This is to eliminate any carbon residues on the photocatalysts. However, the high temperature for calcination sintered the mesoporous TiO_2 structure and decreased the surface area. The average pore size of the samples falls in the mesoporous range, which is consistent with the H2 hysteresis loops

observed in N_2 adsorption-desorption isotherm. There seems to be a trend where the photocatalysts surface area increases with the concentration of Mg^{2+}, a similar trend was also found on Fe^{3+} treated MIL-125 derived TiO_2 materials [162], which suggests successful doping of Mg^{2+} into the mesoporous TiO_2 lattice. This trend is also found in pore volume and pore size distribution. The porous properties of 0.1MA are close to those of pristine mesoporous TiO_2, which is likely caused by very low Mg^{2+} concentration applied in the adsorption process. By further comparing the pore structure of 1MA and 10MA with pristine mesoporous TiO_2, it was noticed that two of the MA photocatalysts exhibit greater surface area and pore volume but narrower average pore size compared with pristine mesoporous TiO_2. The pore size distribution results show that the pore volume of specific pore size on 1MA and 10 MA also increased (magnitude of pore size distribution data), compared with pristine mesoporous TiO_2. Although the SEM and TEM analyses did not show significant differences in macrostructures between pristine mesoporous TiO_2 and 1MA, it seems that more porous channels were created due to the cation adsorption process.

Table 4-3 Surface area, average pore size and pore volume data of pristine mesoporous TiO_2, 0.1MA, 1MA and 10MA.

Sample ID	Surface area (m^2/g)	Average pore size (nm)	Pore volume (cm^3/g)
Pristine	46	5.9	0.1
0.1MA	45	6.2	0.11
1MA	74	5.6	0.15
10MA	92	5.2	0.17

4.3.4. Surface chemistry analyses

X-ray photoelectron spectroscopy (XPS) analyses were performed on pristine mesoporous TiO_2, 0.1MA, 1MA, and 10MA to understand the surface chemical states. XPS survey curves of those photocatalysts can be found in Figure C-1. Analyses of Mg *2p* were also performed.

However, the Mg *2p* peaks of 0.1MA, 1MA, and 10MA were not discernable, and a similar result was observed with EDS mapping, where Mg^{2+} is not detected on 10MA (Figure 4-4). This is likely due to the XPS low response at low binding energy and the Mg^{2+} concentration in the samples is quite little, which makes it difficult for the detection (Figure C-2).

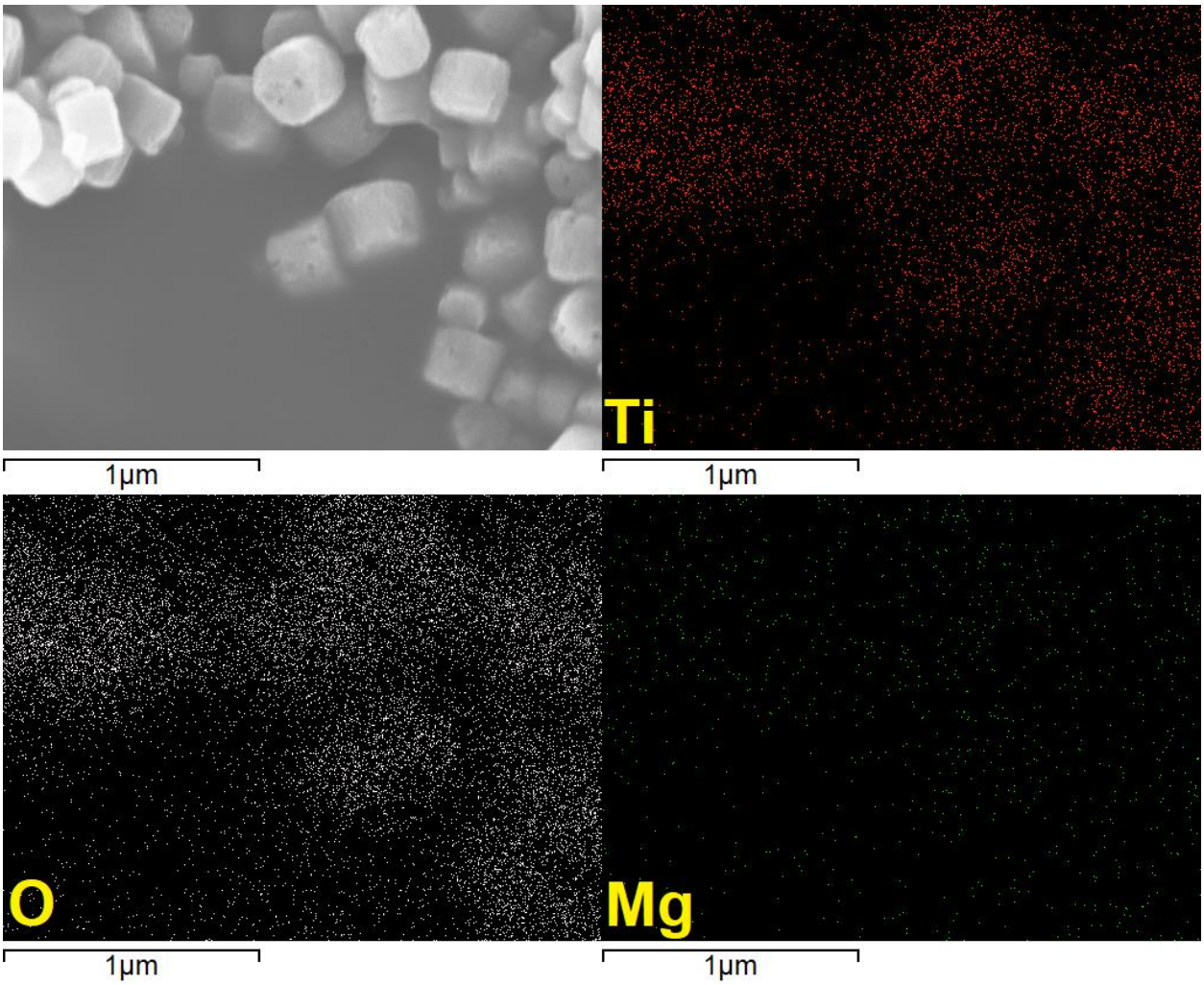

Figure 4-4 EDS mapping of Ti, O and Mg on 10MA.

As previously reported, MgO modification on TiO_2 photocatalysts induced the generation of surface Ti^{3+} [38], which is the result of the Mg^{2+} substitution of Ti^{4+} in TiO_2 lattice, as formulated,

$$MgO \xrightarrow{TiO_2} Mg_{Ti} + O_V + O_L \quad (1)$$

Mg_{Ti} represents a Mg^{2+} in TiO_2 lattice, O_V and O_L represent the oxygen vacancies and lattice oxygen of TiO_2, respectively. The oxygen vacancies are not stable under the ambient condition where water vapor is present, the oxygen vacancy may lead to TiO_2 crystalline structure reorganization to generate Ti^{3+} [145] or can be neutralized by water vapor to generate surface hydroxyls [144]. The Ti^{3+} promotes photoexcited electron/hole separation and thus improves photoactivity, and the surface hydroxyls enhance the interactivity between photocatalyst surface and CO_2 molecules [38, 124]. XPS analyses were therefore conducted on Ti *2p* and O *1s* to confirm the existence of surface Ti^{3+} and surface hydroxyl moieties. Ti^{3+} and Ti^{4+} are located at 458.7 eV (Ti^{4+} $2p_{3/2}$), 464.6 eV (Ti^{4+} $2p_{1/2}$), 457.7 eV (Ti^{3+} $2p_{3/2}$), and 463.4 eV (Ti^{3+} $2p_{1/2}$) in the XPS spectra, while hydroxyl moieties and lattice oxygen are located at 531.9 eV (Ti-OH) and 529.9 eV (Ti-O) [38, 125, 126]. Mg-OH and Mg-O were not included in the deconvolution due to the very low concentration of Mg doping concentration that it was not even detected by XPS (Figure C-2).

Figure 4-5 shows the Ti *2p* peak deconvolution analysis for pristine mesoporous TiO_2, 0.1MA, 1MA, and 10MA. The percentages of surface Ti^{3+} and Ti^{4+} on each photocatalyst are listed in Table 4-4. The XPS analysis determined that 100% of Ti on pristine mesoporous TiO_2 are Ti^{4+}, which is reasonable since pristine mesoporous TiO_2 was treated with a high temperature in air. For 0.1MA, although the Mg^{2+} doping concentration was low, 10.0% of the surface titanium species are in the form of Ti^{3+}. It has been reported by Manzanares *et al.* [38] that the formation of Ti^{3+} on MgO modified TiO_2 is a result of the substitution of magnesium ions into TiO_2 lattice. At a higher concentration of Mg^{2+} doping, on the surface of 1MA, the surface Ti^{3+} content

increased to 34.8%. Interestingly, the surface Ti^{3+} content decreased to 25.4% on 10MA, which had the highest Mg^{2+} doping level. A possible explanation for this observation is that, with a higher concentration of Mg^{2+} doping, MgO clusters started to form, which reduced the amount of Mg^{2+} substituted into the TiO_2 lattice and thus lowered the surface Ti^{3+} content.

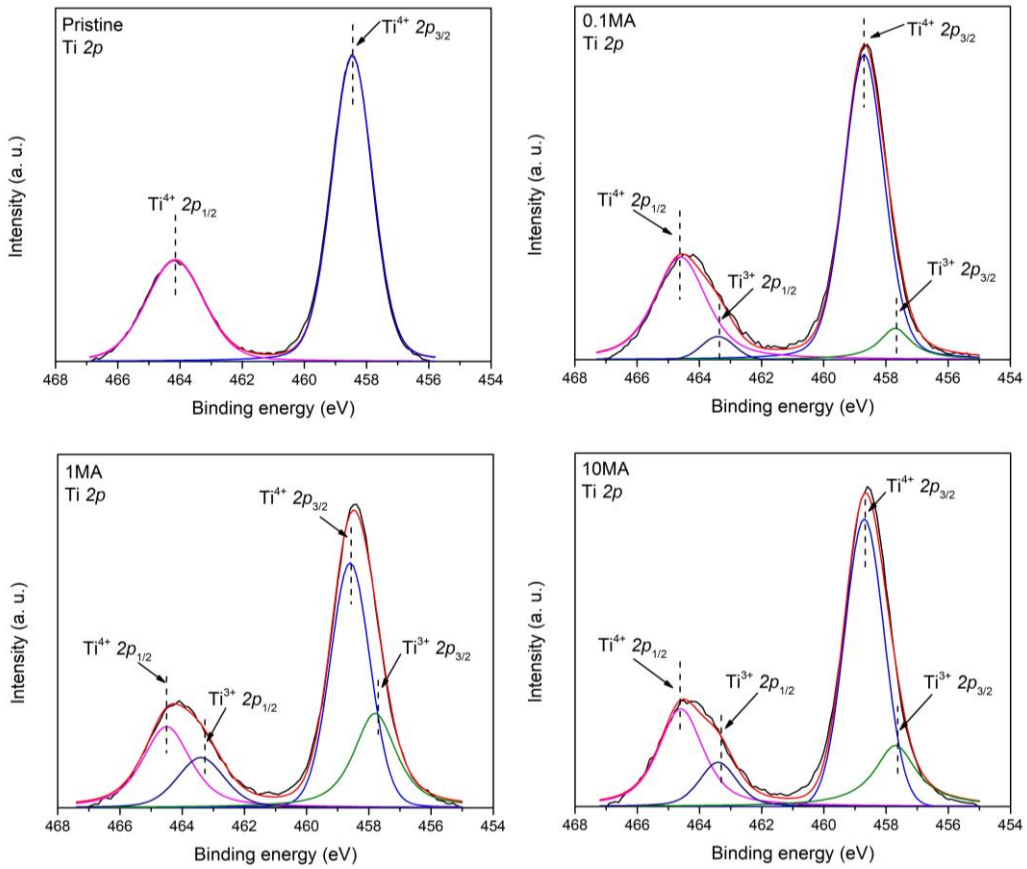

Figure 4-5 Ti *2p* peak deconvolution of pristine mesoporous TiO_2, 0.1MA, 1MA, and 10MA.

Table 4-4 XPS deconvolution results of surface Ti and O species on selected photocatalysts.

Sample ID	Ti *2p* (%)		O *1s* (%)	
	Ti^{3+}	Ti^{4+}	Ti-OH	Ti-O
Pristine	0.0	100.0	5.9	94.1
0.1MA	10.0	900.	10.1	89.9
1MA	34.8	65.2	11.7	88.3
10MA	25.4	74.6	15.3	84.7

Figure 4-6 shows the O *1s* peak deconvolution analysis for pristine mesoporous TiO_2, 0.1MA, 1MA, and 10MA. The percentages of Ti-OH and Ti-O are listed in Table 4-4. On pristine mesoporous TiO_2, 5.9% surface oxygen species were confirmed as hydroxyl moieties, despite high temperature calcination in air. The hydroxyl groups are likely regenerated while the pristine TiO_2 interacts with moisture in air. For 0.1MA, 1MA, and 10MA, a positive correlation on Mg^{2+} doping concentration and surface hydroxyl content was observed. From 0.1MA to 10MA, the surface hydroxyl content ranged from 10.1% to 15.3%. This is likely due to the existence of MgO that enhances the photocatalyst surface affinity to moisture, leading to higher concentration of surface hydroxyl moieties generation.

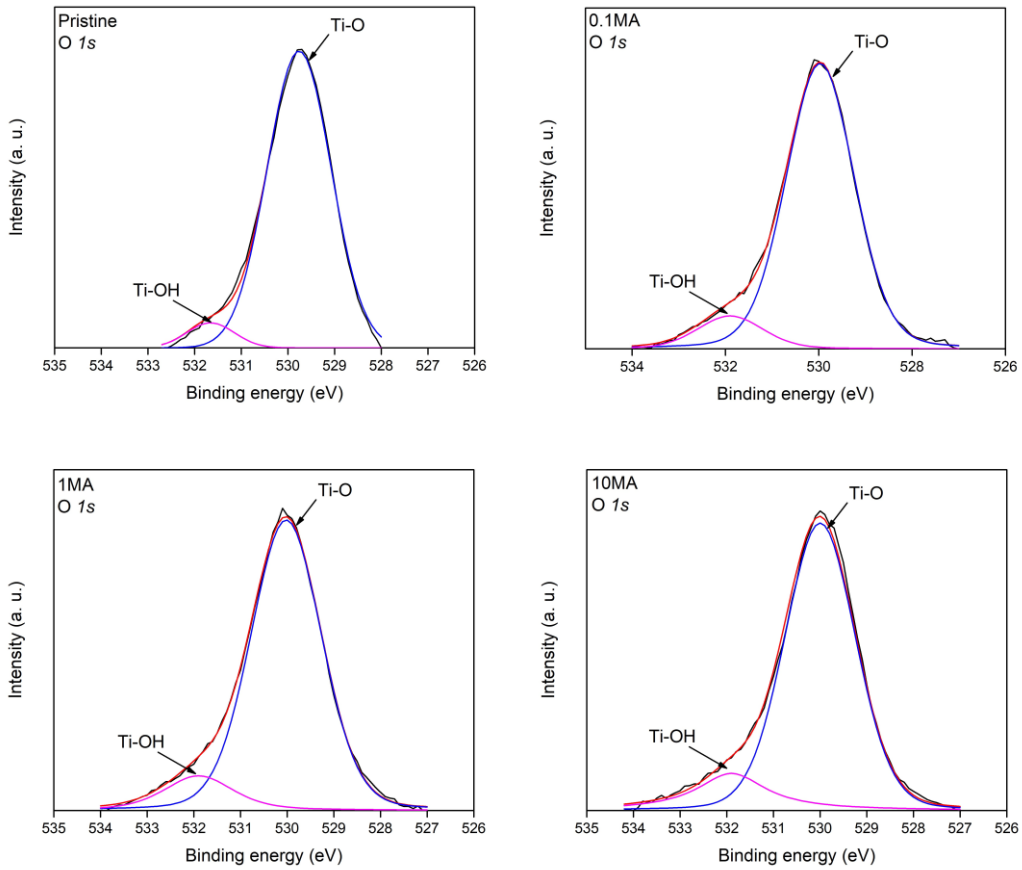

Figure 4-6 O 1s peak deconvolution of pristine mesoporous TiO_2, 0.1MA, 1MA, and 10MA.

4.3.5. Activity of CO_2 photoreduction

Before testing the CO_2 photoreduction activity of the photocatalysts using CO_2 and water vapor as the feedstock, the following control experiments were conducted: (a) humidified CO_2 + light irradiation + no photocatalyst; (b) humidified CO_2 + no light irradiation + photocatalysts; and (c) humidified Ar + light irradiation + photocatalysts. None of the control experiments suggested the production of any carbon-containing products, indicating that products later on produced from the CO_2 photoreduction in the presence of H_2O vapor under light were indeed originated from the feed gas of CO_2. In this study, only CO was detected as a photocatalytic CO_2 reduction product. H_2 was not detected, which is consistent with our previous studies [24, 34, 47]. Therefore, the production amounts of CO were used to determine the photocatalytic CO production performance of as-prepared photocatalysts.

Figure 4-7 shows the comparison of CO_2 photoreduction performance of as-prepared photocatalysts. As a reference material, P25 TiO_2 photocatalyst was used to determine the CO_2 photoreduction activity of as-prepared samples in this study. As shown in Figure 4-7, P25 delivered a CO production of 2.5 μmol/g. Pristine mesoporous TiO_2 delivered a CO production of 12.7 μmol/g, which is 5.1 times that of P25. 0.1MA and 0.2MA only showed a slight enhancement in CO_2 photoreduction compared with pristine mesoporous TiO_2 at 18.3 μmol/g and 24.1 μmol/g, respectively. The CO_2 photoreduction rate continued to increase with Mg^{2+} doping concentration on 0.5MA and 1MA, resulting in 36.5 μmol/g and 50.6 μmol/g, respectively. The increase in CO production can be attributed to (1) surface Ti^{3+} and surface defects induced by Mg^{2+} doping that hinders charge recombination, and (2) favorable surface CO_2 interaction on photocatalysts surface resulting from the alkaline nature of Mg^{2+}. By further increasing the Mg^{2+} doping concentration, however, deterioration in CO production was observed. The CO production on 2MA dropped to

41.0 μmol/g and further diminished to 30.3 μmol/g on 5MA and 26.2 μmol/g on 10MA. The trend of decrease in CO_2 photoreduction performance is likely related to over-concentrated surface defects and Ti^{3+} that act as recombination centers, lowering the photoactivity of photocatalysts, despite the enhanced CO_2 adsorption capacity related to higher Mg^{2+} doping concentration.

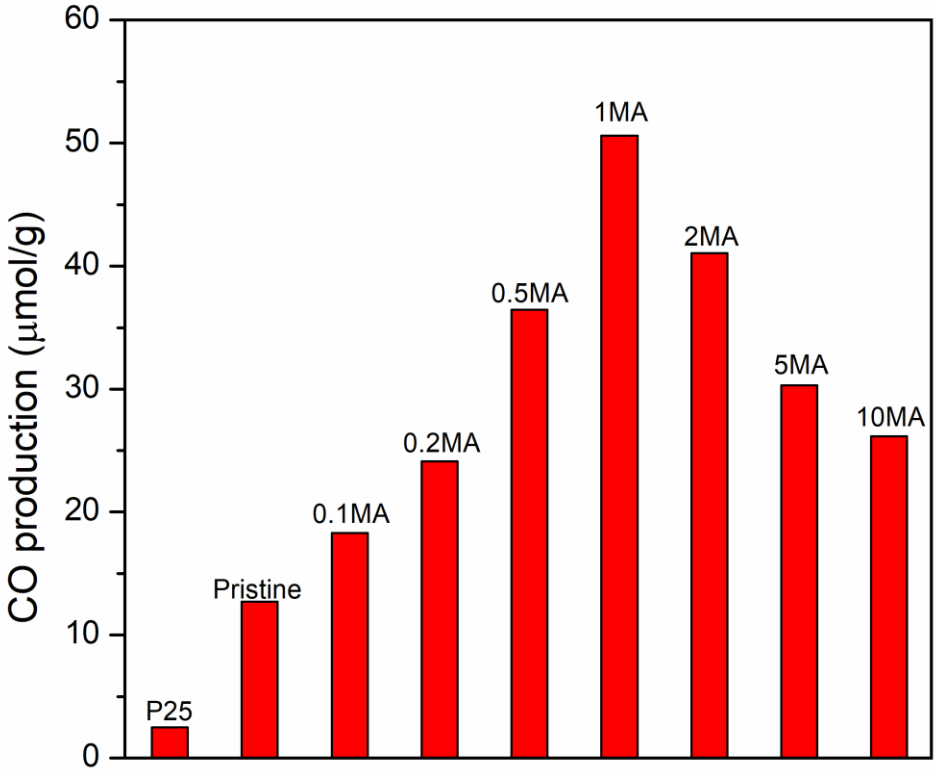

Figure 4-7 Comparison of CO production from CO_2 photoreduction by the various photocatalysts under light irradiation for 4 h.

To rule out interferences of surface area and demonstrate the promotion effect of Mg^{2+} doping on CO_2 photoreduction process, normalized CO production per surface area among pristine mesoporous TiO_2, 0.1MA, 1MA, and 10 MA was calculated and compared. As listed in Table 4-5, CO production per unit surface area of pristine mesoporous TiO_2 was defined as 1.00, this value increased to 1.47 on 0.1MA, even with a very low concentration of Mg^{2+} addition. 1MA showed the highest value in CO production per unit surface area among the four photocatalysts, valued at

2.48. This trend is likely a result of the combination of (1) generation of more surface active sites on photocatalysts, and (2) enhanced CO_2 adsorption as a result of Mg^{2+} doping. However, with a Mg^{2+} concentration that is too high, the normalized CO production per unit surface area on 10MA dropped to 1.03, which is almost the same as pristine mesoporous TiO_2, even though the higher Mg^{2+} concentration on 10MA further enhances CO_2 adsorption strength. It is likely that the over-concentrated Mg^{2+} doping centers act as recombination centers and lower photoactivity [48], which hinders CO_2 photoreduction performance.

Table 4-5 Comparison of CO production amount and normalized CO production per unit surface area of pristine mesoporous TiO_2, 0.1MA, 1MA and 10MA.

Sample ID	CO production (μmol/g)	Normalized CO production per unit surface area
Pristine	12.7	1.00
0.1MA	18.3	1.47
1MA	50.6	2.48
10MA	26.2	1.03

4.3.6. Transient photocurrent density measurements

Transient photocurrent densities of the as-prepared photocatalysts were measured in order to determine the charge transfer properties. The transient photocurrent density measurement results of pristine mesoporous TiO_2 and 1MA are shown in Figure 4-8. The transient photocurrent density curves of other as-prepared samples can be found in Figure C-3. The same light source used in the photocatalytic CO_2 reduction performance measurements was used in the transient photocurrent density measurements. To average out the fluctuation of transient photocurrent density in each light on-and-off cycle, average photocurrent densities were used for comparison purposes, which was calculated with the five measurements of Δj shown in Figure 4-8 (denoted as *avg.* Δj). The calculated average transient photocurrent density data are listed in Table 4-6.

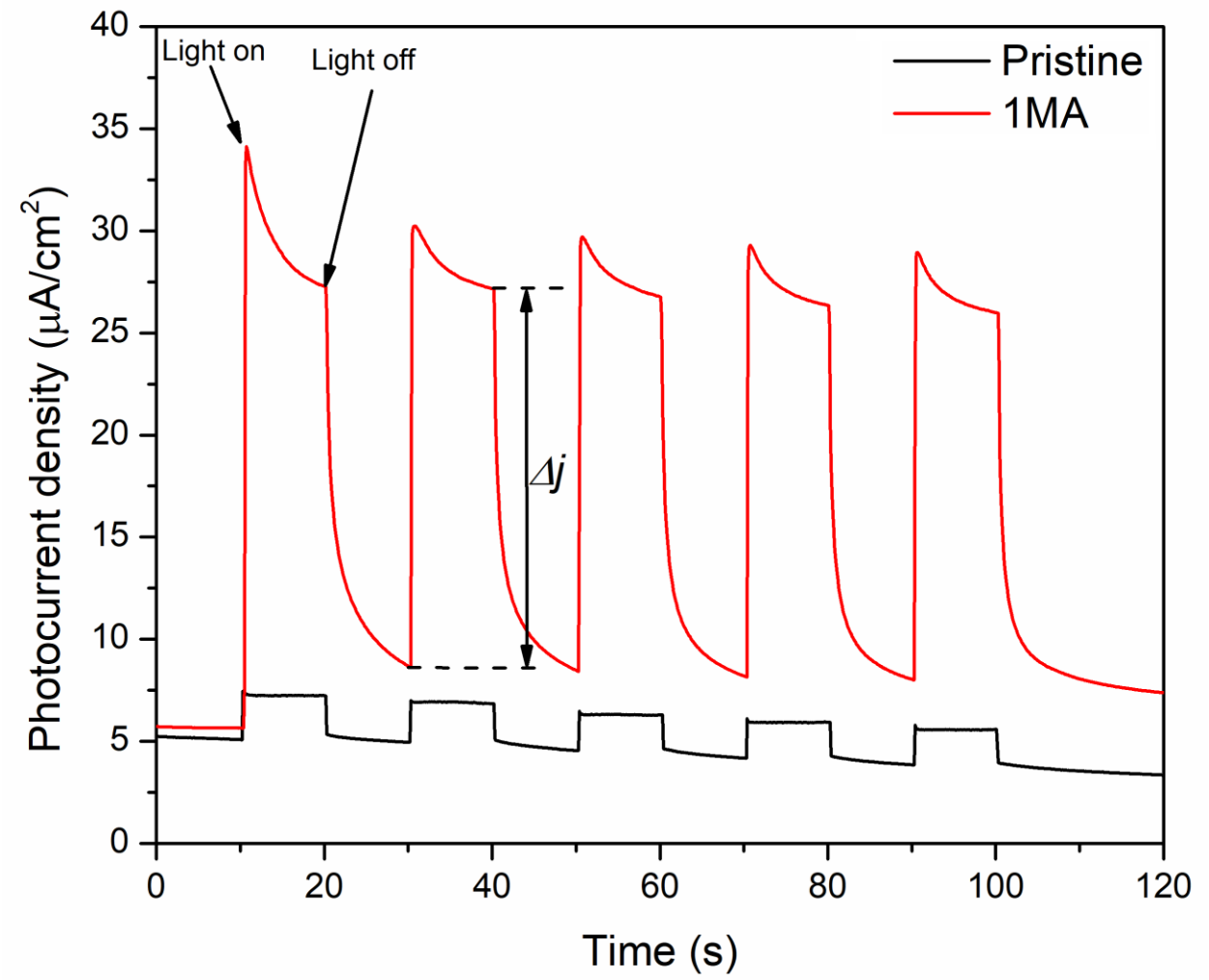

Figure 4-8 Transient photocurrent density comparison between pristine mesoporous TiO_2 and 1MA.

Table 4-6 Average transient photocurrent density of as-prepared photocatalysts.

Sample ID	*avg.* Δj ($\mu A/cm^2$)
Pristine	1.9
0.1MA	10.6
0.2MA	13.1
0.5MA	15.5
1MA	19.0
2MA	11.7
5MA	10.3
10MA	3.1

As listed in Table 4-6, pristine mesoporous TiO_2 shows an *avg. Δj* value of 1.9 μA/cm^2. The *avg. Δj* value of 0.1MA increased significantly to 10.6 μA/cm^2 with a low concentration Mg^{2+} doping. The *avg. Δj* value kept increasing with the increase in Mg^{2+} doping concentration until 1MA, which exhibited the highest average transient photocurrent density at 19.0 μA/cm^2, 10 times that of pristine mesoporous TiO_2. The significant improvements in photocurrent is likely a result of the following factors: (1) elevated surface area and increased porosity, which generated more active sites; (2) higher surface Ti^{3+} concentration originated from Mg^{2+} doping, which facilitates1 photoexcited electron/hole separation. However, a too high a Mg^{2+} doping concentration decreases the transient photocurrent density. As seen from Table 4-6, starting from 2MA, the *avg. Δj* value decreased with the increase of Mg^{2+} doping. The decrease in transient photocurrent density is likely a result of a higher concentration of Ti^{3+}/Mg^{2+} that acted as electron/hole separation centers. Again, a strong discrepancy between transient photocurrent density and CO_2 photoreduction performance was observed on 10MA. This result is likely related to the improvements in CO_2 adsorption ability, despite low transient photocurrent density.

A discrepancy was observed when the CO production performance data and transient photocurrent density data were considered jointly. For example, 0.1MA showed a transient photocurrent density that is more than 5 times of pristine mesoporous TiO_2, but the CO production amount of 0.1MA is only 1.4 times that of pristine mesoporous TiO_2. This discrepancy is likely related to the trade-off between the adsorption effect and the electron/hole hindering effect of Mg^{2+} dopant. For example, the discrepancy in transient photocurrent density and CO_2 photoreduction performance observed on 0.1MA and 0.2MA is likely related to the limited CO_2 surface affinity due to low Mg^{2+} doping concentration. Although the Mg^{2+} doping to the TiO_2 lattice introduced surface Ti^{3+} that hinders electron/hole recombination, which as a result increases transient

photocurrent density, limited CO_2 adsorption capacity due to low Mg^{2+} doping concentration confined the final CO_2 photoreduction performance. This speculation is also true when applying the same analyses on 0.5MA and 0.2MA. 0.5MA exhibited only an 18% increase in transient photocurrent density but showed 51% improvements in CO production compared with 0.2MA, which is most likely accounted for the increased Mg^{2+} doping concentration that favored photocatalyst-CO_2 interaction. The highest CO production rate was observed on 1MA at 50.6 μmol/g. In spite of improved CO_2 affinity, higher Mg^{2+} doping concentration than 1MA led to a deterioration in CO production. The CO production on 2MA dropped to 41.0 μmol/g and further diminished to 30.3 μmol/g on 5MA and 26.2 μmol/g on 10MA.

4.3.7. Optical properties

To determine the light absorption properties and bandgap of as-prepared photocatalysts, UV-vis diffuse reflectance tests were conducted, and the results are shown in Figure 4-9. All the photocatalysts show similar behaviors in light absorption. As listed in Table 4-7, however, it seems that the Mg^{2+} doping does not significantly affect the bandgap of the Mg^{2+} doped TiO_2.

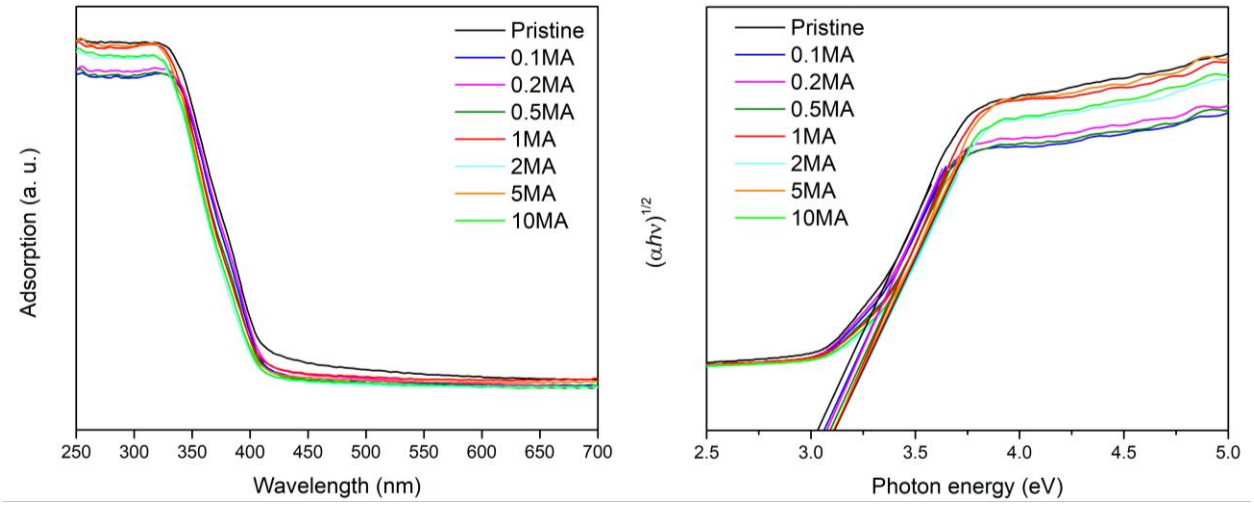

Figure 4-9 Light absorption (right) and Tauc plot (left) of prepared photocatalysts.

Table 4-7 Band gap of photocatalysts read from Tauc plot.

Sample ID	Band gap (eV)
Pristine	3.0
0.1MA	3.1
0.2MA	3.1
0.5MA	3.1
1MA	3.2
2MA	3.2
5MA	3.2
10MA	3.2

The photoluminescence (PL) test was conducted to determine the charge recombination nature of all prepared photocatalysts. As shown in Figure 4-10, pristine mesoporous TiO_2 shows a moderate PL response among all the photocatalysts. With a low amount of Mg^{2+} doping, a decreasing trend in PL signal intensity was observed on 0.1MA and 0.2MA. The decreasing trend of PL signal intensity is likely due to the Ti^{3+} centers and surface defects induced by Mg^{2+} doping, which facilitates charge separation and inhibits change recombination and thus decreases PL signal intensity. However, too high a Mg^{2+} doping concentration in pristine mesoporous TiO_2 showed adverse effects on charge separation. As shown in Figure 4-10, starting from 0.5MA, a trend of the intensifying signal was observed with increased Mg^{2+} doping concentration. The PL signal intensity of 1MA is slightly lower than that of pristine mesoporous TiO_2, and the PL signal intensity kept increasing with Mg doping concentration. This is likely due to the over-concentrated Mg^{2+} heteroatom centers and surface defects that act as recombination centers and promote charge recombination [172].

By comparing the results of CO_2 photoreduction performance and transient photocurrent density measurements with the PL results as a whole, it was noticed that the PL results do not correlate with the other results. For example, compared with 0.1MA, 1MA not only shows higher transient photocurrent density and CO production performance but also a more intensive PL signal.

This observation can probably be attributed to the increase in surface area, which is linked to Mg^{2+} doping. As discussed previously, the Mg^{2+} dopant into the pristine mesoporous TiO_2 structure led to an increase in surface area, which adds the number of active sites on the photocatalyst surface, contributing to the improvement in transient photocurrent density of 1MA, despite higher intensity in PL signal. Additionally, increased concentration of Mg^{2+} doping also facilitates the adsorption of CO_2 molecules. CO_2 photoreduction is a complex process where photo-excitation of photocatalyst, reactant adsorption/reduction, and product desorption are involved. Photocatalyst properties such as surface area, surface Ti^{3+} concentration, and CO_2 affinity originated from Mg^{2+} doping jointly influences the CO_2 photoreduction performance, which is a combination/trade-off between these properties. As a result of the combination/trade-off between the above factors, 1MA stands out among all the prepared photocatalysts for CO_2 photoreduction.

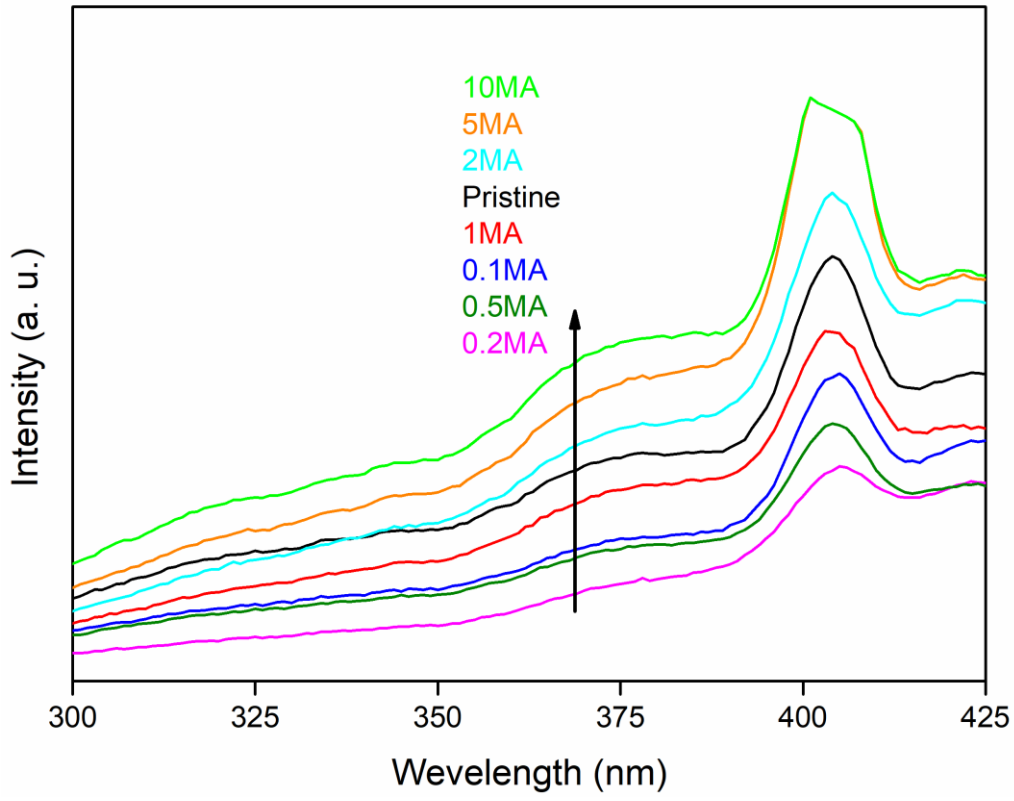

Figure 4-10 Comparison of photoluminescence spectra of all prepared photocatalysts.

4.4. Conclusions

Mg^{2+} doped mesoporous TiO_2 prepared by Mg^{2+} adsorption on metal-organic framework MIL-125 were prepared. The Mg^{2+} doped TiO_2 photocatalysts showed significant enhancements in the efficiency in CO_2 photoreduction, compared with pristine mesoporous TiO_2 prepared from thermal treatment of MIIL-125 without the adsorption process, which is partially enhanced by the alkaline nature of MgO. It was found that Mg^{2+} adsorption process on MIL-125 introduced more microstructures into the TiO_2 particles, which enlarged the surface area. The results of XPS analyses indicated that the introduction of Mg^{2+} dopants in TiO_2 resulted in an increase in surface concentration of Ti^{3+}, which enhanced charge separation. The combination of favorable mesoporous structure, surface chemistry contributed to the enhancement in the efficiency of CO_2 photoreduction on Mg^{2+} doped TiO_2 photocatalysts.

5. SYNGAS PRODUCTION AT A NEAR-UNITY HYDROGEN/CARBON MONOIXDE RATIO FROM PHOTO-THERO-CHEMICAL DRY REFORMING OF METHANE ON A PLATINUM DECORATED ALUMINA-CERIA CATALYST[§]

5.1. Introduction

Recently, our research group introduced a photo-thermo-chemical approach for the DRM process [91, 173], where concentrated sunlight was applied to partially provide thermal energy and photoactive Pt/CeO_2-based catalysts (Pt decorated Si-doped [91] and Zn-doped CeO_2 [173]) were employed to make better use of the concentrated sunlight and further improve the DRM performance. The Pt-CeO_2-based catalysts show highly efficient and stable DRM catalyzing capabilities and exhibit substantial DRM reaction rate enhancements under concentrated sunlight irradiation, compared to those under dark conditions. The Pt-CeO_2-based catalysts convert photon energy into chemical energy through the photo-induced activities on the metal oxide substrate [91, 174, 175]. The high performance and stability of the photo-thermal driven DRM reaction on Pt-CeO_2-based catalysts benefit from both the photoactivity [174] and the high surface oxygen mobility [90] of the CeO_2 substrate, which also promotes the coke resistance capacity of the catalysts.

In addition to the high energy consumption, another issue involved in the DRM process is the H_2/CO ratio that is lower than 1.0 in the products, which is likely related to a side reaction: reverse water-gas shift (RWGS) reaction ($H_2 + CO_2 \rightarrow H_2O + CO$) [78, 176]. DRM process on

[§] Part of this chapter is reprinted with permission from "Syngas production at a near-unity H_2/CO ratio from photo-thermo-chemical dry reforming of methane on a Pt decorated Al_2O_3-CeO_2 catalyst" by Xuhui Feng, Zichen Du, Erik Sarnello, Wei Deng, Cullen R. Petru, Lingzhe Fang, Tao Li, and Ying Li, *Journal of Materials Chemistry A*, 2022, DOI: 10.1039/D1TA10088B. Copyright [2022] by Royal Society of Chemistry.

numbers of noble metal-based catalytic materials, including Ru-based [177, 178], Pt-based [173, 179], Rh-based [180], and Pd-based [181, 182] catalysts, observes deteriorated H_2/CO ratios. For example, Damyanova *et al*. [183] applied a type of Pt/CeO_2-ZrO_2 catalyst for DRM reaction; only a low H_2/CO ratio of 0.51 was observed, which is likely associated with the presence of basic centers on ZrO_2 material [184]. Wysocka *et al*. [185] studied and compared the DRM performance of Ru-Ni/ZrO_2 and Ru-Ni/Al_2O_3 catalysts. However, due to the tendency of Ru catalyst in promoting RWGS reactions [186], only a H_2/CO ratio of ~0.7 was obtained. Advanced catalyst design is demanded to improve H_2 selectivity in the DRM process.

In efforts to design high H_2/CO ratio generation catalysts, Benrabaa *et al*. [101] recently reported the application of SiO_2 supported nickel ferrite catalysts in a thermal-driven DRM process, where it was demonstrated that H_2/CO production ratio can be promoted by Lewis acidic sites on the catalyst surface. However, Hambali *et al.* [187] later indicated that strong catalyst surface acidity may lead to, despite enhanced H_2 selectivity, catalyst coking, and deactivation. In light of these two studies, it seems that an improved H_2/CO ratio can be achieved by coupling a catalyst with a weak acidic promoter. Al_2O_3, a type of abundant and low-cost chemical compound with intrinsic mild acidic characteristics [188, 189] that has long been in catalyst design in a number of industrial processes including hydrocarbon isomerization [189], catalytic cracking [190], etc., can be an ideal addition on DRM catalysts to improve hydrogen production selectivity in DRM process.

In this chapter, Pt decorated equimolar Al_2O_3-CeO_2 catalyst was prepared and applied for the photo-thermal driven DRM (PTC-DRM) process. The first objective of this study is to introduce a facile and economic approach in catalyst design to improve the catalytic activity and H_2/CO ratio in the DRM process. Based on the aforementioned literature review, it is expected

that the Pt/Al_2O_3-CeO_2 material should promotes H_2 generation and enhances the H_2/CO ratio in the DRM process compared with Pt-CeO_2 based catalysts. Additionally, although alumina materials have been long applied as a substrate in conventional DRM processes [191, 192], there are still knowledge gaps regarding the synergetic effects between Al_2O_3 and CeO_2 in the photo-driven DRM processes. Therefore, more importantly, the second objective of this work is to investigate the synergetic effects of Al_2O_3 and CeO_2 as the substrates in the photo-driven DRM process. Thirdly, although a number of studies [88, 91, 98, 173, 193, 194] have demonstrated the effect of light irradiation in promoting the DRM performance on photoactive catalysts, the mechanism behind the performance enhancement is still not fully understood. For this reason, the third objective of this work is to uncover the role of light irradiation in the photo-thermal-chemical DRM process.

5.2. Experimental

5.2.1. Catalyst preparation

The metal oxide substrates were prepared according to previous reports [91, 173] with minor modifications. To prepare the CeO_2 substrate, solutions A and B were prepared. Solution A was prepared by dissolving 5 mmol cetyl trimethyl ammonium bromide (CTAB, $C_{19}H_{42}NBr$, high purity, VWR) in 7.9 g reagent alcohol (>96% ethanol, VWR). Solution B was prepared by mixing 5 mmol cerium nitrate hexahydrate [$Ce(NO_3)_3{\cdot}6H_2O$, 99.99%, BTC] and 5 mmol citric acid ($C_6H_8O_7$, 99.5+%, Alfa Aesar) in 7.9 g reagent alcohol. Solutions A and B were then mixed and stirred at room temperature for 3 h before being placed in an oven maintained at 60 ℃ overnight to allow the solvent to evaporate. The solidified gel was then calcined in air at 500 ℃ for 5 h. Al_2O_3 substrate was prepared by using 5 mmol aluminum nitrate nonahydrate [$Al(NO_3)_3{\cdot}9H_2O$,

≥98%, Sigma-Aldrich] instead of cerium nitrate hexahydrate to prepare solution B. Al_2O_3-CeO_2 hybrid substrate was prepared by using 5 mmol $Al(NO_3)_3 \cdot 9H_2O$ and 5 mmol $Ce(NO_3)_3 \cdot 6H_2O$ (nominal atomic ratio Al : Ce = 1:1) instead of solely $Ce(NO_3)_3 \cdot 6H_2O$ or $Al(NO_3)_3 \cdot 9H_2O$ to prepare solution B.

A wet impregnation method was applied to deposit 1 wt.% Pt on the metal oxide substrates and prepare the DRM catalysts. 100 mg metal oxide substrate was dispersed in a liquid mixture containing 5 g deionized water, 4 g methanol (CH_4O, >99.98%, VWR), 4 g acetone (C_3H_6O, VWR), and 2.1 mg chloroplatinic acid (H_2PtCl_6, 99.9%, Alfa Aesar, equivalent to 1 mg Pt) in an alumina crucible. The crucible was then placed on a hot plate maintained at 100 ℃, and the suspension was stirred with a magnetic bar to allow the solvent to evaporate. After the evaporation, the solid was collected and calcined in air at 500 ℃ for 2 h. The materials prepared with CeO_2 substrate, Al_2O_3 substrate, and Al_2O_3-CeO_2 hybrid substrate are denoted as Pt-Ce, Pt-Al, and Pt-Al-Ce, respectively.

5.2.2. Catalyst characterization

X-ray diffraction (XRD) patterns were obtained on a Bruker-AXS D8 advanced Bragg-Brentano X-ray powder diffractometer. Energy-dispersive X-ray spectroscopy (EDS) analysis was conducted with a JEOL JSM-7500F field emission scanning electron microscope (FE-SEM). The morphology of catalyst samples was investigated on a JEOL JEM2100F transmission electron microscope (TEM). X-ray photoelectron spectroscopy analyses were conducted on an Omicron DAR 400 XPS/UPS system. UV-Vis light absorption data were obtained on a Hitachi U-4100 UV-Vis-NIR spectrophotometer.

5.2.3. Photo-thermal driven DRM performance measurements

The experimental setup of the photo-thermal driven DRM catalyst performance measurements is similar to that employed in our previous studies [91, 173]. A ScienceTech solar simulator (operated at 1200W, equivalent to 30-sun irradiation, the light spectrum is shown in Figure D-1) was used as the light source. 5 mg catalyst sample was dispersed in 2 ml deionized water to form a catalyst suspension. The suspension was then dripped onto a piece of oval quartz fiber, which was later placed onto an oval catalyst holder. The catalyst holder was then placed into a quartz tube reactor. The position of the catalyst holder was carefully aligned inside the reactor to ensure the thermocouple tip contacts the quartz filter surface and aligns with the centerline of the catalyst holder and the reactor. The tube reactor was heated by a tube furnace, where a window was made to allow sunlight to irradiate on the catalyst. Prior to the performance test, the catalyst was firstly reduced at 700 ℃ by a gas mixture of H_2 (20.2 standard cubic centimeter per minute, or 20.2 sccm) and Ar (43.6 sccm) for 1 h, while two mass flow controllers controlled the gas flow rate. After the reduction process, the furnace was powered off, and the tube reactor was then purged with Ar (150 sccm) to eliminate H_2 in the reactor. After 30 min of Ar purging, the solar simulator was powered on at 1200 W and the tube furnace was turned on and set at a desired reaction temperature while maintaining Ar gas flow. The solar lamp operated at 1200 W alone can only heat up the reactor to ~ 450 ℃. Therefore, auxiliary heating from the furnace is needed. Once the reactor reached the desired reaction temperature, Ar gas was turned off and a premixed gas mixture (10% CH_4, 10% CO_2, balanced Ar, hereinafter referred to as “reaction gas”) was introduced into the reactor at a gas flow rate of 12 sccm. The outlet of the reactor is connected to a Shimadzu GC-2014 gas chromatograph to determine the chemical composition of the produced gas. Similar tests were conducted without concentrated solar irradiation.

5.2.4. *In situ* diffuse reflectance infrared Fourier transform spectroscopy (*in situ* DRIFTS) analyses

A similar setup reported in our previous study was applied to conduct the i*n situ* DRIFTS analyses [195]. The data acquisition was performed with a Nicolet 6700 spectrometer (Thermo Electron) equipped with a Praying Mantis DRIFTS accessory and a reaction chamber (Harrick Scientific, HVC-DRP). The highest temperature the reaction chamber can reach is 600 ℃. Prior to each *in situ* DRIFTS test, the catalyst sample was firstly reduced by a gas mixture of H_2 (20.2 sccm) and Ar (43.6 sccm) for 15 min at 600 ℃ in the DRIFTS reaction chamber. After the reduction process, H_2 gas flow was turned off and the reaction chamber was allowed to cool down naturally to the target testing temperature while Ar protected the catalyst sample at a flow rate of 43.6 sccm. Once the DRIFT chamber reached the target temperature, the FTIR background was then taken, followed by introducing the same reaction gas used in the DRM performance test at 12 sccm. The catalyst sample was then allowed to interact with the reaction gas (under continuous flow) while multiple DRIFTS data was taken and recorded under the dark conditions over the next 10 min. It normally takes ~ 3 min before the catalyst surface gets saturated with the reaction gas. Therefore, 10 min is adequate for the catalyst to reach the adsorption equilibrium. After the dark equilibrium DRIFTS spectra were taken, concentrated sunlight was then applied to the sample through the quartz window. The same solar lamp used in the DRM performance test was applied as the light source, the power of the lamp was set at 1200 W. An optical fiber was used to direct the light into the DRIFTS reaction chamber. The intensity of the light exiting the optical fiber was measured to be close to 1 sun, and the light spectrum is shown in Figure D-2. Immediately after the concentrated sunlight was applied to the DRIFTS cell, another set of DRIFTS data acquisition was conducted. Multiple DRIFTS data were taken and recorded over the next 5 minutes, which is

adequate for the catalyst to reach a new absorption equilibrium under solar irradiation (normally takes less than 1 min). Similar *in situ* DRIFTS analyses were also performed with a CO_2 : Ar = 10 : 90 gas mixture and a CH_4 : Ar = 10 : 90 gas mixture.

5.3. Results and discussion

5.3.1. Crystal structure

The XRD patterns of Pt-Ce, Pt-Al-Ce, and Pt-Al are displayed in Figure 5-1. The characteristic XRD pattern of CeO_2 was found on both Pt-Ce and Pt-Al-Ce, while the characteristic peaks of Pt were not found in the XRD patterns of either sample. The Pt nanoparticles are likely tiny and well distributed on the surface of Pt-Ce and Pt-Al-Ce. By comparing the XRD patterns of Pt-Ce and Pt-Al-Ce, it was noted that the XRD peaks of Pt-Al-Ce are broadened. This observation is likely related to the decreased CeO_2 crystalline size due to the combination of CeO_2 and Al_2O_3. The XRD pattern of Pt-Al indicates that the phase of the Al_2O_3 support as γ-Al_2O_3, elementary Pt [111] peak was found at $2\theta = \sim 39.7^{o}$, which confirms the existence of Pt in Pt-Al catalyst. Since the weight percentage of Pt is the same in all of the three catalysts, the observation of Pt [111] in Pt-Al suggests that the size of Pt nanoparticles is significantly larger than that on Pt-Ce and Pt-Al-Ce.

Interestingly, no characteristic peaks of γ-Al_2O_3 were found in the XRD pattern of Pt-Al-Ce, similar results were also previously observed in several studies in Al_2O_3-CeO_2 hybrid metal oxide materials [196-198]. This is likely related to the low crystallinity of the γ-Al_2O_3 substrate, as evidenced by the wide and less-defined peaks in the XRD pattern of Pt-Al. Since the CeO_2 phase in Pt-Ce shows sharp and well-defined peaks, it is likely that in Pt-Al-Ce, the highly crystallized CeO_2 peaks overshadow those of γ-Al_2O_3, resulting in the absence of γ-Al_2O_3 peaks.

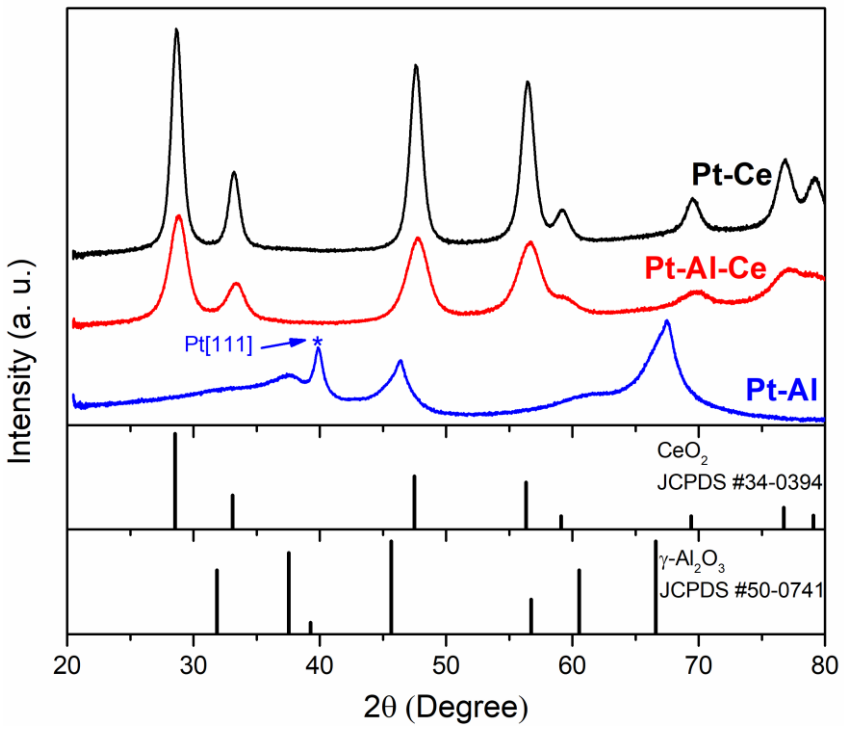

Figure 5-1 XRD patterns of Pt-Ce, Pt-Al and Pt-Al-Ce.

5.3.2. Morphology

Figure 5-2 shows the TEM images of Pt-Ce, Pt-Al-Ce, and Pt-Al. As shown in Figure 5-2a, the particle size of Pt decorated CeO_2 catalyst is ~20 nm, and the catalyst particles show sharp edges and corners. Pt-Al-Ce material particles show a diameter of ~15 nm (Figure 5-2c) and the particles are oval-shaped. Different from Pt-Ce and Pt-Al-Ce, the particle size of Pt-Al is significantly larger. As shown in Figure 5-2e, the particle size distribution of Pt-Al ranges from ~100 nm to several hundred nanometers. CeO_2 [111] (0.31 nm) and CeO_2 [100] (0.27 nm) were noted in Pt-Ce and Pt-Al-Ce, according to Figure 5-2b and d, which coincide with the XRD results. As shown in the CeO_2 lattice Figure 5-2b, the CeO_2 phase in Pt-Ce material shows long-range order, while the CeO_2 phase in Pt-Al-Ce only exhibits short-range order (Figure 5-2d). It seems that Al_2O_3 phase breaks down the long-range order of the CeO_2 crystalline in Pt-Al-Ce, which verifies that the phases of Al_2O_3 and CeO_2 are in segregated phases instead of solid solution form.

Pt [111] (0.21 nm) spacing was found in Pt-Ce, Pt-Al-Ce, and Pt-Al, confirming the existence of Pt. The sizes of Pt nanoparticles on Pt-Ce, Pt-Al-Ce, and Pt-Al were measured with ImageJ based on a number of TEM images. The average Pt particle size on Pt-Ce, Pt-Al-Ce, and Pt-Al was calculated as 1.9 nm, 1.4 nm, and 6.8 nm, respectively. The histograms of Pt nanoparticle sizes on the three catalysts are included as Figure D-3. The Pt nanoparticle sizes on Pt-Al are significantly greater than those on Pt-Ce and Pt-Al-Ce. The large size of Pt nanoparticle size coincides with the XRD pattern of Pt-Al, where Pt [111] peak is prominent.

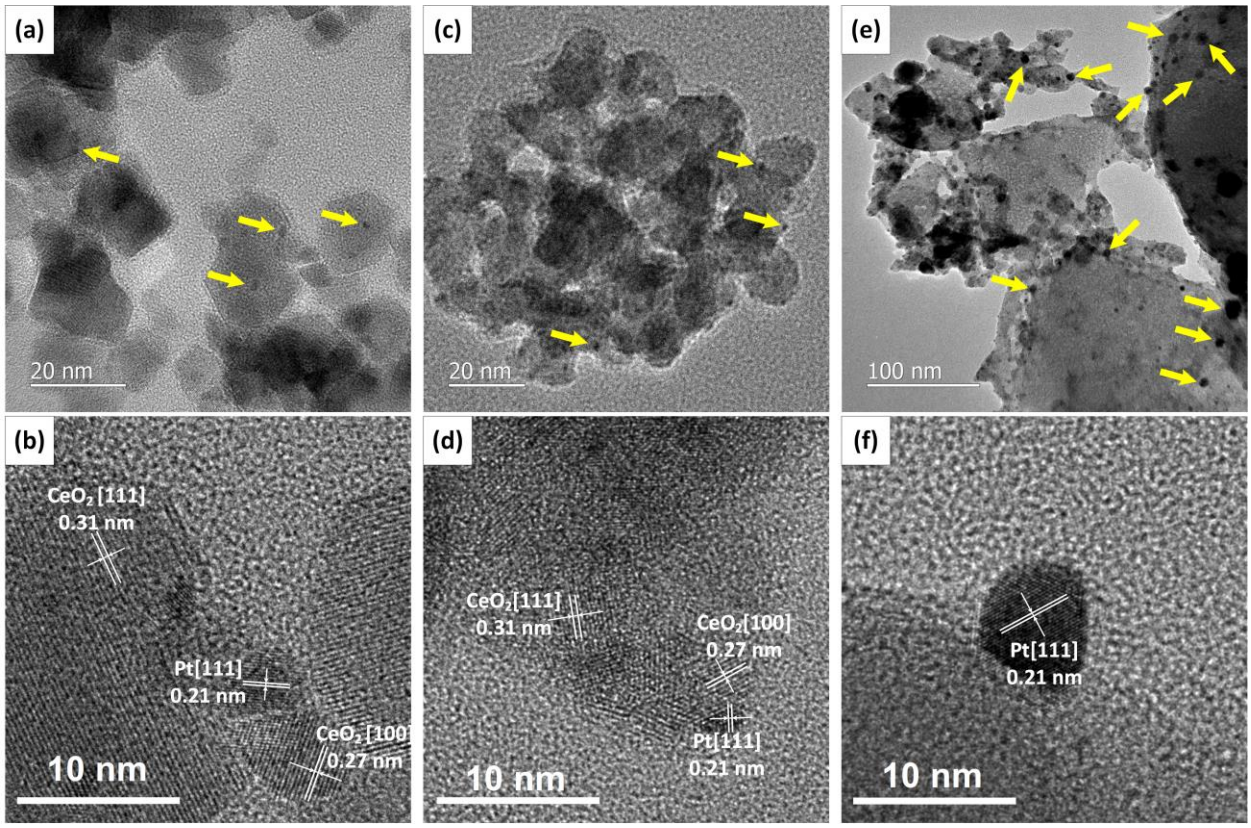

Figure 5-2 TEM images of Pt-Ce (a & b), Pt-Al-Ce (c & d), and Pt-Al (e & f); yellow arrows point to Pt nanoparticles.

To confirm the existence of the Al element in Pt-Al-Ce, Elemental mapping was performed by energy-dispersive X-ray spectroscopy (EDS), which is presented in Figure 5-3. The elemental

mapping of Pt-Al-Ce shows strong signals of Ce and Al, confirming Ce and Al are major elements in Pt-Al-Ce. Pt was also found in the EDS mapping, while Pt signal is much weaker compared to those of Ce and Al, which is reasonable due to the low concentration of Pt (1.0 wt.%) in Pt-Al-Ce.

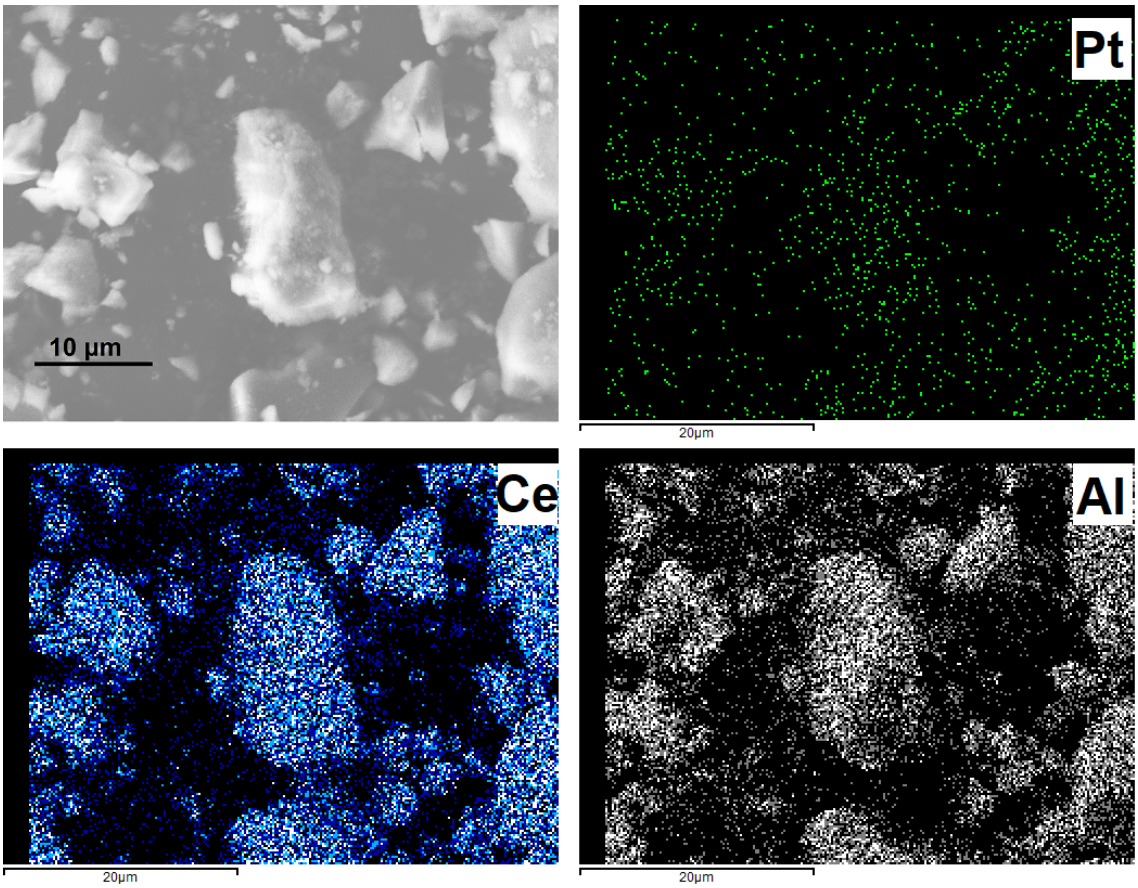

Figure 5-3 Energy dispersive X-ray spectroscopy (EDS) analysis on elemental mapping of Pt, Al, and Ce elements on Pt-Al-Ce catalyst.

5.3.3. Surface chemical properties

X-ray photoelectron spectroscopy (XPS) analysis on Ce *3d* orbital was conducted on Pt-Ce and Pt-Al-Ce to investigate the effect of Al_2O_3-CeO_2 incorporation on the chemical states of CeO_2. Prior to the XPS testing, the catalysts were pre-reduced in Ar/H_2 gas mixture as they would be in DRM performance tests. XPS analyses on Pt or Al were not performed as the XPS binding energies of the two elements overlap, making it impractical to reach meaningful results or

conclusions. The existence of Ce^{3+} in the catalyst surface indicates the formation of oxygen vacancies, likely generated during the H_2 reduction process. The oxygen vacancy has been deemed as a key factor for achieving high DRM performance [173, 199]. As shown in Figure 5-4, the Ce *3d* spectra can be well deconvoluted into Ce^{4+} and Ce^{3+}, where v_o, v', u_o, and u' correspond to Ce^{3+}; v, v'', v''', u, u'', and u''' correspond to Ce^{4+} [173, 200-202]. Based on the Ce *3d* deconvolution results, the molar ratios of $Ce^{3+}/(Ce^{3+} + Ce^{4+})$ on Pt-Ce and Pt-Al-Ce are calculated to be 24.3% and 24.7%, respectively. It seems that the incorporation of Al_2O_3 into Pt-CeO_2 does not significantly promote the formation of Ce^{3+}. The $Ce^{3+}/(Ce^{3+} + Ce^{4+})$ value on both of the catalysts are similar; however, if considering the high concentration of the Al_2O_3 incorporation in Pt-Al-Ce, the oxygen vacancy concentration on Pt-Al-Ce can be significantly lower than that on Pt-Ce.

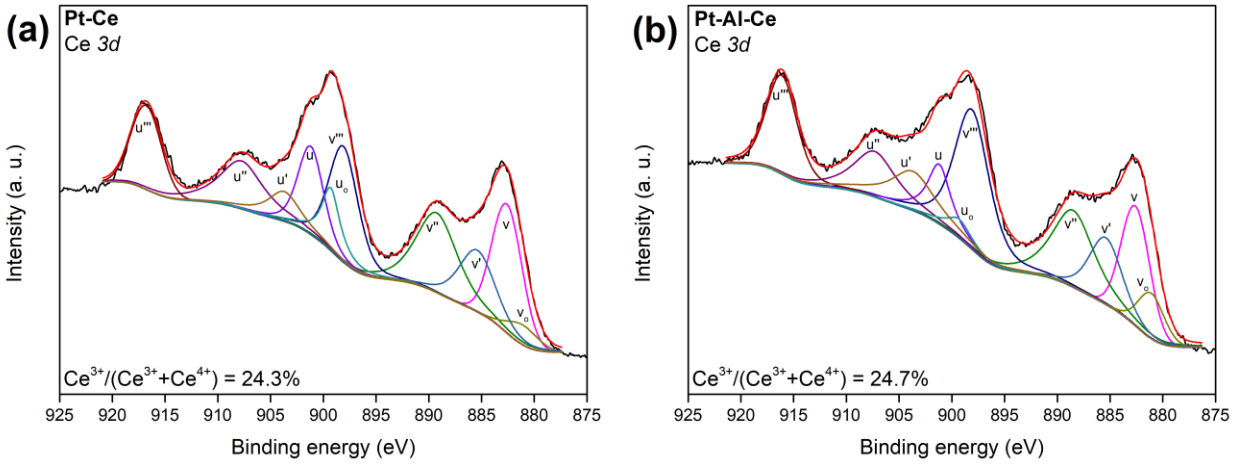

Figure 5-4 Deconvolution of Ce 3d XPS spectra on Pt-Ce and Pt-Al-Ce catalysts.

To better compare the surface oxygen vacancies concentrations between Pt-Ce and Pt-Al-Ce, the deconvolution of O *1s* was also performed. The difference in binding energy values of the lattice oxygen (O_L) on Al_2O_3 and CeO_2 was found to be very close to each other [203-206]. Therefore, the two types of lattice oxygen atoms were considered as a whole, whose peak is located

at ~ 529.9 eV. The peak at ~532.0 eV was identified as adsorbed oxygen (O_A) on oxygen vacancies, which can be applied to determine the concentration of surface vacancies [203, 204, 207]. Based on the O *1s* deconvolution result shown in Figure 5-5, the O_A concentrations on Pt-Ce and Pt-Al-Ce were calculated as 27.0% and 15.5%, respectively. Compared with Pt-Ce, Pt-Al-Ce exhibits a relatively lower concentration of oxygen vacancies, which is reasonable as only CeO_2 is capable of producing oxygen vacancies in a reducing environment and CeO_2 is diluted due to the existence of Al_2O_3 in Pt-Al-Ce.

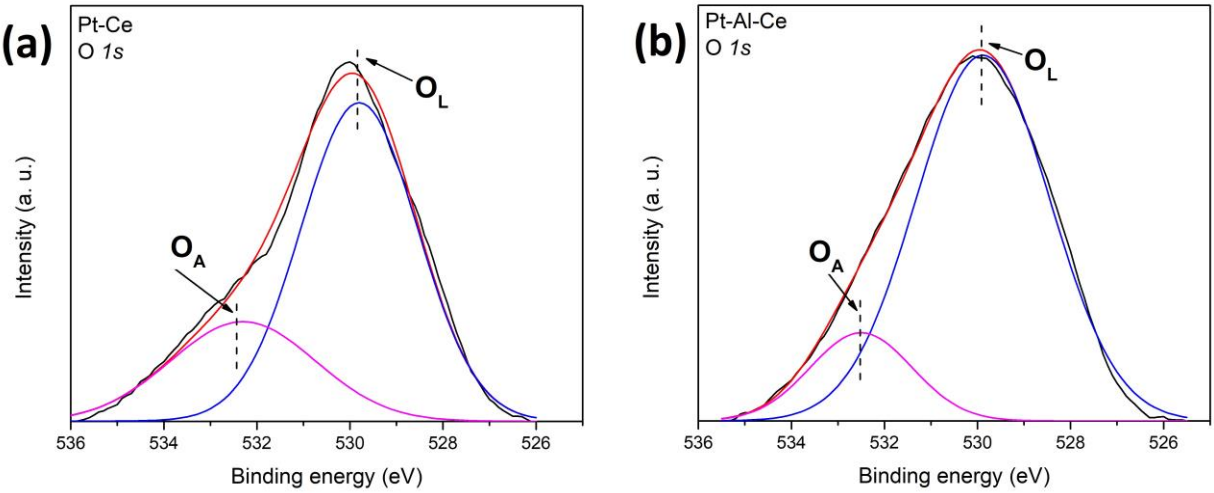

Figure 5-5 Deconvolution of O 1s XPS spectra on Pt-Ce and Pt-Al-Ce catalysts.

5.3.4. Optical properties

To investigate the optical properties and calculate the bandgaps of the as-prepared catalysts, UV-Vis diffuse reflectance spectra and bandgap analyses were performed. As shown in Figure 5-6a, Pt-Ce absorbs light mainly in the wavelength range below 400 nm, showing two major absorption bands located at 250 nm and 351 nm, in agreement with the CeO_2 light absorption property reported in a previous study [208]. Pt-Al-Ce also shows a major light absorption of photons with a shorter wavelength than 400 nm, while the absorption band at ~250 nm shows a

slight intensity decline. Different from Pt-Ce and Pt-Al-Ce, Pt-Al only shows absorption at ~258 nm, which is identified as the light absorption of alumina [209]. The light absorption of Pt nanoparticles likely causes the light absorption in the visible light range.

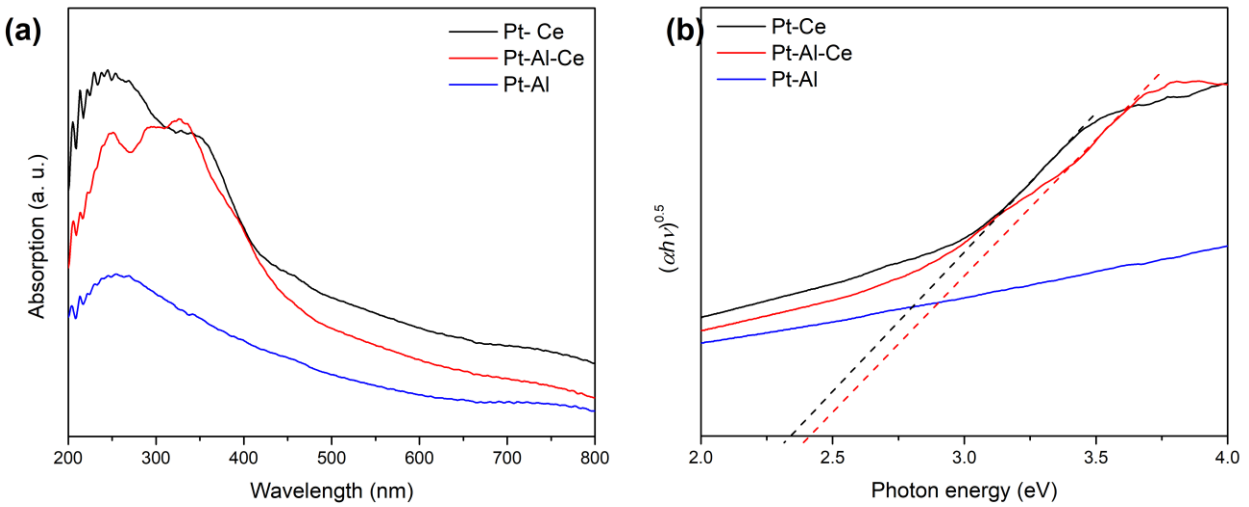

Figure 5-6 UV-Vis light absorption spectra (a) and Tauc plots (b) of Pt-Ce, Pt-Al-Ce, and Pt-Al materials.

Bandgap analysis was performed with Tauc plot based on the procedure reported by Makula *et al*. previously [210]. Figure 5-6b shows the bandgap analyses for Pt-Ce, Pt-Al-Ce, and Pt-Al. The bandgaps of Pt-Ce and Pt-Al-Ce were calculated as 2.3 eV and 2.4 eV, respectively. Pt-Al-Ce material only shows a bandgap value change of 0.1 eV; it seems that the existence of Al_2O_3 does not cause a significant bandgap variation on the CeO_2 component in Pt-Al-Ce. However, according to the Tauc plot of Pt-Al, it is not plausible to determine the bandgap value of Pt-Al. This result suggests the Pt-Al catalyst is not photoactive. The obtained bandgap value of Pt-Ce is lower compared with the calculated values in our previous reported values [91, 173]. As mentioned, the catalysts were reduced prior to the UV-Vis diffuse reflectance measurements. The oxygen vacancy generated from the reduction process is likely responsible for the narrowed bandgaps of Pt-Ce and Pt-Al-Ce [211, 212].

5.3.5. DRM performance

DRM performance data of Pt-Al-Ce, Pt-Ce, and Pt-Al at 700 ℃ under both dark conditions and concentrated sunlight were presented in Figure 5-7. The three catalysts show structure and morphology stability after the experiments, as shown in Figure D-4 and Figure D-5. The numerical results of the DRM performance are listed in Table 5-1, where the listed values are the averages of all DRM performance data presented in Figure 5-7. Both Pt-Ce and Pt-Al-Ce showed good stability under both dark and light conditions for the DRM process at 700 ℃. Both catalysts showed DRM performance enhancement under light conditions compared with those in dark conditions, as shown in Figure 5-7. Notably, under concentrated solar irradiation, Pt-Al-Ce delivered a near-unity H_2/CO production ratio of 0.99, which is significantly improved compared with that of Pt-Ce (0.77 under light conditions).

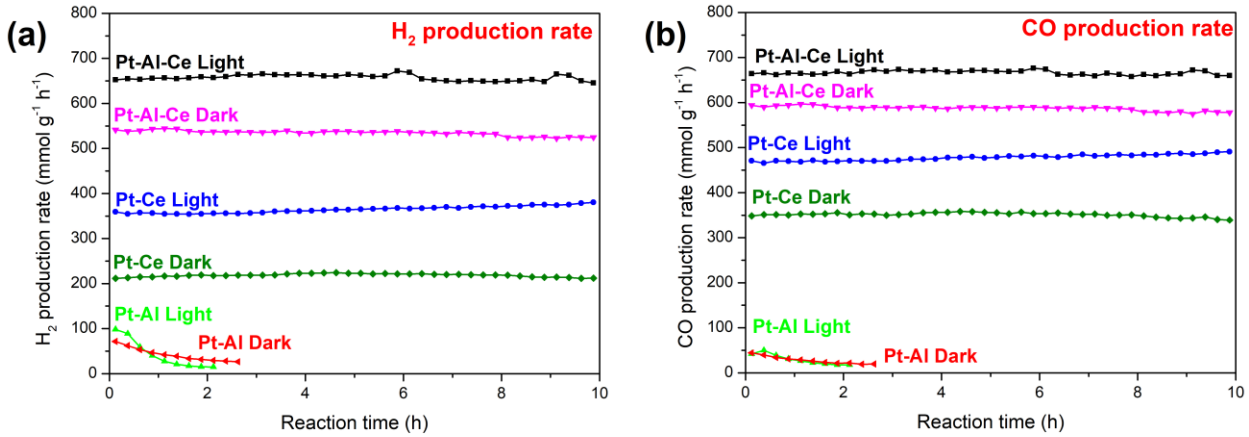

Figure 5-7 DRM performance: (a) H_2 production and (b) CO production of Pt-Ce, Pt-Al and Pt-Al-Ce at 700 ℃ under light and dark conditions.

In contrast, Pt-Al deactivates fast under both reaction conditions within less than 2 h in the DRM process. No significant difference in DRM performance was observed related to solar irradiation. Al_2O_3 is not considered photoactive. It is, therefore, reasonable that the concentrated sunlight does not make a significant difference in the DRM performance of the Pt-Al catalyst.

Regarding the DRM catalyzing stability of Pt-Al, as previously reported by Hambali *et al.* [187], a DRM catalyst with an over-acidic surface may result in deactivation in the DRM process due to coke accumulation. Although Al_2O_3 is a type of material showing only weak surface acidity under DRM reaction conditions [188], it seems that the surface acidity of pure Al_2O_3 support is already too high for the DRM process to maintain a stable catalytic activity. As shown in Table 5-1, the H_2/CO ratios on Pt-Al under light and dark conditions were calculated to be 1.50 and 1.44, respectively. A value of H_2/CO ratio higher than 1.0 in the DRM process suggests a faster methane dissociation rate than coke carbon gasification rate, which leads to coke accumulation and causes performance deactivation.

Table 5-1 DRM performance of Pt-Ce, Pt-Al-Ce and Pt-Al at 700 °C (average of data in Figure 5-7).

Sample ID	H_2 production rate ($mmol \cdot g^{-1} \cdot h^{-1}$)	CO production rate ($mmol \cdot g^{-1} \cdot h^{-1}$)	H_2/CO ratio
Under dark conditions			
Pt-Ce	218	351	0.62
Pt-Al-Ce	535	588	0.91
Pt-Al	42	28	1.50
Under solar irradiation			
Pt-Ce	365	477	0.77
Pt-Al-Ce	657	666	0.99
Pt-Al	43	30	1.44

As determined by the TEM analyses, there is a difference between the size of Pt nanoparticles on Pt-Ce (1.9 nm) and Pt-Al-Ce (1.4 nm). The size of Pt nanoparticles deposited on the catalysts is a crucial factor in determining the DRM reaction rate. However, little information was found in the literature on the Pt nanoparticle sizes on the reaction rate of DRM reactions. In a similar materials system, however, Gascon *et al*. [213] investigated the role of Rhodium (Rh)

particle size on DRM reaction rates, where the Rh nanoparticles were deposited on three substrates, namely CeO_2, CeO_2-ZrO_2, and ZrO_2. It was found that the DRM reaction rates on the catalysts showed a linear correlation with the Rh nanoparticle size in the range of 1.6 - 8.0 nm. This study applied a similar catalyst system and conducted the same reaction process as in the present work. More importantly, as a type of noble metal, Rh nanoparticles promote the DRM reaction rate in a similar way as Pt does. Based on the work of Gascon *et al.*, given the fact that Rh is generally more active as an active species than Pt in the DRM process [71], the small difference in Pt nanoparticle sizes between Pt-Ce and Pt-Al-Ce is unlikely to make a significant difference in the DRM reaction rates on Pt-Ce and Pt-Al-Ce.

An apparent synergy effect of Al_2O_3 and CeO_2 as catalyst support is observed on Pt-Al-Ce. Pt-Al-Ce considerably outperforms both Pt-Ce and Pt-Al in H_2 and CO production rate. Compared with Pt-Ce, Pt-Al-Ce shows significant enhancement in CO and H_2 production rate under both light and dark conditions (67.2% and 144.8% enhancements in CO and H_2 under dark, respectively; 39.6% and 80.0% improvements in CO and H_2 under light, respectively). Compared with Pt-Al, Pt Al-Ce exhibits good stability, in addition to the notably promoted H_2 and CO production rates. The significant improvement in H_2 generation rate on Pt-Al-Ce suggests that methane dissociation was strongly promoted. In this sense, the incorporation of Al_2O_3 with CeO_2 is advantageous due to the high efficiency of CeO_2 in the oxidation of surface deposited coke into CO [183, 214, 215]. In this regard, in Pt-Al-Ce material, Al_2O_3-CeO_2 support is likely bi-functional: firstly, Al_2O_3 promotes methane dissociation on Pt nanoparticles, resulting in improved H_2 generation; secondly, CeO_2 acts as catalyst performance stabilizer by eliminating any possible coke formed from methane dissociation. It is likely that the two possible mechanisms work jointly to promote the DRM performance on Pt-Al-Ce catalyst.

To confirm the above hypotheses and further investigate the synergy effect of Al_2O_3 and CeO_2 in the Al_2O_3-CeO_2 binary substrate, a CeO_2-rich Pt-Al-Ce catalyst (Al : Ce molar ratio = 2 : 10, noted as Ce-Rich-PAC) and an Al_2O_3-rich Pt-Al-Ce catalyst (Al : Ce molar ratio = 10 : 2, noted as Al-Rich-PAC) were prepared and tested for DRM performance under solar irradiation at 700 °C, and the results are shown in Figure 5-8. Ce-Rich-PAC shows stable catalytic activities, and the 10-h average of CO and H_2 production rates of Ce-Rich-PAC are 602 $mmol \cdot g^{-1} \cdot h^{-1}$ and 549 $mmol \cdot g^{-1} \cdot h^{-1}$, respectively. Even with a low Al_2O_3 incorporation concentration in the catalyst, Ce-Rich-PAC shows notable enhancements in catalytic performance than those of Pt-Ce. The H_2/CO production ratio of Ce-Rich-PAC was 0.91, considerably higher than that of Pt-Ce and only slightly lower than that of Pt-Al-Ce. In contrast to the stable DRM performance of Ce-Rich-PAC, Al-Rich-PAC shows a deteriorating catalytic performance over time: the initial CO and H_2 production rates are 641 $mmol \cdot g^{-1} \cdot h^{-1}$ and 728 $mmol \cdot g^{-1} \cdot h^{-1}$, respectively, which dropped to 581 $mmol \cdot g^{-1} \cdot h^{-1}$ and 596 $mmol \cdot g^{-1} \cdot h^{-1}$ after 10 h, respectively. Interestingly, the initial CO production rate on Al-Rich-PAC is slightly lower than that of Pt-Al-Ce, but the initial H_2 production rate on Al-Rich-PAC is ~9% higher than that of Pt-Al-Ce. This result again implies that Al_2O_3 promotes H_2 generation from methane dissociation. Over the 10 h test, the H_2/CO production ratio on Al-Rich-PAC is always greater than 1.0, suggesting a faster methane dissociation reaction rate and coke accumulation on the catalysts, which leads to deactivation in DRM performance. Despite the DRM catalytic deactivation of Al-Rich-PAC over time, compared with Pt-Al, Al-Rich-PAC exhibits remarkable improvements in both catalytic performance and stability, even with a low CeO_2 incorporation concentration. The enhancements are likely related to the superior coke gasification ability of CeO_2¸which minimizes coke accumulation and preserves the activity of the

catalyst [216]. However, with a low CeO_2 incorporation amount, Al-Rich-PAC still shows deterioration in catalytic performance over time.

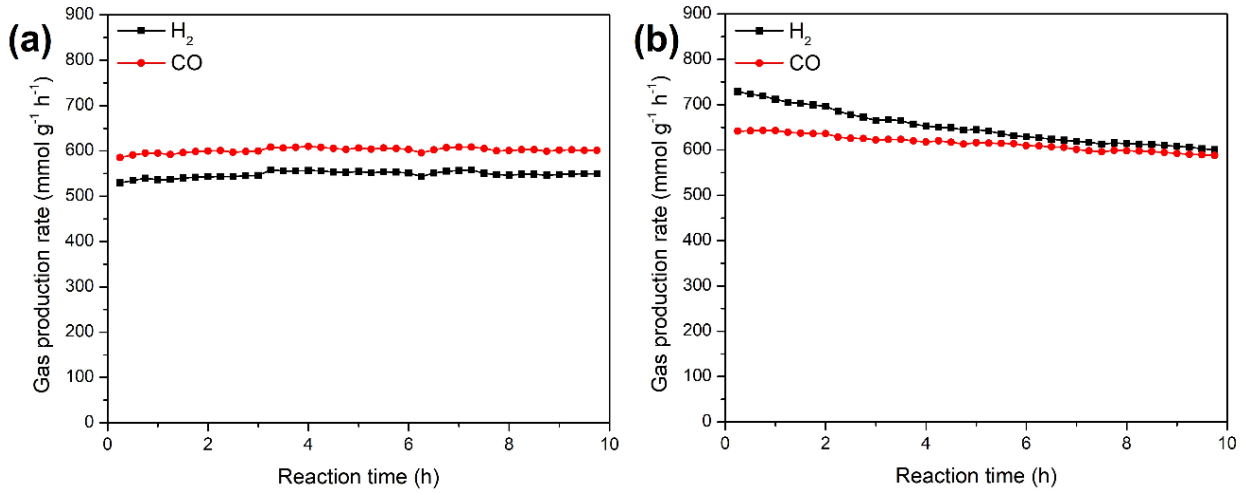

Figure 5-8 DRM catalytic performance of (a) Ce-Rich-PAC and (b) Al-Rich-PAC under 30-sun concentrated solar irradiation at 700 °C.

To determine the effect of Pt concentration of Pt-Al-Ce catalyst on the DRM process, varied amounts of Pt (0.25 wt.%, 0.5 wt.%, and 2 wt.%) were loaded on the equimolar Al_2O_3-CeO_2 hybrid substrate (denoted as 0.25-Pt-Al-Ce, 0.5-Pt-Al-Ce, and 2-Pt-Al-Ce, respectively) and applied for the DRM process. All of the catalysts showed a stable DRM performance, the averaged DRM performances were listed and compared in Table 5-2. It is clear that a higher Pt loading concentration is favorable in promoting the H_2 and CO production rate as well as the H_2/CO ratio. However, by comparing Pt-Al-Ce with 2-Pt-Al-Ce, especially those under solar irradiation, the increase in the H_2/CO ratio is marginal when Pt loading is over 1.0 wt.%, despite the slight enhancement in H_2 and CO production. Since Pt is a noble metal and expensive, by taking the cost of Pt into consideration, it is safe to reach the conclusion that 1.0 wt.% of Pt loading is optimal.

To further investigate the role of solar irradiation in the DRM process on Pt-Al-Ce catalyst, DRM performance tests at 650 °C and 600 °C under both dark and light conditions were conducted

on Pt-Al-Ce catalyst, the performance results of the test are listed along with the 700 ℃ data in Table 5-3. The ln(r) – 1000/T correlations were plotted in Figure 5-9 according to the Arrhenius equation based on the data listed in Table 5-3. The ln(r) - 1000/T regression plots show a good linear correlation, and the linear regressions of the four datasets returned R^2 values close to 1.0, indicating accurate regression results. The apparent activation energy values were listed in Table 5-4 based on the calculated slopes of each regression curve.

Table 5-2 DRM catalytic performance of Pt-Al-Ce catalyst with varied Pt loading amount.

Sample ID	H_2 production rate ($mmol \cdot g^{-1} \cdot h^{-1}$)	CO production rate ($mmol \cdot g^{-1} \cdot h^{-1}$)	H_2/CO ratio
Under dark conditions			
0.25-Pt-Al-Ce	225	337	0.67
0.5-Pt-Al-Ce	446	528	0.85
Pt-Al-Ce	535	588	0.91
2-Pt-Al-Ce	682	685	0.99
Under solar irradiation			
0.25-Pt-Al-Ce	313	424	0.74
0.5-Pt-Al-Ce	489	554	0.88
Pt-Al-Ce	657	666	0.99
2-Pt-Al-Ce	729	717	1.02

Table 5-3 DRM test results of Pt-Al-Ce at varied reaction temperatures.

Reaction temperature	H_2 production rate ($mmol \cdot g^{-1} \cdot h^{-1}$)	CO production rate ($mmol \cdot g^{-1} \cdot h^{-1}$)	H_2/CO ratio
Under dark conditions			
700 ℃	535	587	0.91
650 ℃	382	463	0.82
600 ℃	222	325	0.68
Under concentrated solar irradiation			
700 ℃	657	666	0.99
650 ℃	536	574	0.93
600 ℃	375	450	0.83

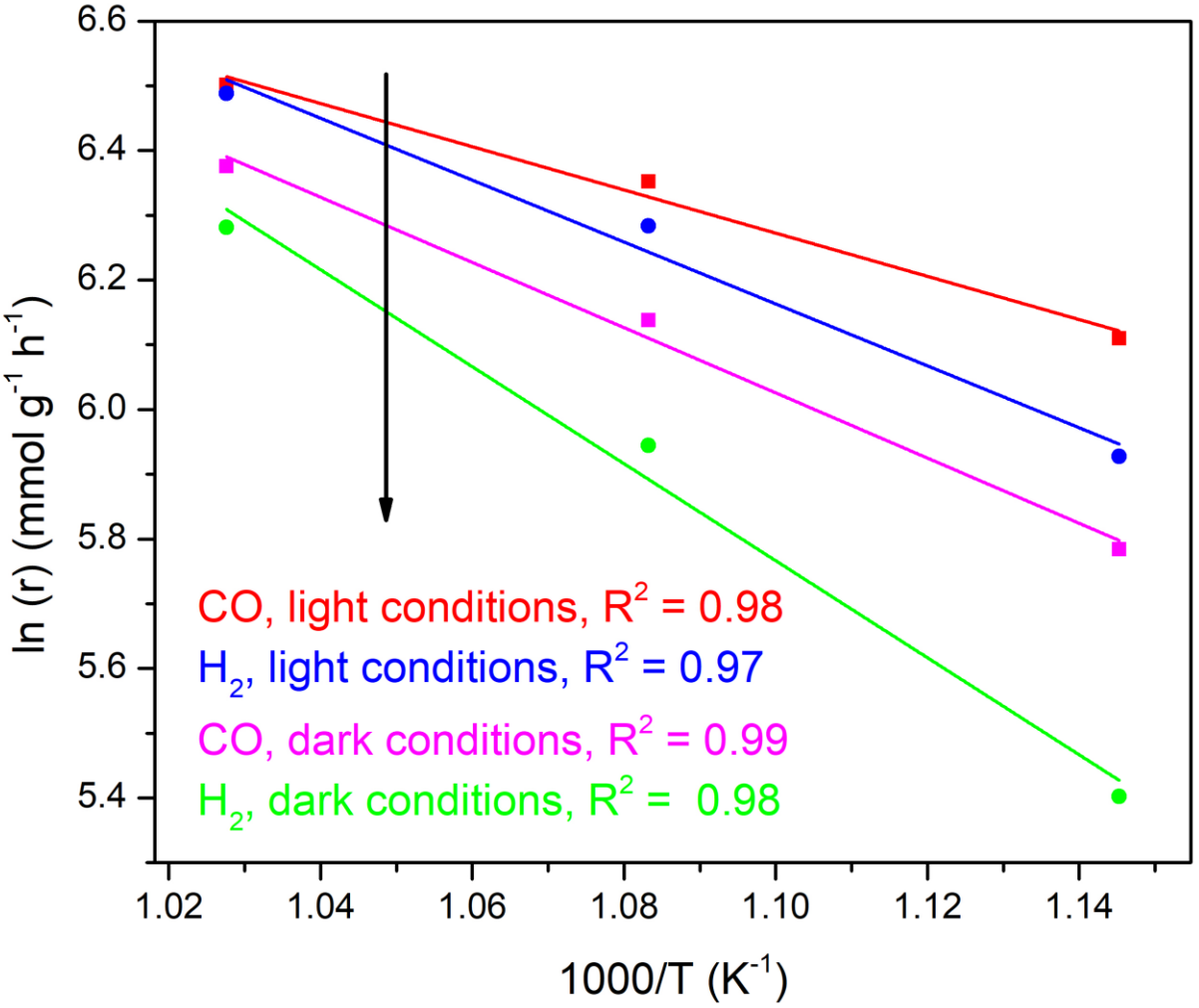

Figure 5-9 Arrhenius ln (r) - 1000/T plot for H_2 and CO gas production rate in DRM process on Pt-Al-Ce catalyst under both dark and light conditions.

Table 5-4 The apparent activation energy of H_2 and CO production on Pt-Al-Ce under dark and light conditions.

Gas species	Apparent E_a (kJ/mol)	
	Dark	Light
H_2	62.3	39.8
CO	41.9	27.8

As shown in Table 5-4, the apparent activation energy for H_2 and CO production under dark conditions is 62.3 kJ/mol and 41.9 kJ/mol, respectively. The apparent E_a of H_2 and CO

production under solar irradiation are 39.8 kJ/mol and 27.8 kJ/mol, which is significantly lowered compared with those calculated under dark conditions, similar observations on the reactant activation effect of light irradiation in DRM process has also been documented by Yoshida *et al.* [84] and Miyauchi *et al.* [99, 100, 217] It seems that the sunlight assisted in the activation of the reactants in the DRM process on Pt-Al-Ce catalysts. However, according to Figure 5-7 and Table 5-1, H_2 and CO production efficiency on Pt-Al is insensitive to light irradiation. Therefore, irradiation alone does not directly activate the reactants. Photoactive CeO_2 seems to be the media assisting the conversion of photon energy into chemical energy and facilitating the reaction. To determine the photoactivities of CeO_2 in Pt-Ce and Pt-Al-Ce, XPS deconvolution of Ce 3d of spent Pt-Ce and Pt-Al-Ce under both light and dark conditions under 700 ℃ was performed, the results are shown in Figure 5-10. The light excitation can weaken the Ce-O bonds in CeO_2 and lead to the generation of Ce^{3+} and oxygen vacancies ($Ce^{4+} + h\nu \rightarrow Ce^{3+} + V_O$) [103, 173]. After DRM reaction under the dark conditions, both Pt-Ce and Pt-Al-Ce exhibit lower molar ratios of $Ce^{3+}/(Ce^{3+} + Ce^{4+})$, valued at 17.4% and 15.6%, respectively, compared with fresh catalysts (fresh Pt-Ce: 24.3%, fresh Pt-Al-Ce: 24.7%) in Figure 5-4, which is likely due to the oxidation of Ce^{3+} to Ce^{4+} by CO_2 in the DRM process [103, 173]. Contrastingly, significantly higher molar ratios of $Ce^{3+}/(Ce^{3+} + Ce^{4+})$ on both catalysts was observed after the DRM reaction under the irradiation of the concentrated sunlight (Pt-Ce: 39.1%, Pt-Al-Ce: 49.8%). This result suggests that the photoactive CeO_2 component in Pt-Ce and Pt-Al-Ce could contribute to the DRM performance under light irradiation through photocatalysis.

To further verify the role of photocatalysis in the photo-driven DRM process on Pt-Al-Ce catalyst, a control experiment was conducted at 700 ℃ with a 530-nm long-pass filter. The cut-off photon energy of the 530-nm filter is 2.34 eV, which is slightly lower than the bandgap energy of

Pt-Al-Ce (2.4 eV). Table 5-5 shows the comparison of 10-h average Pt-Al-Ce DRM performance under full-spectrum, 530 nm cut-off, and dark conditions. Under 530 nm cut-off conditions, where the photon energy is lower than the bandgap energy of Pt-Al-Ce, the DRM performance is almost the same as that under dark conditions. This result suggests that light irradiation enhances the DRM reaction through photocatalytic excitation of the catalyst, where photon energy is converted to chemical energy conversion and leads to the significantly lower apparent activation energy for the production of H_2 and CO.

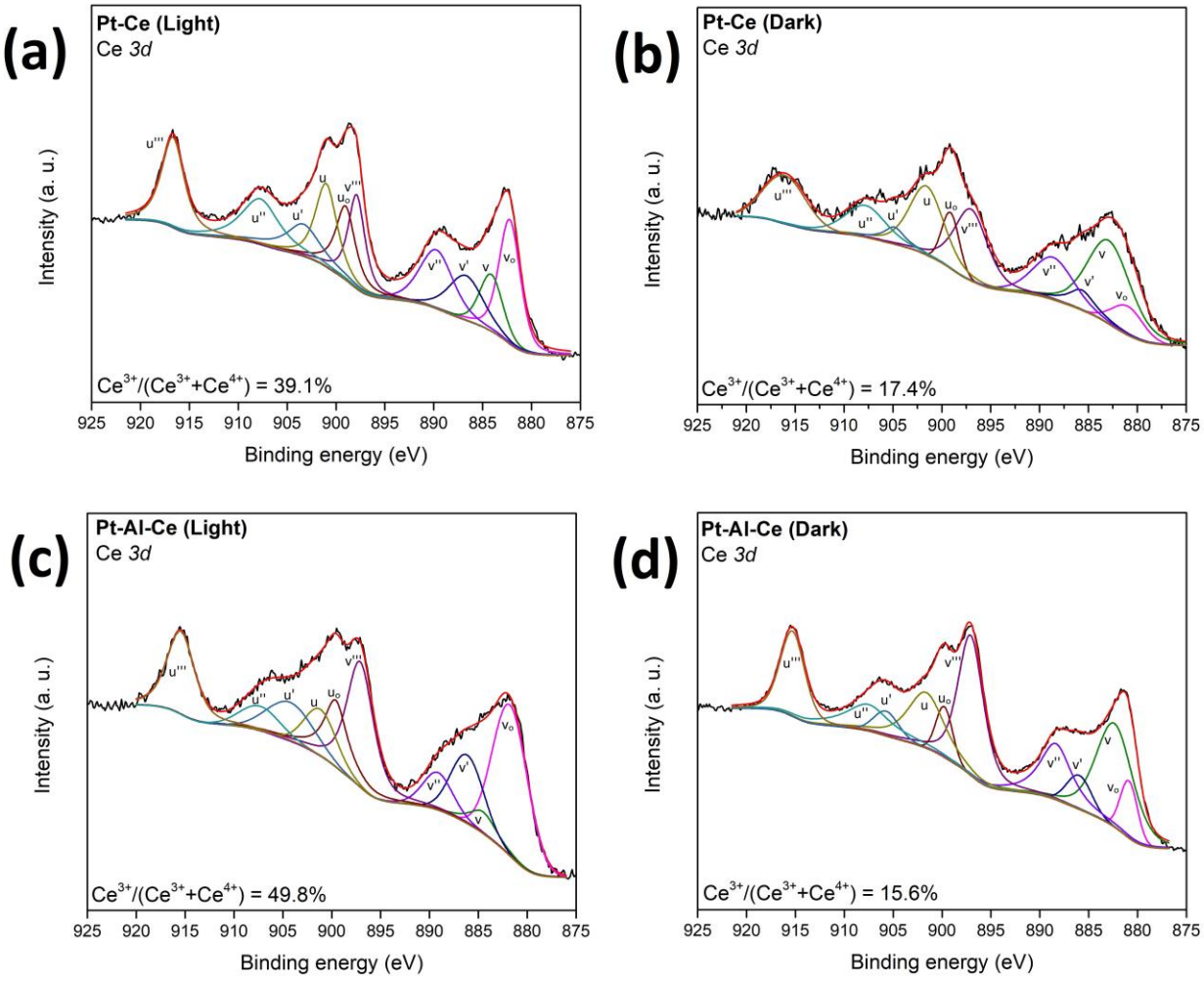

Figure 5-10 Deconvolution of Ce *3d* XPS spectra on spent Pt-Ce and Pt-Al-Ce catalysts after 10 h DRM reaction at 700 °C.

Table 5-5 DRM performance of Pt-Al-Ce at varied light irradiation conditions at 700 ℃.

Reaction conditions	H_2 production rate ($mmol \cdot g^{-1} \cdot h^{-1}$)	CO production rate ($mmol \cdot g^{-1} \cdot h^{-1}$)
Full spectrum	657	666
>530 nm cut-off	531	593
Dark	535	588

5.3.6. *In situ* DRIFTS analysis

To understand the effect of solar irradiation and investigate the intermediates involved in the photo-thermal driven DRM process, *in situ* DRIFTS analysis was conducted at various temperatures on Pt-Ce, Pt-Al-Ce, and Pt-Al under dark and light conditions in three gas environments: (1) DRM reaction gas (CO_2, and CH_4), (2) CO_2 only, and (3) CH_4 only.

Figure 5-11 shows the *in situ* DRIFTS results of Pt-Ce, Pt-Al-Ce and Pt-Al under the reaction gas atmosphere, it was observed that the exposure of DRM reaction gas to Pt-Ce and Pt-Al-Ce led to the generation of surface intermediates including formate (HCOO-) [218-220], bidentate carbonate (b-CO_3^{2-}) [220-223], and monodentate carbonate (m-CO_3^{2-}) [28, 224]. The peaks located at 1338 cm^{-1} and 1308 cm^{-1} were identified as gaseous CH_4 [225] in the reactions. The doublet bands found at 2069 cm^{-1} and 1971 cm^{-1} were identified as CO molecules linearly bonded on Pt atoms (Pt-CO) [226-229]. The CO molecules were likely originated from CO_2 reduction taking place on the catalyst surface. The absorption band located at 2069 cm^{-1} indicated the existence of linearly adsorbed CO on Pt, while the shoulder band centered at ~1971 cm^{-1} indicated the coverage of CO molecules on the boundary of Pt and the metal oxide support [226-229]. On Pt-Al, only Pt-CO and bicarbonate bands [230, 231] were observed. Gaseous CO production was also observed as the duplet band at 2178 cm^{-1} and 2109 cm^{-1} at a temperature higher than 400 ℃ on Pt-Al.

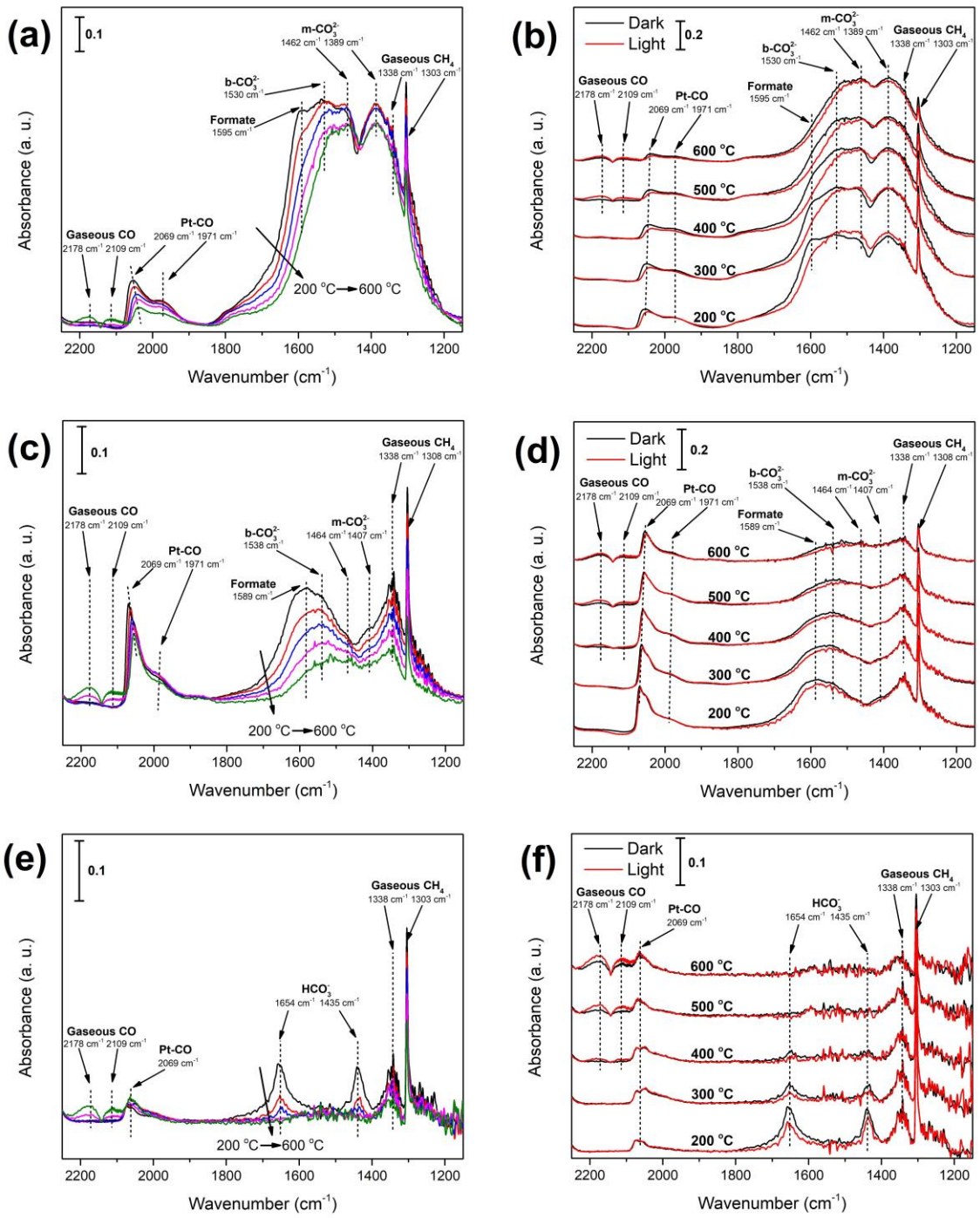

Figure 5-11 *In situ* DRIFTS spectra at DRM reaction conditions in the dark on (a) Pt-Ce, (c) Pt-Al-Ce, (e) Pt-Al, and dark-light comparison on (b) Pt-Ce, (d) Pt-Al-Ce, (f) Pt-Al.

Figure 5-11a shows the surface intermediates behavior on Pt-Ce under reaction gas atmosphere to temperature increase under dark conditions. All surface intermediates were found

to show a decrease in absorption intensity due to the temperature increase. It seems that the formate intermediates are quite sensitive to temperature increases: the formate band intensity almost halved after the temperature increased from 200 ℃ to 600 ℃. Only a small intensity diminish was found on m-CO_3^{2-} and b-CO_3^{2-}. A red-shifting effect was observed on the Pt-CO band as temperature increases, which was likely due to the declined CO adsorption reducing the repulsion forces among CO molecules and leading to red shifting of the CO absorption band [232], indicating CO desorption.

Figure 5-11b shows the comparison between light and dark *in situ* DRIFTS results obtained on Pt-Ce. Under light irradiation, almost all of the surface intermediates showed a slight intensity decline. To rule out the thermal effect of the light irradiation, an IR thermometer was used to determine the temperature change of the sample in the *in situ* DRIFTS cell upon the light irradiation at room temperature. After ~5 min of sunlight irradiation, only a temperature rise of ~5 ℃ was observed on the catalyst surface. With such a minor temperature change at room temperature, the temperature change caused by the light irradiation may be negligible for tests conducted at 200 - 600 ℃. The most noticeable change in the spectra is the sharp intensity decline of the formate band at ~1595 cm^{-1} under light irradiation. The intensity of b-CO_3^{2-} was also found to decline under light irradiation. It seemed that m-CO_3^{2-} was relatively stable upon the light irradiation. Both formate and b-CO_3^{2-} have been viewed as important surface intermediates in CO generation in the DRM process. The intensity declines in the two surface intermediates suggest an accelerated rate of the surface intermediates participating in the reaction process [25]. The activation energy calculation chart shows that solar irradiation activates the surface intermediates and promotes the DRM reactions.

Similar surface intermediates were found on Pt-Al-Ce in dark conditions under reaction

gas atmosphere, as shown in Figure 5-11c. Compared with Pt-Ce, the intensities of all of the carbonate absorption bands in the range of 1600 - 1200 cm^{-1} were significantly weaker on Pt-Al-Ce, which was likely due to the lower concentration of CeO_2 in Pt-Al-Ce material. Interestingly, the Pt-CO absorption band on Pt-Al-Ce was considerably stronger than that on Pt-Ce. In addition, the Pt-CO band on Pt-Al-Ce seemed to be less sensitive to temperature increase: only a small drop in Pt-CO peak height was recorded while the temperature increased from 200 ℃ to 600 ℃. The results indicate (1) a higher number of Pt nanoparticle active reaction sites, and (2) more reactive Pt nanoparticles on Pt-Al-Ce than those on Pt-Ce, which is likely promoted by the synergy effects between Al_2O_3 and CeO_2 in Pt-Al-Ce material. Similar to Pt-Ce, as temperature rises, the intensity of absorption bands on Pt-Al-Ce declines. Similar to the observations on Pt-Ce, formate showed the most intensity decrease as temperature increased, b-CO_3^{2-} and m-CO_3^{2-} was also found to be sensitive to temperature increase. Similar to Pt-Ce, upon the concentrated solar irradiation, the formate and b-CO_3^{2-} intermediates showed a slight decrease in absorption band intensity, as shown in Figure 5-11d, suggesting a promoted reaction rate in the DRM process.

Distinct from Pt-Ce and Pt-Al-Ce, only bicarbonate and Pt-CO were found on the surface of Pt-Al after contacting with the reaction gas. The intensity of Pt-CO absorption band on Pt-Al was significantly weaker compared with Pt-Ce or Pt-Al-Ce, indicating fewer Pt nanoparticle active sites and less reactive Pt nanoparticles. The HCO_3^- intermediates seemed to be very sensitive to temperature increases. By increasing the temperature from 200 ℃ to 400 ℃ under dark conditions, the HCO_3^- absorption intensity decreased fast and disappears at 500 ℃, as shown in Figure 5-11e. Since DRM tests were conducted at high temperatures in this study, it is likely that bicarbonate is not an active intermediate in the DRM process. The low CO_2 affinity on Al_2O_3 might partially contribute to the poor DRM performance on Pt-Al.

To get a deeper understanding of the surface interaction between the catalysts and CO_2 or CH_4, *in situ* DRIFTS analyses were conducted under CO_2 and CH_4 atmosphere, respectively. The *in situ* DRIFTS results of Pt-Ce and Pt-Al-Ce obtained under a CO_2 atmosphere were shown in Figure 5-12. Only weak Pt-CO bands were found on Pt-Al under CO_2 atmosphere, no carbonates bands were found, indicating low CO_2 affinity of Pt-Al catalyst. The spectra obtained with Pt-Al are included in Figure D-6. In Figure 5-12, Pt-Ce and Pt-Al-Ce showed similar surface intermediates and DRIFTS spectra shape when the two catalysts were exposed to CO_2 gas. A formate band was found on both Pt-Ce and Pt-Al-Ce in the 1200-1400 cm^{-1} range (Figure 5-12a-d) [218], which was overshadowed by CH_4 gas in Figure 5-11. Both formate bands were sensitive to temperature increase and concentrated solar irradiation, coinciding with the results observed under the DRM gas atmosphere. Similar to the observation made in Figure 5-11, Pt-Al-Ce shows a stronger Pt-CO band, suggesting highly active and concentrated Pt nanoparticle reactions sites.

Under light irradiation, Pt-Ce shows formate absorption band intensity decline at all temperatures. Under 200 ℃ and 300 ℃, interestingly, it was found that the concentrated solar irradiation led to increases m-CO_3^{2-} and b-CO_3^{2-} band intensity on Pt-Ce. The light irradiation likely caused oxygen vacancy generation on CeO_2 through a photocatalytic self-reduction process ($CeO_2 + h\nu \rightarrow CeO_{2-x} + O_2$) [233] which further promoted CO_2 adsorption and led to a slight intensity increase in m-CO_3^{2-} and b-CO_3^{2-} bands. At higher temperatures, all band intensities of surface absorbed intermediates drop under light irradiation. Formate, m-CO_3^{2-}, and b-CO_3^{2-} are active intermediates in CO_2 reduction reactions [25, 234]. The photo-induced band intensity declines likely suggest the occurrence of CO_2 reduction. However, gaseous CO bands were not observed in Figure 5-12b, which is possibly due to the very low gaseous CO concentration on Pt-Ce. As shown in Figure 5-12d, the light irradiation on Pt-Al-Ce resulted in considerable band

intensity drops for the formate, m-CO_3^{2-}, and b-CO_3^{2-} in the temperature range of 200 ℃ - 500 ℃. A weak gaseous CO band was observed starting at 500 ℃, confirming the occurrence of CO_2 reduction reactions. The existence of a gaseous CO band with Pt-Al-Ce catalyst suggests higher reactivity of Pt-Al-Ce compared to Pt-Ce.

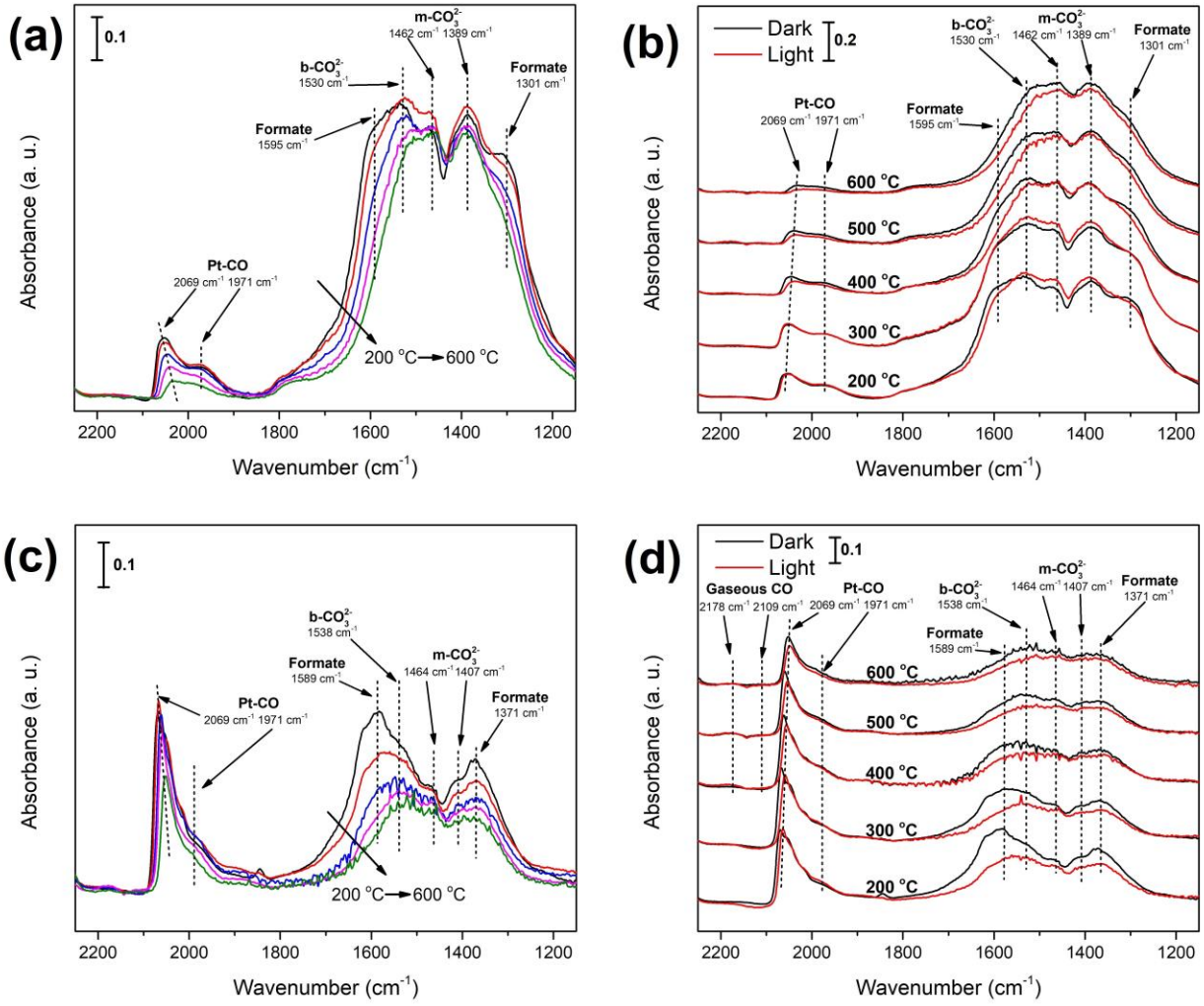

Figure 5-12 *In situ* DRIFTS spectra under CO_2 atmosphere in the dark on (a) Pt-Ce, (c) Pt-Al-Ce, and dark-light comparison on (b) Pt-Ce, (d) Pt-Al-Ce.

The *in situ* DRIFTS results obtained under the CH_4 atmosphere are shown in Figure 5-13, where spectra obtained 300 - 600 ℃ were shown. For Pt-Ce, starting from 300 ℃, strong carbonate

bands were observed in the range of 1200 - 1600 cm^{-1}. The carbonates are likely the product of CH_4 oxidation by CeO_2. Weak Pt-CO bands were found. Compared with the Pt-CO bands observed under reaction gas and CO_2 atmospheres, a significant redshift was detected: from 2069 cm^{-1} under CO_2-rich atmosphere to 2033 cm^{-1} under CH_4 atmosphere, indicating a low CO coverage on Pt nanoparticles. This observation is reasonable as only a trace amount of CH_4 can be converted into CO on Pt-Ce surface under a CH_4 atmosphere. Formate was not found from the CH_4-DRIFTS results, which suggests that CO_2 is the source for formate intermediate generation. The intensities of the b-CO_3^{2-} bands observed under CH_4 atmosphere were considerably lower than those found under CO_2 or reaction gas atmosphere. This is likely because the conversion from m-CO_3^{2-} to b-CO_3^{2-} requires excessive CO_2 supply, which, however, was lacking under the CH_4 atmosphere. In addition, it does not seem that the surface intermediates are sensitive to concentrated solar irradiation under the CH_4 atmosphere, as compared by Figure 5-13a and b. Pt-Al-Ce showed similar behavior as noticed on Pt-Ce catalyst and similar surface intermediates were found (Figure 5-13c and d). However, compared with Pt-Ce, Pt-Al-Ce showed a significantly stronger Pt-CO absorption band. The Pt-CO band on Pt-Al-Ce was evident even at a low temperature of 300 ℃, which is a clear indicator of the occurrence of strong CH_4 oxidation. This result suggests that the Pt-Al-Ce material shows substantially higher surface reactivity compared to Pt-Ce. The DRIFTS data obtained on Pt-Al is included in Figure D-7. No carbonate intermediates were found on Pt-Al, suggesting poor catalyst-CH_4 surface interaction. Surprisingly, however, a weak Pt-CO peak was found on Pt-Al under the CH_4 atmosphere. Without the presence of CO_2, the origin of Pt-CO can only be the oxidation of CH_4. It seems that Pt-Al is capable of dissociating trace amounts of CH_4 even at 300 ℃. By combining the fact that Pt-CO was found on Pt-Al-Ce and Pt-Al under

CH_4 atmosphere, it seems the existence of Al_2O_3 promotes the dissociation of CH_4, even at a relatively low temperature.

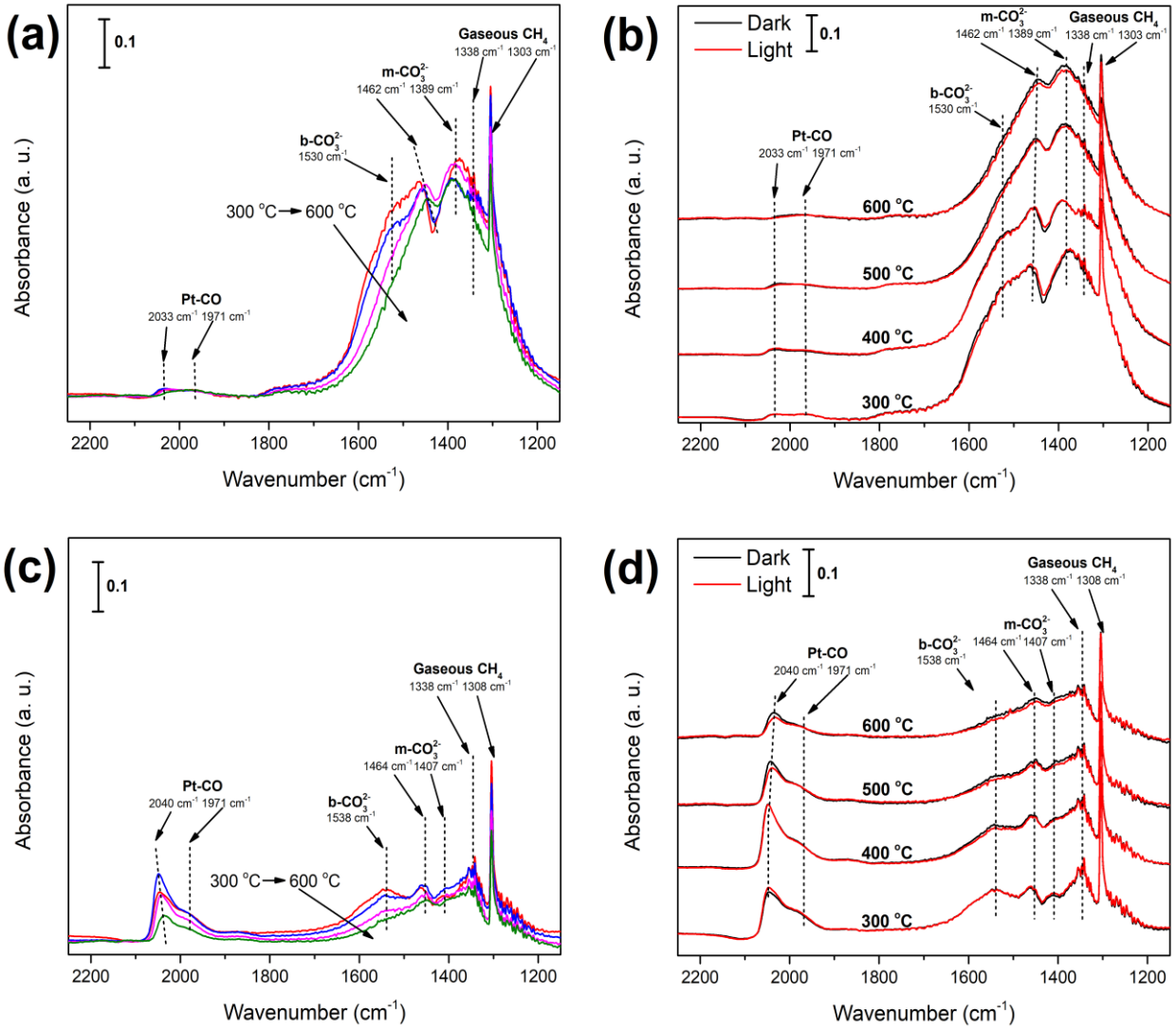

Figure 5-13 *In situ* DRIFTS spectra under CH_4 atmosphere in the dark on (a) Pt-Ce, (c) Pt-Al-Ce, and dark-light comparison on (b) Pt-Ce, (d) Pt-Al-Ce.

The observation that Pt nanoparticles on Pt-Al-Ce were more reactive and provides more reaction sites is well aligned with material characterizations and the DRM catalytic performances. Firstly, the synergy effects between Al_2O_3 and CeO_2 significantly promote the reactivity of Pt

nanoparticles on Pt-Al-Ce. Secondly, since methane dissociation in the DRM process takes place on Pt nanoparticles [103], a higher reactivity in Pt nanoparticles suggests a promoted methane dissociation process on Pt-Al-Ce, which leads to an improved H_2 generation rate and a higher H_2/CO ratio in the produced gas.

5.3.7. Photo-thermal-driven DRM reaction mechanism on Pt-Al-Ce

Based on the experimental results and *in situ* DRIFTS analyses, a possible DRM reaction mechanism is proposed. CH_4 dissociation has been widely accepted to take place on Pt reactions sites forming C* and H* intermediates (reactions 1-2), where Pt active sites activate methane and weaken the C-H bonding [64, 173]. Two H* may couple and form H_2 (reaction 3). The reaction mechanism of CO_2 reduction into CO is slightly complicated. CO_2 can react with H* intermediates and form surface formate (reaction 6) [64, 235], which is converted into CO and -OH (reaction 7). The formate intermediates may also react with H* and form CO and H_2O through the RWGS mechanism (reaction 8). CO can also be formed through the direct reduction of CO_2 by oxygen vacancies (V_O) on the catalyst surface (reaction 9). Due to the high oxygen mobility property of CeO_2, C* may be oxidized by CeO_2 lattice oxygen (O_L) and form CO (reaction 10). Bidentate carbonate (b-CO_3^{2-}) was also believed to be active in reacting with C* intermediate and form CO (reaction 11) [236].

The concentrated solar irradiation can additionally promote the DRM performance of Pt-Al-Ce catalyst through the photocatalytic effect. In the photocatalytic process, CeO_2 is excited by photon and generate electrons (e^-) and holes (h^+) (reaction 12). The electrons can reduce the bulk CeO_2 and generate V_O on the catalyst surface (reaction 13), which enhances CO generation. As for methane dissociation, the photoexcited holes can extract H atoms from activated methane

molecules on Pt nanoparticles [237], which facilitates dissociation of CH_x* (reactions 14-15) and leads to promoted H_2 production.

$$CH_4 \rightarrow CH_x^* + (4-x)H^* \quad (1)$$

$$CH \rightarrow C^* + H^* \quad (2)$$

$$2H^* \rightarrow H_2 \quad (3)$$

$$CO_2 + O_L \rightarrow m\text{-}CO_3^{2-} \quad (4)$$

$$m\text{-}CO_3^{2-} \rightarrow b\text{-}CO_3^{2-} \text{ (under excessive } CO_2) \quad (5)$$

$$H^* + CO_2 \rightarrow HCOO^- \quad (6)$$

$$HCOO^- \rightarrow CO + {}^-OH \quad (7)$$

$$H^* + HCOO^- \rightarrow CO + H_2O \quad (8)$$

$$V_O + CO_2 \rightarrow CO + O_L \quad (9)$$

$$C^* + O_L \rightarrow CO + V_O \quad (10)$$

$$b\text{-}CO_3^{2-} + C^* \rightarrow 2CO + O_L \quad (11)$$

$$CeO_2 + h\nu \rightarrow CeO_2 + e^- + h^+ \quad (12)$$

$$Ce^{4+} + e^- \rightarrow Ce^{3+} + V_O \quad (13)$$

$$CH_x^* + h^+ \rightarrow CH_{(1-x)}^* + H^* \quad (14)$$

$$CH^* + h^+ \rightarrow C^* + H^* \quad (15)$$

5.4. Conclusions

In this chapter, Pt decorated Al_2O_3-CeO_2 catalyst was prepared and applied for photo-thermal driven DRM process. Strong synergy effects were observed on the Pt-Al-Ce catalyst. Investigations revealed the bi-functional characteristics of Al_2O_3-CeO_2 binary substrate: Al_2O_3

stimulates CH_4 dissociation while CeO_2 facilitates CO_2 reduction and coke elimination, leading to remarkable DRM catalyzing efficiency. Pt-Al-Ce catalyst shows a near-unity H_2/CO production ratio, which is likely related to the promoted reactivity and concentrated reaction sites of the Pt nanoparticles on the catalyst, as evidenced by the *in situ* DRIFTS analyses. Concentrated solar irradiation was found to facilitate reactant activation and reduce the reaction activation energy through the photocatalytic effect of the CeO_2 components, which leads to promoted DRM catalyzing efficiency.

6. CONCLUSION

6.1. Research summary

Firstly, this work demonstrated the MIL-125 derived porous TiO_2 material as an effective TiO_2 photocatalytic for the applications of CO_2 photoreduction, showing a CO_2 photoreduction performance that is more than 4 times as high compared with commercially available P25 materials. The applied MgO ALD coating on the porous TiO_2 further enhanced the CO generation rate on the catalyst. As a comparison, a conventional wet-impregnation (WI) method was also applied to incorporate MgO on porous TiO_2 and tested for CO_2 photoreduction as control experiments. Samples modified with ALD methods were found to be more advantageous in the photocatalytic CO_2 reduction process over the WI samples due to the higher concentrations of surface Ti^{3+} and Mg-bonded hydroxyl groups, which led to hindered charge recombination and improved surfaced affinity with CO_2 molecules.

Secondly, this work investigated the synergetic effects between Ag nanoparticles and ALD enabled MgO coating in photocatalytic CO_2 reduction with MgO-Ag co-modified porous TiO_2 photocatalysts. The MgO-Ag co-modification on TiO_2 was found to significantly promote CO_2 photoreduction performance. The sequence of MgO/Ag modification and thus the different surface materials structures were found to have a clear impact on the materials property and photocatalytic performance. The catalysts modified firstly by ALD and then deposited with Ag nanoparticles were found to perform better than the catalysts modified with Ag NPs sandwiched between MgO and TiO_2. The organ of the higher performance is likely the result of more uniform distribution of Ag and a larger number of Ag NPs or clusters on the surface.

Thirdly, this work also demonstrated the high performance of a type of Mg^{2+} doped mesoporous TiO_2 prepared by Mg^{2+} adsorption on MOF material MIL-125. The CO_2 photoreduction performance promotion effects of the MgO doping in porous TiO_2 catalyst in the photocatalytic CO_2 reduction process were investigated and discussed. The MgO doping in the porous TiO_2 was found to increase the specific surface area of the porous TiO_2 catalyst. In addition, it was also determined that the MgO dopant promoted the generation of surface Ti^{3+} on the photocatalyst, which enhanced the separation of photoexcited electrons and holes and resulted in considerable increase in photocurrent density. The combination of favorable mesoporous structure and surface chemistry leading to effective photocatalytic CO_2 reduction efficiency.

Lastly, this study also demonstrated a simple and facile way to promote the PTC-DRM efficiency and H_2 selectivity on Pt/CeO_2-based catalysts. The combination of Al_2O_3 and CeO_2 as the binary metal oxide substrate in the Pt-Al-Ce material led to favorable synergetic effects in promoting the PTC-DRM catalytic performance. Surface active intermediates were also identified by *in* situ DRIFTS analyses for reaction mechanism investigations. In addition, concentrated solar irradiation was found to facilitate reactant activation and reduce the reaction activation energy through the photocatalytic effect of the CeO_2 components, which leads to promoted DRM catalyzing efficiency.

6.2. Future directions

After decades of research, many breakthroughs have been made in the development of high performance photocatalysts for both photocatalytic CO_2 reduction and PTC-DRM processes, while there are still plenty of research opportunities exist in these research areas.

Firstly, the light utilization rate of the photoactive catalyst is still low, the development of visible-light-responsive or even near-infrared-light-responsive catalysts can be a promising research direction for both photocatalytic CO_2 reduction and PTC-DRM research. The development of narrow bandgap catalyst can be a key in boosting the activity of photocatalysts and reducing energy input for the greenhouse gas conversion processes. Secondly, many highly effective catalysts take advantage of the stability and high reactivity of noble metals, which is not economically-friendly. In this sense, the development and design of noble-metal-free photocatalytic material is of specific interest. Thirdly, despite the fast advancements in the design and preparation of high-performance catalysts, the reaction mechanism of the CO_2 photoreduction process and the PTC-DRM process is still not fully understood. Research that combines both experimental and computational investigations can be a promising way to unravel the reaction mechanisms.

REFERENCES

[1] S. A. Montzka, E. J. Dlugokencky, J. H. Butler, Non-CO_2 greenhouse gases and climate change, *Nature*, 476 (2011) 43-50.

[2] J. Srinivasan, Climate change, greenhouse gases and aerosols, *Resonance*, 13 (2008) 1146-1155.

[3] United States Environmental Protection Agency, Overview of greenhouse gases, 2021.

[4] P. K. Thornton, P. J. Ericksen, M. Herrero, A. J. Challinor, Climate variability and vulnerability to climate change: a review, *Global Change Biology*, 20 (2014) 3313-3328.

[5] F. Yuan, Y. Wang, D. M. Ricciuto, X. Shi, F. Yuan, P. J. Hanson, S. Bridgham, J. Keller, P. E. Thornton, X. Xu, An integrative model for soil biogeochemistry and methane processes. II: Warming and elevated CO_2 effects on peatland CH_4 emissions, *Journal of Geophysical Research: Biogeosciences*, 126 (2021) e2020JG005963.

[6] H.-B. Duan, Y. Fan, L. Zhu, What's the most cost-effective policy of CO_2 targeted reduction: An application of aggregated economic technological model with CCS? *Applied Energy*, 112 (2013) 866-875.

[7] J. Gibbins, H. Chalmers, Carbon capture and storage, *Energy Policy*, 36 (2008) 4317-4322.

[8] M. C. Gerstenberger, A. Christophersen, R. Buxton, G. Allinson, W. Hou, G. Leamon, Nicol, Integrated risk assessment for CCS, *Energy Procedia*, 37 (2013) 2775-2782.

[9] H. Zhao, F. Pan, Y. Li, A review on the effects of TiO_2 surface point defects on CO_2 photoreduction with H_2O, *Journal of Materiomics*, 3 (2017) 17-32.

[10] Q. Lu, F. Jiao, Electrochemical CO_2 reduction: Electrocatalyst, reaction mechanism, and process engineering, *Nano Energy*, 29 (2016) 439-456.

[11] F. Pan, B. Li, E. Sarnello, S. Hwang, Y. Gang, X. Feng, X. Xiang, N. M. Adli, T. Li, D. Su, G. Wu, G. Wang, Y. Li, Boosting CO_2 reduction on Fe-N-C with sulfur incorporation: Synergistic electronic and structural engineering, *Nano Energy*, 68 (2020) 104384.

[12] F. Pan, H. Zhao, W. Deng, X. Feng, Y. Li, A novel N,Fe-decorated carbon nanotube/carbon nanosheet architecture for efficient CO_2 reduction, *Electrochimica Acta*, 273 (2018) 154-161.

[13] X. Feng, F. Pan, P. Zhang, X. Wang, H.-C. Zhou, Y. Huang, Y. Li, Metal-organic framework MIL-125 derived Mg^{2+}-doped mesoporous TiO_2 for photocatalytic CO_2 reduction, *ChemPhotoChem*, 5 (2021) 79-89.

[14] X. Feng, F. Pan, B. Z. Tran, Y. Li, Photocatalytic CO_2 reduction on porous TiO_2 synergistically promoted by atomic layer deposited MgO overcoating and photodeposited silver nanoparticles, *Catalysis Today*, 339 (2020) 328-336.

[15] X. Feng, F. Pan, H. Zhao, W. Deng, P. Zhang, H.-C. Zhou, Y. Li, Atomic layer deposition enabled MgO surface coating on porous TiO_2 for improved CO_2 photoreduction, *Applied Catalysis B: Environmental*, 238 (2018) 274-283.

[16] C.-S. Chen, J.-H. Lin, J.-H. Wu, C.-Y. Chiang, Growth of carbon nanofibers synthesized from CO_2 hydrogenation on a K/Ni/Al_2O_3 catalyst, *Catalysis Communications*, 11 (2009) 220-224.

[17] W.-H. Wang, Y. Himeda, J. T. Muckerman, G. F. Manbeck, E. Fujita, CO_2 hydrogenation to formate and methanol as an alternative to photo- and electrochemical CO_2 reduction, *Chemical Reviews*, 115 (2015) 12936-12973.

[18] S. N. Habisreutinger, L. Schmidt-Mende, J. K. Stolarczyk, Photocatalytic reduction of CO_2 on TiO_2 and other semiconductors, *Angewandte Chemie International Edition*, 52 (2013) 7372-7408.

[19] K. Li, X. An, K. H. Park, M. Khraisheh, J. Tang, A critical review of CO_2 photoconversion: Catalysts and reactors, *Catalysis Today*, 224 (2014) 3-12.

[20] L. Yuan, Y.-J. Xu, Photocatalytic conversion of CO_2 into value-added and renewable fuels, *Applied Surface Science*, 342 (2015) 154-167.

[21] S. G. Kumar, L. G. Devi, Review on modified TiO_2 photocatalysis under UV/Visible light: selected results and related mechanisms on interfacial charge carrier transfer dynamics, *The Journal of Physical Chemistry A*, 115 (2011) 13211-13241.

[22] X. Li, J. Yu, M. Jaroniec, X. Chen, Cocatalysts for Selective Photoreduction of CO_2 into Solar Fuels, *Chemical Reviews*, 119 (2019) 3962-4179.

[23] S. Kwon, P. Liao, P. C. Stair, R. Q. Snurr, Alkaline-earth metal-oxide overlayers on TiO_2: application toward CO_2 photoreduction, *Catalysis Science & Technology*, 6 (2016) 7885-7895.

[24] L. Liu, C. Zhao, D. Pitts, H. Zhao, Y. Li, CO_2 photoreduction with H_2O vapor by porous MgO-TiO_2 microspheres: Effects of surface MgO dispersion and CO_2 adsorption-desorption dynamics, *Catalysis Science & Technology*, 4 (2014) 1539-1546.

[25] L. Liu, Y. Jiang, H. Zhao, J. Chen, J. Cheng, K. Yang, Y. Li, Engineering coexposed {001} and {101} facets in oxygen-deficient TiO_2 nanocrystals for enhanced CO_2 photoreduction under visible light, *ACS Catalysis*, 6 (2016) 1097-1108.

[26] W.-N. Wang, W.-J. An, B. Ramalingam, S. Mukherjee, D. M. Niedzwiedzki, S. Gangopadhyay, P. Biswas, Size and structure matter: Enhanced CO_2 photoreduction efficiency by size-resolved ultrafine Pt nanoparticles on TiO_2 single crystals, *Journal of the American Chemical Society*, 134 (2012) 11276-11281.

[27] L. Liu, C. Zhao, J. T. Miller, Y. Li, Mechanistic study of CO_2 photoreduction with H_2O on Cu/TiO_2 nanocomposites by *in situ* X-ray absorption and infrared spectroscopies, *The Journal of Physical Chemistry C*, 121 (2017) 490-499.

[28] L. Liu, C. Zhao, J. Xu, Y. Li, Integrated CO_2 capture and photocatalytic conversion by a hybrid adsorbent/photocatalyst material, *Applied Catalysis B: Environmental*, 179 (2015) 489-499.

[29] L. Zhang, W. Wang, D. Jiang, E. Gao, S. Sun, Photoreduction of CO_2 on BiOCl nanoplates with the assistance of photoinduced oxygen vacancies, *Nano Research*, 8 (2015) 821-831.

[30] C.-C. Lo, C.-H. Hung, C.-S. Yuan, J.-F. Wu, Photoreduction of carbon dioxide with H_2 and H_2O over TiO_2 and ZrO_2 in a circulated photocatalytic reactor, *Solar Energy Materials and Solar Cells*, 91 (2007) 1765-1774.

[31] A. Crake, K. C. Christoforidis, A. Kafizas, S. Zafeiratos, C. Petit, CO_2 capture and photocatalytic reduction using bifunctional TiO_2/MOF nanocomposites under UV–vis irradiation, *Applied Catalysis B: Environmental*, 210 (2017) 131-140.

[32] M. Wang, D. Wang, Z. Li, Self-assembly of CPO-27-Mg/TiO_2 nanocomposite with enhanced performance for photocatalytic CO_2 reduction, *Applied Catalysis B: Environmental*, 183 (2016) 47-52.

[33] X. Xiang, F. Pan, Y. Li, A review on adsorption-enhanced photoreduction of carbon dioxide by nanocomposite materials, *Advanced Composites and Hybrid Materials*, 1 (2018) 6-31.

[34] H. Zhao, J. Chen, G. Rao, W. Deng, Y. Li, Enhancing photocatalytic CO_2 reduction by coating an ultrathin Al_2O_3 layer on oxygen deficient TiO_2 nanorods through atomic layer deposition, *Applied Surface Science*, 404 (2017) 49-56.

[35] O. Ola, M. M. Maroto-Valer, Review of material design and reactor engineering on TiO_2 photocatalysis for CO_2 reduction, *Journal of Photochemistry and Photobiology C: Photochemistry Reviews*, 24 (2015) 16-42.

[36] F. Wang, Y. Zhou, P. Li, L. Kuai, Z. Zou, Synthesis of bionic-macro/microporous MgO-modified TiO_2 for enhanced CO_2 photoreduction into hydrocarbon fuels, *Chinese Journal of Catalysis*, 37 (2016) 863-868.

[37] E. Pipelzadeh, V. Rudolph, G. Hanson, C. Noble, L. Wang, Photoreduction of CO_2 on ZIF-8/TiO_2 nanocomposites in a gaseous photoreactor under pressure swing, *Applied Catalysis B: Environmental*, 218 (2017) 672-678.

[38] M. Manzanares, C. Fàbrega, J. Oriol Ossó, L. F. Vega, T. Andreu, J. R. Morante, Engineering the TiO_2 outermost layers using magnesium for carbon dioxide photoreduction, *Applied Catalysis B: Environmental*, 150–151 (2014) 57-62.

[39] L. Liu, Y. Li, Understanding the reaction mechanism of photocatalytic reduction of CO_2 with H_2O on TiO_2-based photocatalysts: A review, *Aerosol and Air Quality Research*, 14 (2014) 453-469.

[40] D. Liu, Y. Fernández, O. Ola, S. Mackintosh, M. Maroto-Valer, C. M. A. Parlett, A. F. Lee, J. C. S. Wu, On the impact of Cu dispersion on CO_2 photoreduction over Cu/TiO_2, *Catalysis Communications*, 25 (2012) 78-82.

[41] F. Song, Y. Zhao, Q. Zhong, Adsorption of carbon dioxide on amine-modified TiO_2 nanotubes, *Journal of Environmental Sciences*, 25 (2013) 554-560.

[42] F. Song, Y. Zhao, Y. Cao, J. Ding, Y. Bu, Q. Zhong, Capture of carbon dioxide from flue gases by amine-functionalized TiO_2 nanotubes, *Applied Surface Science*, 268 (2013) 124-128.

[43] Y. Liao, S.-W. Cao, Y. Yuan, Q. Gu, Z. Zhang, C. Xue, Efficient CO_2 capture and photoreduction by amine-functionalized TiO_2, *Chemistry – A European Journal*, 20 (2014) 10220-10222.

[44] H. Li, X. Wu, J. Wang, Y. Gao, L. Li, K. Shih, Enhanced activity of $AgMgOTiO_2$ catalyst for photocatalytic conversion of CO_2 and H_2O into CH_4, *International Journal of Hydrogen Energy*, 41 (2016) 8479-8488.

[45] Q. Li, L. Zong, C. Li, J. Yang, Photocatalytic reduction of CO_2 on MgO/TiO_2 nanotube films, *Applied Surface Science*, 314 (2014) 458-463.

[46] S. Xie, Y. Wang, Q. Zhang, W. Deng, Y. Wang, MgO- and Pt-promoted TiO_2 as an efficient photocatalyst for the preferential reduction of carbon dioxide in the presence of water, *ACS Catalysis*, 4 (2014) 3644-3653.

[47] L. Liu, C. Zhao, H. Zhao, D. Pitts, Y. Li, Porous microspheres of MgO-patched TiO_2 for CO_2 photoreduction with H_2O vapor: Temperature-dependent activity and stability, *Chemical Communications*, 49 (2013) 3664-3666.

[48] R. Daghrir, P. Drogui, D. Robert, Modified TiO_2 for environmental photocatalytic applications: A review, *Industrial & Engineering Chemistry Research*, 52 (2013) 3581-3599.

[49] L. Gomathi Devi, R. Kavitha, A review on plasmonic metal-TiO_2 composite for generation, trapping, storing and dynamic vectorial transfer of photogenerated electrons across the Schottky junction in a photocatalytic system, *Applied Surface Science*, 360 (2016) 601-622.

[50] H. Zhao, X. Zheng, X. Feng, Y. Li, CO_2 reduction by plasmonic Au nanoparticle-decorated TiO_2 photocatalyst with an ultrathin Al_2O_3 interlayer, *The Journal of Physical Chemistry C*, 122 (2018) 18949−18956.

[51] M. Tasbihi, F. Fresno, U. Simon, I. J. Villar-García, V. Pérez-Dieste, C. Escudero, V. A. de la Peña O'Shea, On the selectivity of CO_2 photoreduction towards CH_4 using Pt/TiO_2 catalysts supported on mesoporous silica, *Applied Catalysis B: Environmental*, 239 (2018) 68-76.

[52] Q.-Y. Li, L.-L. Zong, C. Li, Y.-H. Cao, X.-D. Wang, J.-J. Yang, Photocatalytic reduction of CO_2 to methane on Pt/TiO_2 nanosheet porous film, *Advances in Condensed Matter Physics*, 2014 (2014) 6.

[53] K. L. Miller, C. W. Lee, J. L. Falconer, J. W. Medlin, Effect of water on formic acid photocatalytic decomposition on TiO_2 and Pt/TiO_2, *Journal of Catalysis*, 275 (2010) 294-299.

[54] J. Jana, M. Ganguly, T. Pal, Enlightening surface plasmon resonance effect of metal nanoparticles for practical spectroscopic application, *RSC Advances*, 6 (2016) 86174-86211.

[55] J. Low, B. Cheng, J. Yu, Surface modification and enhanced photocatalytic CO_2 reduction performance of TiO_2: A review, *Applied Surface Science*, 392 (2017) 658-686.

[56] T. Billo, F.-Y. Fu, P. Raghunath, I. Shown, W.-F. Chen, H.-T. Lien, T.-H. Shen, J.-F. Lee, T.-S. Chan, K.-Y. Huang, C.-I. Wu, M. C. Lin, J.-S. Hwang, C.-H. Lee, L.-C. Chen, K.-H. Chen, Ni-nanocluster modified black TiO_2 with dual active sites for selective photocatalytic CO_2 reduction, *Small*, 14 (2018) 1702928.

[57] T. Wang, X. Meng, G. Liu, K. Chang, P. Li, Q. Kang, L. Liu, M. Li, S. Ouyang, J. Ye, *In situ* synthesis of ordered mesoporous Co-doped TiO_2 and its enhanced photocatalytic activity and selectivity for the reduction of CO_2, *Journal of Materials Chemistry A*, 3 (2015) 9491-9501.

[58] K. Bhattacharyya, G. P. Mane, V. Rane, A. K. Tripathi, A. K. Tyagi, Selective CO_2 photoreduction with Cu-doped TiO_2 photocatalyst: Delineating the crucial role of Cu-oxidation state and oxygen vacancies, *The Journal of Physical Chemistry C*, 125 (2021) 1793-1810.

[59] C. Di Valentin, G. Pacchioni, Trends in non-metal doping of anatase TiO_2: B, C, N and F, *Catalysis Today*, 206 (2013) 12-18.

[60] W. Qian, P. A. Greaney, S. Fowler, S.-K. Chiu, A. M. Goforth, J. Jiao, Low-temperature nitrogen doping in ammonia solution for production of N-doped TiO_2-hybridized graphene as a highly efficient photocatalyst for water treatment, *ACS Sustainable Chemistry & Engineering*, 2 (2014) 1802-1810.

[61] J. Choi, H. Park, M. R. Hoffmann, Effects of single metal-ion doping on the visible-light photoreactivity of TiO_2, *The Journal of Physical Chemistry C*, 114 (2009) 783-792.

[62] A. Khlyustova, N. Sirotkin, T. Kusova, A. Kraev, V. Titov, A. Agafonov, Doped TiO_2: The effect of doping elements on photocatalytic activity, *Materials Advances*, 1 (2020) 1193-1201.

[63] D. Wu, J. Guo, H. Wang, X. Zhang, Y. Yang, C. Yang, Z. Gao, Z. Wang, K. Jiang, Green synthesis of boron and nitrogen co-doped TiO_2 with rich B-N motifs as Lewis acid-base couples for the effective artificial CO_2 photoreduction under simulated sunlight, *Journal of Colloid and Interface Science*, 585 (2021) 95-107.

[64] J. Niu, X. Du, J. Ran, R. Wang, Dry (CO_2) reforming of methane over Pt catalysts studied by DFT and kinetic modeling, *Applied Surface Science*, 376 (2016) 79-90.

[65] A. Iulianelli, S. Liguori, J. Wilcox, A. Basile, Advances on methane steam reforming to produce hydrogen through membrane reactors technology: A review, *Catalysis Reviews*, 58 (2016) 1-35.

[66] A. Abdulrasheed, A. A. Jalil, Y. Gambo, M. Ibrahim, H. U. Hambali, M. Y. Shahul Hamid, A review on catalyst development for dry reforming of methane to syngas: Recent advances, *Renewable and Sustainable Energy Reviews*, 108 (2019) 175-193.

[67] M. A. Llosa Tanco, J. A. Medrano, F. Gallucci, D. A. Pacheco Tanaka, Chapter 17 - Membrane optimization and process condition investigation for enhancing the CO_2 separation from natural gas, in: A. Basile, E. P. Favvas (Eds.) Current Trends and Future Developments on (Bio-) Membranes, Elsevier, 2018, pp. 469-509.

[68] U. Izquierdo, V. L. Barrio, J. Requies, J. F. Cambra, M. B. Güemez, P. L. Arias, Tri-reforming: A new biogas process for synthesis gas and hydrogen production, *International Journal of Hydrogen Energy*, 38 (2013) 7623-7631.

[69] S. Li, Z. Zong, S. J. Zhou, Y. Huang, Z. Song, X. Feng, R. Zhou, H. S. Meyer, M. Yu, M. A. Carreon, SAPO-34 membranes for N_2/CH_4 separation: Preparation, characterization, separation performance and economic evaluation, *Journal of Membrane Science*, 487 (2015) 141-151.

[70] Z. Zong, X. Feng, Y. Huang, Z. Song, R. Zhou, S. J. Zhou, M. A. Carreon, M. Yu, S. Li, Highly permeable N_2/CH_4 separation SAPO-34 membranes synthesized by diluted gels and increased crystallization temperature, *Microporous and Mesoporous Materials*, 224 (2016) 36-42.

[71] M. Usman, W. M. A. Wan Daud, H. F. Abbas, Dry reforming of methane: Influence of process parameters—A review, *Renewable and Sustainable Energy Reviews*, 45 (2015) 710-744.

[72] S. Dasappa, H. V. Sridhar, G. Sridhar, P. J. Paul, H. S. Mukunda, Biomass gasification—a substitute to fossil fuel for heat application, *Biomass and Bioenergy*, 25 (2003) 637-649.

[73] M. Kushida, A. Yamaguchi, Y. Cho, T. Fujita, H. Abe, M. Miyauchi, Gas-phase photoelectrocatalysis mediated by oxygen ions for uphill conversion of greenhouse gases, *ChemPhotoChem*, 5 (2021) 275-281.

[74] A. Z'Graggen, P. Haueter, D. Trommer, M. Romero, J. C. de Jesus, A. Steinfeld, Hydrogen production by steam-gasification of petroleum coke using concentrated solar power—II. Reactor design, testing, and modeling, *International Journal of Hydrogen Energy*, 31 (2006) 797-811.

[75] P. Charvin, A. Stéphane, L. Florent, F. Gilles, Analysis of solar chemical processes for hydrogen production from water splitting thermochemical cycles, *Energy Conversion and Management*, 49 (2008) 1547-1556.

[76] O. Anjaneyulu, K. Takeda, S. Ishii, S. Ueda, T. Nagao, P. Xiaobo, T. Fujita, M. Miyauchi, H. Abe, Light-promoted conversion of greenhouse gases over plasmonic metal–carbide nanocomposite catalysts, *Materials Chemistry Frontiers*, 2 (2018) 580-584.

[77] M. Li, Z. Sun, Y. H. Hu, Thermo-photo coupled catalytic CO_2 reforming of methane: A review, *Chemical Engineering Journal*, 428 (2022) 131222.

[78] N. A. K. Aramouni, J. G. Touma, B. A. Tarboush, J. Zeaiter, M. N. Ahmad, Catalyst design for dry reforming of methane: Analysis review, *Renewable and Sustainable Energy Reviews*, 82 (2018) 2570-2585.

[79] X. Feng, Z. Du, E. Sarnello, W. Deng, C. R. Petru, L. Fang, T. Li, Y. Li, Syngas production at a near-unity H_2/CO ratio from photo-thermo-chemical dry reforming of methane on a Pt decorated Al_2O_3-CeO_2 catalyst, *Journal of Materials Chemistry A*, (2022), DOI: 10.1039/D1TA10088B.

[80] Z. Li, Q. Lin, M. Li, J. Cao, F. Liu, H. Pan, Z. Wang, S. Kawi, Recent advances in process and catalyst for CO_2 reforming of methane, *Renewable and Sustainable Energy Reviews*, 134 (2020) 110312.

[81] C. He, S. Wu, L. Wang, J. Zhang, Recent advances in photo-enhanced dry reforming of methane: A review, *Journal of Photochemistry and Photobiology C: Photochemistry Reviews*, 51 (2022) 100468.

[82] Y. Kohno, T. tanaka, T. Funabiki, S. Yoshida, Photoreduction of carbon dioxide with methane over ZrO_2, *Chemistry Letters*, 26 (1997) 993-994.

[83] K. Teramura, T. Tanaka, H. Ishikawa, Y. Kohno, T. Funabiki, Photocatalytic reduction of CO_2 to CO in the presence of H_2 or CH_4 as a reductant over MgO, *The Journal of Physical Chemistry B*, 108 (2004) 346-354.

[84] L. Yuliati, H. Itoh, H. Yoshida, Photocatalytic conversion of methane and carbon dioxide over gallium oxide, *Chemical Physics Letters*, 452 (2008) 178-182.

[85] B. Tahir, M. Tahir, N. A. S. Amin, Tailoring performance of La-modified TiO_2 nanocatalyst for continuous photocatalytic CO_2 reforming of CH_4 to fuels in the presence of H_2O, *Energy Conversion and Management*, 159 (2018) 284-298.

[86] M. Chen, J. Wu, C. Lu, X. Luo, Y. Huang, B. Jin, H. Gao, X. Zhang, M. Argyle, Z. Liang, Photoreduction of CO_2 in the presence of CH_4 over g-C_3N_4 modified with TiO_2 nanoparticles at room temperature, *Green Energy & Environment*, 6 (2021) 938-951.

[87] B. Han, W. Wei, L. Chang, P. Cheng, Y. H. Hu, Efficient visible light photocatalytic CO_2 reforming of CH_4, *ACS Catalysis*, 6 (2016) 494-497.

[88] M. Mao, Q. Zhang, Y. Yang, Y. Li, H. Huang, Z. Jiang, Q. Hu, X. Zhao, Solar-light-driven CO_2 reduction by methane on Pt nanocrystals partially embedded in mesoporous CeO_2 nanorods with high light-to-fuel efficiency, *Green Chemistry*, 20 (2018) 2857-2869.

[89] K. Zhou, Z. Yang, S. Yang, Highly reducible CeO_2 nanotubes, *Chemistry of Materials*, 19 (2007) 1215-1217.

[90] P. Li, X. Chen, Y. Li, J. W. Schwank, A review on oxygen storage capacity of CeO_2-based materials: Influence factors, measurement techniques, and applications in reactions related to catalytic automotive emissions control, *Catalysis Today*, 327 (2019) 90-115.

[91] F. Pan, X. Xiang, W. Deng, H. Zhao, X. Feng, Y. Li, A novel photo-thermochemical approach for enhanced carbon dioxide reforming of methane, *ChemCatChem*, 10 (2018) 940-945.

[92] L. Zhou, J. M. P. Martirez, J. Finzel, C. Zhang, D. F. Swearer, S. Tian, H. Robatjazi, M. Lou, L. Dong, L. Henderson, P. Christopher, E. A. Carter, P. Nordlander, N. J. Halas, Light-driven methane dry reforming with single atomic site antenna-reactor plasmonic photocatalysts, *Nature Energy*, 5 (2020) 61-70.

[93] D. Takami, Y. Ito, S. Kawaharasaki, A. Yamamoto, H. Yoshida, Low temperature dry reforming of methane over plasmonic Ni photocatalysts under visible light irradiation, *Sustainable Energy & Fuels*, 3 (2019) 2968-2971.

[94] Z. Rao, Y. Cao, Z. Huang, Z. Yin, W. Wan, M. Ma, Y. Wu, J. Wang, G. Yang, Y. Cui, Z. Gong, Y. Zhou, Insights into the nonthermal effects of light in dry reforming of methane to enhance the H_2/CO ratio near unity over Ni/Ga_2O_3, *ACS Catalysis*, 11 (2021) 4730-4738.

[95] C. Wang, Y. Su, A. Tavasoli, W. Sun, L. Wang, G. A. Ozin, D. Yang, Recent advances in nanostructured catalysts for photo-assisted dry reforming of methane, *Materials Today Nano*, 14 (2021) 100113.

[96] S. Luo, X. Ren, H. Lin, H. Song, J. Ye, Plasmonic photothermal catalysis for solar-to-fuel conversion: Current status and prospects, *Chemical Science*, 12 (2021) 5701-5719.

[97] H. Liu, H. Song, X. Meng, L. Yang, J. Ye, Light irradiation enhanced CO_2 reduction with methane: A case study in size-dependent optical property of Ni nanoparticles, *Catalysis Today*, 335 (2019) 187-192.

[98] H. Liu, X. Meng, T. D. Dao, H. Zhang, P. Li, K. Chang, T. Wang, M. Li, T. Nagao, J. Ye, Conversion of carbon dioxide by methane reforming under visible-light irradiation: Surface-plasmon-mediated nonpolar molecule activation, *Angewandte Chemie International Edition*, 54 (2015) 11545-11549.

[99] S. Shoji, X. Peng, A. Yamaguchi, R. Watanabe, C. Fukuhara, Y. Cho, T. Yamamoto, S. Matsumura, M.-W. Yu, S. Ishii, T. Fujita, H. Abe, M. Miyauchi, Photocatalytic uphill conversion of natural gas beyond the limitation of thermal reaction systems, *Nature Catalysis*, 3 (2020) 148-153.

[100] Y. Cho, A. Yamaguchi, M. Miyauchi, Photocatalytic methane reforming: Recent advances, *Catalysts*, 11 (2021) 18.

[101] R. Benrabaa, A. Löfberg, J. Guerrero Caballero, E. Bordes-Richard, A. Rubbens, R.-N. Vannier, H. Boukhlouf, A. Barama, Sol–gel synthesis and characterization of silica supported nickel ferrite catalysts for dry reforming of methane, *Catalysis Communications*, 58 (2015) 127-131.

[102] H. Liu, X. Meng, T. D. Dao, L. Liu, P. Li, G. Zhao, T. Nagao, L. Yang, J. Ye, Light assisted CO_2 reduction with methane over SiO_2 encapsulated Ni nanocatalysts for boosted activity and stability, *Journal of Materials Chemistry A*, 5 (2017) 10567-10573.

[103] Z. Du, F. Pan, E. Sarnello, X. Feng, Y. Gang, T. Li, Y. Li, Probing the origin of photocatalytic effects in photothermochemical dry reforming of methane on a Pt/CeO_2 catalyst, *The Journal of Physical Chemistry C*, 125 (2021) 18684-18692.

[104] H. Huang, M. Mao, Q. Zhang, Y. Li, J. Bai, Y. Yang, M. Zeng, X. Zhao, Solar-light-driven CO_2 reduction by CH_4 on silica-cluster-modified Ni nanocrystals with a high solar-to-fuel efficiency and excellent durability, *Advanced Energy Materials*, 8 (2018) 1702472.

[105] A. Nikokavoura, C. Trapalis, Alternative photocatalysts to TiO_2 for the photocatalytic reduction of CO_2, *Applied Surface Science*, 391 (2017) 149-174.

[106] H. Li, M. Eddaoudi, M. O'Keeffe, O. M. Yaghi, Design and synthesis of an exceptionally stable and highly porous metal-organic framework, *Nature*, 402 (1999) 276-279.

[107] X. Xu, R. Cao, S. Jeong, J. Cho, Spindle-like mesoporous α-Fe_2O_3 anode material prepared from MOF template for high-rate lithium batteries, *Nano Letters*, 12 (2012) 4988-4991.

[108] Z. Xie, C. Jiang, W. Xu, X. Cui, C. de los Reyes, A. A. Martí, Y. Wang, Facile self-assembly route to Co_3O_4 nanoparticles confined into single-walled carbon nanotube matrix for highly reversible lithium storage, *Electrochimica Acta*, 235 (2017) 613-622.

[109] Z. Wang, X. Li, H. Xu, Y. Yang, Y. Cui, H. Pan, Z. Wang, B. Chen, G. Qian, Porous anatase TiO_2 constructed from a metal-organic framework for advanced lithium-ion battery anodes, *Journal of Materials Chemistry A*, 2 (2014) 12571-12575.

[110] W.-W. Zhan, Q.-L. Zhu, S. Dang, Z. Liu, M. Kitta, K. Suenaga, L.-S. Zheng, Q. Xu, Synthesis of highly active sub-nanometer Pt@Rh core–shell nanocatalyst via a photochemical route: Porous titania nanoplates as a superior photoactive support, *Small*, (2017) 1603879-1603879.

[111] J. Dou, Y. Li, F. Xie, X. Ding, M. Wei, Metal–organic framework derived hierarchical porous anatase TiO_2 as a photoanode for dye-sensitized solar cell, *Crystal Growth & Design*, 16 (2016) 121-125.

[112] Z. Xiu, M. H. Alfaruqi, J. Gim, J. Song, S. Kim, P. T. Duong, J. P. Baboo, V. Mathew, J. Kim, MOF-derived mesoporous anatase TiO_2 as anode material for lithium–ion batteries with high rate capability and long cycle stability, *Journal of Alloys and Compounds*, 674 (2016) 174-178.

[113] Z. Xiu, M. H. Alfaruqi, J. Gim, J. Song, S. Kim, T. V. Thi, P. T. Duong, J. P. Baboo, V. Mathew, J. Kim, Hierarchical porous anatase TiO_2 derived from a titanium metal-organic framework as a superior anode material for lithium ion batteries, *Chemical Communications*, 51 (2015) 12274-12277.

[114] C. Li, Z. Li, Q. Li, Z. Zhang, S. Dong, L. Yin, MOFs derived hierarchically porous TiO_2 as effective chemical and physical immobilizer for sulfur species as cathodes for high-performance lithium-sulfur batteries, *Electrochimica Acta*, 215 (2016) 689-698.

[115] Z. Xiong, Z. Lei, C.-C. Kuang, X. Chen, B. Gong, Y. Zhao, J. Zhang, C. Zheng, J. C. S. Wu, Selective photocatalytic reduction of CO_2 into CH_4 over Pt-Cu_2O TiO_2 nanocrystals: The interaction between Pt and Cu_2O cocatalysts, *Applied Catalysis B: Environmental*, 202 (2017) 695-703.

[116] G. Rao, H. Zhao, J. Chen, W. Deng, B. Jung, A. Abdel-Wahab, B. Batchelor, Y. Li, FeOOH and Fe_2O_3 co-grafted TiO_2 photocatalysts for bisphenol A degradation in water, *Catalysis Communications*, 97 (2017) 125-129.

[117] C. G. Morales-Guio, M. T. Mayer, A. Yella, S. D. Tilley, M. Grätzel, X. Hu, An optically transparent iron nickel oxide catalyst for solar water splitting, *Journal of the American Chemical Society*, 137 (2015) 9927-9936.

[118] H. Irie, K. Kamiya, T. Shibanuma, S. Miura, D. A. Tryk, T. Yokoyama, K. Hashimoto, Visible light-sensitive Cu(II)-grafted TiO_2 photocatalysts: Activities and X-ray absorption fine structure analyses, *The Journal of Physical Chemistry C*, 113 (2009) 10761-10766.

[119] F. Xu, J. Zhang, B. Zhu, J. Yu, J. Xu, $CuInS_2$ sensitized TiO_2 hybrid nanofibers for improved photocatalytic CO_2 reduction, *Applied Catalysis B: Environmental*, 230 (2018) 194-202.

[120] S. Bai, W. Yin, L. Wang, Z. Li, Y. Xiong, Surface and interface design in cocatalysts for photocatalytic water splitting and CO_2 reduction, *RSC Advances*, 6 (2016) 57446-57463.

[121] H. Rietveld, A profile refinement method for nuclear and magnetic structures, *Journal of applied Crystallography*, 2 (1969) 65-71.

[122] R. Jin, W. Gao, J. Chen, H. Zeng, F. Zhang, Z. Liu, N. Guan, Photocatalytic reduction of nitrate ion in drinking water by using metal-loaded $MgTiO_3$-TiO_2 composite semiconductor catalyst, *Journal of Photochemistry and Photobiology A: Chemistry*, 162 (2004) 585-590.

[123] Z. ALOthman, A review: Fundamental aspects of silicate mesoporous materials, *Materials*, 5 (2012) 2874.

[124] H. Yu, S. Yan, P. Zhou, Z. Zou, CO_2 photoreduction on hydroxyl-group-rich mesoporous single crystal TiO_2, *Applied Surface Science*, 427 (2018) 603-607.

[125] F. El-Gohary, A. Tawfik, U. Mahmoud, Comparative study between chemical coagulation/precipitation (C/P) versus coagulation/dissolved air flotation (C/DAF) for pre-treatment of personal care products (PCPs) wastewater, *Desalination*, 252 (2010) 106-112.

[126] B. Erdem, R. A. Hunsicker, G. W. Simmons, E. D. Sudol, V. L. Dimonie, M. S. El-Aasser, XPS and FTIR surface characterization of TiO_2 particles used in polymer encapsulation, *Langmuir*, 17 (2001) 2664-2669.

[127] B. Ohtani, O. O. Prieto-Mahaney, D. Li, R. Abe, What is Degussa (Evonik) P25? Crystalline composition analysis, reconstruction from isolated pure particles and photocatalytic activity test, *Journal of Photochemistry and Photobiology A: Chemistry*, 216 (2010) 179-182.

[128] M. Yan, F. Chen, J. Zhang, M. Anpo, Preparation of controllable crystalline titania and study on the photocatalytic properties, *The Journal of Physical Chemistry B*, 109 (2005) 8673-8678.

[129] S. Bakardjieva, J. Šubrt, V. Štengl, M. J. Dianez, M. J. Sayagues, Photoactivity of anatase–rutile TiO_2 nanocrystalline mixtures obtained by heat treatment of homogeneously precipitated anatase, *Applied Catalysis B: Environmental*, 58 (2005) 193-202.

[130] T. Ohno, K. Tokieda, S. Higashida, M. Matsumura, Synergism between rutile and anatase TiO_2 particles in photocatalytic oxidation of naphthalene, *Applied Catalysis A: General*, 244 (2003) 383-391.

[131] H. Onishi, T. Aruga, C. Egawa, Y. Iwasawa, Adsorption of CH_3OH, HCOOH and SO_2 on TiO_2(110) and stepped TiO_2(441) surfaces, *Surface Science*, 193 (1988) 33-46.

[132] X. Xin, T. Xu, J. Yin, L. Wang, C. Wang, Management on the location and concentration of Ti^{3+} in anatase TiO_2 for defects-induced visible-light photocatalysis, *Applied Catalysis B: Environmental*, 176-177 (2015) 354-362.

[133] E. Karamian, S. Sharifnia, On the general mechanism of photocatalytic reduction of CO_2, *Journal of CO_2 Utilization*, 16 (2016) 194-203.

[134] S. S. Tan, L. Zou, E. Hu, Kinetic modelling for photosynthesis of hydrogen and methane through catalytic reduction of carbon dioxide with water vapour, *Catalysis Today*, 131 (2008) 125-129.

[135] Kamila Kočí, Lucie Obalová, O. Šolcová, Kinetic study of photocatalytic reduction of CO_2 over TiO_2, *Chemical and Process Engineering* 31 (2010) 395-407.

[136] L. Liu, C. Zhao, Y. Li, Spontaneous Dissociation of CO_2 to CO on defective surface of Cu(I)/TiO_{2-x} nanoparticles at room temperature, *The Journal of Physical Chemistry C*, 116 (2012) 7904-7912.

[137] L. Gomathi Devi, K. Mohan Reddy, Photocatalytic performance of silver TiO_2: Role of electronic energy levels, *Applied Surface Science*, 257 (2011) 6821-6828.

[138] D. Sarkar, C. K. Ghosh, S. Mukherjee, K. K. Chattopadhyay, Three dimensional Ag_2O/TiO_2 type-II (p–n) nanoheterojunctions for superior photocatalytic activity, *ACS Applied Materials & Interfaces*, 5 (2013) 331-337.

[139] J. Ahmad, K. Majid, *In-situ* synthesis of visible-light responsive Ag_2O/graphene oxide nanocomposites and effect of graphene oxide content on its photocatalytic activity, *Advanced Composites and Hybrid Materials*, 1 (2018) 374-388.

[140] L. Liu, D. T. Pitts, H. Zhao, C. Zhao, Y. Li, Silver-incorporated bicrystalline (anatase/brookite) TiO_2 microspheres for CO_2 photoreduction with water in the presence of methanol, *Applied Catalysis A: General*, 467 (2013) 474-482.

[141] C. Zhao, A. Krall, H. Zhao, Q. Zhang, Y. Li, Ultrasonic spray pyrolysis synthesis of Ag/TiO_2 nanocomposite photocatalysts for simultaneous H_2 production and CO_2 reduction, *International Journal of Hydrogen Energy*, 37 (2012) 9967-9976.

[142] H. Zhao, W. Deng, Y. Li, Atomic layer deposited TiO_2 ultrathin layer on Ag_ZnO nanorods for stable and efficient photocatalytic degradation of RhB, *Advanced Composites and Hybrid Materials*, 1 (2018) 404-413.

[143] L. Nie, J. Yu, X. Li, B. Cheng, G. Liu, M. Jaroniec, Enhanced performance of NaOH-modified Pt/TiO_2 toward room temperature selective oxidation of formaldehyde, *Environmental Science & Technology*, 47 (2013) 2777-2783.

[144] E. M. Samsudin, S. B. A. Hamid, J. C. Juan, W. J. Basirun, A. E. Kandjani, S. K. Bhargava, Effective role of trifluoroacetic acid (TFA) to enhance the photocatalytic activity of F-doped TiO_2 prepared by modified sol–gel method, *Applied Surface Science*, 365 (2016) 57-68.

[145] S. Na-Phattalung, M. F. Smith, K. Kim, M.-H. Du, S.-H. Wei, S. B. Zhang, S. Limpijumnong, First-principles study of native defects in anatase TiO_2, *Physical Review B*, 73 (2006) 125205.

[146] A. Gannoruwa, B. Ariyasinghe, J. Bandara, The mechanism and material aspects of a novel Ag_2O/TiO_2 photocatalyst active in infrared radiation for water splitting, *Catalysis Science & Technology*, 6 (2016) 479-487.

[147] K. Sutthiumporn, S. Kawi, Promotional effect of alkaline earth over $Ni–La_2O_3$ catalyst for CO_2 reforming of CH_4: Role of surface oxygen species on H_2 production and carbon suppression, *International Journal of Hydrogen Energy*, 36 (2011) 14435-14446.

[148] M. Li, H. Liu, T. Liu, Y. Qin, Design of a novel dual Z-scheme photocatalytic system composited of Ag_2O modified Ti^{3+} self doped TiO_2 nanocrystals with individual exposed (001) and (101) facets, *Materials Characterization*, 124 (2017) 136-144.

[149] C. S. Kumarasinghe, M. Premaratne, Q. Bao, G. P. Agrawal, Theoretical analysis of hot electron dynamics in nanorods, *Scientific Reports*, 5 (2015) 12140.

[150] H. Liang, Y. Bu, F. Pan, J. Zhang, Transformation of Freon to 3D graphene frameworks for high-rate supercapacitors with high capacity retention, *Journal of Power Sources*, 405 (2018) 1-6.

[151] H. Liu, S. Cheng, M. Wu, H. Wu, J. Zhang, W. Li, C. Cao, Photoelectrocatalytic degradation of sulfosalicylic acid and its electrochemical impedance spectroscopy investigation, *The Journal of Physical Chemistry A*, 104 (2000) 7016-7020.

[152] W. H. Leng, Z. Zhang, J. Q. Zhang, C. N. Cao, Investigation of the kinetics of a TiO_2 photoelectrocatalytic reaction involving charge transfer and recombination through surface states by electrochemical impedance spectroscopy, *The Journal of Physical Chemistry B*, 109 (2005) 15008-15023.

[153] A.-W. Xu, Y. Gao, H.-Q. Liu, The preparation, characterization, and their photocatalytic activities of rare-earth-doped TiO_2 nanoparticles, *Journal of Catalysis*, 207 (2002) 151-157.

[154] M. Iwasaki, M. Hara, H. Kawada, H. Tada, S. Ito, Cobalt ion-doped TiO_2 photocatalyst response to visible light, *Journal of Colloid and Interface Science*, 224 (2000) 202-204.

[155] J. Wen, X. Li, W. Liu, Y. Fang, J. Xie, Y. Xu, Photocatalysis fundamentals and surface modification of TiO_2 nanomaterials, *Chinese Journal of Catalysis*, 36 (2015) 2049-2070.

[156] Q. Liu, Photovoltaic performance improvement of dye-sensitized solar cells based on Mg-doped TiO_2 thin films, *Electrochimica Acta*, 129 (2014) 459-462.

[157] M. A. Behnajady, B. Alizade, N. Modirshahla, Synthesis of Mg-doped TiO_2 nanoparticles under different conditions and its photocatalytic activity, *Photochemistry and Photobiology*, 87 (2011) 1308-1314.

[158] G. S. Pozan, A. Kambur, Removal of 4-chlorophenol from wastewater: Preparation, characterization and photocatalytic activity of alkaline earth oxide doped TiO_2, *Applied Catalysis B: Environmental*, 129 (2013) 409-415.

[159] L. Chevallier, A. Bauer, S. Cavaliere, R. Hui, J. Rozière, D. J. Jones, Mesoporous nanostructured Nb-doped titanium dioxide microsphere catalyst supports for PEM fuel cell electrodes, *ACS Applied Materials & Interfaces*, 4 (2012) 1752-1759.

[160] Y. Li, W.-N. Wang, Z. Zhan, M.-H. Woo, C.-Y. Wu, P. Biswas, Photocatalytic reduction of CO_2 with H_2O on mesoporous silica supported Cu/TiO_2 catalysts, *Applied Catalysis B: Environmental*, 100 (2010) 386-392.

[161] D. Chen, W. Shen, S. Wu, C. Chen, X. Luo, L. Guo, Ion exchange induced removal of Pb(II) by MOF-derived magnetic inorganic sorbents, *Nanoscale*, 8 (2016) 7172-7179.

[162] M. J. Valero-Romero, J. G. Santaclara, L. Oar-Arteta, L. van Koppen, D. Y. Osadchii, J. Gascon, F. Kapteijn, Photocatalytic properties of TiO_2 and Fe-doped TiO_2 prepared by metal organic framework-mediated synthesis, *Chemical Engineering Journal*, 360 (2019) 75-88.

[163] L. G. Devi, B. N. Murthy, S. G. Kumar, Photocatalytic activity of TiO_2 doped with Zn^{2+} and V^{5+} transition metal ions: Influence of crystallite size and dopant electronic configuration on photocatalytic activity, *Materials Science and Engineering*: B, 166 (2010) 1-6.

[164] H. Kaur, H. S. Bhatti, K. Singh, Dopant incorporation in ultrasmall quantum dots: A case study on the effect of dopant concentration on lattice and properties of SnO_2 QDs, *Journal of Materials Science: Materials in Electronics*, 30 (2019) 2246-2264.

[165] G. Li, N. M. Dimitrijevic, L. Chen, J. M. Nichols, T. Rajh, K. A. Gray, The important role of tetrahedral Ti^{4+} sites in the phase transformation and photocatalytic activity of TiO_2 nanocomposites, *Journal of the American Chemical Society*, 130 (2008) 5402-5403.

[166] J. Zhang, M. Li, Z. Feng, J. Chen, C. Li, UV raman spectroscopic study on TiO_2. I. Phase transformation at the surface and in the bulk, *The Journal of Physical Chemistry B*, 110 (2006) 927-935.

[167] J.-H. Xu, W.-L. Dai, J. Li, Y. Cao, H. Li, H. He, K. Fan, Simple fabrication of thermally stable apertured N-doped TiO_2 microtubes as a highly efficient photocatalyst under visible light irradiation, *Catalysis Communications*, 9 (2008) 146-152.

[168] C. He, B. Tian, J. Zhang, Thermally stable SiO_2-doped mesoporous anatase TiO_2 with large surface area and excellent photocatalytic activity, *Journal of Colloid and Interface Science*, 344 (2010) 382-389.

[169] P. Periyat, S. C. Pillai, D. E. McCormack, J. Colreavy, S. J. Hinder, Improved high-temperature stability and sun-light-driven photocatalytic activity of sulfur-doped anatase TiO_2, *The Journal of Physical Chemistry C*, 112 (2008) 7644-7652.

[170] P. Viswanathamurthi, N. Bhattarai, C. K. Kim, H. Y. Kim, D. R. Lee, Ruthenium doped TiO_2 fibers by electrospinning, *Inorganic Chemistry Communications*, 7 (2004) 679-682.

[171] Y. Zhang, Z. Xie, Z. Wang, X. Feng, Y. Wang, A. Wu, Unveiling the adsorption mechanism of zeolitic imidazolate framework-8 with high efficiency for removal of copper ions from aqueous solutions, *Dalton Transactions*, 45 (2016) 12653-12660.

[172] J. Schneider, M. Matsuoka, M. Takeuchi, J. Zhang, Y. Horiuchi, M. Anpo, D. W. Bahnemann, Understanding TiO_2 photocatalysis: mechanisms and materials, *Chemical Reviews*, 114 (2014) 9919-9986.

[173] F. Pan, X. Xiang, Z. Du, E. Sarnello, T. Li, Y. Li, Integrating photocatalysis and thermocatalysis to enable efficient CO_2 reforming of methane on Pt supported CeO_2 with Zn doping and atomic layer deposited MgO overcoating, *Applied Catalysis B: Environmental*, 260 (2020) 118189.

[174] R. Ma, S. Zhang, T. Wen, P. Gu, L. Li, G. Zhao, F. Niu, Q. Huang, Z. Tang, X. Wang, A critical review on visible-light-response CeO_2-based photocatalysts with enhanced photooxidation of organic pollutants, *Catalysis Today*, 335 (2019) 20-30.

[175] Y. Wang, J. Zhao, T. Wang, Y. Li, X. Li, J. Yin, C. Wang, CO_2 photoreduction with H_2O vapor on highly dispersed CeO_2/TiO_2 catalysts: Surface species and their reactivity, *Journal of Catalysis*, 337 (2016) 293-302.

[176] D. Pakhare, J. Spivey, A review of dry (CO_2) reforming of methane over noble metal catalysts, *Chemical Society Reviews*, 43 (2014) 7813-7837.

[177] P. Djinović, I. G. O. Črnivec, J. Batista, J. Levec, A. Pintar, Catalytic syngas production from greenhouse gasses: Performance comparison of $Ru\text{-}Al_2O_3$ and $Rh\text{-}CeO_2$ catalysts, *Chemical Engineering and Processing: Process Intensification*, 50 (2011) 1054-1062.

[178] C. Carrara, J. Múnera, E. A. Lombardo, L. M. Cornaglia, Kinetic and stability studies of Ru/La_2O_3 used in the dry reforming of methane, *Topics in Catalysis*, 51 (2008) 98-106.

[179] N. H. Elsayed, N. R. M. Roberts, B. Joseph, J. N. Kuhn, Low temperature dry reforming of methane over Pt–Ni–Mg/ceria–zirconia catalysts, *Applied Catalysis B: Environmental*, 179 (2015) 213-219.

[180] D. Takami, A. Yamamoto, H. Yoshida, Dry reforming of methane over alumina-supported rhodium catalysts at low temperatures under visible and near-infrared light, *Catalysis Science & Technology*, 10 (2020) 5811-5814.

[181] C. Shi, P. Zhang, Effect of a second metal (Y, K, Ca, Mn or Cu) addition on the carbon dioxide reforming of methane over nanostructured palladium catalysts, *Applied Catalysis B: Environmental*, 115-116 (2012) 190-200.

[182] P. G. Schulz, M. G. Gonzalez, C. E. Quincoces, C. E. Gigola, Methane reforming with carbon dioxide. The behavior of Pd/α-Al_2O_3 and Pd−CeO_x/α-Al_2O_3 catalysts, *Industrial & Engineering Chemistry Research*, 44 (2005) 9020-9029.

[183] S. Damyanova, B. Pawelec, K. Arishtirova, M. V. M. Huerta, J. L. G. Fierro, The effect of CeO_2 on the surface and catalytic properties of Pt/CeO_2–ZrO_2 catalysts for methane dry reforming, *Applied Catalysis B: Environmental*, 89 (2009) 149-159.

[184] F. Maleki, G. Pacchioni, Characterization of acid and basic sites on zirconia surfaces and nanoparticles by adsorbed probe molecules: A theoretical study, *Topics in Catalysis*, 63 (2020) 1717-1730.

[185] I. Wysocka, J. Hupka, A. Rogala, Catalytic activity of nickel and ruthenium–nickel catalysts supported on SiO_2, ZrO_2, Al_2O_3, and $MgAl_2O_4$ in a dry reforming process, *Catalysts*, 9 (2019) 540.

[186] R. Tang, Z. Zhu, C. Li, M. Xiao, Z. Wu, D. Zhang, C. Zhang, Y. Xiao, M. Chu, A. Genest, G. Rupprechter, L. Zhang, X. Zhang, L. He, Ru-catalyzed reverse water gas shift reaction with near-unity selectivity and superior stability, *ACS Materials Letters*, 3 (2021) 1652-1659.

[187] H. U. Hambali, A. A. Jalil, A. A. Abdulrasheed, T. J. Siang, T. A. T. Abdullah, A. Ahmad, D.-V. N. Vo, Fibrous spherical Ni-M/ZSM-5 (M: Mg, Ca, Ta, Ga) catalysts for methane dry reforming: The interplay between surface acidity-basicity and coking resistance, *International Journal of Energy Research*, 44 (2020) 5696-5712.

[188] H. Pines, W. O. Haag, Alumina: Catalyst and support. I. Alumina, its intrinsic acidity and catalytic activity, *Journal of the American Chemical Society*, 82 (1960) 2471-2483.

[189] D. Zhang, J. Zhang, D. Sun, Synthesis of cis-1,3,3,3-tetrafluoropropene by catalytic isomerization of trans-1,3,3,3-tetrafluoropropene over alumina catalysts, *Applied Catalysis A: General*, 606 (2020) 117800.

[190] T. Li, L. Zhang, Z. Tao, C. Hu, C. Zhao, F. Yi, X. Gao, X. Wen, Y. Yang, Y. Li, Synthesis and characterization of amorphous silica-alumina with enhanced acidity and its application in hydro-isomerization/cracking, *Fuel*, 279 (2020) 118487.

[191] S. Wu, Y. Li, Q. Zhang, Z. Jiang, Y. Yang, J. Wu, X. Zhao, High light-to-fuel efficiency and CO_2 reduction rates achieved on a unique nanocomposite of Co/Co doped Al_2O_3 nanosheets with UV-vis-IR irradiation, *Energy & Environmental Science*, 12 (2019) 2581-2590.

[192] S. Wu, Y. Li, Q. Zhang, Q. Hu, J. Wu, C. Zhou, X. Zhao, Formation of NiCo alloy nanoparticles on Co doped Al_2O_3 leads to high fuel production rate, large light-to-fuel efficiency, and excellent durability for photothermocatalytic CO_2 reduction, *Advanced Energy Materials*, 10 (2020) 2002602.

[193] H. Liu, T. D. Dao, L. Liu, X. Meng, T. Nagao, J. Ye, Light assisted CO_2 reduction with methane over group VIII metals: Universality of metal localized surface plasmon resonance in reactant activation, *Applied Catalysis B: Environmental*, 209 (2017) 183-189.

[194] G. Zhang, S. Wu, Y. Li, Q. Zhang, Significant improvement in activity, durability, and light-to-fuel efficiency of Ni nanoparticles by La_2O_3 cluster modification for photothermocatalytic CO_2 reduction, *Applied Catalysis B: Environmental*, 264 (2020) 118544.

[195] L. Liu, H. Zhao, J. M. Andino, Y. Li, Photocatalytic CO_2 reduction with H_2O on TiO_2 nanocrystals: Comparison of anatase, rutile, and brookite polymorphs and exploration of surface chemistry, *ACS Catalysis*, 2 (2012) 1817-1828.

[196] B. M. Reddy, K. N. Rao, G. K. Reddy, A. Khan, S.-E. Park, Structural characterization and oxidehydrogenation activity of CeO_2/Al_2O_3 and $V_2O_5/CeO_2/Al_2O_3$ catalysts, *The Journal of Physical Chemistry C*, 111 (2007) 18751-18758.

[197] S. Boullosa-Eiras, E. Vanhaecke, T. Zhao, D. Chen, A. Holmen, Raman spectroscopy and X-ray diffraction study of the phase transformation of ZrO_2–Al_2O_3 and CeO_2–Al_2O_3 nanocomposites, *Catalysis Today*, 166 (2011) 10-17.

[198] L. S. F. Feio, C. E. Hori, S. Damyanova, F. B. Noronha, W. H. Cassinelli, C. M. P. Marques, J. M. C. Bueno, The effect of ceria content on the properties of $Pd/CeO_2/Al_2O_3$ catalysts for steam reforming of methane, *Applied Catalysis A: General*, 316 (2007) 107-116.

[199] Z. Li, K. Sibudjing, Facile synthesis of multi-Ni-core@Ni phyllosilicate@CeO_2 shell hollow spheres with high oxygen vacancy concentration for dry reforming of CH_4, *ChemCatChem*, 10 (2018) 2994-3001.

[200] C. Anandan, P. Bera, XPS studies on the interaction of CeO_2 with silicon in magnetron sputtered CeO_2 thin films on Si and Si_3N_4 substrates, *Applied Surface Science*, 283 (2013) 297-303.

[201] C. Lv, C. Zhu, C. Wang, D. Li, X. Ma, D. Yang, Ultraviolet-visible electroluminescence from metal-oxide-semiconductor devices with CeO_2 films on silicon, *AIP Advances*, 5 (2015) 037107.

[202] R. Murugan, G. Ravi, G. Vijayaprasath, S. Rajendran, M. Thaiyan, M. Nallappan, M. Gopalan, Y. Hayakawa, Ni–CeO_2 spherical nanostructures for magnetic and electrochemical supercapacitor applications, *Physical Chemistry Chemical Physics*, 19 (2017) 4396-4404.

[203] K. Wang, Y. Chang, L. Lv, Y. Long, Effect of annealing temperature on oxygen vacancy concentrations of nanocrystalline CeO_2 film, *Applied Surface Science*, 351 (2015) 164-168.

[204] M. Li, X. Pan, M. Jiang, Y. Zhang, Y. Tang, G. Fu, Interface engineering of oxygen-vacancy-rich CoP/CeO_2 heterostructure boosts oxygen evolution reaction, *Chemical Engineering Journal*, 395 (2020) 125160.

[205] P. M. A. Sherwood, Introduction to studies of aluminum and its compounds by XPS, *Surface Science Spectra*, 5 (1998) 1-3.

[206] J. van den Brand, W. G. Sloof, H. Terryn, J. H. W. de Wit, Correlation between hydroxyl fraction and O/Al atomic ratio as determined from XPS spectra of aluminium oxide layers, *Surface and Interface Analysis*, 36 (2004) 81-88.

[207] M. Yang, G. Shen, Q. Wang, K. Deng, M. Liu, Y. Chen, Y. Gong, Z. Wang, Roles of oxygen vacancies of CeO_2 and Mn-doped CeO_2 with the same morphology in benzene catalytic oxidation, *Molecules*, 26 (2021) 6363.

[208] A. Elaziouti, N. Laouedj, A. Bekka, R.-N. Vannier, Preparation and characterization of p–n heterojunction $CuBi_2O_4$/CeO_2 and its photocatalytic activities under UVA light irradiation, *Journal of King Saud University - Science*, 27 (2015) 120-135.

[209] R. Singh, R. K. Soni, Laser synthesis of aluminium nanoparticles in biocompatible polymer solutions, *Applied Physics A*, 116 (2014) 689-701.

[210] P. Makuła, M. Pacia, W. Macyk, How to correctly determine the band gap energy of modified semiconductor photocatalysts based on UV–Vis spectra, *The Journal of Physical Chemistry Letters*, 9 (2018) 6814-6817.

[211] L. Tao, Y. Shi, Y.-C. Huang, R. Chen, Y. Zhang, J. Huo, Y. Zou, G. Yu, J. Luo, C.-L. Dong, S. Wang, Interface engineering of Pt and CeO_2 nanorods with unique interaction for methanol oxidation, *Nano Energy*, 53 (2018) 604-612.

[212] B. Choudhury, P. Chetri, A. Choudhury, Annealing temperature and oxygen-vacancy-dependent variation of lattice strain, band gap and luminescence properties of CeO_2 nanoparticles, *Journal of Experimental Nanoscience*, 10 (2015) 103-114.

[213] M. Alabdullah, M. Ibrahim, D. Dhawale, J. A. Bau, A. Harale, S. Katikaneni, J. Gascon, Rhodium nanoparticle size effects on the CO_2 reforming of methane and propane, *ChemCatChem*, 13 (2021) 2879-2886.

[214] T. Wang, F. Jiang, G. Liu, L. Zeng, Z.-j. Zhao, J. Gong, Effects of Ga doping on Pt/CeO_2-Al_2O_3 catalysts for propane dehydrogenation, *AIChE Journal*, 62 (2016) 4365-4376.

[215] A. Arslan, T. Doğu, Effect of calcination/reduction temperature of Ni impregnated CeO_2–ZrO_2 catalysts on hydrogen yield and coke minimization in low temperature reforming of ethanol, *International Journal of Hydrogen Energy*, 41 (2016) 16752-16761.

[216] K. Tomishige, T. Kimura, J. Nishikawa, T. Miyazawa, K. Kunimori, Promoting effect of the interaction between Ni and CeO_2 on steam gasification of biomass, *Catalysis Communications*, 8 (2007) 1074-1079.

[217] Y. Cho, S. Shoji, A. Yamaguchi, T. Hoshina, T. Fujita, H. Abe, M. Miyauchi, Visible-light-driven dry reforming of methane using a semiconductor-supported catalyst, *Chemical Communications*, 56 (2020) 4611-4614.

[218] D. G. Araiza, A. Gómez-Cortés, G. Díaz, Reactivity of methanol over copper supported on well-shaped CeO_2: A TPD-DRIFTS study, *Catalysis Science & Technology*, 7 (2017) 5224-5235.

[219] G. Jacobs, U. M. Graham, E. Chenu, P. M. Patterson, A. Dozier, B. H. Davis, Low-temperature water–gas shift: Impact of Pt promoter loading on the partial reduction of ceria and consequences for catalyst design, *Journal of Catalysis*, 229 (2005) 499-512.

[220] L. F. Bobadilla, J. L. Santos, S. Ivanova, J. A. Odriozola, A. Urakawa, Unravelling the role of oxygen vacancies in the mechanism of the reverse water–gas shift reaction by *operando* DRIFTS and ultraviolet–visible spectroscopy, *ACS Catalysis*, 8 (2018) 7455-7467.

[221] I. Tankov, W. H. Cassinelli, J. M. C. Bueno, K. Arishtirova, S. Damyanova, DRIFTS study of CO adsorption on praseodymium modified Pt/Al_2O_3, *Applied Surface Science*, 259 (2012) 831-839.

[222] A. Yee, S. J. Morrison, H. Idriss, A study of the reactions of ethanol on CeO_2 and Pd/CeO_2 by steady state reactions, temperature programmed desorption, and *in situ* FT-IR, *Journal of Catalysis*, 186 (1999) 279-295.

[223] Z. Hou, X. Zhou, T. Lin, Y. Chen, X. Lai, J. Feng, M. Sun, The promotion effect of tungsten on monolith $Pt/Ce_{0.65}Zr_{0.35}O_2$ catalysts for the catalytic oxidation of toluene, *New Journal of Chemistry*, 43 (2019) 5719-5726.

[224] F. Zhao, Z. Liu, W. Xu, S. Yao, A. Kubacka, A. C. Johnston-Peck, S. D. Senanayake, A.-Q. Zhang, E. A. Stach, M. Fernández-García, J. A. Rodriguez, Water-gas shift reaction on Ni-W-Ce

catalysts: Catalytic activity and structural characterization, *The Journal of Physical Chemistry C*, 118 (2014) 2528-2538.

[225] P. J. Linstrom, W. G. Mallard, Eds., NIST Chemistry WebBook, NIST Standard Reference Database Number 69, National Institute of Standards and Technology, Gaithersburg MD, 20899, 2020.

[226] O. Pozdnyakova-Tellinger, D. Teschner, J. Kröhnert, F. C. Jentoft, A. Knop-Gericke, R. Schlögl, A. Wootsch, Surface water-assisted preferential CO oxidation on Pt/CeO_2 catalyst, *The Journal of Physical Chemistry C*, 111 (2007) 5426-5431.

[227] M. J. Kappers, J. T. Miller, D. C. Koningsberger, Deconvolution and curve fitting of IR spectra for CO adsorbed on Pt/K-LTL: Potassium promoter effect and adsorption site distribution, *The Journal of Physical Chemistry*, 100 (1996) 3227-3236.

[228] O. Pozdnyakova, D. Teschner, A. Wootsch, J. Kröhnert, B. Steinhauer, H. Sauer, L. Toth, F. C. Jentoft, A. Knop-Gericke, Z. Paál, R. Schlögl, Preferential CO oxidation in hydrogen (PROX) on ceria-supported catalysts, Part I: Oxidation state and surface species on Pt/CeO_2 under reaction conditions, *Journal of Catalysis*, 237 (2006) 1-16.

[229] G. Jacobs, L. Williams, U. Graham, D. Sparks, B. H. Davis, Low-temperature water-gas shift: *In-situ* DRIFTS−reaction study of a Pt/CeO_2 catalyst for fuel cell reformer applications, *The Journal of Physical Chemistry B*, 107 (2003) 10398-10404.

[230] C. Morterra, A. Zecchina, S. Coluccia, A. Chiorino, I.R. spectroscopic study of CO_2 adsorption onto η-Al_2O_3, *Journal of the Chemical Society, Faraday Transactions 1: Physical Chemistry in Condensed Phases*, 73 (1977) 1544-1560.

[231] J. Szanyi, J. H. Kwak, Dissecting the steps of CO_2 reduction: 1. The interaction of CO and CO_2 with γ-Al_2O_3: An *in situ* FTIR study, *Physical Chemistry Chemical Physics*, 16 (2014) 15117-15125.

[232] A. Kaftan, M. Kusche, M. Laurin, P. Wasserscheid, J. Libuda, KOH-promoted Pt/Al_2O_3 catalysts for water gas shift and methanol steam reforming: An *operando* DRIFTS-MS study, *Applied Catalysis B: Environmental*, 201 (2017) 169-181.

[233] H. R. Park, A. U. Pawar, U. Pal, T. Zhang, Y. S. Kang, Enhanced solar photoreduction of CO_2 to liquid fuel over rGO grafted NiO-CeO_2 heterostructure nanocomposite, *Nano Energy*, 79 (2021) 105483.

[234] W. Bi, Y. Hu, N. Jiang, L. Zhang, H. Jiang, X. Zhao, C. Wang, C. Li, Ultra-fast construction of plaque-like Li_2TiO_3/TiO_2 heterostructure for efficient gas-solid phase CO_2 photoreduction, *Applied Catalysis B: Environmental*, 269 (2020) 118810.

[235] X. Su, X. Yang, B. Zhao, Y. Huang, Designing of highly selective and high-temperature endurable RWGS heterogeneous catalysts: Recent advances and the future directions, *Journal of Energy Chemistry*, 26 (2017) 854-867.

[236] X. Li, Z.-J. Zhao, L. Zeng, J. Zhao, H. Tian, S. Chen, K. Li, S. Sang, J. Gong, On the role of Ce in CO_2 adsorption and activation over lanthanum species, *Chemical Science*, 9 (2018) 3426-3437.

[237] Q. Li, Y. Ouyang, H. Li, L. Wang, J. Zeng, Photocatalytic conversion of methane: Recent advancements and prospects, *Angewandte Chemie International Edition*, 61 (2021) e202108069.

[238] National Renewable Energy Laboratory, Reference Solar Spectral Irradiance: Air Mass 1.5, 2004.

APPENDIX A. SUPPORTING INFORMATION FOR CHAPTER 2[**]

Table A-1 UV, visible, and IR light intensity of the Xe lamp measured at the location of the photocatalyst with or without the shield of quartz tube reactor.

Light Spectrum	Measured intensity (mW/cm^2) without the quartz tube	Measured intensity (mW/cm^2) with the quartz tube
UV (<400 nm)	22.9	16.5
Visible (400-750 nm)	172.5	113.9
IR (>750 nm)	116.8	86.5
Total	312.2	216.9

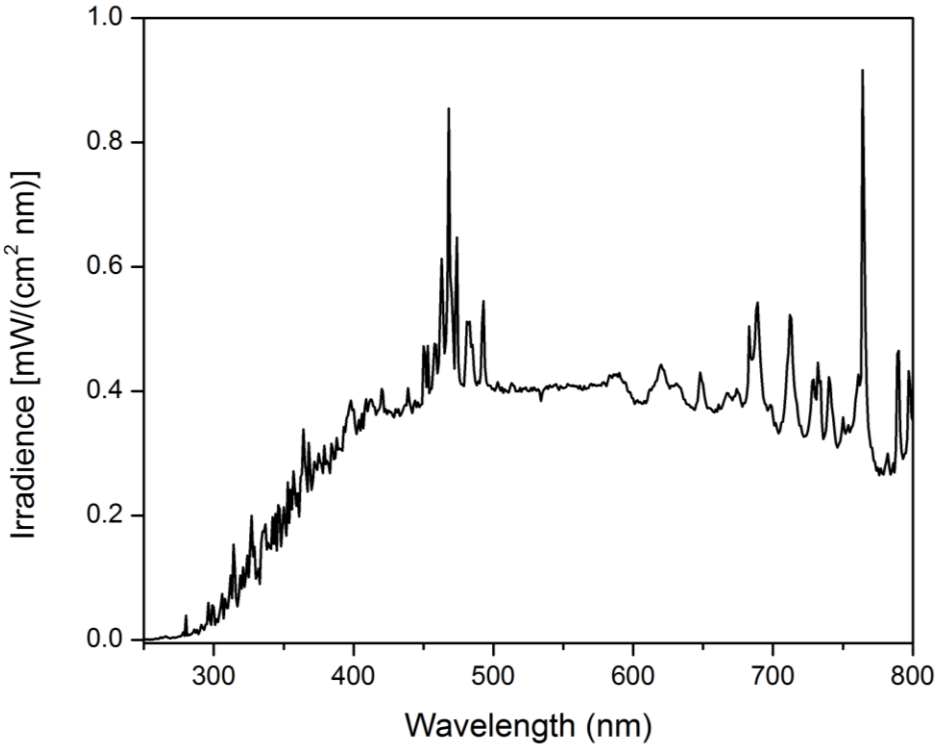

Figure A-1 Irradiation spectrum of the Xe lamp equipped with a water filter (measured 30 nm away from the bulb).

[**] Part of this appendix is reprinted with permission from "Atomic layer deposition enabled MgO surface coating on porous TiO_2 for improved CO_2 photoreduction" by Xuhui Feng, Fuping Pan, Huilei Zhao, Wei Deng, Peng Zhang, Hong-Cai Zhou, and Ying Li, *Applied Catalysis B: Environmental*, 2018, 238, 274-283. Copyright [2018] by Elsevier B.V.

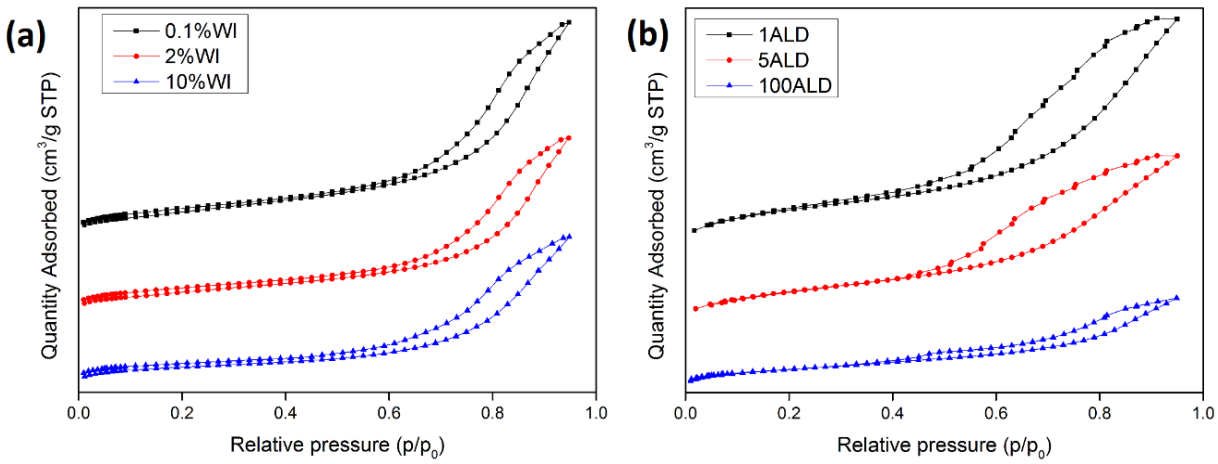

Figure A-2 N_2 adsorption-desorption isotherm of representative WI and ALD samples.

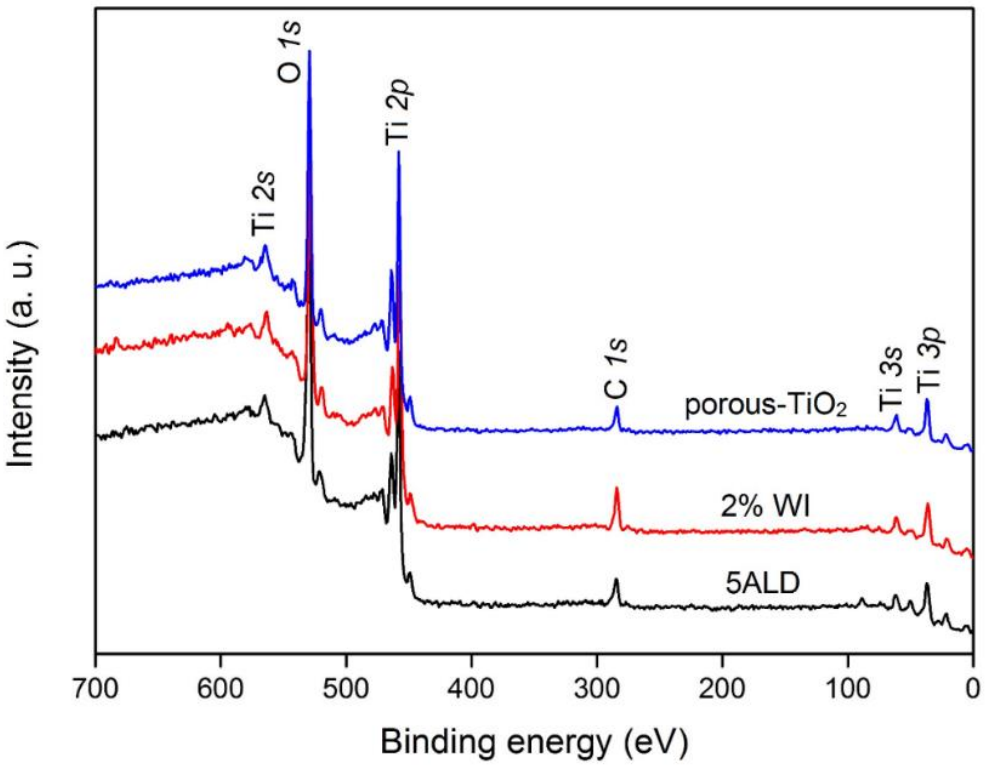

Figure A-3 XPS survey of porous-TiO_2, 2%WI, and 5ALD, where the carbon peak comes from carbon double sided tape.

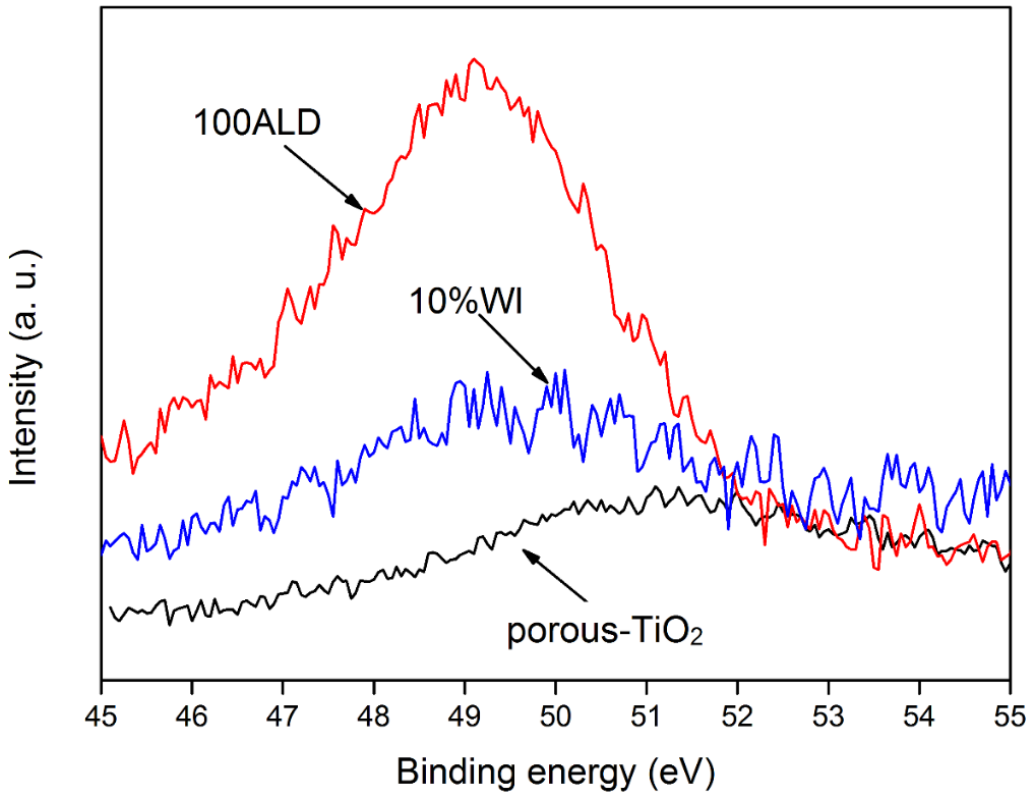

Figure A-4 Mg 2*p* XPS spectra of porous-TiO_2, 10%WI and 100ALD.

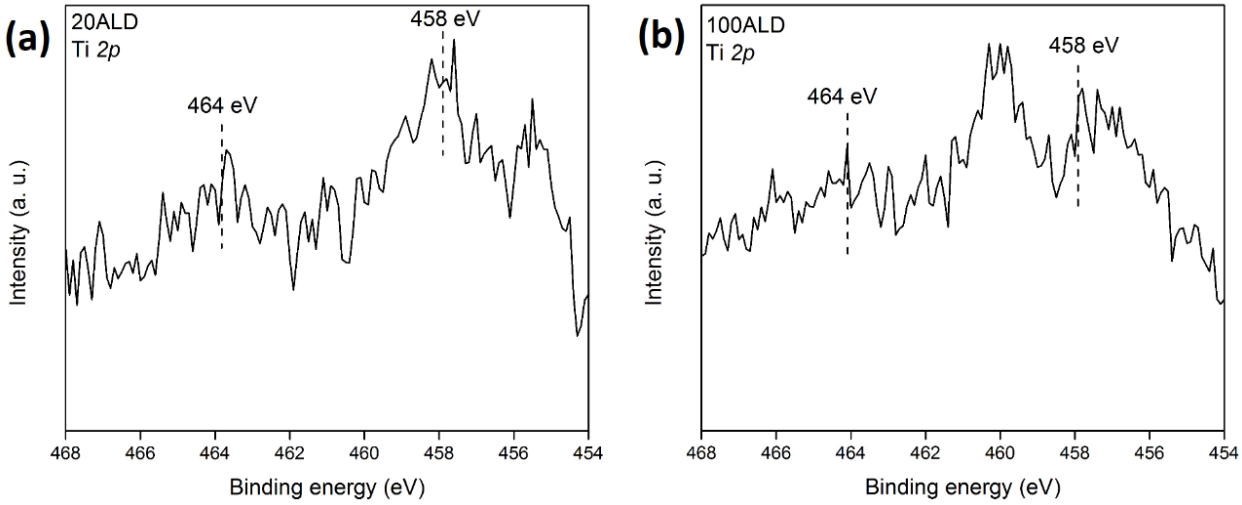

Figure A-5 (a) Ti *2p* XPS pattern of 20 ALD and (b) 100ALD.

APPENDIX B. SUPPORTING INFORMATION FOR CHAPTER 3[††]

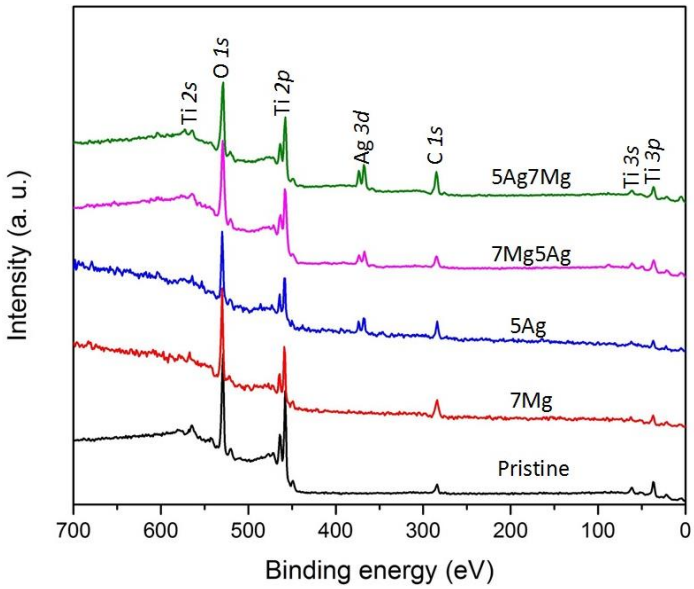

Figure B-1 XPS survey of as-prepared samples, C *1s* peaks are result of double-sided tape used in XPS analysis.

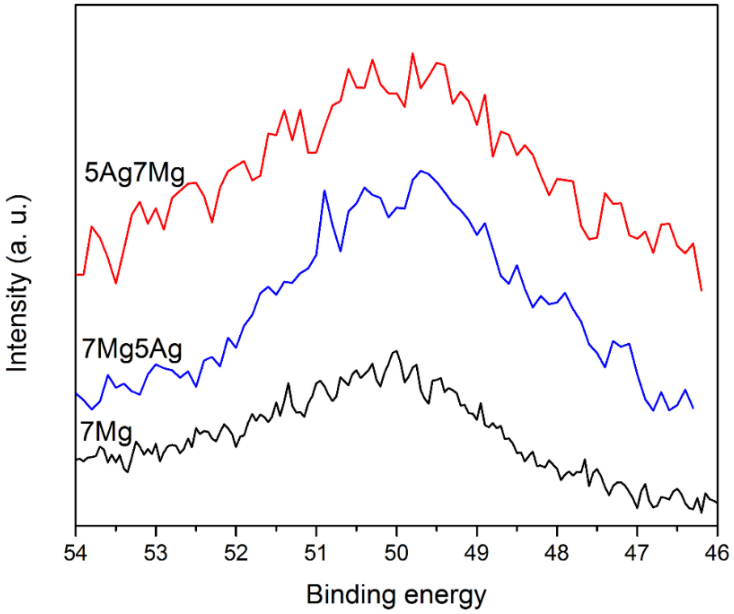

Figure B-2 Mg *2s* XPS spectra of 7Mg, 7Mg5Ag and 5Ag7Mg.

[††] Part of this appendix is reprinted with permission from "Photocatalytic CO_2 reduction on porous TiO_2 synergistically promoted by atomic layer deposited MgO overcoating and photodeposited silver nanoparticles" by Xuhui Feng, Fuping Pan, Brandon Z. Tran, and Ying Li, *Catalysis Today*, 2020, 339, 328-336. Copyright [2020] by Elsevier.

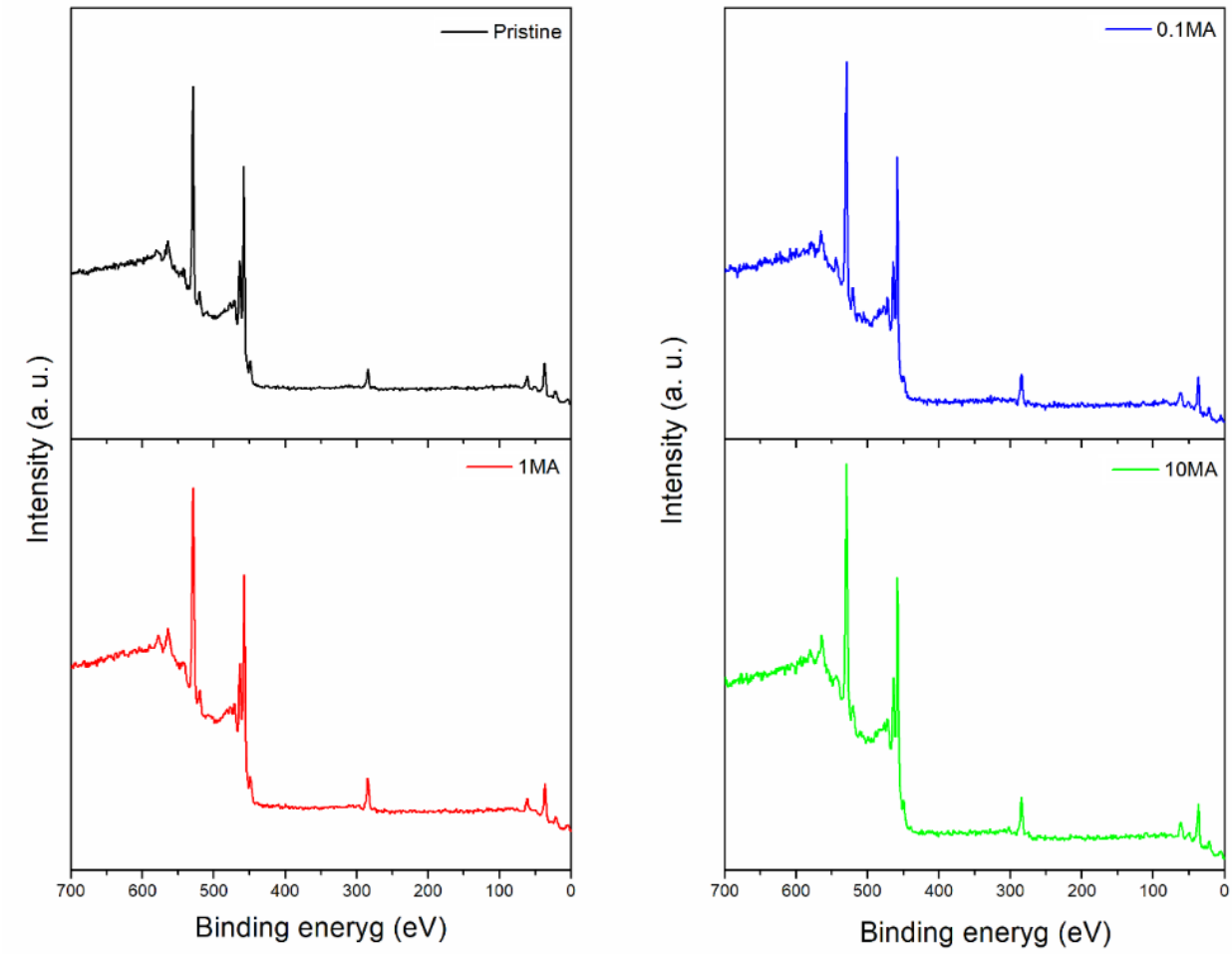

Figure C-1 XPS survey of pristine porous TiO_2, 0.1MA, 1MA and 10MA. The presence of C *1s* peak is originated from double-sided tape used in the XPS analyses.

‡‡ Part of this chapter is reprinted with permission from "Metal-organic framework MIL-125 derived Mg^{2+}-doped mesoporous TiO_2 for photocatalytic CO_2 reduction" by Xuhui Feng, Fuping Pan, Peng Zhang, Xiao Wang, Hong-Cai Zhou, Yongheng Huang, and Ying Li, *ChemPhotoChem*, 2021, 5, 79-89. Copyright [2021] by John Wiley & Sons, Inc.

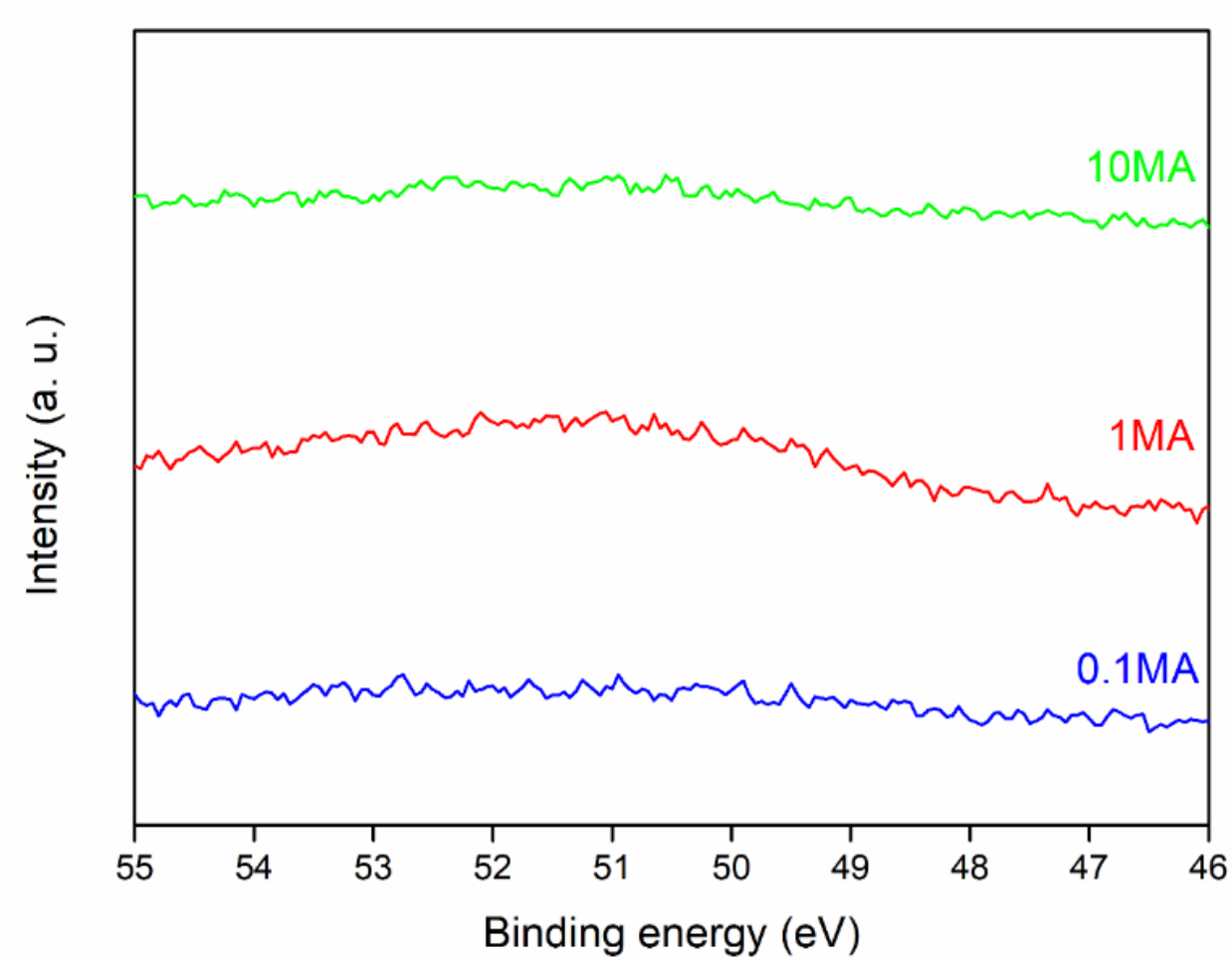

Figure C-2 Mg 2*p* XPS spectra of 0.1MA, 1MA and 10MA.

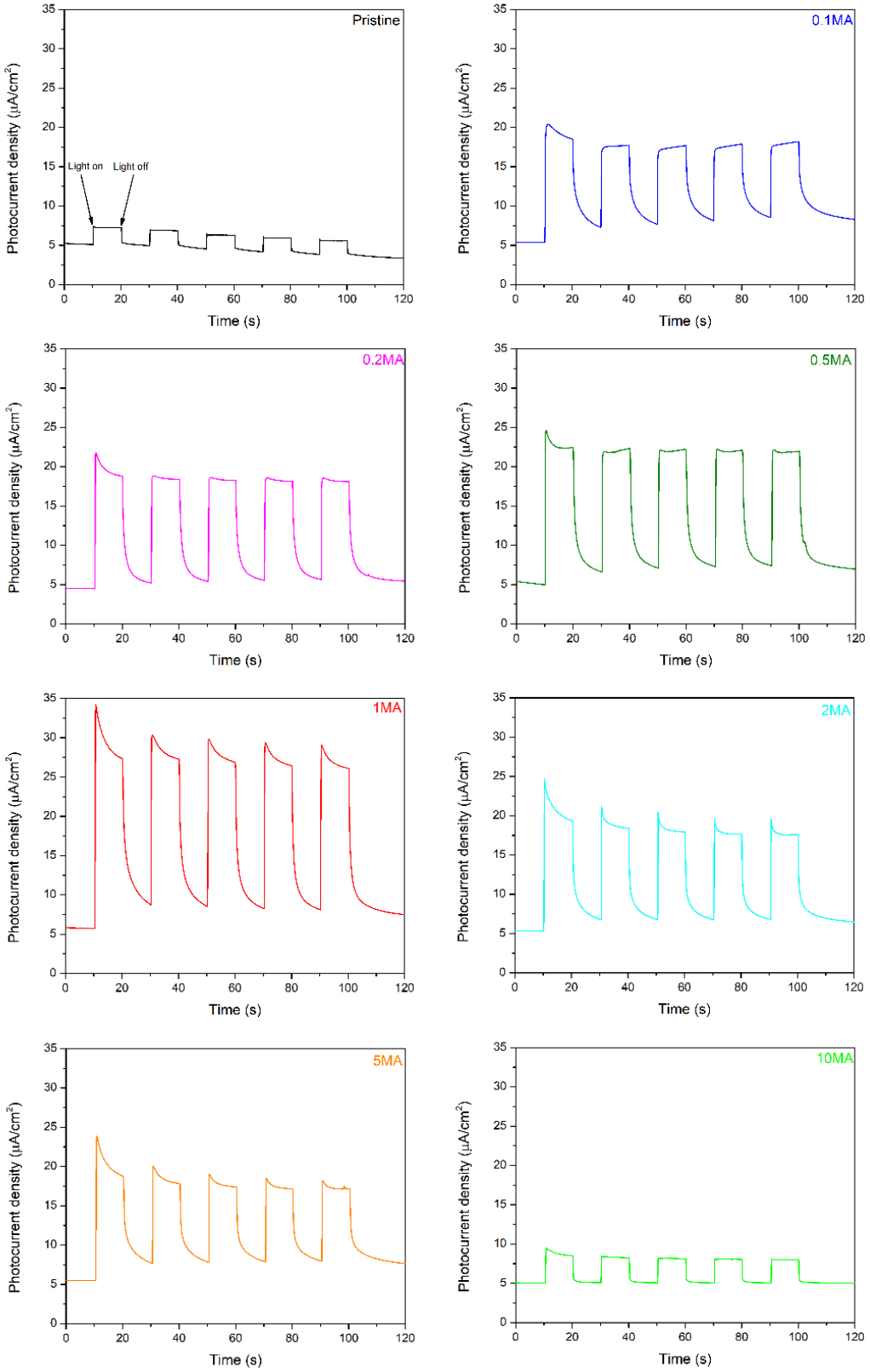

Figure C-3 Transient photocurrent density analyses of as-prepared samples.

APPENDIX D. SUPPORTING INFORMATION FOR CHAPTER 5[§§]

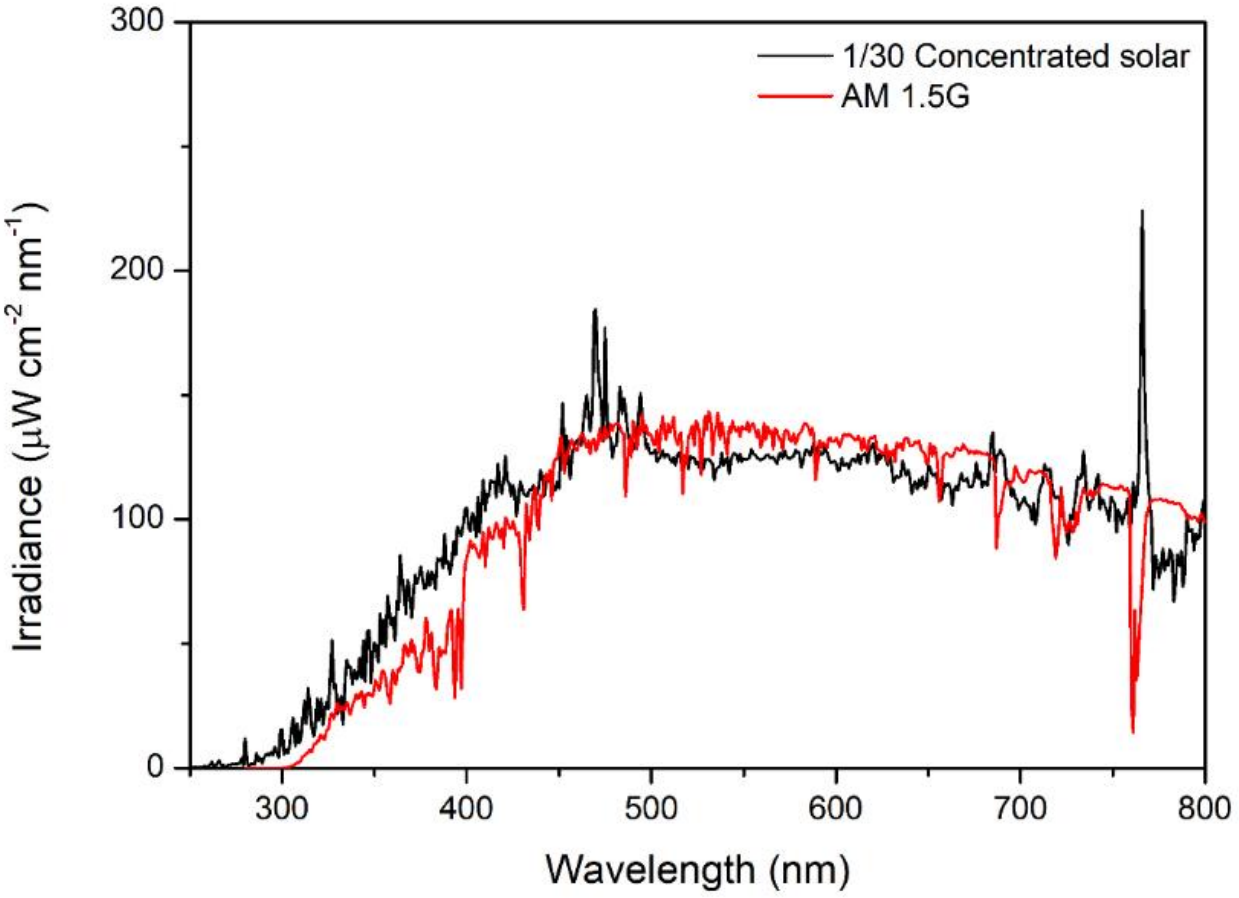

Figure D-1 Irradiation spectrum of the concentrated solar light applied in the photo-thermal driven DRM testing. AM 1.5G spectrum credit: U.S. National Renewable Energy Laboratory [238].

[§§] Part of this chapter is reprinted with permission from "Syngas production at a near-unity H_2/CO ratio from photo-thermo-chemical dry reforming of methane on a Pt decorated Al_2O_3-CeO_2 catalyst" by Xuhui Feng, Zichen Du, Erik Sarnello, Wei Deng, Cullen R. Petru, Lingzhe Fang, Tao Li, and Ying Li, *Journal of Materials Chemistry A*, 2022, DOI: 10.1039/D1TA10088B. Copyright [2022] by Royal Society of Chemistry.

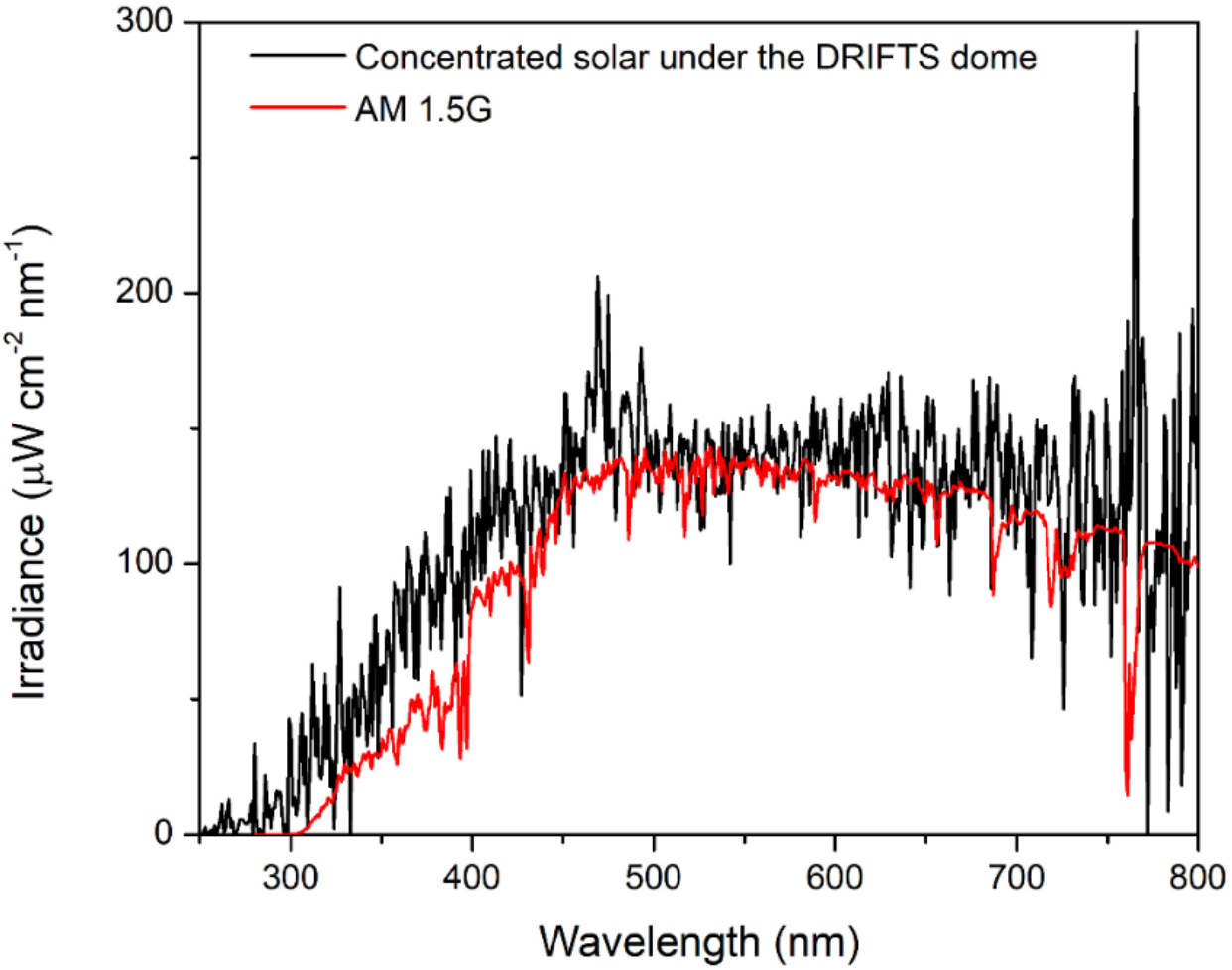

Figure D-2 Irradiation spectrum of the concentrated solar light exiting the optical fiber applied in the *in situ* DRIFTS testing. AM 1.5G spectrum data credit: U.S. National Renewable Energy Laboratory [238].

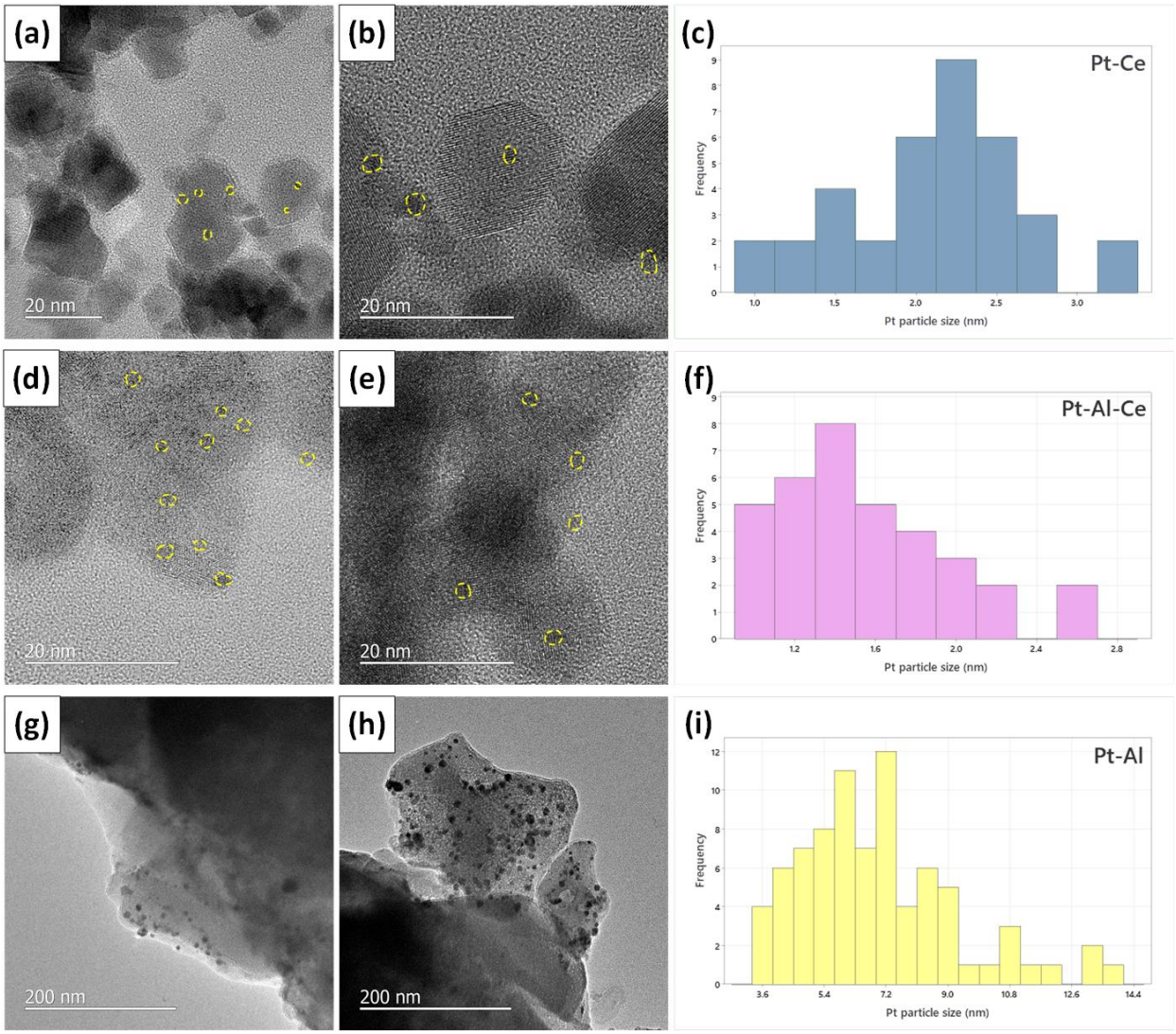

Figure D-3 (a-b) TEM images of Pt nanoparticles on Pt-Ce, (c) histogram for Pt-Ce; (d-e) TEM images of Pt nanoparticles on Pt-Al-Ce, (f) histogram for Pt-Al-Ce; (g-h) TEM images of Pt nanoparticles on Pt-Al, (i) histogram for Pt-Al.

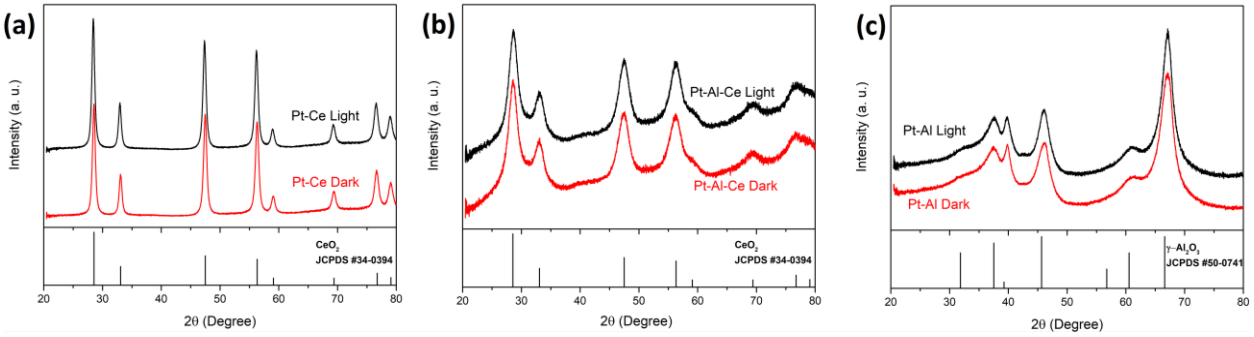

Figure D-4 XRD patterns of spent catalysts (a) Pt-Ce, (b), Pt-Al-Ce, and (c) Pt-Al.

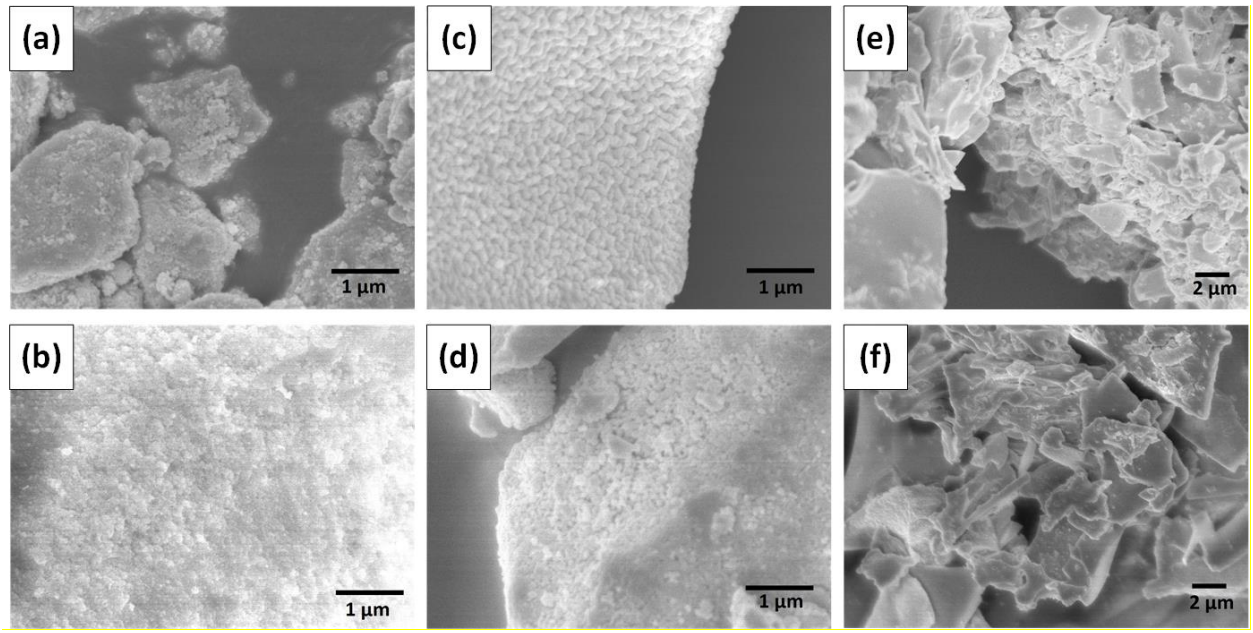

Figure D-5 SEM images of fresh catalysts: (a) Pt-Ce, (c) Pt-Al-Ce, and (e) Pt-Al; and spent catalysts after 10 h DRM reaction under concentrated sunlight: (b) Pt-Ce, (d) Pt-Al-Ce, and (f) Pt-Al.

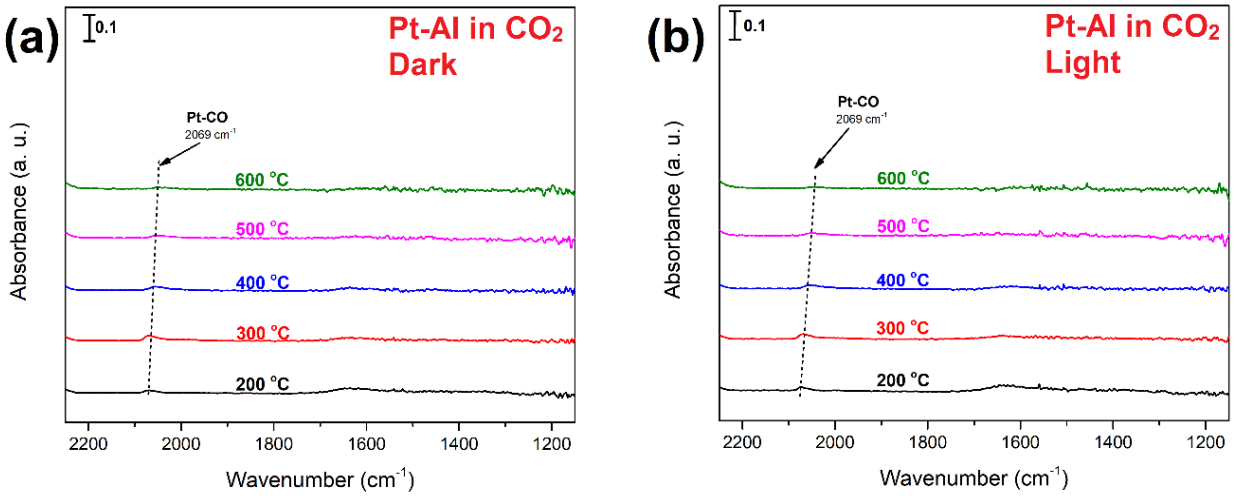

Figure D-6 *In situ* DRIFTS spectra of Pt-Al sample recorded in CO_2 atmosphere. (a) Spectra recorded in dark conditions; (b) spectra recorded in light conditions.

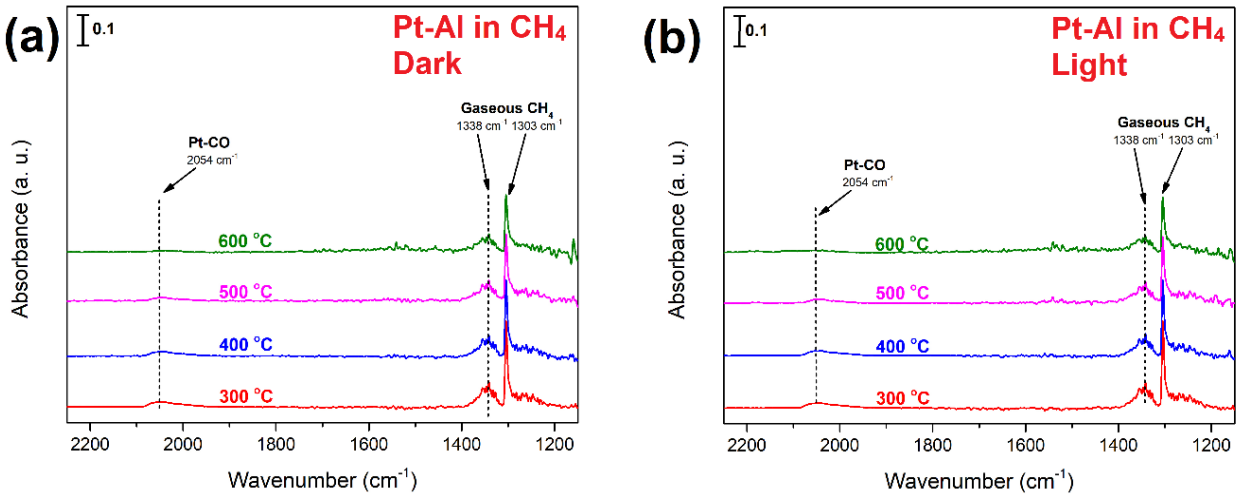

Figure D-7 *In situ* DRIFTS spectra of Pt-Al sample recorded in CH_4 atmosphere. (a) Spectra recorded in dark conditions; (b) spectra recorded in light conditions.